Experimental Studies of the Astrophysical Nuclear Reaction ^{3}He(α,γ)^{7}Be

Estudios Experimentales de la Reacción Nuclear con Interés Astrofísico ^{3}He(α,γ)^{7}Be

Mariano Carmona Gallardo

MEMORIA PRESENTADA PARA LA OBTENCIÓN DEL TÍTULO DE DOCTOR EN FÍSICA POR LA U.C.M.

JULY 2014

Directors:

Prof. Olof Tengblad
Instituto de Estructura de la Materia (CSIC)

Dr. B.S. Nara Singh
University of York

"Physics isn't the most important thing. Love is."
Richard P. Feynman
....

A mis padres

CONTENTS

LIST OF FIGURES

LIST OF TABLES

ACKNOWLEDGEMENTS

I think the first page of this thesis should be devoted to say thanks to all people who made this work possible: First of all, I would like to thank both Olof and Nara Singh for giving me the opportunity of doing something I love. Thanks for all the support, fruitful discussions, wise counsel and, above all, for their patience. Special thanks are due to Olof for encouraging me all these years and giving me the opportunity for learning physics by participating in different kinds of experiments and to attend conferences and courses. I will never forget the first time when I saw Olof in the lab with thousands of cables around and I thought: "oh my god! this is crazy I will never understand anything here". Now, long time since then, thanks to him, I am proud of understanding much more about setting up nuclear physics experiments, electronics and many more things. Thanks, Nara Singh; from you I learnt a lot of physics, our discussions were always very useful for me and without your experience and my trips to York to work with you, this thesis could have never happened. From the beginning to the last moment you have always been an important support, in not only doing physics, but in general aspects such as nice conversations and going out.

Thanks are also due to María José, first of all for trusting me when I contacted her long ago and for supporting me to get my scholarship. Thanks to her tenacity and experience, I can now write and give presentations in a better way, even in Spanish. Thanks to her for giving me valuable advice, being patient with me and worrying about me.

I am also indebted to all the people from the DRAGON group, for teaching me a lot about astrophysics, reactions, separators and techniques. Thanks to Jennifer Fallis, Greg Christian, Lars Martin, Ulrike Hager, Sarah Revee, Dave Hutcheon and specially to Barry Davids and to Chris Ruiz, for giving me all the help, support and passing me their experience. Thanks a lot to Alex Rojas, without him and his help the TRIUMF experiment could have not been possible, gracias. Thanks are also due to Michael Hass for the fruitful conversations at TRIUMF and to the CMAM crew: Ángel Muñoz, Arantza, Jaime, Antonio... the Madrid experiment was a success only because of your support.

And now, even most important is to say thanks to my colleagues and good FRIENDS who shared with me the most enjoyable discussions about physics, politics, sex or whatever, and who also suffered from my stress and bad mood from time to time. Thanks to Manoli, Miguel, Martín, Ricardo, Carlos, Jorge, Andrea, Riccardo, Mario, Jan, Irene, Ángel, Ale, Kike, Andrés, Jose, Guille, Vicente and thanks to Briz, always a big friend and person who I started this adventure with. It was a pleasure for me to share this time with all of you and I will never be grateful enough to each of you.

Special thanks to Xan, for the continuous support and for so many things.

And of course, finally thanks to my family, which I am really proud of. To my parents and to my sisters, for understanding and encouraging me to do what I like, even though they were worried and suffering a little with my madness and each time I had to take a flight to cross the ocean. Without your support I could have never reached this. Thanks, thanks and thanks.

Also, acknowledgements to the CSIC-JAEpredoc grant partly funded by the European Social Funds and to the Spanish Research Funding Agency CICYT under Project FPA2009-07387.

"Physics is like sex. Sure, it may give some practical results, but that's not why we do it"

Richard P. Feynman

PREFACE

It has been long time, since the first theories of the composition of matter were postulated. The concept of atom was already introduced in the IV century B.C. by the Greek philosopher Democritus referring to the basic component of matter, which could not be divided into smaller pieces. This idea remained during the next 25 centuries, until the experimental works of Dalton, Avogadro and co-workers, that allowed elucidating the phenomenological laws governing the different kind of atoms and their combinations. New developments of experimental techniques played crucial roles in investigating the structure of small microscopic objects. One highlight in 1895, that astonished the world due to their applicability in various fields including crystal structures, was the discovery of X-rays by the German physicist Wilhelm Röntgen.

In 1896 the French scientist Henry Becquerel studied uranium compounds, which emitted radiation continuously without requiring any gas-discharge tube to be switched on. Becquerel found that any of the uranium or its compound emitted this kind of radiation. Further investigations in this field led to identify other radioactive substances, e.g. thorium by the Polish scientist M. Curie in 1898. At this time, the British physicist J.J. Thomson, who was interested in why the X-rays made air conducts electricity, discovered that the so-called cathode rays were particles, which he called corpuscles. The name **electron** was given afterwards by the Irish physics George FitzGerald.

The New Zealand-born physicist E. Rutherford went to Britain to work with Thomson. He classified the radiation according to its penetrability: *alpha*-radiation, which is easily absorbed by matter, *beta*-radiation that is more penetrating and *gamma*-radiation that can even pass through several centimetres of lead. With this knowledge at hand, he used the radiation to probe the atom itself. In one of the most famous physics experiment by H. Geiger and E. Marsden, carried out in 1909 under the supervision of Rutherford, alpha particles impinged onto a Gold foil and the angular distribution of the scattered particles was studied. The interpretation of the results lead Rutherford to suggest in 1911 that the atom is composed of a positively-charged atomic nucleus concentrated in a reduced volume at the centre of the atom leaving the electrons to orbit around it. This model discarded the plum-pudding atomic model of Thomson and meant the discovery of the **atomic nucleus** and a new research field, **Nuclear Physics**, was born.

A large number of experiments have been and still are devoted to study the atomic nucleus and its properties since 1911. The name **proton** was given by Rutherford to the lightest nucleus, hydrogen, as possible candidate for being one of the building blocks of nuclei, as these were emitted from nitrogen atoms when alpha particles collided with them. Later, in 1932, the English physicist J. Chadwick discovered the other type of particle present in atomic nuclei, the **neutron**, which have similar mass to the proton but no electric charge.

Today, the nuclei are still seen in the same way; a collection of protons and neutrons interacting between themselves by the strong, weak and electromagnetic forces. Since the Rutherford experiment there has been a rapid progress in understanding of nuclear phenomena due to focused experimental efforts and the development of particles accelerators. Since the first linear accelerator build by Cockroft and Walton in 1930, first cyclotron by Lawrence in 1939, and first synchrotron in 1940, radiative ions beam (RIB) production has become possible using highly sophisticated accelerators even allowing exploration of highly unbound nuclei.

With the recent artificial production of the element with Z=117 [OAB10], the periodic table, where all natural or artificial chemical elements are represented, completes all species between Z=1 and Z=118. For each of the chemical elements, characterised by its number of protons, nuclei with different number of neutrons, called isotopes, exist. All these isotopes are represented in the *Chart of nuclei*, where all known nuclei (around 3000) are classified according to their number of protons and number of neutrons. It is worth noting that ∼3000 more are predicted to exit but not experimentally observed. Figure 1 shows a diagram of the *Chart of Nuclei* with neutron and proton numbers on x and y axes, respectively. Here, the different colours indicate how the nuclei decay, see the caption for more details. A review about the evolution, properties and the information displayed in the chart is available, for example, in reference [NM10].

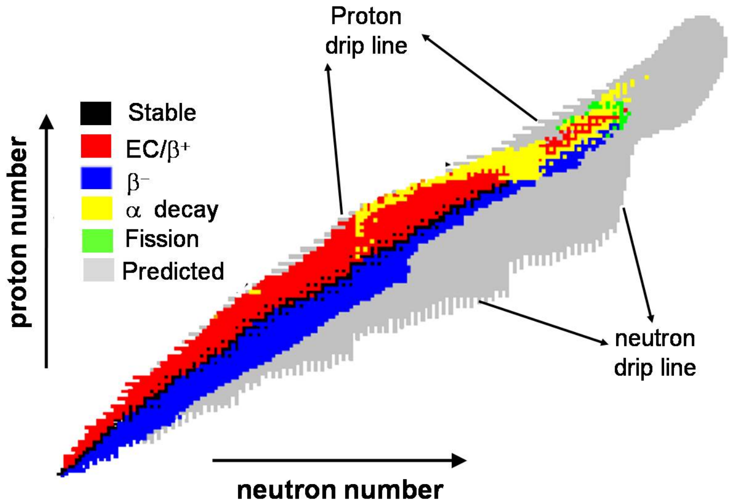

Figure 1: *A diagram of the Chart of Nuclei with the horizontal and vertical axes showing the number of neutrons and protons, respectively. All the stable isotopes and those whose half-lifes are higher than the Universe life time are shown in black. The β^+/electron capture decaying nuclei (red), those decaying by β^- process (blue), the α particle emitters (yellow), and those decaying by spontaneous fission (green) are also shown. The theoretically predicted nuclei that are not experimentally produced so far are displayed in grey. The whole region is bounded by the proton and neutron drip lines, which indicate for each element (same atomic number Z) the minimum (proton drip line) and maximum (neutron drip line) number of neutrons that can form bound nuclei.*

The nuclear landscape is still an open play ground to understand the properties of all nuclei, how they form and how they interact. The nucleus contains 99% of the total mass of the ordinary matter, therefore, information of nuclear properties and interactions is crucial in the understanding the synthesis of elements in the universe, i.e. the observable matter itself. Studying the atomic nucleus is much more rich and interesting due to its applicability in fields beyond fundamental science. Example of scientific fields where understanding of nucleus is directly applicable include medical imaging, hadron-therapy and nuclear energy.

The expert committee *Nuclear Physics European Collaboration Committee (NuPECC)* published in 2010 the *Long Range Plan: Perspectives of Nuclear Physics in Europe*. Among other issues, they review the recent achievements and current state of the art in Nuclear Physics and identify the open problems to be solved, which forms a broad part of motivation for our work. The documents is available at http://www.nupecc.org/index.php?display=lrp2010/main.

The work presented in this thesis has direct relevance to the *Nuclear Astrophysics*. However, direct implications on *Nuclear Structure and Dynamics* are also expected. Directly from the NuPECC Long Range Plan 2010, the key questions to be answered from nuclear astrophysics include:

- How and where are the elements made?
- Can we understand, and recreate on Earth, the critical reactions that drive the energy generation and the associated synthesis of new elements in Stars?
- How does the fate of a star depend on the nuclear reactions that control its evolution?
- What are the properties of dense matter in a compact star such as a neutron star o a hypothetical quark star?

The studies here presented aim to address part of the first question. Specifically, we study the production of the isotope ^{7}Be via the ^{3}He(α,γ)^{7}Be nuclear reaction. This reaction is important in two astrophysical scenarios. Firstly, it is relevant to the Big-Bang Nucleosynthesis, that is responsible for the abundance of the primordial ^{7}Li element in the universe. Secondly, it plays an important role in the helium burning stage in the stars. Specifically, this reaction is important in order to explain the high energy neutrino flux from the Sun.

This thesis is divided into seven main chapters. In the first chapter, general concepts used in nuclear astrophysics will be discussed. Different astrophysical processes responsible of creating the nuclei will also be briefly explained and those where our reaction plays a determining role will be detailed. In addition, previous experimental knowledge of this reaction will be explained. In the second chapter, the theoretical formalisms used to describe the underlying physics are discussed. In the third chapter, the two experimental techniques used to determine the capture cross sections will be described in detail. In the fourth chapter, the simulations performed in order to determine the acceptance of DRAGON will be presented. The fifth chapter gives the analysis techniques used to extract different experimental observables that lead to the results. In the sixth chapter, discussions about the experimental results comparing with other experiments and theories as well as future work will be presented. Finally, in the seventh chapter, the main outcomes of this research are listed.

Writing, I have tried that whoever physicist reading this thesis can understand the physics case, the procedure, the results and the discussion. For this reason I have added three appendix at the end. The first appendix, (A), details how a silicon detector works (kind of detector used in our experiments) works. Also the electronic used is explained as an example of typical nuclear physics modules used to process electric signals. In appendix B, the centre of mass reference system, commonly used when describing nuclear reaction and therefore throughout this thesis, is explained. Moreover, the kinematics of the reaction is detailed for reference. Finally, in appendix C, general concepts related to error estimation are briefly recalled and how the errors are estimated for one of the experiments is detailed. Appendixes D and E are Spanish and English summaries, respectively.

"Learn from yesterday, live for today, hope for tomorrow. The important thing is to not stop questioning."

Albert Einstein

CHAPTER 1

INTRODUCTION

Abstract: *In this chapter some of the essential nuclear astrophysics concepts are introduced in order to motivate the capture reaction studied in this thesis. Concepts such as the astrophysical S-Factor and the Gamow Peak will be discussed. In continuation, the nuclear astrophysical processes responsible for producing different nuclear isotopes and the astrophysical sites where they originate will briefly be presented. The two distinct scenarios where the* ^{3}He(α,γ)^{7}Be *reaction plays an important role, namely "The solar neutrino flux" and "The primordial* ^{7}Li *production" will be briefly introduced. Finally, previous experimental studies will be discussed.*

Since the beginning of time the Human Being has wondered, What are we? Where do we come from?, or What is the origin of the Universe?. Answering these metaphysical questions have been an ongoing quest not only from a philosophical or religious point of view but also from a scientific scenario. It is questions such as What is the origin of the elements? that nuclear physics research specifically addresses.

The current composition of the Universe is the result of the nucleosynthesis proceed from the initial material, namely H and ^{4}He nuclei created a few minutes after the Big Bang, [Hoy46, Hoy54]. Nuclear reactions, together with other processes such as β decay, are the mechanisms responsible of this synthesis, and they need to be understood in order to explain the evolution, structure and composition of the past, present, and future Universe.

Specifically, this thesis focuses on studying the synthesis of ^{7}Be through the nuclear reaction ^{3}He(α,γ)^{7}Be. The cross section of this reaction is required by the *Standard Solar Model (SSM)* that explains the evolution, behaviour and composition of the Sun. It is also an important input parameter for theoretical calculations explaining the cosmological origin of light elements in the early Universe due to the *Big Bang Nucleosynthesis (BBN)* .

1.1 Nuclear Astrophysics: Some Relevant Basic Concepts

In stars (or in astrophysical scenarios such as the Big Bang) energy is released via the fusion of two atomic nuclei, i.e. through nuclear reactions. Nuclear reactions are usually denoted as:

$$a + X \rightarrow Y + b$$

where a is the projectile, X is the target, Y is the recoiling nucleus and b is the ejectile of the reaction. Normally, a and b are light nuclei but occasionally they can be γ-rays, which cases the reactions are called *nuclear photoeffect* and *radiative capture*, respectively. When the nuclear reactions are carried out in laboratories, a is usually accelerated as a beam and X is a stationary target. In the case of direct kinematics the projectile is lighter than the target while reactions in inverse kinematics are carried with beams heavier than targets. The nuclear reactions are also denoted in a compact way as:

$$X(a, b)Y$$

This convention will be used in the following section, specifically to discuss (p,γ) or (α,n) astrophysical reactions involving the same type of one interacting nucleus and one reaction product. It should be pointed out that following the nuclear astrophysics convention of (α,γ) reactions, our reaction of interest will be denoted as ^{3}He(α,γ)^{7}Be independently that the beam is ^{3}He or ^{4}He (α).

The available energy in the above reactions, by the fact of converting some nuclear masses in others ($E = mc^2$), is known as the *Q-value* of the reaction and it is defined as:

$$Q = (m_a + m_X - m_b - m_Y)\, c^2 \tag{1.1}$$

If Q<0, then the reaction is endothermic and only proceed upon providing an extra energy. If Q>0 the reaction is exothermic and, in principle it could occur even at zero energy. In reality, exothermic reaction may not proceed at zero energy due to the existence of Coulomb and centrifugal barriers as well as the competing reaction channels (barriers and competing channels are also present in endothermic reactions). Therefore, there is a probability for the reaction to occur, the **cross section** $\boldsymbol{\sigma(E)}$, which is defined by:

$$\boldsymbol{\sigma(E)} = \frac{N_R/t}{(N_X/A)(N_a/t)} \tag{1.2}$$

where N_R/t is the number of reactions per unit of time, N_X/A is the number of target nuclei per unit area and N_a/t is the number of incident beam particles per unit of time.

For charged particle induced reactions[a], the Coulomb barrier energy between the interacting nuclei, E_C, is given by:

$$E_c = \frac{Z_a Z_X e^2}{R_n} \tag{1.3}$$

here, Z_a and Z_X are the atomic number of the interacting nuclei, R_n is the square well radius, and e is the electron charge. The potential seen by a projectile when approaches a nucleus assuming no centrifugal barriers is shown in Figure 1.1. Classically, if we consider no centrifugal barriers (ℓ=0) and assuming the target at rest, the beam energy should be higher than E_c to overcome the Coulomb barrier and proceed to the reaction by dropping into the well potential.

[a] Also neutron induced reactions are relevant in nuclear astrophysics but they will not be discussed here

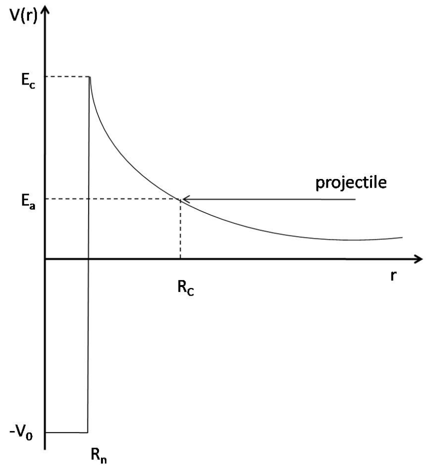

Figure 1.1: *A schematic diagram of the potential seen by a projectile "a" with incoming energy E_a in a nuclear reaction considering no centrifugal barriers (ℓ=0, s-wave). The total potential is given by an attractive potential well for r<R_n and by the Coulomb potential for r>R_n. R_c is the radius at which the incident energy is equal to the Coulomb potential energy, $E_a = Z_a Z_X e^2/R_c$ where Z_X and Z_a are the atomic number of the target and the beam in the nuclear reaction, respectively.*

Nevertheless, despite the fact that the incoming energy is lower than E_c, quantum mechanics predicts a probability for penetrating the barrier by *tunnel effect*. The transmission coefficient, giving the probability for penetrating the Coulomb barrier for an s-wave (which is a likely scenario at astrophysical energies) can be given by [Ili07]:

$$P_{\ell=0} \approx exp\left(-\frac{2}{\hbar}\sqrt{\frac{2m}{E}}Z_a Z_X e^2\left[\frac{\pi}{2} - 2\sqrt{\frac{E}{E_c}} + \frac{1}{3}\left(\frac{E}{E_c}\right)^{3/2}\right]\right) \tag{1.4}$$

where E is the energy in the **centre of mass system** or relative energy. For the astrophysical energies of interest, which are well-below the Coulomb barrier, i.e. E«E_C, the $P_{\ell=0}$, (in the following P_0) can be approximated to:

$$P_0 \simeq exp\left(-\frac{2\pi}{\hbar}\sqrt{\frac{m}{2E}}Z_a Z_X e^2\right) \equiv e^{-2\pi\eta(E)} \tag{1.5}$$

known as **Gamow factor**. The Sommerfeld parameter, η, is given by

$$\eta(E) = \frac{2\pi Z_a Z_X e^2}{hv} \tag{1.6}$$

where v is the relative velocity of the interacting nuclei and h is the Plank constant. Numerically, $2\pi\eta = 0.989534 Z_a Z_X \sqrt{\frac{1}{E}\frac{M_a M_X}{M_a+M_X}}$.

Moreover, the cross section is also proportional to a geometrical factor[b] $\pi/k^2 \propto 1/E$, being k the wave-number. Therefore, the reaction cross section, $\sigma(E)$, can be written as the product of three factors:

$$\sigma(E) = \frac{1}{E}S(E)e^{-2\pi\eta(E)} \tag{1.7}$$

[b]It can be proved that the total cross section for all reaction channels different from the elastic scattering is given by: $\sigma_\ell = \frac{\pi}{k^2}(2\ell+1)\left(1-\left|e^{2i\delta_\ell}\right|^2\right)$ [Ili07]

where the factor $S(E)$ is the **astrophysical S-factor** and E is the **centre of mass energy**. It is worth pointing out that the S-factor contains all the information related to nuclear properties (effects of finite nuclear size, higher partial waves, anti-symmetrisation etc...). Moreover, the high and well-known energy dependence of the reaction cross section due to the Coulomb interaction is avoided in the astrophysical factor, and this allows easier extrapolations of this factor to low energies. The situation is demonstrated in Figure 1.2 using the ^{3}He(α,γ)^{7}Be reaction. While the dependence of σ with E is doubly exponential, with the S-factor is nearly linear.

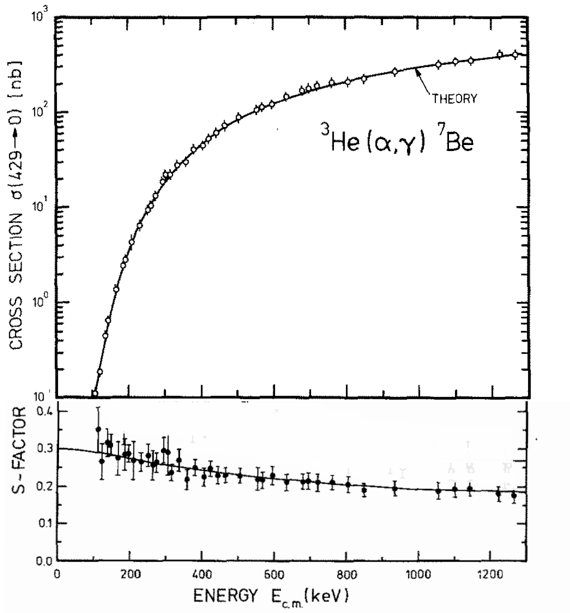

Figure 1.2: *Energy dependence of the cross section and the S-factor for the ^{3}He(α,γ)^{7}Be reaction. While the cross section, in the upper panel, shows a doubly exponential dependence with energy, the S-factor in the lower panel, shows a smooth energy dependence and allows reliable extrapolations. Figure is taken and adapted from reference [KBB82].*

It should be also pointed out that the Gamow factor is an approximation of the s-wave Coulomb barrier penetration probability. However, even when there is a contribution from the other partial waves (p-waves, d-waves...), the expression 1.7 results also in a reduced energy dependence for the S-factor.

The **reaction rate** between the two interacting nuclei a and X in astrophysical environments can now be rewritten as (see expression 1.2):

$$r_{aX} = N'_a N'_X v\sigma(v) \tag{1.8}$$

where $r_{aX} = N_R/(Vt)$ is the number of reactions per unit of volume and time, and $N'_a = N_a/V$, and $N'_X = N_X/V$ are the number of interacting nuclei per unit of volume. In the astrophysical environments as stellar plasmas, there is a relative velocity distribution for the interacting nuclei, $P(v)$. This kinetic energy distribution results from the thermal motion of the nuclei, hence the reactions are referred as *thermonuclear reactions*. The probability of finding a nucleus with a velocity v+dv is given by $P(v)dv$ and the expression 1.8 is converted into:

$$r_{aX} = N'_a N'_X \int_0^\infty vP(v)\sigma(v)dv \equiv N'_a N'_X \langle v\sigma(v)\rangle. \tag{1.9}$$

Under the conditions of hydrostatic equilibrium of stellar plasmas, the velocities of the motion of the interacting nuclei are non-relativistic and the nuclei gas is non-degenerate. Thus, the relative velocity distribution of the interacting nuclei is given in most cases by a Maxwell-Boltzmann distribution:

$$P(v) = 4\pi v^2 \left(\frac{\mu}{2\pi k_B T}\right)^{3/2} e^{\frac{-\mu v^2}{2k_B T}} \tag{1.10}$$

here k_B is the Boltzmann constant, $\mu = m_a m_X/(m_a + m_X)$ is the reduced mass, T is the temperature and v the relative velocity. From expressions 1.7, 1.9 and 1.10 we now obtain

$$\langle \sigma v \rangle = \left(\frac{8}{\pi\mu}\right)^{1/2} \left(\frac{1}{k_B T}\right)^{3/2} \int_0^\infty S(E) e^{-\frac{E}{k_B T}} e^{-2\pi\eta} dE. \tag{1.11}$$

The highest energy dependence of the rate in the expression 1.11 is in the two exponential terms in the integral. The first one, related to the Maxwell-Boltzmann distribution of the nuclei energies (which have a maximum at $\frac{1}{2}k_B T$) goes to zero at high energies, and the second one related to the tunnelling probability through the barrier which goes to zero for low energies. Therefore, the energy at which the reaction probability is maximum can be obtained by convoluting the two functions. The resulting function is known as **Gamow Peak** and the energy at which the reaction rate maximises is known as the **Gamow Energy**.

The Gamow Peak for the ^{3}He(α,γ)^{7}Be reaction in the Sun is shown in Figure 1.3. The green curve shows the Maxwell Boltzmann distribution factor, $e^{-\frac{E}{k_B T}}$, for T$_{sun}$ $\sim$ $1.55 \cdot 10^7$ K. The energy which maximise the probability for this reaction is $\frac{1}{2}k_B T \simeq 0.65$ keV and the probability drops for energies higher than this one. The red line shows the tunnel effect probability $e^{-2\pi\eta}$ (recall that this has been taken for s-waves and E«E_C approximations) indicating that the higher the energy is the more likely to cross the barrier. The blue line shows the convolution of both curves, whose maximum of $\sim$22 keV is the Gamow Energy for ^{3}He+^{4}He capture reaction.

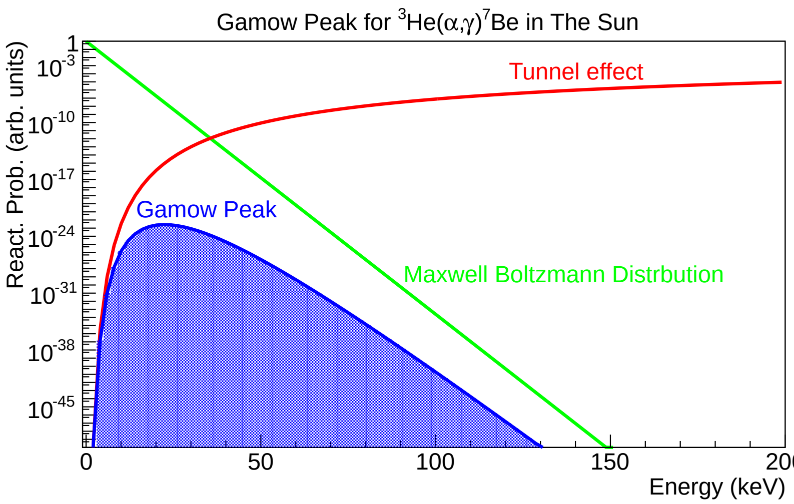

Figure 1.3: *The Gamow Peak for the ^{3}He(α,γ)^{7}Be reaction in the Sun. The red line shows the probability of tunnel effect given by $e^{-2\pi\eta}$. The green line shows the Maxwell Boltzmann energy distribution of nuclei with temperature T$_{sun}$ $\sim 1.55 \cdot 10^7$ K and the blue shaded region shows the convoluted function resulting with the Gamow Peak. The maximum in the Gamow Peak is known as Gamow Energy, which in this case is $\sim$22 keV.*

For a constant value of S(E) respect to E in the Gamow Peak region, the Gamow Energy can be estimated by equalling to zero the first derivative of the integrand in equation 1.11 respect to E. This calculation results in:

$$E_{\text{Gamow Energy}} = \left[\left(\frac{\pi}{\hbar}\right)^2 \left(Z_a Z_X e^2\right)^2 \left(\frac{\mu}{2}\right) (k_B T)^2 \right]^{1/3} \tag{1.12}$$

1.2 Nuclear Astrophysical Processes

Although in general it can be claimed that the Universe is rather static with little global activity, it is worth noting that there are some very active local scenarios, as stars or supernovae explosions, where nearly all nuclei are continuously being produced. And these are, indeed, the elements which will create new different astrophysical sites, as future galaxies or planets. Thinking for example of Earth, a lot of nuclear processes occurred in different time periods before producing the big quantity of elements present in it. Not only different periods, but also different scenarios under different conditions are needed to explain the production of all the elements from the primordial H and ^{4}He that were created following the Big Bang explosion.

Figure 1.4, adopted from [SR01], shows a part of the chart of nuclei where nuclei, the processes by which they are usually produced and the corresponding astrophysical sites are colour coded (see caption for more details).

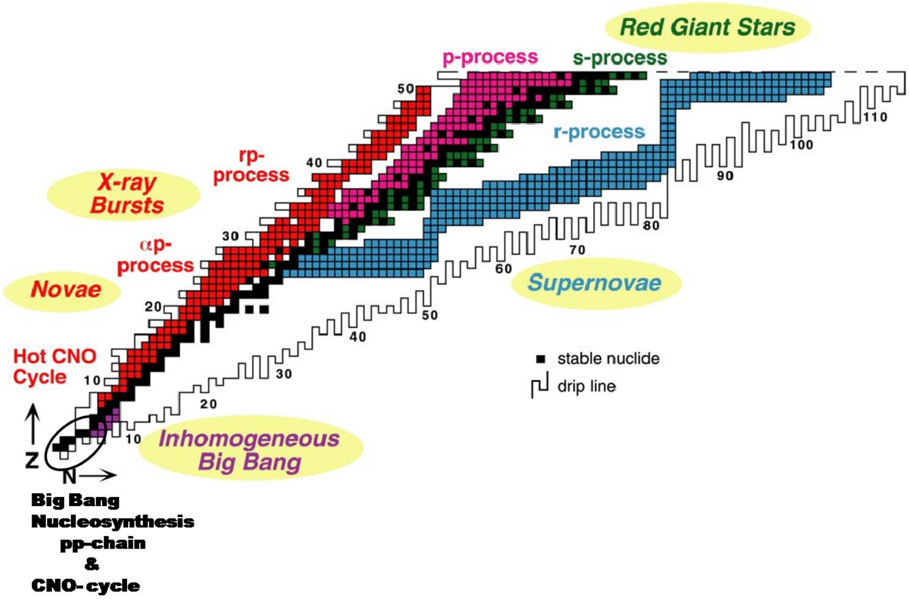

Figure 1.4: *A diagram adapted from reference [SR01] where the nuclei produced in a given process are plotted with the same colour. The astrophysical scenarios in which the nuclei are created are also indicated with the same colour inside ellipses filled with yellow. The black open ellipse, enclosing the nuclei produced in the Big Bang Nucleosynthesis, pp-chain and CNO-cycle has been added to the original plot in order to show the names of processes creating the light nuclei.*

The primordial nucleosynthesis was the origin of the synthesis of light nuclei up to mass A=7. The main remaining nucleus is H, but also $^{3,4}He$, D, and small quantities of $^{6,7}Li$. All other higher masses nuclei were created in negligible quantities. Later, stars are formed via gravitational attraction and the hydrogen burning starts when the temperature inside rises up to $T \sim (10-15)\cdot 10^6 K$. In light stars, with masses smaller than eight solar masses, the pp-chain, triple-α reaction and CNO cycle are the main mechanisms fusing nuclei with masses no higher than ^{20}Ne. These processes (excluding the triple-α) together with the BBN, where our reaction plays a determining role, will be detailed in the next sections. The triple α-process, which also produce light nuclei, will be briefly described bellow.

The other processes shown in Figure 1.4 occur in higher-mass stars and stellar explosions. These processes are required to explain e.g. the abundance of high-mass elements in the Solar System. In the following a brief description of some of the processes is presented together with the triple-α process. For more details see for example [Rol88]:

triple-α

In light stars with a high quantity of α particles originated from the Big Bang, there is a small probability of trapping two α particles in the low-lying resonances in ^{8}Be. This small probability is large enough to allow for a third α particle to collide with the resonance producing a triple-α composite. This composite is an excited state in ^{12}C, which can either decay back to three α particles, or by γ emission to lower energy states in ^{12}C . The key point of this process is that there is a narrow 0^+ resonance in the ^{8}Be+α=^{12}C* system at 287 keV above the 3α breakup threshold. This resonant state, known as the *Hoyle state*, is essential in order to explain the relative high abundance of ^{12}C in the Universe.

α-burning

After the pp-chain, CNO-cycle and triple-α process some residual nuclei, mainly oxygen and carbon, exist. In high-mass stars, the gravitational pressure is high enough to increase the temperature allowing the α particles to overcome the Coulomb barrier of the residual nuclei. Thus, a series of α-capture reactions can occur producing higher mass nuclei up to ^{56}Fe.

s-process

In Red Giants, some extra neutrons can be produced via the (α,n) reactions during the α-burning. These neutrons will react, for example, with the iron seed nuclei produced in the α-burning stages via (n,γ) reactions. These reactions will be followed through the stable iron isotopes line until some unstable isotope is reached, then, as the (n,γ) is a much slower process (therefore is called s(slow)-process) than the β decay, the nucleus will β-decay to the (Z+1,N-1) daughter nucleus. This nucleus can undergo the (n,γ) process until another β^- unstable nucleus is produced and thus the nucleosynthesis proceeds. With this process, nuclei as heavy as uranium can be produced.

r-process

Although by the previous processes nearly all stable elements are produced, the abundances seen for example in the Solar System cannot be explained and additional processes and scenarios are needed. One of these scenarios are the Supernova explosions. In a Supernova explosion, the higher temperatures and neutron abundances allow for the (n,γ) reactions to reach more unstable isotopes as the reaction times at these temperature are faster (r(rapid)-process) than the β decay times. The (n,γ) reactions end either when the neutron drip line is reached (unbound nuclei) after which β-decay will follow until reaching a stable nuclei with the same mass or, where the closed-shell nuclei at N=82,126 and 184 are found. In the latter case, the process times are comparable to β decay times. These are known as *waiting point* nuclei.

rp-process

The rp-process mainly occurs in binary systems involving neutron stars. In such binary system, hydrogen is exchanged between the two starts. As a result X-rays are produced with high flux, and thus these systems are known as *X-Ray bursters*. An increase in temperature leads to a series of (p,γ) reactions usually hindered by Coulomb barriers. The (p,γ) reactions will follow until either the proton drip line is reached, or the β decay times are fast enough to compete with the proton capture rate. After β-decays, (p,γ) reactions continue up to nuclei with A$\sim$100 where the higher Coulomb barriers hinder the reaction.

p-process

In order to explain some neutron deficient nucleus abundances, processes other than those described above are needed. The p-process is thought to happen in the core collapse supernova explosion. A shock wave passing through the material initiate a sequence of (γ,n), (γ,p) and (γ,α) reactions on stable seed nuclei producing proton-rich nuclei.

1.3 The Sun and the Solar Neutrino Problem

Pauli postulated in 1931 a new particle in order to justify the energy and momentum conservation in the β decay process, that afterwards was named as *neutrino-ν* (small neutral particle) by Fermi. Since then, due to the particle was postulated by the Standard Model as a massless neutral particle interacting weakly with matter, a lot of complex experiments have been carried out in order to directly detect this particle and study its properties.

As the Sun is the nearest star to us, it is the best studied. In the context of neutrino physics it is invaluable as the Sun produces neutrinos. The *Standard Solar Model* (SSM) treats the processes happening in the Sun and models the astrophysical environment to predict solar neutrino fluxes based on the following input parameters (see for example [BHL82]):

- Nuclear reactions **cross sections** (cf. Figure 1.5)
- Solar constant
- Abundances for solar elements heavier than helium
- Opacities
- Equation of state
- Solar Age

About 99% of the energy produced in the Sun is originated via a series of nuclear reactions, the so called *pp*-chain, whose overall effect is to convert four protons into one ^{4}He nucleus. The remaining 1% is created through the CNO cycle (Carbon-Nitrogen-Oxygen). The ^{12}C seed for the CNO cycle is produced by means of the triple-α process. Both the *pp*-chain and the CNO cycle are shown in Figure 1.5, where the originated neutrinos can be observed in bold. It must be pointed out that among the three different neutrino flavours, those produced in the Sun are electron neutrinos (ν_e).

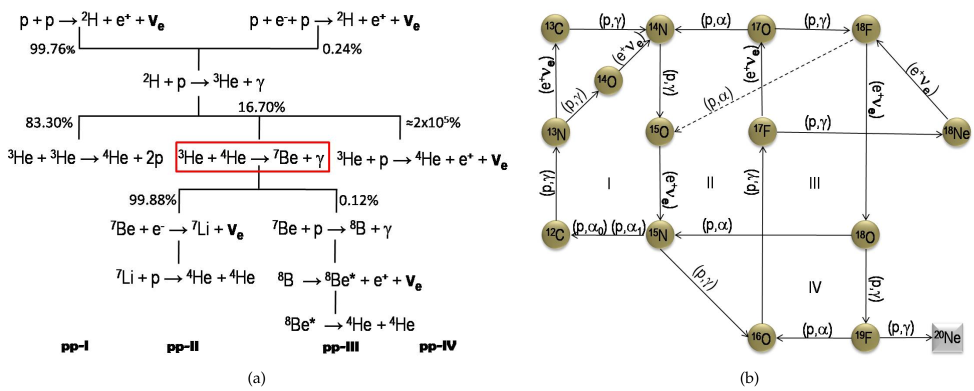

Figure 1.5: *(a) The four reaction sub-chains in the pp-chain with branching ratios given in percentages. (b) The CNO cycle divided into the four CNO sub-cycles. The sub-cycle marked as I produces most of the energy and significant solar neutrino flux among the CNO cycle.*

From an experimental point of view the historical motivation for the detection of solar neutrinos was related to determine the possible neutrino mass and the likely oscillations between the three neutrino flavours. Furthermore, the detection of solar neutrinos is vital in probing the astrophysical conditions and verifying the hypothesis that the thermonuclear reactions are the solar energy source. Nowadays, the detection of solar neutrino fluxes is still ongoing with ever increasing accuracy and improved experimental techniques utilising complex setups. A corroboration between the experimentally measured neutrino fluxes with the SSM estimations addresses several important questions in physics.

The solar model calculations in the sixties [BFI63, Sea64, PR64, Bah64b, Bah66, BCD67, BBS68] already established that the Sun emits a neutrino flux from the ^{8}B decay as shown in Figure 1.6, which the initial experimental investigations aimed to detect. The ^{8}B is created in the *pp*-chain via the reaction ^{7}Be(p,γ)^{8}B, and decays afterwards via the β^{+} decay to ^{8}Be which breaks into two alpha particles.

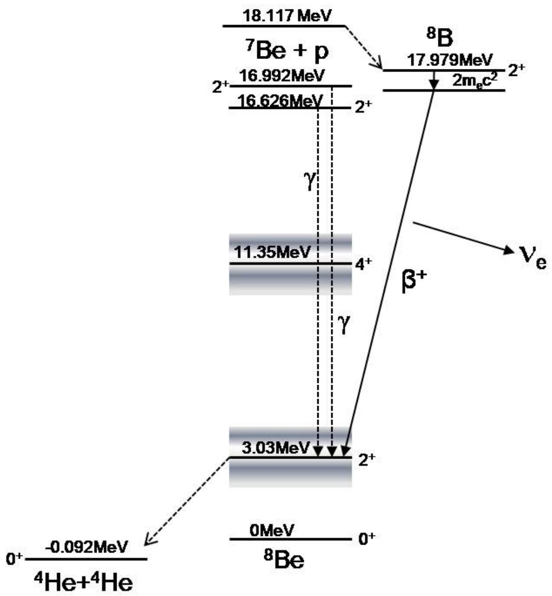

Figure 1.6: *^{8}B decay. This decay is the origin of part of the high energy neutrino flux in the Sun.*

This β^{+} decay emits the second highest energy neutrino among the neutrinos produced in the Sun. From an experimental point of view, the detection of this high energy neutrinos allows to select a high energy detection threshold avoiding thus the contamination produced by the cosmic radiation which plays an important role when detecting weak interacting particles like neutrinos.

In an attempt to detect the solar neutrinos from the ^{8}B decay, and based on the suggestions by John N. Bahcall that these high energy neutrino can be captured via the ^{37}Cl(ν,e^{-})^{37}Ar reaction [Bah64a], Raymond Davis and collaborators devised an experiment. They used a big tank of C_2Cl_4 as target, the ^{37}Ar was extracted from the tank using a circulating ^{4}He gas system, which was guided to a proportional counter for observing their β^{+} decay and thus estimate the solar neutrino flux. The setup was placed 4400 m underground in order to reduce the cosmic ray background due to muons, which can produce protons that subsequently could produce ^{37}Ar via the ^{37}Cl(p,n)^{37}Ar reaction. This experiment yield a value of $2{\cdot}10^{6}$ cm^{2} s^{-1} or less for the neutrino flux from the ^{8}B decay [DJHH68], which was approximately seven times lower than the theoretical estimations. The discrepancy between the direct measurements and theoretical estimations is the so-called *Solar Neutrino Problem*.

Two different solutions were put forward, namely, either the experimental measurements were correct and thus the theory should be changed, or the neutrinos changed their characteristic, or decay, while they travel from the Sun to the Earth. This latter solution was based on the instability of neutrinos initially studied by Reines and collaborators [RSP80].

It is clear these days that the initial SSM calculations overestimated the neutrino flux due to the lack of knowledge of for example the ^{3}He(^{3}He,2p)^{4}He reaction rate, that affects the origin of the high energy flux indirectly because it competes with the $^{3}\mathbf{He}(\alpha,\gamma)^{7}\mathbf{Be}$ reaction (see Figure 1.5(a)). In particular, the rate for this reaction is five times higher than the predictions at this time.

The uncertainties in most of the reactions, ^{3}He(^{3}He,2p)^{4}He,^{3}He(α,γ)^{7}Be and ^{7}Be(p,γ)^{8}B, were reduced in the sixties. In the following decades a lot of improvements were made in determining the cross sections for reactions responsible for direct and indirect solar neutrino production (see for example the review by Bahcall and Pinsonneault, [BP95]). On the other hand, new unexpected progress in the theoretical calculations based on the SSM made possible a new physics beyond the electro-weak standard model. However, the results from the experiments continued showing a discrepancy with the theoretical predictions in spite of the joined efforts to solve the problem.

During the 90's the big neutrino observatories continued detecting the solar neutrino fluxes from the ^{8}B decay. A comparison between the results obtained by Raymond Davis [Dav94] using a chlorine detector and the Kamiokande collaboration [FHI96] using a Cherenkov image water detector in the II$^{\text{nd}}$ and III$^{\text{rd}}$ stages (in 2079 days of measurement Kamiokande collaboration observed 597 events against the 1213 expected) showed inconsistencies with each other which pointed to the possibility that the neutrinos undergone oscillations between their flavours as they travelled from the centre of Sun to the detector. Indeed, the discrepancy could be solved with the suggestion by Bahcall and Bethe [BB90]. Based on the calculations by Mikheyev-Smirnow-Wolfenstein showing the mechanism by which a big fraction of the solar electron neutrinos ν_e would change to muonic neutrinos ν_μ when they travel from the centre of the Sun to the earth (MSW effect [Mik86]), Bahcall and Bethe proved that the measured spectra were in perfect agreement with the non-adiabatic solution of the MSW effect assuming a mass defect between the neutrinos of Δm^{2}=1$\cdot$10$^{-8}\cdot$sin$^{-2}\Theta_\nu$eV against the one predicted previously by Bethe of 6$\cdot$10^{-5} [Bet86].

Furthermore, in case of not considering neutrino oscillations, in order to interpret the results from gallium detectors GALLEX (GaLLium EXperiment [Kir98]) and SAGE (Soviet-American Gallium Experiment [Gav01]), no neutrinos coming from the ^{7}Be decay with energies bellow 4.5 MeV would be required. However, their existence was known ([AAB98] section VIII) and they have been detected for the first time using the BOREXINO detector at the Laboratori Nazionalli dil Gran Sasso, in Italy [ABB08].

Additionally, the success of the SNO (Sudbury Neutrinos Laboratory) experiment [AAA01, AAA02] revealed the neutrino oscillations from the direct detection of solar neutrinos, providing explanation to the deficit of neutrinos observed in the other experiments. The SNO experiment consists of a water Cherenkov detector placed 6100 m underground in Sudbury, Ontario (Canada) that is able to detect not only electron neutrinos but also mounic and taunic neutrino flavors using the reactions:

$$\begin{array}{lcll} \nu_e +^2\mathrm{H} & \rightarrow & \mathrm{p}+\mathrm{p}+\mathrm{e}^- & \quad\quad (\mathrm{CC}) \\ \nu_x +^2\mathrm{H} & \rightarrow & \mathrm{p}+\mathrm{n}+\nu_\mathrm{x} & \quad\quad (\mathrm{NC}) \\ \nu_x + e^- & \rightarrow & \nu_x + e^- & \quad\quad (\mathrm{ES}) \end{array}$$

The first charge current (CC) reaction is only sensitive to electron neutrinos, while the neutral current (NC) and the elastic scattering (ES) are sensitive to all the three e, μ and τ neutrino flavors. The fact that even though thermonuclear fusion reactions in the Sun only produce electron neutrinos, non-zero neutrino fluxes are measured for all the three flavors (i.e. ϕ_e=1.76$\cdot$10^{6}cm$^{-2}s^{-1}$ and $\phi_{\mu,\tau}$=3.41$\cdot$10^{6}cm$^{-2}s^{-1}$) in the SNO detector demonstrates the neutrino oscillations with approximately two thirds of the electron neutrino flux produced in the Sun transforming to the neutrinos of the other flavors during their travel from the Sun to the SNO detector (see reference [AAA07] for the experiment specifications and the detailed results).

On the other hand, in nuclear reactors, neutron rich nuclei are created abundantly and decay afterwards by the β^- process emitting electron-anti-neutrinos. Detections of these particles also proved the neutrinos oscillations without the need of a massive medium such as the Sun. The KamLAND (kamilka Liquid scintillator Antri-Neutrino Detector) studied the neutrino oscillations from the anti-neutrinos observations from reactors with an experimental setup which replaced to the Super-Kamiokande [FFI01], and reported the same evidence for the neutrino oscillations[AEE08].

Even more surprising are the new investigations with the liquid organic scintillator target at BOREXINO detector, that have been able to detect anti-neutrinos coming directly, possibly, from the Sun. A limit on the transition probability from solar neutrinos to anti-neutrinos of 1.3$\cdot$10^{-4} has been reported [BBB11].

The current solar neutrino spectrum predicted by the SSM is shown in the Figure 1.7.

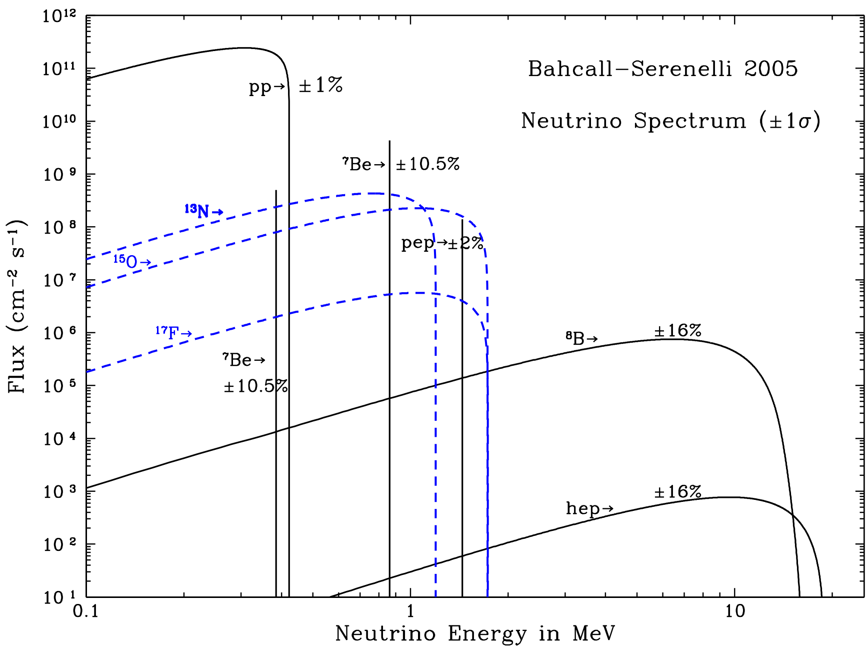

Figure 1.7: *The solar neutrino spectrum calculated using the Standard Solar Model [BSB05]. The present reaction contributes to the errors in ^{7}Be and ^{8}B neutrino fluxes.*

Although the main discrepancies between the estimations by SSM and direct observations seems to be understood by means of neutrino oscillations, the estimated error by the SSM for the solar neutrinos fluxes are not still low enough and the experimental uncertainties of the nuclear reactions cross sections, which are used as input parameters, need to be reduced. While the main neutrino flux in the low energy range is due to neutrinos emitted in the p+p reaction the high energy part of the spectrum is mainly produce by the ^{8}B β^{+}-decay, and also influenced by the ^{7}Be. Models estimate that the neutrino fluxes from the ^{8}B and ^{7}Be decays are directly proportional to the S-factor of the ^{3}He(α,γ)^{7}Be reaction via $\phi_{\nu}(^{7}\mathrm{Be}) \propto$ $S_{34}(0)^{0.86}$ and $\phi_{\nu}(^{8}\mathrm{B}) \propto S_{34}(0)^{0.81}$. Therefore, a precise determination of the cross section of this reaction is highly required. Indeed, the ^{3}He(α,γ)^{7}Be cross section is currently one with the largest experimental uncertainties among the nuclear input parameters. This is reflected in the uncertainties of the SSM predictions (cf. Figure 1.7). The nuclear rates also have a determining role in constraining the parameters governing the solar neutrino oscillations.

On the other hand, the solar Gamow Peak energy for the ^{3}He(α,γ)^{7}Be reaction is ≈22 keV, as can be seen in Figure 1.3, and the measurements at this energy are impossible with the current experimental devices. Thus, theoretical models are used to extrapolate the cross sections measured at higher energies, which essentially is the driving motivation for the present thesis work.

1.4 Big Bang Nucleosynthesis and the Primordial ^{7}Li Problem

Currently, the *Big Bang Model* is the most successful cosmological theory as it can explain three important features: the expansion of the Universe, the cosmic microwave background radiation and the primordial nuclear abundances.

Approximately, 13.8 billion years have passed since the Big Bang Explosion resulting in the present expanding and cold (T_0=2.73 K) Universe. An artistic timeline of the expanding Universe is shown in Figure 1.8, where different eras as the Dark Ages or the Development of Galaxies and Planets are labelled.

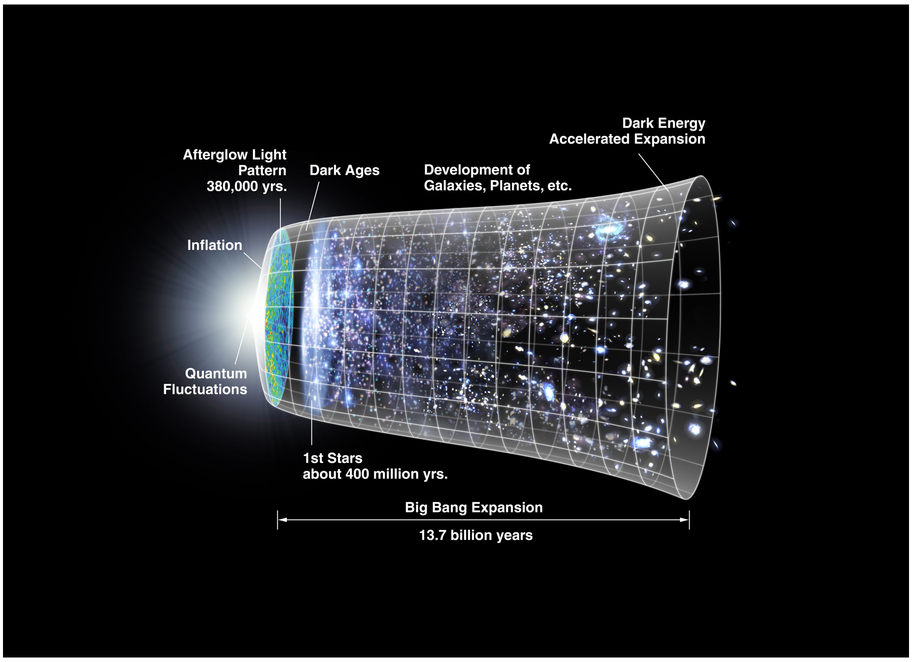

Figure 1.8: *The figure taken from NASA shows an impression of the Universe expansion timeline, since the initial Big Bang quantum fluctuations. Some of the eras such as the Dark Ages, prior to the creation of Galaxies are marked.*

During the initial hot expansion, the Universe was filled with particles moving at relativistic velocities and interacting via weak interaction. Once the protons and neutrons had been created within t$\sim 10^{-6}$ s and following the Big Bang and the early times of the Universe, t<1 s, the thermal energy was high enough (>1293.3 keV) to convert free protons into free neutrons and vice-versa by weak interaction as well as the $e^- + e^+ \leftrightarrow \gamma + \gamma$ reaction. It was only after two seconds when the temperature was low enough to allow protons and neutrons to retain their identities. After $\sim$200 s of cooling and expansion and with a temperature of $\sim$0.9 GK the nuclear reactions could compete with the destruction of nuclei by photons.

In this framework and under the assumptions of an homogeneous and isotropic Universe, the Standard Big Bang Nucleosynthesis (SBBN) explains the production of the first elements during the time window between $\sim$200-1000 s following the Big Bang. The Standard Big Bang Nucleosynthesis is a vast field and it is out of the scope of this thesis to explain all the details. The main aspects of the model related to our ^{3}He(α,γ)^{7}Be reaction will be recalled, based on the details presented in [MM93, OSW00].

Primordial nucleosynthesis started with the production of deuterium (d) via the $p(n,\gamma)d$ reaction, which is the seed for the rest of the reaction network. The main reaction network showing the production

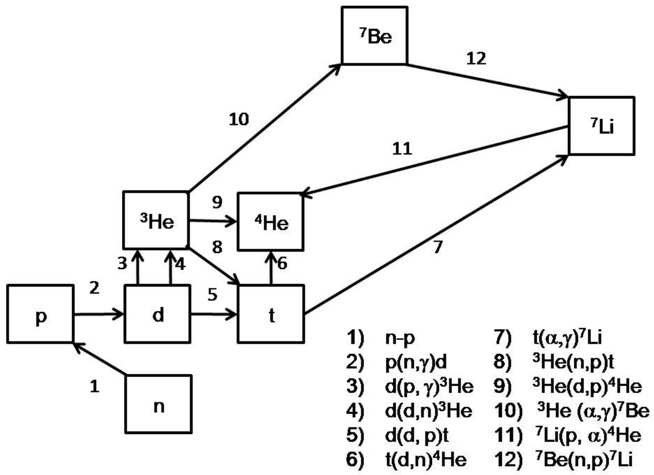

Figure 1.9: *A part of the reaction network involved in the Big Bang Nucleosynthesis that is also relevant to the current reaction.*

and destruction of the main primordial elements is shown in Figure 1.9. The most relevant remaining light nuclei are d, tritium (t) ^{3}He, ^{4}He, and ^{7}Li; the gap at A=8 prevents the production of heavier nuclei in significant amounts. The aim of the SBBN is to determine how the mass flowed through the network for a temperature range of $1.2 \cdot 10^9 \geq T \geq 3 \cdot 10^8$ K. For the ^{3}He(α,γ)^{7}Be reaction, the relative Gamow Peak energies corresponding to these temperatures are in the interval of $180 \leq$ E$_{\text{CM}}$ ≤ 400 keV which are accessible in the laboratory.

Historically, the BBN was a three free parameter theory, namely, the baryon density, the neutron lifetime and the number of neutrino flavours. After obtaining knowledge of the number of neutrino flavors inferred from the LEP experiment at CERN, N$_\nu$=2.9840±0.0082, and the neutron mean lifetime, $\tau_n = 885.7 \pm 0.8s$ [Gro08], it became a one parameter theory. In this framework with the experimental cross sections as input model parameter, it was possible to estimate the expected abundances of the primordial elements as a function of the free parameter η (baryon/photon ratio). Figure 1.10 shows the SBBN estimations of the primordial abundances as a function of the baryon/photon density ratio, η. From a comparison with the primordial abundances obtained from the direct observations of poor metal stars, one could infer η.

More recently, the Wilkinson Microwave Anisotropy Probe (WMAP) has measured with high sensitivity the Cosmic Microwave Background (CMB) spectrum originated from the acoustic oscillations when the electrons coupled to nuclei to form atoms $4 \cdot 10^5$ years after the Big Bang. The CMB is sensitive to the initial mass distribution (n_B) and thus the baryon to photon ratio can be derived precisely, quoting $\eta_{10} = 6.23$±0.17, where $\eta = n_B/n_\gamma = 10^{-10}\eta_{10}$ [KDN09]. n_γ is the photon density and is considered to be constant after that almost all positrons and electrons annihilated ~14 s after the Big Bang. The WMPA value for η can now be used as input parameter in the SBBN and the calculated primordial abundances can be compared with the direct astronomical observations.

Figure 1.11, from [CFO08], shows a comparison between the primordial elements abundances directly observed (in yellow) and those estimated in the SBBN model including five years of measurements by WMAP and the revision of the data for the ^{3}He(α,γ)^{7}Be reaction in [CD08] (in blue). There is a good agreement of the abundances for d , ^{3}He, and ^{4}He. However, a discrepancy by a factor of three can be observed for the ^{7}Li/H ratio between the estimations by the SBBN (blue) and the direct observations from poor metal stars (yellow). This is the so-called *Primordial ^{7}Li Problem*.

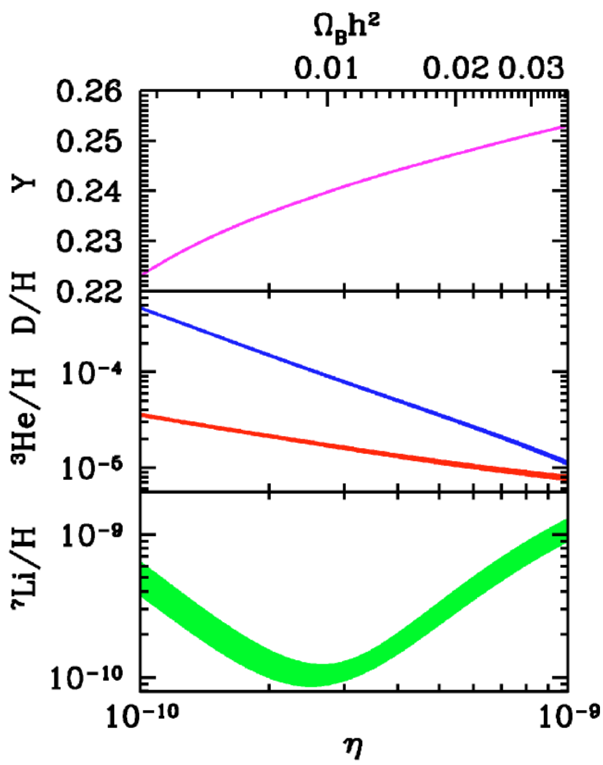

Figure 1.10: *Primordial light element abundances as functions of the baryon/photon ratio (η) (taken from [Cyb04]). The ^{4}He abundance is expressed as mass fraction relative to hydrogen (Y), while the abundances for deuterium, ^{3}He, and ^{7}Li are expressed as mole ratios relative also to hydrogen.*

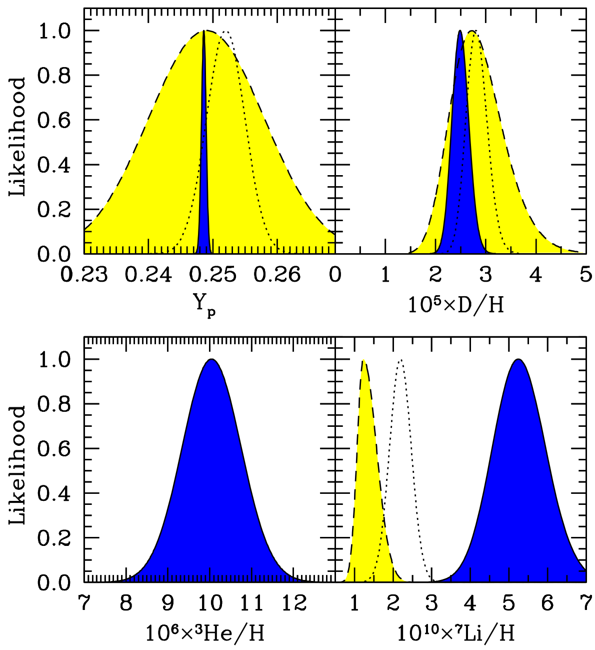

Figure 1.11: *Calculated and observed likelihoods representing the probability distribution for ^{4}He (Y_p), D/H, ^{3}He/H and ^{7}Li/H abundances. The dark blue areas show the likelihood calculated with the SBBN calculations using the η parameter from WMAP observations. The yellow shaded regions and the dotted lines show the observational likelihoods distributions. For the ^{7}Li/H, the shaded yellow area shows the value inferred from the observation of halo stars. The dotted function shows the determination from a globular cluster. A disagreement between the calculations and both direct observations can be seen for the ^{7}Li/H probability distributions. Figure has been taken from [CFO08]*

The origin of this discrepancy is still unknown. Different solutions have been suggested including physics beyond the Standard Model and the cosmological variation of the fine structure constant. The latter would suppose a variation in the deuterium binding energy and thus a decrease in the estimations for the ^{7}Li abundance. The reliability of the observed primordial abundances in poor metal stars is also under discussion as the current Universe conditions are far from those in the primordial conditions. Some other sources of systematic uncertainties could arise from a possible scenario that ^{7}Li would have been depleted if the outer layers of the stars were transported deep enough and ^{7}Li was mixed with the hot material inside the star.

Currently, information of the reaction rates on accuracy levels are not seen as solutions to the discrepancy. However, accurate information on the reaction rates is required to estimate the abundances precisely an thus constrain the discrepancy. The ^{7}Li is mainly produced by the ^{3}He(α,γ)^{7}Be and subsequent ^{7}Be(n,p)^{7}Li reactions and destroyed by the large cross section of the ^{7}Li(p,α)^{4}He reaction (see Figure 1.9). Particularly, the ^{7}Li abundance is directly proportional to the the ^{3}He(α,γ)^{7}Be reaction rate as $^7\mathrm{Li/H} \propto \mathrm{S}_{34}^{0.96}$ where S_{34} is the astrophysical S-factor of the reaction. A precise determination of the ^{3}He(α,γ)^{7}Be cross section will help to reduce the uncertainty in the model predictions and will constrain the underlying physics, eventually helping to solve the *Primordial ^{7}Li problem*. This effect is demonstrated for example in reference [CFO08] where a new data evaluation for the ^{3}He(α,γ)^{7}Be reaction shows an upward shift of 16% in central value of the ^{7}Li abundance.

Finally, it is also worth noting here that other new nuclear physics solutions are continuously searched but without success. For example, in reference [KD11] authors studied the 16.8 MeV state in ^{9}B and found that it is unable to enhance the ^{7}Be(d,p) reaction rate by the amount needed to resolve the cosmological lithium problem. Other examples are studied in [CGX12] where a complete network of more than 400 reactions have been included in the BBN calculations, yet finding no solutions. The discrepancy of the estimated primordial ^{7}Li is still persistent, which also motivates our experiment.

1.5 The ^{3}He(α,γ)^{7}Be Reaction: Experimental Previous Knowledge

Due to the relevance of the ^{3}He(α,γ)^{7}Be reaction in the SSM and the SBBN, the reaction cross section has been studied experimentally using different techniques with ever-increasing accuracy. The decay scheme of the ^{3}He+^{4}He direct capture is shown in Figure 1.12. This radiative capture reaction (details are given in Chapter 2) creates a ^{7}Be nucleus with a Q-value of 1.587(1) MeV. Prompt γ-rays of two different energies[c] are emitted in the process corresponding to the population of the ground state (γ_0) or the first excited state (γ_1) in the ^{7}Be. The latter de-excites via emission of a 429 keV γ-ray to the ground state (γ_2). The created ^{7}Be is an unstable nucleus. It decays via electron capture process to ^{7}Li with a half life of 53.24(4) d. The Q value of this process is 862 keV and with a well known branching ratio of 10.44(4)% the decay populates the first excited state in ^{7}Li at 478 keV from which a γ-ray emanates (γ_3).

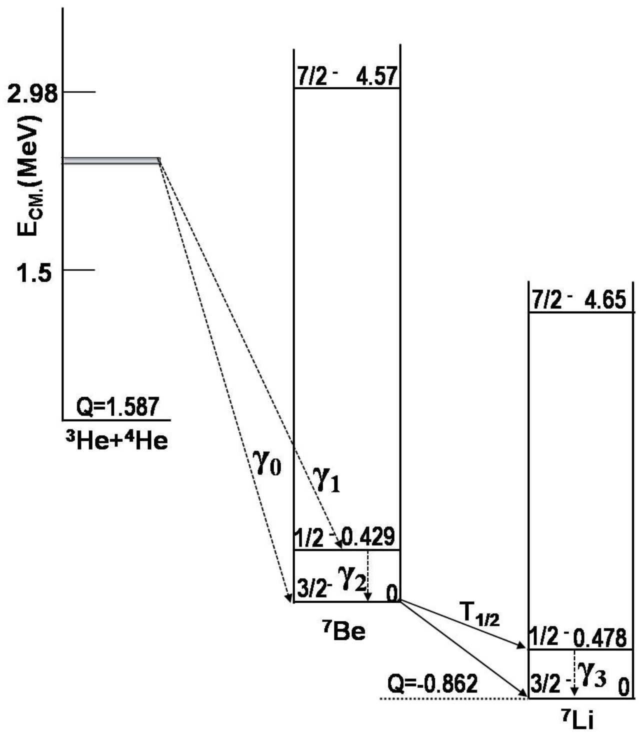

Figure 1.12: *Decay scheme of ^{3}He+^{4}He direct capture reaction via the emission of prompt γ-rays, indicated as γ_0 and γ_1. The ^{7}Be electron capture decay to ^{7}Li is also shown. The energies and Q-values of the reactions are displayed in MeV.*

The three different techniques used for determining the cross section consist of measuring either, the prompt γ_0/γ_1-rays of the reaction ("*Prompt γ-Detection Method*"), the ^{7}Be recoils ("*Direct Recoil Count-*

[c] Note that the energies of the two γ depend on the reaction energy

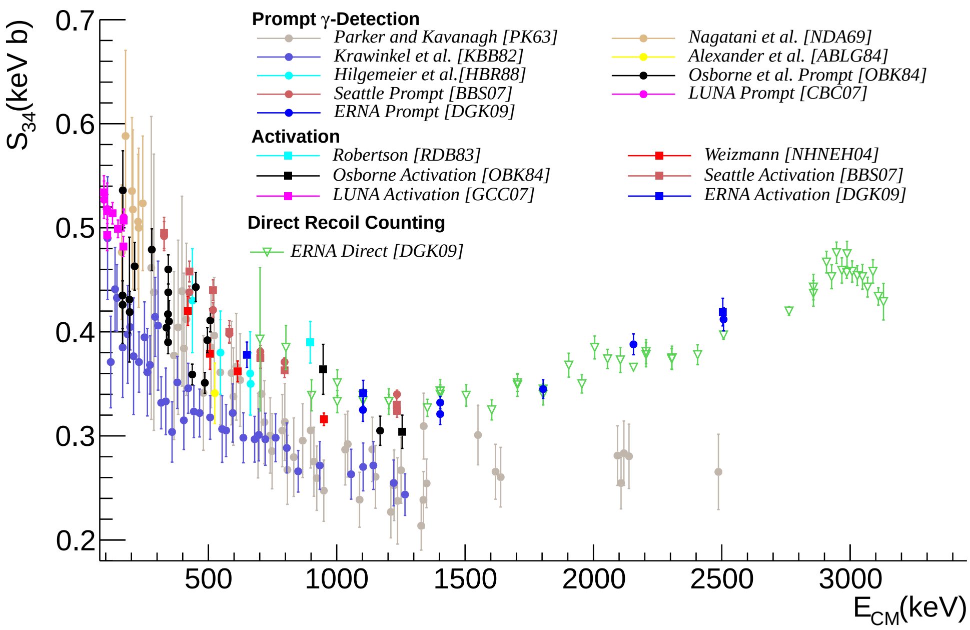

Figure 1.13: *The available data of the astrophysical S-factors for the $^3He(\alpha,\gamma)^7Be$ reaction (S_{34}). Data from measurements performed by the Prompt γ-Detection Method, Activation Method and Direct Recoil Counting Method ares shown in circles, squares and triangles, respectively. Marked discrepancies are evident at energies > 1000 keV, which essentially sparked the interest leading to this thesis work.*

ing Method") or the subsequent γ_3-ray from the de-excitation of the first excited state in ^{7}Li to its ground state ("*Activation Method*"). The first experiment performed in order to determine the cross section of the ^{3}He(α,γ)^{7}Be reaction was done by Holmgren and Johnston in the late fifties [HJ59] using the *Prompt γ-Detection Method*. Measurements using the same method were carried out by [PK63, NDA69, KBB82, ABLG84, HBR88], while in [RDB, VKSW83, NHNEH04] the *Activation Method* was the choice. Both methods were used simultaneously in the works presented in [OBK84, BBS07] and by the LUNA collaboration (Laboratory for Underground Nuclear Astrophysics) [CBC07]. The activation measurements performed at LUNA are also detailed in [BCC06] and [GCC07]. Recently, the *Direct Recoil Counting Method* was employed for the first time using the European Recoil separator for Nuclear Astrophysics (ERNA), [DGK09] where measurements using the *Prompt γ-Detection Method* and *Activation Method* were also performed simultaneously. At the same time of the work presented here two other measurements were carried out, one using the *Activation Method* [BGH13] and other using the *Prompt γ-Detection Method* [KUD13].

The centre of mass energy range covered in the mentioned experiments is between 93 and 3130 keV. Energies above 1200 keV were covered only by measurements [PK63] and [DGK09], and they show a big discrepancy with each other. A summary of all experimental measurements performed before the work presented here is shown in Figure 1.13, except those from [HJ59]. The violet points from reference [KBB82] are increased by 40% as recommended in [HBR88] to account for the a wrong estimation of the target thickness. As can be seen, there is a big dispersion among the different set of measurements, especially, in the range span between 1000 keV and 2500 keV. Resolving this discrepancy is one of the motivations of this work.

The different set of measurements have used different theoretical models (which will be detailed in the next chapter) in order to obtain the extrapolated $S_{34}(0)$ value. Figure 1.14 shows a comparison between the $S_{34}(0)$ values as extracted from the different experimental measurements . Green circles show the $S_{34}(0)$ values obtained by experiments using the *Prompt γ-Detection Method*, red squares represent the $S_{34}(0)$ values obtained using the *Activation Method*, and open black squares show the values obtained by combination of different methods (see caption for more details). As can be observed, the discrepancy between prompt and activation methods is significant.

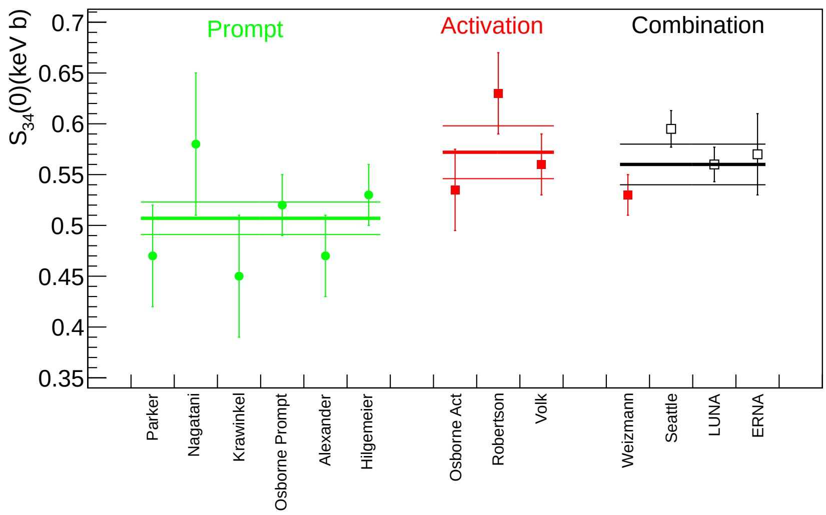

Figure 1.14: *The $S_{34}(0)$ values obtained from different types of experiments carried out before the measurements presented here. Results obtained by using the Prompt γ-Detection Method (green circles), the Activation Method (red squares) and different methods simultaneously (open black squares) are shown. Seattle [BBS07] and LUNA [CBC07] employed both the Activation and Prompt γ-Detection Methods while ERNA [DGK09] used the Activation, Prompt γ-Detection and Direct Recoil Counting methods. The Nagatani value is the result from a reanalysis of the data found in reference [AAB98], and the Kräwinkel values are normalised as specified in [HBR88]. The thick green line is the value recommended in [AAB98] based on the Prompt γ-Detection experiments at the time of the review, and the thin green lines are the associated errors. The red lines refer the same for the Activation method. The black line is the recommended $S_{34}(0)$ value in the [AGR11] review corresponding to an evaluation of Weizmann [NHNEH04], Seattle, LUNA and ERNA data. It should be noted that while the open squares for Seattle, LUNA and ERNA are obtained by a combination of the different methods used in each case, the evaluation [AGR11], takes into account only the activation measurements from Seattle and LUNA, and direct counting measurements from ERNA.*

In the 1998 evaluation by Adelberger et al. [AAB98], the weighted mean value for the $S_{34}(0)$ factor using the *Prompt* measurements at the time of the review was quoted to be 0.507±0.016 keV b (green lines in Figure 1.14). For the Activation measurements, it was 0.572±0.026 keV b (red lines in Figure 1.14). Two possible solutions for this apparent discrepancy between the two methods were discussed, namely, a possible systematic error in one of these methods, for example ^{7}Be contamination in the *Activation Method*, or the presence of a non radiative channel (small monopole contribution -E0-) to which the *Prompt Method* would not be sensitive. The results in [BBS07] and [CBC07] and subsequently in [DGK09] ruled out the latter possibility by determining the cross sections using these two techniques, simultaneously. Also, the studies in [SH03] conclude that the E0 pair emission, E0 resonance emission, and E1 pair emission and internal conversion are negligible for this reaction.

In the new 2011 review of modern physics [AGR11], the evaluation was only based on the most recent activation measurements [NHNEH04, BBS07, CBC07] and the direct measurements up to 1 MeV energy in [DGK09]. This choice was justified by the fact that while the *Activation* measurements determine the total cross sections directly, the *Prompt* measurements must include a correction due to the γ anisotropy, but suffer from the fact that no angular distribution at the necessary level of precision are available. For example, while LUNA [CBC07] used the Tombrello and Parker angular distribution to correct [TP63a], Seattle [BBS07] and ERNA [DGK09] prompt data consider an isotropic angular distribution. Theoretical models of Kajino et al. [Kaj86] and Nollet [Nol01] (detailed in the next chapter) were used to fit the data and the recommended value for $S_{34}(0)$ was given as 0.56±0.02(expt)±0.02(theor) keV b (black line in Figure 1.14). Due to the discrepancies above 1 MeV, new data in this energy region are recommended by the authors in order to constrain the theoretical models, strongly supporting the work presented here. Furthermore, prompt γ-ray distribution measurements in this energy range are also recommended and thus one of the objectives of our measurements is also to obtain this information. In this context, it is worth pointing out that the prompt γ-ray angular distribution measured by [KBB82] up to 1.29 MeV were in agreement with the almost isotropic angular distribution in [TP63a].

Finally, measurements of the cross section identifying the population of the first excited state (σ_{429}) and the ground state ($\sigma_{g.s.}$) in the ^{7}Be nucleus have been carried out by different authors [PK63, NDA69, KBB82, ABLG84, OBK82, BBS07, DGK09]. In Figure 1.15, where those cross sections are plotted by using the $\sigma_{429}/\sigma_{g.s.}$ ratio, one can observe the discrepancies among the experimental data. New information of the $\sigma_{429}/\sigma_{g.s.}$ ratio would also help to resolve these discrepancies and constrain the theoretical models.

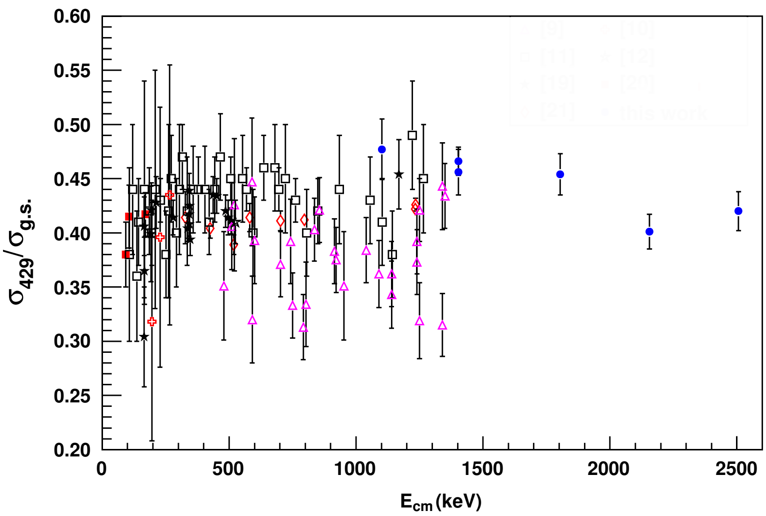

Figure 1.15: *The $\sigma_{429}/\sigma_{g.s.}$ ratio of the cross section of the ^{3}He(α,γ)^{7}Be reaction populating the first excited state (σ_{429}) and the ground state ($\sigma_{g.s.}$) in the ^{7}Be nucleus as a function of E_{CM}. The Figure is taken from [DGK09]. The data corresponding to blue dots are the values taken from [DGK09], open pink triangles are from [PK63], red open crosses are from [NDA69], open black squares are from [KBB82], small black stars are from [ABLG84], big black stars are from [OBK82], red squares are from [CBC07] and red diamonds are from [BBS07].*

1.6 Conclusion

The ^{3}He(α,γ)^{7}Be reaction plays a determining role in the *Big Bang Nucleosynthesis* and the *Standard Solar Model* calculations. Specifically, the discrepancies seen among the existing S-factor data for the ^{3}He(α,γ)^{7}Be reaction have a direct influence on the estimated values of the primordial ^{7}Li abundance and high energy solar neutrino flux. Both estimations demand low uncertainties of at least 3% in the $S_{34}(0)$ value. However, due to the experimental limitations it is not possible to determine the cross section of this reaction at very low energies and thus theoretical models (explained in the next chapter) are used to obtain the extrapolated $S_{34}(0)$ factor using the measured $S_{34}(E)$ at higher energies. In addition to the

$S_{34}(E)$ values at low energies, it has become clear that these data at medium energies play important roles as they help us to constrain the theoretical models in obtaining an accurate extrapolated $S_{34}(0)$ value. Currently, the available two data sets for centre of mass energies above 1 MeV disagree with each other and new measurements are required in order to resolve the discrepancy and put further constraints on the extrapolations. Moreover, no information about the prompt γ-ray angular distribution is available in this medium-high energy region which would also help to constrain the theoretical models. Furthermore, discrepancies exist in the ratio between the population of the ground state and first excited state in the ^{7}Be fed by the direct capture state and also here new data would help to resolve the discrepancy. These observations motivated the present work, in which measurements to obtain the aforementioned data were carried out.

"A theory with mathematical beauty is more likely to be correct than an ugly one that fits some experimental data."

Paul Dirac

CHAPTER 2

THEORETICAL FORMALISM

Abstract: *In this chapter some of the theoretical approaches used for explaining the ^{3}He(α,γ)^{7}Be radiative capture reaction will be discussed. The framework for this reaction and the general theoretical procedures to determine the reaction cross sections will be given. Complementary, the phase shift analyses will be detailed, which can be used to constrain the calculations.*

Similar to the usage of light and processes such as reflection or refraction to determine the properties of light, in Nuclear Physics, the beam of particles are used to study the properties of nuclei and nuclear interactions. One of the main methods used to determine those properties in order to understand the underlying physics is to carry out reactions between the nuclei of interest (nuclear reactions).

In the previous chapter, different existing experimental data for the astrophysical S-factor of the ^{3}He(α,γ)^{7}Be reaction were presented. Significant discrepancies between different sets of measurements have been pointed out. Different theoretical models apparently reproduce the experimental results and provide some knowledge of the reaction mechanism and the structural properties of the partners. The models that are usually employed can be grouped as Potential Models, Microscopic Models and R-matrix analysis. Moreover, recent pioneering work using the ab-initio approach has been performed. A general overview of these models will be presented in this chapter.

Furthermore, the reliability of the models rests on simultaneous explanations of the ^{3}He+^{4}He capture and the phase shift analysis of the ^{3}He+^{4}He elastic scattering data. Therefore, these aspects will also be briefly discussed.

2.1 Nuclear Reactions

Nuclear reactions can be defined as interaction processes between the reaction partner nuclei that are generally governed by the strong nuclear force with a possibility of the electromagnetic force playing a determining role. They can be classified according to different criteria, for example, the reaction time scales:

- Direct Reactions: These are the fastest ones and happen within $\sim 10^{-22}$ s with cross sections varying smoothly with the incident kinetic energy. Either a few nucleons on the surface or the nucleus as a whole participate in this process. Quantum mechanically, these reactions are modelled as *one step transitions* between the initial and final states. Examples for direct reactions are:

  - Elastic Reactions: Rutherford scattering processes where the products in the outgoing final state are the same as the nuclei in the incoming initial channel: A(b,b)A
  - Inelastic Reactions: Similar to the elastic scattering but one of the nuclei in the outgoing channel is excited: A(b,b*)A or A(b,b)A*
  - Transfer Reactions[a]: In this reactions nucleons are transferred either from the projectile to the target, referred as stripping reactions, or from the target to the projectile (pickup reactions)
  - Breakup Reactions: One of the two ejectile is broken in two or more fragments, e.g. A(b,b=c+d)A
  - Knockout Reactions: These reactions involve removal of a nucleon or cluster of nucleons from a nucleus, leaving one of the residual nuclei in its excited state.
  - Direct Capture Reactions: The two incident nuclei (A+B) capture each other. To form a composite state that lives long enough and avoid going back to the initial A+B state, some energy must be released, either by direct emission of particles or by γ-radiation. The latter are called **radiative capture** reactions -A(b,γ)C- and will be detailed in the next sections.

- Resonance Reactions: These are longer lived configurations of nucleons. The resonances can be identified using the cross sections, as they have a peak structure when plotted against energy. The peak widths (Γ) are typically between 100 keV and 1 MeV. The incoming particles form a quasi-state, "the resonance state", which can live for a time between 10^{-19} and 10^{-21} s.

- Compound Nucleus Reactions: These involve all possible interactions between the nucleons in the two interacting nuclei. The two nuclei fuse creating an intermediate nucleus (where the interacting nuclei loose their identities) generally in an excited state which de-excites via emission of γ radiation by electromagnetic processes, or decays by particle evaporation or fission. The compound nucleus will live for a time between 10^{-16} and 10^{-18} s.

2.2 Electromagnetic Transitions: Direct Radiative Capture Reactions

The electromagnetic transitions connect an initial wave function Ψ_i for a group of charged particles with energy E_i described by the Hamiltonian operator $H=H_0$, to a final wave function Ψ_f for the charged particles plus electromagnetic radiation (photons), with energy E_f and described by the Hamiltonian $H=H_0+H_\gamma$. Here, H_γ is the electromagnetic operator and transition probability can in general be given by: $w_i \sim | < \Psi_f | H_\gamma | \Psi_i > |^2$.

The electromagnetic transitions can be classified using the relative energies involved in the initial and final states as (cf. Figure 2.1):

[a] Together with Radiative Capture Reactions, Transfer Reactions are the most relevant in Nuclear Astrophysics

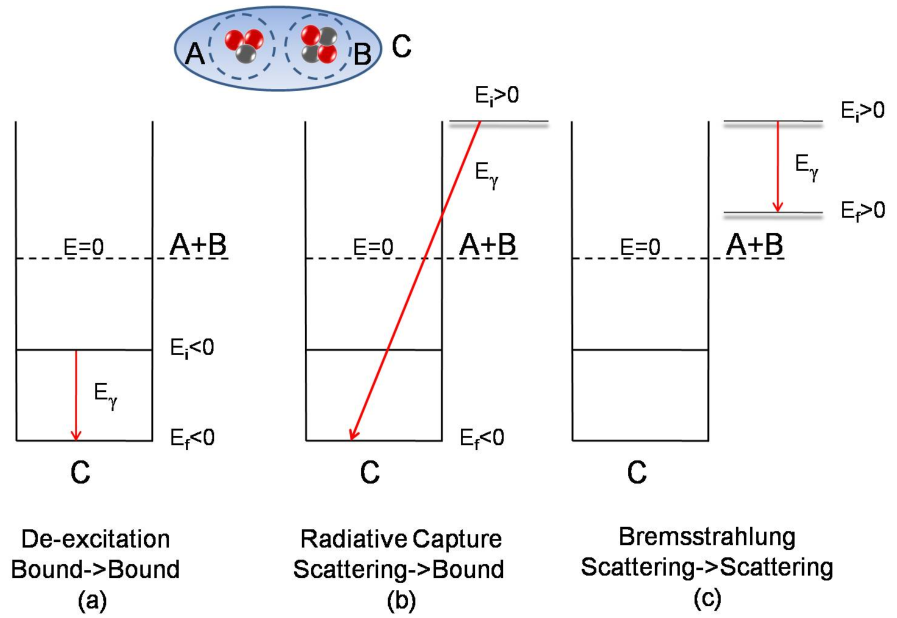

Figure 2.1: *Electromagnetic transitions. (a) De-excitation between two bound states in a nucleus "C". (b) Decay in a radiative capture reaction from a scattering state (A+B state) to a bound state (C nucleus). (c) Bremsstrahlung electromagnetic radiation from the transition between two scattering states.*

- E$_i$<0 and E$_f$<0: The transition occurs between two bound states by emitting the corresponding γ-ray (**de-excitation**). The initial and final states are characterised by spins and parities $J_i\pi_i$ and $J_f\pi_f$, respectively. The transition probability, given by w$_i \sim |<\Psi^{J_f\pi_f}|\mathrm{H}_\gamma|\Psi^{J_i\pi_i}|^2$, provides the, γ-width $\Gamma_\gamma = \hbar$w, which is related to the mean life of the state by $\tau = \hbar/\Gamma_\gamma$.

- E$_i$>0 and E$_f$<0: The transition occurs from a scattering state to a bound state by emitting the corresponding electromagnetic radiation. In the **direct radiative capture reactions**, the colliding nuclei fuse with a photon emission. Therefore, the reaction cross sections to a final bound state in the fused system is related to the overlap between this state transformed to a different state upon its interaction with the electromagnetic force, and the scattering wave function of the colliding nuclei (e.g. see Section 3.3 in reference [Des03]). The initial and final states are characterised by spins and parities $J_i\pi_i$ and $J_f\pi_f$, respectively. The initial scattering wave function, $\Psi(E)$ can be described as an expansion in partial waves, $\Psi(E) = \sum_{J_i}\Psi^{J_i\pi_i}(E)$ and the transition probability, w$_i \sim |<\Psi^{J_f\pi_f}|\mathrm{H}_\gamma|\Psi(E)>|^2$, provides the capture cross section.

- E$_i$>0 and E$_f$>0: The transition occurs from a scattering state to a scattering state emitting the so-called **bremsstrahlung** radiation. This is a transition in the continuum.

Direct Radiative Capture Reactions

While in the fusion reactions all channels with mass higher than the projectile and the target are available and statistical approaches are used, in the radiative capture only the electromagnetic channel is allowed. The cross section have a smooth variation with energy and the γ emission is usually isotropic, characteristic of an electric dipole p to s transition and no spin flip, i.e. the spin is uncoupled from the orbit, [CD61]. Such processes are said to be external as the capture occurs by electromagnetic force at larger distances outside the range of the strong interaction. Therefore, in principle, the cross section is expected to be insensitive to structural details of the interacting nuclei.

Figure 2.2 shows a diagram of the ^{3}He(α,γ) direct radiative capture reaction in the centre of mass system (see appendix B for the discussion about centre of mass system). The transitions can populate different bound states by emitting the corresponding electromagnetic radiation, which are known as prompt γ-rays[b]. If an excited state is populated in the final nucleus a subsequent γ-ray connecting the two bound states is emitted. The corresponding wavelength of the prompt γ-rays are ~1500 fm, that are much larger than the nuclear radii, justifying that the long wavelength approximation can be considered in the calculations.

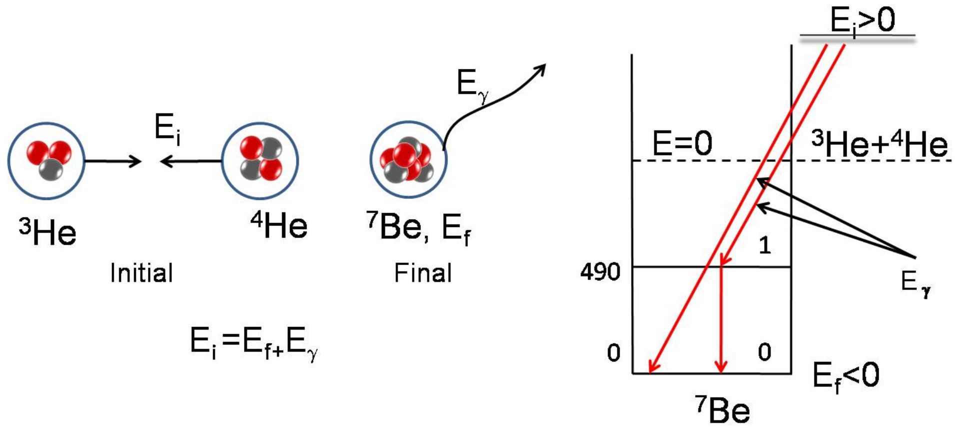

Figure 2.2: *(Left) A schematic of ^{3}He(α,γ)^{7}Be Direct Radiative Capture Reaction in the centre of mass system. (Right) The direct radiative capture of the He nuclei can be described as electromagnetic transitions from a scattering state to a bound state (right). The initial scattering state with energy E_i>0 connects to a final state in the ^{7}Be nucleus by populating the 1^{st} excited and ground states and emitting the corresponding prompt γ-rays.*

Due the relatively small strength of the H_γ operator, perturbation theory can be applied for the electromagnetic transitions described above. The electromagnetic processes have lower probability compared to, for example, nuclear reactions governed by the strong force. Thus, the electromagnetic radiation widths Γ_γ are smaller compared to the particle emission widths (i.e. $\Gamma_\gamma/\Gamma_p < 1$).

The electromagnetic operator H_γ depends on the nuclear coordinates (nuclei or nucleons according to the model) and the photon properties (E_γ, emission angle Ω_γ...) and can be expressed as:

$$H_\gamma \sim \sum_{\lambda\mu\sigma} k_\gamma^\lambda \mathcal{M}_\mu^{\sigma\lambda}(r_1, ..., r_A)\mathcal{D}_{\mu q}^\lambda(\Omega_\gamma) \tag{2.1}$$

where $\sigma\lambda$ is equal to Eλ or Mλ depending on the **E**lectric or **M**agnetic transition character, λ is the order of the multipole, which in principle can take values between 1 to ∞ although in practice $\lambda = 1$ or 2, μ is an integer number between -λ to +λ, $\mathcal{M}_\mu^{\sigma\lambda}$ is the multipole operator that depends on the nucleon coordinates r_i, and $\mathcal{D}_{\mu q}^\lambda(\Omega_\gamma)$ is the Wigner function depending on the photon emission angle (Ω_γ).

The electric operator is given by:

$$\mathcal{M}_\mu^{E\lambda} = e\sum_i \left(\frac{1}{2} - t_{iz}\right) r_i^\lambda Y_\lambda^\mu(\Omega_{ri}) \tag{2.2}$$

[b]Although the electromagnetic radiation from direct radiative capture reaction is called γ-ray, these cannot be understood as the usual γ-rays in the sense of radiation emitted in the transition between two states

where t_{iz} is the isospin, taking values of +1/2(neutrons) and -1/2(protons), $\mathbf{r}_i$=(r_i,Ω_i) is the nucleon space coordinate and $Y^\mu_\lambda(\Omega_{ri})$ are the spherical harmonics [Des03]. On the other hand, the magnetic operator can be expressed by:

$$\mathcal{M}^{M\lambda}_\mu = \frac{\mu_N}{\hbar}\sum_i \left[\nabla(r^\lambda Y^\mu_\lambda(\Omega_r)\right]_{r=r_i}\cdot\left(\frac{2g_l(i)}{\lambda+1}\mathbf{L}_i + g_s(i)\mathbf{S}_i\right) \tag{2.3}$$

where $\mathbf{S}_i$ and $\mathbf{L}_i$ are the spin and orbital angular momenta of the nucleon i, respectively. μ_N is the Bohr magneton, $g_\ell(i) = \frac{1}{2} - t_{iz}$ and $g_s(i) = g_p(\frac{1}{2} - t_{iz}) + g_n(\frac{1}{2} - t_{iz})$ where g_p and g_n are the gyromanetic factors of the proton and neutron, respectively.

Therefore, integrating over Ω_γ, the transition probability is given by:

$$W_{J_i\pi_i\to J_f\pi_f} \sim \sum_{\lambda\sigma}\underbrace{k_\lambda^{2\lambda+1}}_{\text{Photon}}\underbrace{|<\Psi^{J_f\pi_f}||\mathcal{M}^{\sigma\lambda}||\Psi^{J_i\pi_i}>|^2}_{\text{Nucleus}} \tag{2.4}$$

while the reduced transition probability can be expressed by:

$$B(\sigma\lambda, J_i\pi_i\to J_f\pi_f) = \frac{2J_f+1}{2J_i+1}|<\Psi^{J_f\pi_f}||\mathcal{M}^{\sigma\lambda}||\Psi^{J_i\pi_i}>|^2 \tag{2.5}$$

and the width, Γ_γ, by:

$$\Gamma_\gamma(J_i\pi\to J_f\pi_f) = \hbar W_{J_i\pi\to J_f\pi_f} \tag{2.6}$$

Some of the properties of the electromagnetic transitions in the direct radiative capture reactions are:

- There is a hierarchy between the multipoles: $\frac{w(\sigma,\lambda+1)}{w(\sigma,\lambda)} \sim (k_\gamma R)^2 << 1 \Longrightarrow E1 >> E2 \approx M1 >> E3 \approx M2, ...$ Therefore, only a few multipoles (usually just one) are important for a given transition.
- The multipole order λ must satisfy: $|J_i - J_f| \leq \lambda \leq |J_i + J_f|$
- The transition parity is given by:
  - $\pi_i\pi_f = (-1)^\lambda$ for electric transitions
  - $\pi_i\pi_f = (-1)^{\lambda+1}$ for magnetic transitions
- There is no transition with $\lambda = 0$ and the $E1$ transitions are forbidden in N=Z nuclei

In astrophysical reactions energies are low, thus, the low total momentum J_i=0 has dominant contribution to the transition probability of the reaction rate.

2.3 Radiative Capture Cross Section in a Potential Model

For the radiative capture reactions, which are the most important in astrophysical sites in case that transfer reaction channels are closed, the cross sections for a given final state J_f can be written as (see expression 2.4):

$$\sigma(J_f, E) \sim \sum_{\lambda\sigma} k_\lambda^{2\lambda+1}|<\Psi^{J_f\pi_f}||\mathcal{M}^{\sigma\lambda}||\Psi^{J_i\pi_i}>|^2. \tag{2.7}$$

This is a general definition valid for any of the theoretical calculations used to describe the radiative capture reactions. The electromagnetic operator $\mathcal{M}^{\sigma\lambda}$ was discussed in the previous sections, and the wave functions $\Psi^{J_i\pi_i}$ and $\Psi^{J_f\pi_f}$ are model specific. Here, some general descriptions of the *potential models* will be given as an example.

In general, potential models (includes optical models, direct captures models...) are based on the descriptions of nuclear processes by a Schrödinger equation using local potentials in the entrance and exit channels [BD85]. In the Direct Capture Reactions, the direct capture model (DC) is used[c], where the calculations are simple due to the assumed structureless point-like nuclei and the usage of potentials such as the Optical Models without any imaginary part and spin dependence.

If $\mathbf{R}_{\text{CM}}$ is the position of the centre of mass, and $\mathbf{r}$ is the relative coordinate between the two interacting nuclei, the position of each nuclei can be given by:

$$\mathbf{r_1} = R_{\text{CM}} - \frac{A_1}{A}\mathbf{r} \tag{2.8}$$

$$\mathbf{r_2} = R_{\text{CM}} - \frac{A_2}{A}\mathbf{r} \tag{2.9}$$

The initial wave functions with E^{ℓ_i} scattering energy can be defined as:

$$\Psi^{\ell_i m_i}(\mathbf{r}) = \frac{1}{r}u_{\ell_i}(r)Y_{\ell_i}^{m_i}(\Omega) \tag{2.10}$$

while the final wave function with final energy E^{ℓ_f} can be given as:

$$\Psi^{\ell_f m_f}(\mathbf{r}) = \frac{1}{r}u_{\ell_f}(r)Y_{\ell_f}^{m_f}(\Omega) \tag{2.11}$$

The radial functions $u(r)$ are obtained by solving the Schrödinger equation:

$$-\frac{\hbar^2}{2\mu}\left(\frac{d^2}{dr^2} - \frac{\ell(\ell+1)}{r^2}\right)u_\ell + V(r)u_\ell = E^\ell u_\ell \tag{2.12}$$

where the potentials $V(r)$, including electromagnetic and nuclear interactions, can be different in the initial and final states and the parameters are adjusted to reproduce properties such as **phase shifts** (details in next section), bound states energies etc...

Examples of the typical potentials used are:

$$V_{\text{Coul}}(R) = Z_p Z e^2 \begin{cases} \left(\frac{3}{2} - \frac{R^2}{2R_{\text{Coul}}^2}\right)\frac{1}{R_{\text{Coul}}} & \text{for R} \leq R_{\text{Coul}} \\ \frac{1}{R} & \text{for R} \geq R_{\text{Coul}} \end{cases} \tag{2.13}$$

for the Coulomb potential, where $R_{\text{Coul}} = r_{\text{Coul}}A^{1/3}$ is the radius of the nucleus considered as an sphere with uniformly distributed total charge of Ze, and r_{Coul} a constant depending on the nucleus. For the nuclear interaction the most commonly used potential is the "Woods-Saxon" shape:

$$V(R) = -\frac{V_r}{1 + e^{\frac{R-R_r}{a_r}}} \tag{2.14}$$

where V_r is the depth, a_r is the diffuseness, and R_r is the nuclear radius, which is commonly expressed by $R_r = 1.2 \cdot A^{1/3}$ for A the number of nucleons.

For example, the electric operator for two particles, this can be rearranged as:

$$\mathcal{M}_\mu^{E\lambda} = e\left(Z_1|\mathbf{r_1} - \mathbf{R}_{\text{CM}}|^\lambda Y_\lambda^\mu\left(\Omega_{r_1-R_{\text{CM}}}\right) + Z_2|\mathbf{r_2} - \mathbf{R}_{\text{CM}}|^\lambda Y_\lambda^\mu\left(\Omega_{r_2-R_{\text{CM}}}\right)\right) \tag{2.15}$$

[c] Among potential models, *optical models* are used for elastic scattering analysis and *distorted-wave Born approximation (DWBA)* are used for transfer reactions

which provides

$$\mathcal{M}_{\mu}^{E\lambda} = e \underbrace{\left[Z_1 \left(-\frac{A_2}{A} \right)^{\lambda} + Z_2 \left(-\frac{A_1}{A} \right)^{\lambda} \right]}_{Z_{\text{eff}}} r^{\lambda} Y_{\lambda}^{\mu}(\Omega_r) = e Z_{\text{eff}} r^{\lambda} Y_{\lambda}^{\mu}(\Omega_r) \tag{2.16}$$

thus, the matrix elements can be expressed by

$$< \Psi^{J_f m_f} | \mathcal{M}_{\mu}^{E\lambda} | \Psi^{J_i m_i} >= e Z_{\text{eff}} < Y_{J_f}^{m_f} | Y_{\lambda}^{\mu} | Y_{J_i}^{m_i} > \int_0^{\infty} u_{J_i}(r) u_{J_f}(r) r^{\lambda} dr \tag{2.17}$$

and the reduced matrix elements by:

$$< \Psi^{J_f} || \mathcal{M} || \Psi^{J_i} >= e Z_{eff} < J_f 0 \lambda \;\; 0 | J_i 0 > \cdot \left(\frac{(2J_i + 1)(2\lambda + 1}{4\pi(2J_f + 1)} \right)^{1/2} \int_0^{\infty} u_{J_i}(r) u_{J_f}(r) r^{\lambda} dr \tag{2.18}$$

Therefore, for given values of J_i, J_f and λ, the integrated cross section result in:

$$\sigma_{\lambda}(E) = \frac{8\pi}{k^2} \frac{e^2}{\hbar c} Z_{eff}^2 k_{\gamma}^{2\lambda+1} F(\lambda, J_i, J_f) \left| \int_0^{\infty} u_{J_i}(r, E) u_{J_f}(r) r^{\lambda} dr \right|^2 \tag{2.19}$$

with:

$$F(\lambda, J_i, J_f) \quad = \quad < J_i \lambda 0 \;\; 0 | J_i 0 > (2J_i + 1) \frac{(\lambda + 1)(2\lambda + 1)}{\lambda(2\lambda + 1)^2} \tag{2.20}$$

$$k_{\gamma} \quad = \quad \frac{E - E_f}{\hbar c} \tag{2.21}$$

The normalisation procedure leads to obtain the radial wave functions:

$$u_J \longmapsto F_j(kr) cos\delta_J + G_J(kr) sin\delta_J \tag{2.22}$$

for the initial continuum state, and

$$u_J \longmapsto \text{Cexp}(-k_B r) \tag{2.23}$$

for the final bound state, and the total (integrated) cross section will given by:

$$\sigma(E) = \sum_{\lambda} \sigma_{\lambda}(E). \tag{2.24}$$

Moreover, as there is no interference between the multipolarities, the differential cross sections can be given by:

$$\frac{d\sigma}{d\theta} = \left| \sum_{\lambda} a_{\lambda}(E) P_{\lambda}(\theta) \right|^2 \tag{2.25}$$

where $P_{\lambda}(\theta)$ are the Legendre polynomial. Thus, the angular distribution measurements are necessary to separate the multipolarities, although usually one of the multipolarities contributes dominantly.

Apart from potential models, microscopic models, based for example on *Resonating group methods* (RGM), are also used to describe the cross section of radiative capture reaction. RGM are fully microscopic in nature, which solve the seven-body problem (in case of ^{3}He(α,γ)^{7}Be) using nucleon-nucleon potentials with the parameters adjusted to reproduce the bound state and resonance properties. It is out of the scope of this thesis to describe this method here, details can be found in [Wee37, Whe37, Des01].

R-matrix calculations [LT58] have also been used for determining the astrophysical $S_{34}(0)$ factor. In nuclear astrophysics, this method aims to parametrise experimental known quantities as the phase shifts of cross sections with a small number of parameters, which are used to extrapolate down to the astrophysical relevant energies. The "poles" in the R-matrix calculations correspond to the bound states or resonances and it is assumed that the space is divided into two regions, (i) the internal region where the nuclear force takes place and, (ii) the external region where only the Coulomb interaction is present.

2.4 Phase-shifts Analysis: Elastic Scattering of ^{3}He and ^{4}He and its Relevance to S_{34}(E) Data

In the previous section (see expression 2.12), it was already discussed that the parameters of the potentials V(r) used to describe our ^{3}He(α,γ)^{7}Be reaction are adjusted to reproduce the phase shifts obtained from the ^{3}He-^{4}He elastic scattering data. Moreover, the reliability of different theoretical models describing the ^{3}He(α,γ)^{7}Be reaction will be gauged by evaluating their ability to reproduce the experimental phase shifts for the elastic channel of the ^{3}He+^{4}He reaction. Here, the definition of phase shift and different phase shift analyses related to our reaction will be discussed:

Quantically, a mono-energetic beam of particles is represented by a plane wave, which suffers scattering upon passing through a region where the influence of a potential $V(r)$ created by a nucleus is present. In nuclear physics experiments performed to study elastic scattering reactions, the detectors are placed far away from the scattering centre, that is, in a region where particles do not significantly feel the presence of the potential anymore. Thus, one will be interested only in the asymptotic part of the wave function, i.e. $r \to \infty$. Clearly, a detector placed in the asymptotic region will detect not only the plane waves, but also its scattered component. For the simple case of spherically symmetric potentials V(r) the stationary part of the incident plane wave can be described as:

$$\Psi = e^{i\mathbf{k}\cdot\mathbf{r}} = e^{ikz} = e^{ikrcos\theta} = \sum_{\ell=0}^{\infty}(2\ell+1)i^{\ell}j_{\ell}(kr)P_{\ell}(cos\theta) \tag{2.26}$$

where j_ℓ(x) and P$_\ell(cos\theta)$ are the Bessel functions and the Legendre polynomials, respectively. Therefore, the outgoing wave functions far from the scattering centre can be expressed by:

$$\Psi \sim \underbrace{e^{ikz}}_{\text{incoming}} + \underbrace{f(\theta)\frac{e^{ikr}}{r}}_{\text{scattered}} \tag{2.27}$$

where the symbol $\sim$ refers to the asymptotic value, and the θ dependence in the scattering amplitude function $f(\theta)$, accounts for the probabilities as a function of the angle with respect to the incoming beam. Therefore, the elastic scattering cross section is given by:

$$\frac{d\sigma^s}{d\Omega} = |f(\theta)|^2 \tag{2.28}$$

When the interactions are governed by central potentials $V(r)$, the solutions of the Schrödinger equation

$$\nabla^2\Psi + \frac{2m}{\hbar^2}\left[E - V(r)\right]\Psi = 0 \tag{2.29}$$

can be expressed as linear combinations of the separable radial and angular parts

$$\Psi = \sum_{\ell,m} a_{\ell m}\frac{u_\ell(r)}{r}Y_\ell^m(\theta,\phi) \tag{2.30}$$

where $u_l(r)$ is obtained from the radial Schrödinger equation:

$$\frac{d^2u}{dr^2} + \frac{2m}{\hbar^2}\left[E - V(r) - \frac{\hbar^2}{2n}\frac{\ell(\ell+1)}{r^2}\right]u = 0 \tag{2.31}$$

with the boundary condition $u_\ell(0) = 0$. The dependence of ϕ can be eliminated because of the symmetry in the scattering process of particles due to a central potential, and the wave function takes the form of:

$$\Psi = \sum_{\ell} a_\ell P_\ell(cos\theta)\frac{u_\ell(r)}{kr} \tag{2.32}$$

On the other hand, at large distances from the origin the spherical Bessel functions reduce to a simple expression:

$$j_\ell(kr) \sim \frac{sin(kr - \frac{\ell\pi}{2})}{kr} = \frac{e^{i(kr-\frac{\ell\pi}{2})} - e^{-i(kr-\frac{\ell\pi}{2})}}{2ikr}, \tag{2.33}$$

therefore, by substituting in the expression 2.26 we have

$$e^{ikrcos\theta} \sim \frac{1}{2i}\sum_{\ell=0}^{\infty}(2\ell+1)i^\ell P_\ell(cos\theta)\left[\frac{e^{i(kr-\frac{\ell\pi}{2})} - e^{-i(kr-\frac{\ell\pi}{2})}}{kr}\right] \tag{2.34}$$

which represents the asymptotic form of a plane wave. The first term in brackets corresponds to an outgoing spherical wave and the second to an incoming spherical wave. The asymptotic form of Ψ can be obtained if we observe that the presence of a potential cause a perturbation in the outgoing part of the plane wave, and such a perturbation can be represented for the elastic scattering by a unitary module function:

$$S_\ell(k) = e^{2i\delta_\ell} \tag{2.35}$$

We now have,

$$\Psi \sim \frac{1}{2i}\sum_{\ell=0}^{\infty}(2\ell+1)i^\ell P_\ell(cos\theta)\left[\frac{S_\ell(k)e^{i(kr-\frac{\ell\pi}{2})} - e^{-i(kr-\frac{\ell\pi}{2})}}{kr}\right] \tag{2.36}$$

and from a comparison with expression 2.32, the asymptotic form of $u_\ell(r)$ can be seen as

$$u_\ell(r) \sim sin\left(kr - \frac{\ell\pi}{2} + \delta_\ell\right). \tag{2.37}$$

Thus, due to the effect of potential on the outgoing channel, $u(r)$ differs from the radial function of a free particle by the presence of the **phase shift $\boldsymbol{\delta_\ell}$**. From expressions 2.27, 2.34 and 2.36 we have

$$f(\theta) = \frac{1}{k}\sum_{\ell=0}^{\infty}(2\ell+1)e^{i\delta_\ell}sin\delta_\ell P_\ell(cos\theta) \tag{2.38}$$

and integrating the expression 2.28 the total elastic scattering cross section takes the form of

$$\sigma^s = \frac{4\pi}{k^2}\sum_\ell(2\ell+1)sin^2\delta_\ell \tag{2.39}$$

The previous results were obtained by assuming a central potential, V(r)$\sim$1/r^2, however, in case that the incoming particles are affected by, for example, Coulomb interaction, as in the ^{3}He+^{4}He system, the potential takes the form of V(r)$\sim$1/r and the Bessel functions in equation 2.33 takes the form of Coulomb functions, and the scattering amplitude becomes:

$$f_C(\theta) = -\frac{\eta}{2ksin^2\frac{1}{2}\theta}\exp[-i\eta\cdot ln(\sin^2\frac{1}{2}\theta) + 2i\cdot arg\Gamma(1+i\eta)] \tag{2.40}$$

For a more general case where the nuclear interaction also plays a role, the scattering amplitude can be expressed as:

$$f(\theta) = f_C(\theta) + 1/(2ik)\sum(2\ell+1)P_l(\cos\theta)\exp(2i\sigma_\ell)(S_{n\ell}-1) \tag{2.41}$$

where σ_ℓ are the Coulomb phase shifts given by: σ_ℓ=arg$\Gamma(\ell$+1+i$\eta)$ and the nuclear partial wave, $S_{n\ell}$, is related to the nuclear phase shift, $\delta_{n\ell}$, by: $S_{n\ell}$=exp($2i\delta_{n\ell}$), which is 1 when there is no nuclear force.

This, in turn, is determined by the asymptotic form for larger r of the radial wave function F_ℓ(r) of the relative motion of the target and projectile:

$$F_\ell(r) \sim \sin(kr - \frac{1}{2}\ell\pi + \eta \cdot ln2kr + \sigma_\ell + \delta_{n\ell}). \tag{2.42}$$

The elastic scattering cross section will be given now by $\sigma^s = |f(\theta)|^2$. Thus, the usual optical procedure for obtaining the phase shifts is to solve the radial Schrödinger equation for F$_\ell$(r) numerically

$$\frac{\hbar^2}{2\mu}\left(-\frac{d^2}{dr^2} + \frac{\ell(\ell+1)}{r^2}\right)F_\ell(r) + V(r)F_\ell(r) = EF_\ell(r) \tag{2.43}$$

to match the numerical solution on to a Coulomb wave function at some point outside the range of the nuclear optical potential and then to extract the phase shift by comparison with the asymptotic form in equation 2.42.

Therefore, for a given potential V(r) between, e.g. two interacting nuclei as ^{3}He and ^{4}He, the evaluated phase shifts obtained by solving the equation 2.43 must reproduce the measured elastic scattering cross section. In other words, the potential V(r) to be used in the theoretical capture model for our ^{3}He(α,γ)^{7}Be reaction can be validated by using the ^{3}He+^{4}He elastic scattering data.

The asymptotic wave functions of ^{7}Be bound states are well known. However, differences among models originate from differing s-wave phase shifts and from short-range contributions of the potentials. The latter are difficult to compute and can only be tested by capture reaction experiments above 1 MeV centre of mass energy. Concerning the phase shifts, most of the ^{3}He(α,γ)^{7}Be studies are informed only by the phase shift analysis of Tombrello and Parker [TP63b]. They measured the elastic scattering of ^{3}He ions from ^{4}He target gas at incoming energies above 5.75 MeV. They obtained the excitation curves, i.e. cross section versus energy at a fixed angle, for eight different angles and the angular distributions at four different bombarding energies. Figure 2.3 shows an example of the excitation curves at three different angles (a) and the angular distributions (differential cross sections) at two different bombarding energies (b). In both cases the solid line represents the fit to the data using derived phase shifts.

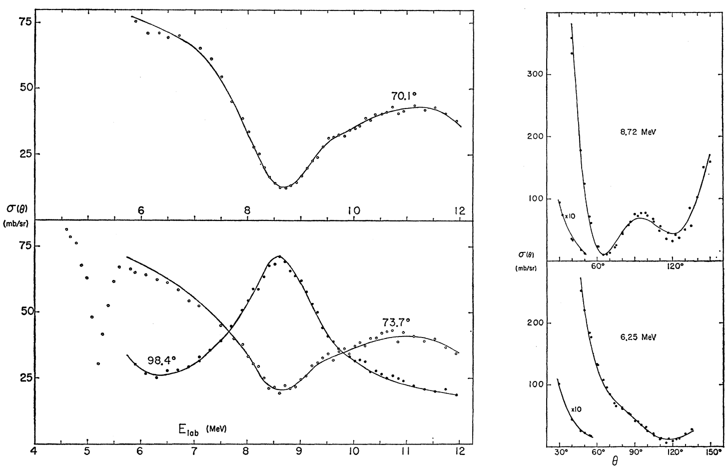

(a) (b)

Figure 2.3: *The elastic scattering data for ^{3}He+^{4}He system as shown in [TP63b]. The dots represent data and the solid lines represent calculations. (a) The excitation curves for 70.1°, 73.7° and 98.4°, where the dip (peak) at excitation energy of 8.7 MeV and forward (backward) angles corresponds to a new resonance predicted by the authors using the phase shift analysis. (b) The scattering cross section for the bombarding energies of 8.72 and 6.25 MeV (see text for more details).*

As one can see there is a good agreement between experimental data and the calculations from a phase shift analysis. It is worth pointing that the properties of the four lowest levels in the ^{7}Be level scheme could also be reproduced by these calculations.

A different phase shift analysis has been done by Mohr et al. [MAK93, Moh09] where the strength parameters λ and λ_{LS} of the potential (obtained by a folding procedure [SL79]):

$$V(r) = \lambda V_F(r) + \lambda_{LS} \frac{fm^2}{r} \frac{dV_F(r)}{dr} \overrightarrow{L}\,\overrightarrow{S} + V_C(r) \tag{2.44}$$

are adjusted to the measured phase shifts at energies relative higher compared to Spiger and Tombrello [ST67], Boykin et al. [BBH72] and Hardy et al. [HSB72]. The results are compared with the ^{3}He(α,γ)^{7}Be cross section data from ERNA [DGK09] and with the elastic scattering angular distributions measured at lower energies in [MAK93] and [BJP64], covering the same energy range. The results are shown in Figure 2.4, where (a) shows the ^{3}He+^{4}He elastic scattering angular distributions with the different curves representing different values of the λ and λ_{LS} parameters and (b) the same for the ^{3}He(α,γ)^{7}Be astrophysical S-Factor. The elastic scattering cross sections are reproduced with the black ($\lambda = 1.45$) or dash green line ($\lambda = 1.40$). This corresponds to the $L = 2$ elastic phase shift weak potential strength. However, the ^{3}He(α,γ)^{7}Be reaction cross section at high energy from ERNA [DGK09] can be described only with a significantly enhanced $L = 2$ potential ($\lambda \sim 1.60$).

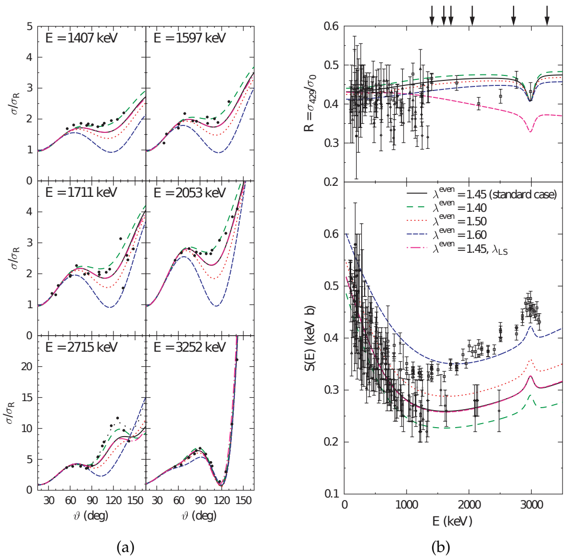

Figure 2.4: *Direct Capture model calculation by P. Mohr [Moh09] where the potential parameters are obtained from a phase shift analysis of the elastic scattering data. (a) The ^{3}He+^{4}He elastic scattering angular distributions. The points represent the experimental data from [MAK93, BJP64] and the different fits correspond to the calculations for different potential strengths (λ). (b) The astrophysical S-factor for the ^{3}He(α,γ)^{7}Be reaction. The colour of the fits are the same as those in (a). See text for the discussion.*

Finally, it should be stressed that even though the phase shift analysis is a good constraining tool in validating the theoretical models, to date, most of the theoretical models rely on one experiment from the early 1960's without any error estimations [TP63b]. Although, the experimental data were extended to lower energies by Mohr et al.[MAK93], they do not include error estimations in the phase shifts analysis [AGR11].

2.5 Theoretical Descriptions of the ^{3}He(α,γ)^{7}Be Reaction

The reaction ^{3}He(α,γ)^{7}Be occurs via the radiative capture process. The ground state spins for ^{4}He and ^{3}He are 0^+ and $1/2^+$, respectively. As mentioned in the previous chapter, at low energies, the $\ell = 0$ relative orbital angular momentum of the pair of nuclei (i.e. s-wave channel) has dominant contribution to the reaction probability. Thus, for this channel, the total incoming angular momentum is $J_i = 1/2^+$. On the other hand, the ^{7}Be ground and first excited states have spins of J_f=3/2$^-$ and J_f=1/2$^-$, respectively. Therefore, in line with the properties of electromagnetic transitions described in section 2.2, the E1 transition from the s-wave channel dominates for this reaction both for the ground and for the first excited states. Figure 2.5 shows calculated contributions of $\ell = 0, 1, 2$ and 3 partial waves and E1, E2 and M1 multipoles from reference [KIN81]. As can be seen the s-wave partial contribution from the E1 transitions are the dominant ones at low energies. As the energy is increased other partial wave contributions become significant ($\ell = 2$, d-wave).

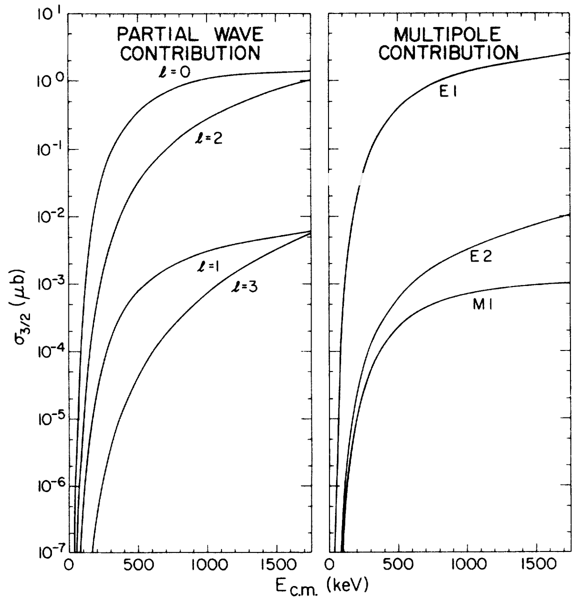

Figure 2.5: *Different partial wave (s,p,d,f) and electromagnetic transition (E1,E2,M1) contributions to the cross sections populating the ground state of ^{7}Be by the radiative capture reaction ^{3}He(α,γ)^{7}Be. Figure is taken from [KIN81].*

The initial calculations for this reaction were performed by Christy and Duck [CD61] and by Tombrello and Phillips [TP61]. The first experimental results for this reaction by Holmgren and Johnston [HJ59] were already explained in a quantitative way by assuming an extra-nuclear direct capture by electric dipole emission (E1) from the s-wave ($\ell = 0$) of the initial state to the final bound p-wave states ($1p_{3/2}$,$1p_{1/2}$) that were assumed to be of two body form: ^{3}He+^{4}He cluster.

Several theoretical calculations followed in order to both reproduce the experimental data and achieve further insight into the physics mechanism of the reaction by, for example, considering different potential models. Differences arise, for example, from considering non-external contributions (nuclear effects) and initial-states phase-shifts (previous section). The ^{3}He+^{4}He cluster configuration has overlaps with the two bound states of ^{7}Be populated in the reaction. Therefore the Pauli principle requires radial nodes in these overlaps with a small (but non-zero) short-range contribution [AGR11]. Here, only an overview of the representative models highlighting the main qualitative features will be presented.

Tombrello and Parker use an external capture potential model and first order perturbation theory. Only the asymptotic forms of the bound and scattering states wave functions are considered, neglecting the behaviour of the wave functions at short distances [TP63a]. The ^{3}He and ^{4}He nuclei are treated as point particles and the hard sphere scattering radius considered is determined by the phase shift analysis in [TP63b]. Also potential models with more realistic treatment of contributions from 2.8 to 7.0 fm distances are provided by Kim et al. [KIN81], Buck et al. [BBR85, BM88] and Mohr et al. [MAK93]. They use nucleus-nucleus potentials such as Wood-Saxon or folding potentials. The wave functions are calculated from potentials, which simultaneously describe the bound-state properties and phase shifts. Therefore, the energy behaviour of the astrophysical S-factor in this models is almost fixed by the spectroscopic factors considered in the calculations.

Other calculations are based on microscopic cluster model frameworks, where the system is described by antisymmetrized wave functions of two clusters using phenomenological nucleon-nucleon potentials. The relative motion of the clusters is solved using resonating group or generator coordinate methods. The energy dependence in this case, particularly the evaluation of Kajino et al. using microscopic cluster models and resonating group method (RGM) [KTA87] is similar to that determined using hard-sphere model by Tombrello and Parker. This RGM model, details can also be found in [KA84, Kaj86], also reproduces the phase shifts of Tombrello and Parker [TP63b] without employing any fitting procedure. The potential models have a justification in the resonating group work in the form of microscopic potential model of Langanke [Lan86]. This model, and those using RGM [KA84, KTA87] predicted the energy dependence of the isospin mirror reaction ^{3}H(α,γ)^{7}Li reaction before this was experimentally measured by Brune et al. [BWR94] (see Figure 2.6(b)). However, some variations appear between different RGM models in that they employ different types of interaction. These differences depend on the diffuseness of the ^{7}Be ground state [Kaj86, CL00]. Moreover, large differences are observed in the astrophysical S-factor and phase shift values if the model space is expanded, for example when cluster states of ^{6}Li+p channel are added to the RGM wave functions [MH86, CL00]. Other microscopic approaches were due to Walliser et al. [WKT84] and Liu et al. [QKT81] while [DDK95] used a potential model approach.

Kenneth Nollet considers an accurate realistic nucleon-nucleon interaction to derive the wave functions employing a variational Monte Carlo technique [Nol01]. In this approach, the relative motion of the initial states is based on the potential used by Kim et al. [KIN81], and it accurately reproduces the s-wave shift of Tombrello and Parker [TP63b]. Other electromagnetic observables in ^{7}Li and ^{7}Be nuclei are in reasonable agreement with those from the microscopic calculations of Kajino [Kaj86]. Also, the energy dependence is the same as the seen in [Kaj86] while the absolute $S_{34}(0)$ value is 25% smaller.

Some experimental data evaluations have been also carried out. Descouvemont et al. use R-matrix fit analysis (essentially reduced to a potential model) to determine the $S_{34}(0)$ [DAA04]. Cyburt and Davids evaluated the experimental modern data from Weizmann [NHNEH04], Seattle [BBS07], and LUNA [BCC06, GCC07, CBC07] using a minimal model-dependent approach [CD08]. They based their work on the fact that the reaction is dominated by an external capture and the S-factor exhibits subthreshold poles in low energy astrophysical range according to Mukhamedzhanov and Nunes [MN02]. The *Solar Fusion Cross Section II* evaluation [AGR11], uses rescaled theoretical models of Nollet [Nol01] and Kajino [Kaj86] (the energy dependence is the same) to fit the same modern data used in the evaluation of Cyburt and Davids, plus the ERNA data [DGK09] up to 1 MeV.

Finally, the first ab-initio calculations by Thomas Neff [Nef11] are based on a fully microscopic fermionic molecular dynamics (FMD) approach with a realistic interaction that reproduces the nucleon-nucleon scattering data. Specifically, this model uses the Argonne V18 Interaction [WSS95] which reproduces the deuteron properties and the nucleon-nucleon phase shifts. The known properties of the bound states such as the charge radii, quadrupole moments or energy could be well reproduced by the calculations. The calculated phase shifts in the s-wave and d-wave channels agree also fairly well with the experimental data in [ST67, BBH72]. To obtain the cross section of the ^{3}He(α,γ)^{7}Be reaction only dipole transitions (E1) from the s- and d-waves are considered. There seems to be a significant contribution of the internal part of the nuclei and therefore the reaction should not be considered purely external. The agreement with the modern data is remarkable up to 2.5 MeV (note that the Solar Fusion Cross Section II considered only up to 1 MeV) as it can be seen in Figure 2.6(a) [Nef]. However, for the isospin mirror ^{3}H(α,γ)^{7}Li reaction, even though the energy dependence is well described when comparing with the

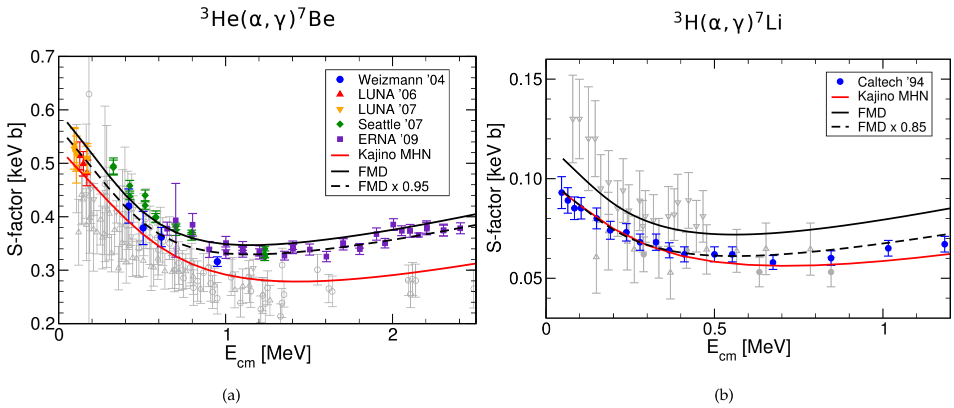

Figure 2.6: *The black line shows the ab-initio calculations for the astrophysical S-factor of the $^3He(\alpha,\gamma)^7Be$ (a) and $^3H(\alpha,\gamma)^7Li$ (b) reactions [Nef]. The red line shows the calculations by Kajino et al. [Kaj86].*

new experimental data of Brune et al. [BWR94], the absolute scale is off by a 15% (see Figure 2.6(b)). This should be further investigated. Modifications in theory may be required to reproduce both reactions if new experimental data are obtained for both reactions at medium energies.

Table 2.1 shows $S_{34}(0)$ values from for different evaluations and models highlighting the discrepancies among them.

Model/Evaluation	$S_{34}(0)$ (keV·b)
R-matrix [DAA04]	0.51±0.04
Cyburt and Davids [CD08]	0.580±0.043
Solar Fusion Cross Sections II [AGR11]	0.56±0.02(expt)±0.02(theor)
Ab-initio calculations [Nef11]	0.593

Table 2.1: *$S_{34}(0)$ values from different theoretical models and evaluations. R-matrix and Cyburt and Davids use experimental data evaluation. Solar Fusion Cross Section II evaluation use the theoretical models of Kajino et al. [KTA87] and Nollet [Nol01] and the experimental data up to 1 MeV. Finally, the FMD ab-initio calculation do not utilise any data but directly gives the $S_{34}(0)$.*

In Figure 2.7 the most used theoretical calculations are plotted together with the modern experimental data. It should be pointed out here that the usage of spectroscopic factors by potential models can justify the fact of considering rescaling parameters in order to fit the experimental data and extrapolate to lower energies. Rescaled Microscopic models should be as accurate as potential models and more accurate than hard-sphere model [AGR11]. Nevertheless, the theoretical curves are given without any normalisation in Figure 2.7. Regardless of the effect of normalisation, there is a discrepancy in the energy dependence at high energies, and none of them completely reproduce the observed resonance corresponding to the $7/2^-$ state in ^{7}Be . New experimental data in the range of 1-3 MeV will constrain the theoretical models and will help understanding the importance of the non-external nuclear contributions.

Finally, it should be pointed out that the models discussed above, that are generally applied in nuclear astrophysics, are good for low densities only; for high densities or high energy reactions one should resort to the Hauser-Feshbach theory [TAT86].

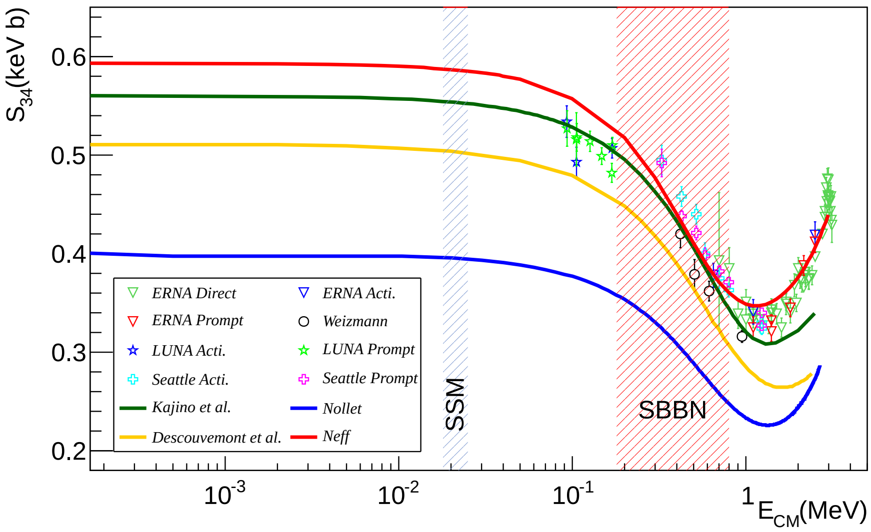

Figure 2.7: *A comparison between the theoretical models from Kajino et al. [KTA87], Nollet [Nol01], Descouvemont et al. [DAA04] and Neff [Nef11], plotted together with the modern data from the ERNA [DGK09], Weizmann [NHNEH04], LUNA [BCC06, CBC07, GCC07] and Seattle [BBS07] collaborations. A big discrepancy among the different models and calculated $S_{34}(0)$ is observed.*

2.6 Conclusion

In this chapter, the ^{3}He(α,γ)^{7}Be nuclear reaction has been described in terms of an electromagnetic transition between an ^{3}He+^{4}He scattering state and a bound state in the ^{7}Be. The general formalism to obtain the cross section of such reactions has been described together with the relevant phase shift analysis procedure for the elastic channel. The main features of different theoretical models have been described. Differences between the theoretical models at medium-high energies are observed, not only in the absolute scale of the S-factor curve, but also in its energy dependence. New experiments in the range of E_{CM}= 1-3 MeV will help us to constrain the theoretical models and to investigate the importance of the non-external nuclear contribution to the cross section. Although it will be discussed in Chapter 6, it is worth mentioning here that new experimental elastic scattering data would be needed as most of the potential and microscopic models rely on the phase shift analysis of one experiment carried out in the 1960's and the new experimental developments could improve the situation.

"A theory is something nobody believes, except the person who made it. An experiment is something everybody believes, except the person who made it."

Albert Einstein

CHAPTER 3

EXPERIMENTAL TECHNIQUES

Abstract: *In this chapter the two experimental techniques used to determine the cross section of the ^{3}He(α,γ)^{7}Be reaction will be described. Firstly, the experimental approaches used in previous works will be recalled. Later, the two main sections will detail the two complementary methods together with the setups used in our measurements to determine $\sigma(E)$ and evaluate the astrophysical S-factor. How to extract the observables as well as all other necessary details to determine the cross section and the consistency checks for the two types of methodologies will also be discussed.*

In the previous chapters the motivation for obtaining the S-factor for the ^{3}He(α,γ)^{7}Be reaction and the theoretical background have been detailed. Here, the experimental techniques used in order to determine the cross section, and thus the S-factor are described.

A well designed experimental setup with optimum control of the different settings is the key for successful measurements and reliable results with minimised uncertainties. Different approaches have already been used aiming to determine accurately the cross section of this reaction at different energies. A few pros and cons of some of these methods will be presented in this chapter.

In our case, two experiments using alternative and complementary techniques were performed in order to determine the cross section for the ^{3}He(α,γ)^{7}Be reaction at medium-high energies. The reason for selecting this energy range was discussed in the first Chapter and will be recalled here. In the first experiment, the *Activation Method* was chosen for simplicity allowing us a better control of the setup. For the second type of experiment, the *Direct Recoil Counting Method* was chosen employing the DRAGON spectrometer at TRIUMF. In contrast to the activation method this is a complicated setup and requires extensive characterised tests. Complementary, information related to the prompt γ-ray angular distributions as well as the $\sigma_{429}/\sigma_{g.s.}$ ratio were also aimed for in this experiment.

3.1 The Reaction and the Methods for Cross Section Measurements

In Chapter 1 the important role of the ^{3}He(α,γ)^{7}Be reaction in the Sun and in the Big Bang Nucleosynthesis was discussed. A schematic picture of how the reaction takes place, for example in the Sun, can be seen in Figure 3.1. ^{4}He and ^{3}He nuclei approach each other and when the nuclei overcome the Coulomb and centrifugal barriers the fusion occurs, creating a ^{7}Be nucleus and emitting a prompt γ-ray. The ^{7}Be ions are unstable and decay to the first excited state at 478 keV in ^{7}Li by the electron capture process with a half life of 53.24(4) days and a branching ratio of 10.44(4)%. A γ-ray of 478 keV is subsequently emitted by the de-excitation of the excited ^{7}Li to the ground state.

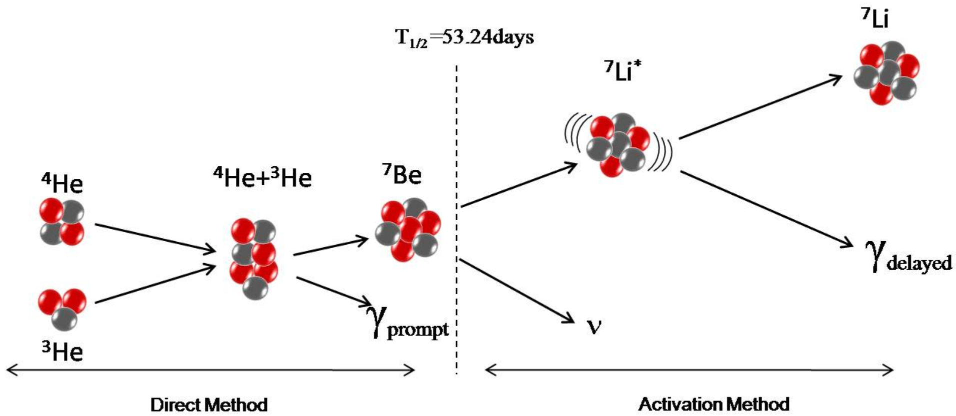

Figure 3.1: *Diagram showing the ^{3}He capture on ^{4}He, emission of the prompt γ-ray and the subsequent decay of the reaction product, ^{7}Be. The ^{7}Be ions decay via electron capture producing ^{7}Li* in its first excited state and emitting a neutrino with a branching ratio of 10.44(4)%. The subsequent 478 keV γ-ray from ^{7}Li* is also shown. In the lower part, where the two experimental methods used in the present work takes place are also indicated.*

A sketch of the decay scheme of the reaction is shown in Figure 1.12 and Table 3.1 specifies some information relevant for this reaction.

$Q_{^{3}\mathrm{He}(\alpha,\gamma)^{7}\mathrm{Be}}$	1580(1) keV
E (^{7}Be$^{*}_{1^{st}state}$)	429 keV
$T_{1/2}$(^{7}Be)	53.24(4) d
$Q_{^{7}\mathrm{Be}(e^{-},\nu)^{7}\mathrm{Li}}$	862 keV
B.R. (^{7}Li$^{*}_{1^{st}state}$)	10.44(4)%
E (^{7}Li$^{*}_{1^{st}state}$)	478 keV

Table 3.1: *Some details of the ^{3}He(α,γ)^{7}Be reaction, ^{7}Be and ^{7}Li nuclei. "Q" represents the Q-value for the reaction and for the ^{7}Be decay. E corresponds to the excitation energies for the different states in ^{7}Li and ^{7}Be . $T_{1/2}$ is the half life of the ^{7}Be nucleus and B.R. is the branching ratio populating the first excited state in ^{7}Li.*

The relevant parameter for the astrophysical models is the S(E) factor, given through the cross section σ(E) as it was detailed in the expression 1.7. Therefore, the aim of our measurements is to determine the absolute cross section of the ^{3}He(α,γ)^{7}Be reaction and from there estimate the S-factor, which will be denoted as S_{34}(E), being E the centre of mass energy. Accurate determinations of an absolute cross sections need careful measurements of different observables. For our case, taking a glance at the Figure 3.1, if one wants to determine the absolute cross section of the reaction, the number of total ^{7}Be produced ($Y_{^7\mathrm{Be}}$) and the total number of interacting nuclei ($\mathrm{N°}_{^4\mathrm{He}}, \mathrm{N°}_{^3\mathrm{He}}$) must be known. In order to determine S_{34}(E) by carrying out measurements in the laboratory, one of the interacting helium isotopes must be accelerated as a beam and the other should be the target (recall that at atmospheric conditions the natural state of the helium is gaseous). Therefore, the expression 1.2 for σ(E) takes the following form in this case:

$$\sigma_{34}(E) = \frac{Y_{^7\mathrm{Be}}}{\mathrm{N°}_{^4\mathrm{He}} \cdot \mathrm{N°}_{^3\mathrm{He}}} \tag{3.1}$$

From a close look at Figure 3.1, it can be seen that there are three possible methods in order to obtain the cross section, namely:

- *Direct Recoil Counting Method:* The ^{7}Be recoils produced are counted directly.
- *Prompt γ-Detection Method:* The number of recoils are determined by detecting the prompt γ-rays.
- *Activation Method:* The recoils are collected and their total number is estimated by detecting the 478 keV γ-rays from the ^{7}Li* de-excitation.

Apart from the three different experimental techniques already discussed, two other approaches can be found in the literature, namely *Accelerator Mass Spectrometry* (AMS) and the *Coulomb Breakup* techniques (see below).

Furthermore, even though the goal of the different techniques is the same, when determining the cross section differences appear, for example, in how the total number of incoming beam particles are measured, whether kinematic is direct or inverse, and in the assumptions made e.g. of the prompt γ-ray distributions. An overview of all experiments using the three different techniques was presented in the section 1.5. Here, some differences among the different setups will be briefly described, in particular, those performed at LUNA (Laboratory for Underground Nuclear Astrophysics) and ERNA (European Recoil separator for Nuclear Astrophysics) facilities.

LUNA SETUP

The Laboratory for Underground Nuclear Astrophysics [GAB94, Bro11] in Italy's National Gran Sasso underground Laboratory (LNGS) was designed for measuring low cross sections of nuclear astrophysical reactions. The ^{3}He(α,γ)^{7}Be cross section measurement was carried out using the 400 kV LUNA2 accelerator where the *Prompt γ-Detection* and *Activation Methods* were used covering a centre of mass energy range from 93 keV to 170 keV . The setup used is shown in Figure 3.2(a). A ^{4}He beam impinged onto a windowless differentially pumped ^{3}He gas target. The beam was stopped in a copper disk placed in front of the calorimeter, used to estimate the incoming number of beam particles. The ^{7}Be recoils were deposited in the same copper plate. A silicon detector monitored the ^{3}He gas density by detecting the double scattered beam particles with the gas and the carbon foil. In the *Prompt γ-Detection Method* the prompt γ-rays were detected in the shielded **H**igh **P**urity **Ge**rmanium (HPGe) detector, while for the *Activation Method* the copper plates were removed and the subsequent γ-ray from the ^{7}Li* de-excitation was detected with another germanium detector in a low-background environment.

ERNA SETUP

The European Recoil separator for Nuclear Astrophysics (ERNA) is located at the 4 MV Dynamitron Tandem Laboratorium of the Ruhr-Universität, Bochum, Germany (a general definition of recoil separators is given in section 3.3.1). A layout of the global ERNA setup is shown in Figure 3.2(b) and details can be found in [DDS08] and references therein. The three techniques mentioned above were used by the ERNA collaboration to determine the cross section of the ^{3}He(α,γ)^{7}Be reaction in the centre of mass energy region of 700-3100 keV. A recirculating gas system was used to maintain a constant ^{3}He gas

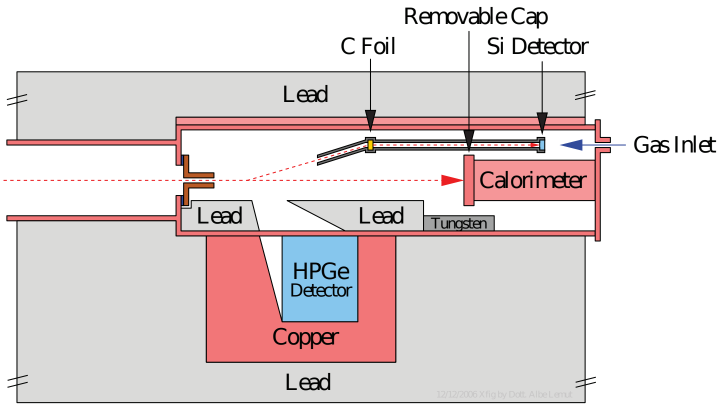

(a)

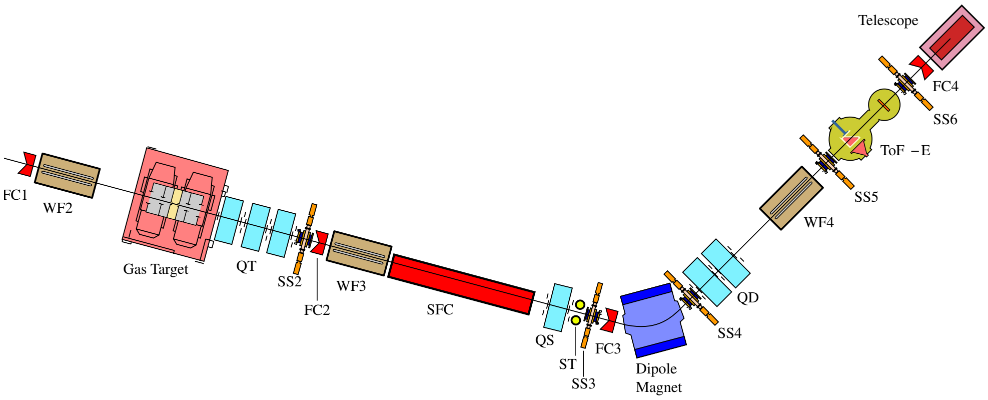

(b)

Figure 3.2: *Examples of different experimental setups used for determining the cross section of the $^3He(\alpha,\gamma)^7Be$ reaction. (a)Sketch of LUNA setup [CBC07]. (b) ERNA layout from [DDS08]*

pressure in the target cell that was impinged by a ^{4}He beam. The number of incoming beam particles was measured by using Faraday cups placed along the separator and the ^{3}He target density was scaled from previous measurements using a ^{4}He gas target. For the *Direct Recoil Counting Method* the ^{7}Be recoils were separated from the leaky beam by using various electric and magnetic elements of the separator. Eventually, the recoils were directly counted in a Gas Silicon Telescope placed at the end of the separator. In the *Prompt γ-Detection Method* the prompt γ-rays were detected using three NaI detectors placed close to the gas cell. Finally, in the *Activation Method*, a copper catcher was placed at 31 cm from the target cell, where the ^{7}Be nuclei were deposited. The ^{7}Be activity was measured in the LNGS facility using the same setup than the one used in LUNA work.

The ^{7}Be recoils implanted in a catcher could also be counted using the *AMS technique*. In order to prove the reliability of the technique, a known quantity of ^{7}Be was produced by using the reaction ^{7}Li(p,n)^{7}Be in the 3 MeV Van de Graaff accelerator of the Weizmann Institute. Later, using the deposited ^{7}Be, BeO$^-$ samples were prepared by adding a precisely determined quantity of ^{9}Be. While the ratio ^{7}Be/^{9}Be chemically calculated was expected to be $4.4{\cdot}10^{-13}$, the measured ratio with the AMS quoted $1.2{\cdot}10^{-13}$. Several potential sources were suggested to explain these discrepancies and further investigation was planned according to [BBBH01]. However, there have been no such further measurements up to date.

On the other hand, two indirect experiments were also tried in an attempt to reduce the uncertainties of the cross section of the ^{3}He(α,γ)^{7}Be reaction: ^{7}Be break up on a ^{208}Pb target at 100 MeV/u at the National Superconducting Cyclotron Laboratory and on a ^{12}C target at 25 MeV/u (*Coulomb Breakup* technique). The idea was to extract the $S_{34}(0)$ value from the indirect Coulomb breakup. In order to do so the nuclear and Coulomb effect must be clearly separated. As it was concluded in [SN04], it is not clear whether this method will help to improve the $S_{34}(0)$ precision as it is not possible to eliminate the nuclear contribution by just angular selection criterion. No further improvements on this method have been reported so far.

To summarise, different energy regions can be addressed using different facilities, techniques, and detectors. In the following subsections the energy region of our interest, the techniques, and the facilities employed to carry out our experiments will be reasoned out [Nar13]. The details of the two experimental setups will follow.

3.1.1 Energy range for the present work

As it was discussed in Chapter 1, there is a large dispersion among the experimental $S_{34}(E)$ data; this is particularly remarkable between the two data sets [PK63, DGK09] in the region from 1 to 3 MeV centre of mass energy (see Figure 3.3).

The experimental limitations to determine the cross sections at low energies have already been mentioned. The cross section decreases doubly exponentially with decreasing energy (see for example the upper panel in figure 1.2) and thus measuring the cross section of the ^{3}He(α,γ)^{7}Be reaction at the relevant energies corresponding to the SSM (Gamow Peak $\sim$22 keV) results impossible. As a consequence, theoretical models are often used (Chapter 2) to get the $S_{34}(0)$ value. As it can be observed in Figure 3.3, these theoretical models also show discrepancy between themselves in the same energy region of 1-3 MeV.

Therefore, we have measured the cross section of the ^{3}He(α,γ)^{7}Be reaction in the centre of mass energy region from 0.8 to 3 MeV aiming to address the current discrepancies between the data sets [PK63, DGK09]. Despite being far from the astrophysical energy region, these measurements are crucial to constrain the theoretical extrapolations, which currently disagree not only in absolute value of the $S_{34}(0)$ factor but also in the energy dependence of the $S_{34}(E)$ curves (see Figure 3.3).

3.1.2 Experimental methods: our choices

Among the different approaches employed to determine the cross section of the ^{3}He(α,γ)^{7}Be reaction, the *Coulomb breakup* and the *AMS* are not suitable to obtain results with sufficient accuracy. In the *Prompt γ-Detection Method*, assumptions must be made about the prompt γ-ray angular distributions.

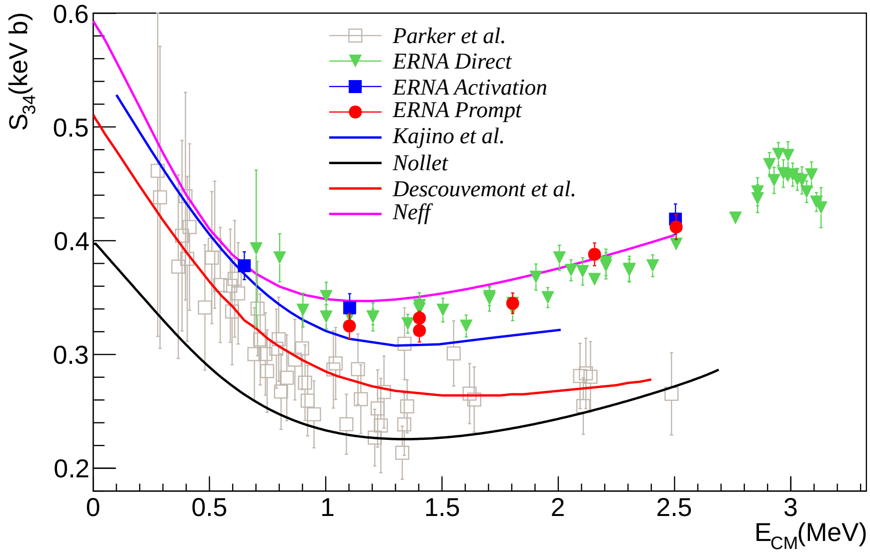

Figure 3.3: *Comparison between the previous experimental values (points) of $S_{34}(E)$ from Parker et al. [PK63] and ERNA collaboration [DGK09], and theoretical models (lines) of Kajino et al.[KA84], Nollet [Nol01], Descouvemont et al. [DAA04] and Neff [Nef11] in the region of E_{CM}= 1-3 MeV.*

Moreover, HPGe detector are the best option in order to clearly resolve the prompt γ peaks; but low efficiency and usage of extended gas targets increase statistical uncertainties.

We thus decided to measure the cross section of the ^{3}He(α,γ)^{7}Be reaction by using the two different and complementary techniques: *Activation* and *Direct Recoil Counting* methods [CGRB14].

3.1.3 Facilities and setups for the present work

After establishing the energy range of interest and the experimental methods of our choice, the facilities utilised for our measurements are introduced. The criteria for the choice of the laboratories include availability of stable (non radioactive) ion beams of ^{3}He or ^{4}He with well defined and stable (within a fraction of keVs) beam energies in the region of 2-7 MeV (E_{CM} ~1-3 MeV).

Nowadays, there are many particle accelerator facilities around the world. Among those devoted to nuclear physics and astrophysics many of them are dedicated mainly to produce radioactive ion beamx (RIB facilities) such as ISOLDE at CERN (Geneva, Switzerland), IGISOL (Jyväskylä, Finland), GSI (Darmstadt, Germany) and RIKEN (Tokyo, Japan). There are also others including small scale accelerator facilities as CNA (Seville, Spain) which fulfil the criteria for our measurements without the need of using a large scale accelerator.

On the other hand, in order to carry out an experiment using the *Direct Recoil Counting Method*, further arrangements are required. Due to the kinematic conditions of the reaction, the recoils are produced with momentum in forward direction following the beam path. In order to count the recoils, we need to separate and identify them from the beam particles. In principle one could use a detector such as a double sided silicon strip detector (DSSSD), an ionisation chamber, or configuration of different detectors as telescopes which would allow an identification of particles based on their energies and masses. However, with the high beam currents required in our case due to the low cross sections, such detectors could not be used as they would get damaged if particles with high rates hit them.

Taking into account the previous issues two different types of experiments were performed employing the *Activation* and *Direct Recoil Counting* techniques . The *Activation* experiment was performed using the tandem accelerator at the CMAM facility, in Madrid, Spain. We used the setup that was successfully used at the Weizmann Institute to determine the cross section of the same reaction in the centre of mass energy region of 420-950 keV [NHNEH04]. For the *Direct Recoil Counting* experiment we used the DRAGON recoil separator at the TRIUMF laboratory in Vancouver, Canada. This separator has already been used for measuring several astrophysical reaction cross sections. The capture reaction studies in the present work has beam and target particles of similar mass which yields a recoil cone angle that is at the limits of the DRAGON separator acceptance. However, as we will see, it will allow us to separate beam ions from recoils and together with simulations reliable cross sections measurements can be performed.

In the *activation method* a ^{3}He$^+$ beam at nine different energies in the range of E$^{\mathrm{beam}}$= 2.1-5.3 MeV and a ^{4}He gas target were used. The ^{7}Be recoils produced were collected on a Cu catcher and the subsequent γ-rays from the de-excitation of the ^{7}Li* were detected offline. Recall here that even the standard way to denote this reaction in this case would be ^{4}He(^{3}He,γ)^{7}Be because the beam is ^{3}He, I will follow the convention of the typical astrophysical (α,γ) reactions and I will denote it as ^{3}He(α,γ)^{7}Be.

In the *direct recoil counting method* the target consisted of a windowless ^{3}He gas, and the beam was ^{4}He$^+$. Four different beam energies between 3.5 and 6.5 MeV were used. In this case, the ^{7}Be recoils were directly counted in a double sided silicon strip detector (DSSSD) at the focal plane of the DRAGON separator.

3.2 Activation Method @ CMAM

The experiment was performed at CMAM (Centro de MicroAnálisis de Materiales) in Madrid [CMA]. CMAM houses an electrostatic linear tandetron accelerator and different beam lines displayed in the layout shown in Figure 3.4. The *Nuclear Physics Line* was used to perform our measurements. This line was developed, designed and built by the Experimental Nuclear Physics Group at the Instituto de Estructura de la Materia (CSIC) -see [Sab03] for more details- . It is operating since the first experiment performed in April 2005 by the same group to study the excited states of ^{12}C using complete kinematic techniques [Alc06].

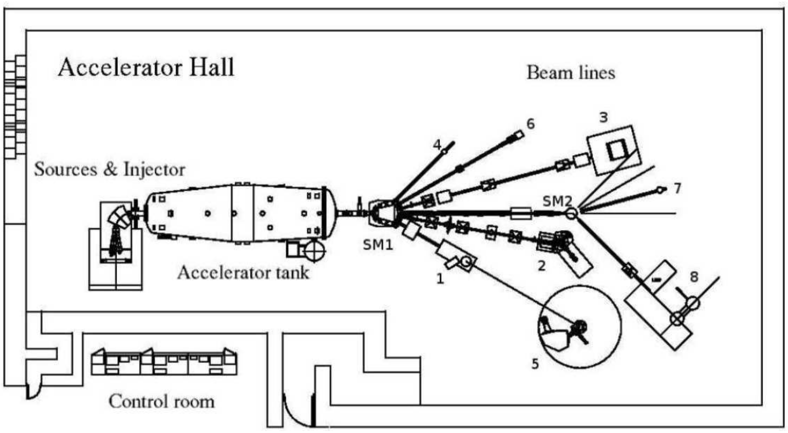

Figure 3.4: *Layout of the CMAM accelerator hall (courtesy of [Pas04]). The magnet, SM1, switches the beam between several beam lines meant for: (1) Multi-purpose, (2) Time-of-Flight, (3) External Micro-beam, (4) Environmental Studies, (5) Magnetic Spectrograph, (6) Nuclear Physics, (7) Ion-beam Modification of Material, and (8) Ultra-High Vacuum experiments. Our setup was installed at the end of the nuclear physics beam line, 6.*

At the CMAM accelerator, by the use of the Duoplasmatron or the Sputtering ion sources can nearly all elements be produced and accelerated. The Duoplasmatron ion source is mainly used to generate He ions and was used in our experiment to produce $^{3}He^{+}$ ions in two discharge stages. The ions were then injected into a Lithium charge exchange canal producing the $^{3}He^{-}$ ions to be accelerated in the tandetron accelerator. A sketch of the ion source and the charge exchange canal are shown in Figure 3.5. The sputtering ion source is used for producing any other stable negative beam from solid sputter targets.

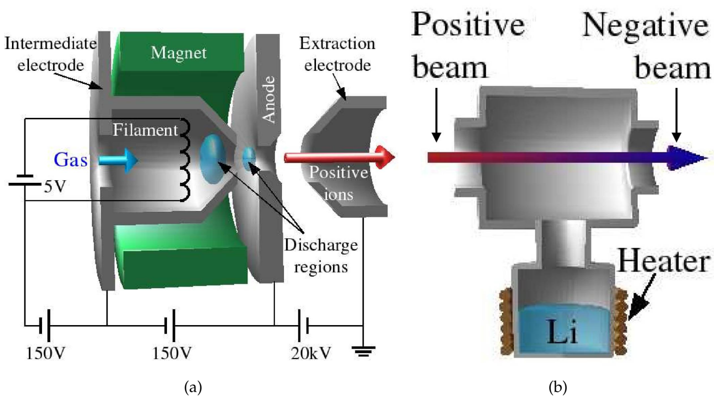

Figure 3.5: *Sketches of the (a) Duoplasmatron ion source and (b) Lithium charge exchange canal (courtesy of [Alc10]). The He^{+} ions are generated in two discharge stages in the ion source. A strong axial magnetic field causes confinement into a small volume resulting in high densities for plasmas. The He^{+} ions flow through the aperture at the centre of the anode into the extraction region. They are then injected into a Lithium charge-exchange canal where they exchange electrons with Li vapour and get converted into $^{3}He^{-}$ ions.*

The accelerator is a 5 MV coaxial high current tandetron using a Cockroft-Walton power supply system [GMH02]. The Cockroft-Walton system supplies beams highly stable in energy. This is a crucial requirement for this experiment because of the dependence of the cross section with energy, which demands not only a beam with precisely known energy but also constant energy throughout the runs. The maximum terminal voltage is 5 MV. The negative ions from the ion source are injected into the accelerator and are accelerated through a vacuum pipe towards the positive terminal placed at the centre of the accelerator. They cross a N_2 gas target, which strips the beam particles of atomic electrons producing positive ion beams. The ions with a charge state "q" are then repelled down to the end of the accelerator which is at ground potential.

3.2.1 Experimental setup

The experimental setup consisted mainly of a cylindrical reaction chamber placed at the end of the Nuclear Physics beam line. A schematic view of the reaction chamber is shown in Figure 3.6 and two photographs of the real setup are displayed in Figure 3.7. The reaction was produced by using a ^{3}He beam which impinged onto a ^{4}He gas target, and the ^{7}Be ions created were collected in a 25 mm radius Cu catcher fixed on a movable arm placed at the end of the chamber.

The ^{4}He gas target at pressures of ≈ 60 Torr was kept within the reaction chamber and was separated from the upstream beam line vacuum by a Ni foil window. A bypass system (see Figure 3.7(a)) was used in order to get pressures below 10^{-6}mbar in the chamber before filling it with the ^{4}He gas, guaranteeing no air contamination in the gas target. A constant ^{4}He gas flow of ≈ 1 litre/hour using a valve system ([Ten96]) was set in order not to overheat the target due to the beam intensity and to maintain the purity of the gas during the measurements. The pressure was monitored using a high precision pressure gauge, and the fluctuations during the measurements were below 0.2%.

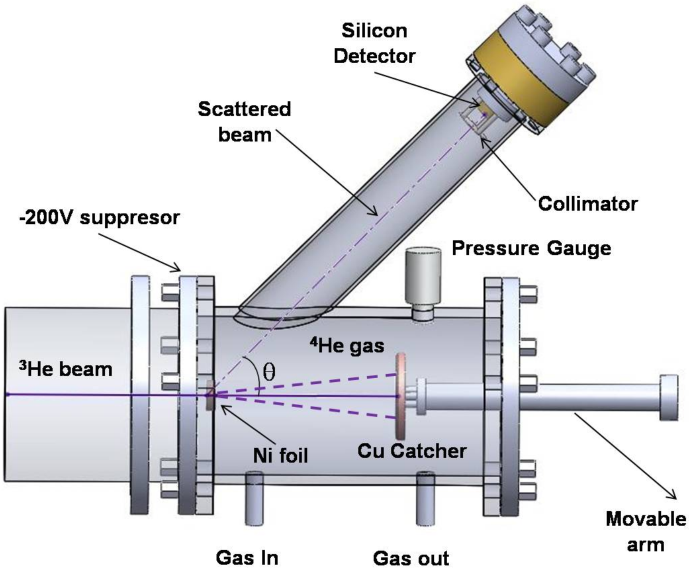

Figure 3.6: *A schematic view of various components that are part of the reaction chamber. The reaction was produced using a ^{3}He beam impinging onto a ^{4}He gas target that is "vacuum isolated" from the beam line by a Ni foil. A silicon detector was placed at $\approx 45°$ with respect to the beam axis for monitoring the scattered beam from the Ni foil. A Cu catcher placed on a movable arm at the end of the chamber was used to collect the ^{7}Be recoils. The subsequent γ-rays of the ^{7}Be were measured off-line using a specialised low-background station based on HPGe detectors. An electron suppressor kept at -200 V was placed before the Ni foil. The movable arm is used in order to optimise the target length for each beam energy. See text for more details.*

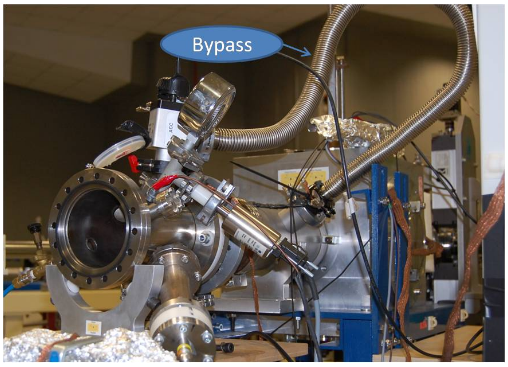

(a)

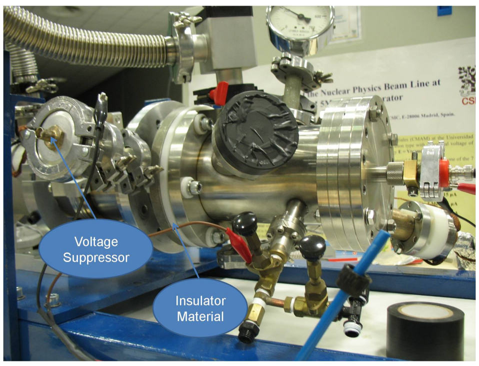

(b)

Figure 3.7: *Photographs of the setup installed at the Nuclear Physics Line at CMAM. (a) A general view of the setup placed at the end of the beam line without the final closing flange. The bypass tube connecting the beam line and the chamber is marked. Before filling the reaction chamber with the ^{4}He gas, a pressure of $\approx 10^{-6}$ mbar was achieved inside the chamber using the turbo pumps in the beam line with the bypass open. The bypass was then closed and the chamber was filled with the ^{4}He gas target. (b) A closer view of the reaction chamber where the electron suppressor and the insulator plate are indicated. See Figure 3.6 for more details about the setup.*

A collimated silicon detector placed at $\theta \approx 45°$ with respect to the beam direction was used in order to monitor the scattered beam from the Ni foil at the different energies. Details of how this silicon detector works can be found in appendix A.

The chamber was electrically isolated from the beam line. The Cu catcher and detector were electrically connected to the chamber and together they acted as a Faraday cup to also monitor the incoming beam. An electron suppressor with an applied voltage of -200 V was set before the Ni foil, avoiding an increased current due the secondary electrons from the beam impact escaping from the Ni foil. The current was measured using a calibrated NIM Digital Current Integrator (ORTEC module 439 ([ORT]) whose output signal was displayed on a NIM scaler (CAEN module N1145 [CAE]), showing the current rate (incoming beam particles per second), and the accumulated current for each measurement.

The output signals of the silicon detector and the integrated charge signal were processed and saved using the electronic setup shown in Figure 3.8. When a ^{3}He ion hits the Si detector, it creates an electric signal proportional to the deposited energy. The signal usually has a low amplitude and must be amplified and processed before being digitised and saved. The detector output signal was doubled at the first stage of the processing (in the preamplifier) and they were processed separately. With the first chain ("energy chain") the information about the deposited energy is kept, while the second chain ("temporal chain") keeps temporal information of the signal, required to gate the energy signal in order to select the region of interest and to avoid making the DAQ system busy with noise. The caption in Figure 3.8 describes in more details and the specifications of the modules can be found in appendix A.

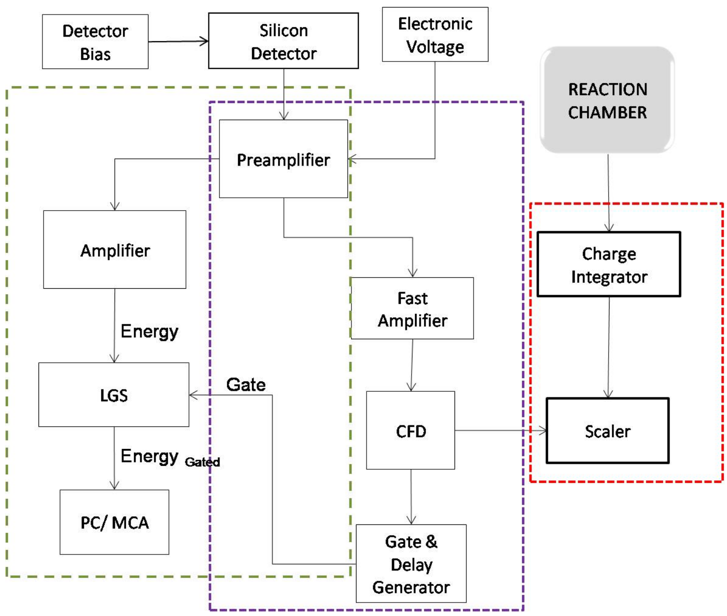

Figure 3.8: *A block diagram of the electronic used in the activation experiment at CMAM. The dash green line includes modules used to obtain the energy spectrum in the silicon detector ("energy chain") and the violet one contains those modules used to filter the signals in order to discard electronic noise and background signals ("temporal chain"). The red dash lines encloses the electronic modules used to integrate the electric charge collected on the chamber. The output signal from the detector is firstly pre-amplified. Two equal output signals come out from the preamplifier, one to be processed in the energy chain and the other in the temporal chain. LGS: Linear Gate Stretcher, MCA: Multichannel Analyzer, CFD: Constant Fraction Discriminator. Appendix A describes different modules.*

3.2.2 Details of the measurements

The experiment was performed during two periods, in 2009 and 2011. Five measurements for different ^{3}He beam energies were used during each of these periods. In order to reduce the uncertainties, every variable, i.e. pressure, target length or beam energy are kept under control and continuously monitored during the experiment. If the chamber is filled with the gas target and the catcher is placed in its position, as soon as the beam hits the target the ^{7}Be implantation starts. Therefore, all the tests were carried out with no gas in the chamber. If a catcher was present during a test done with the target-gas, then a new catcher was placed for the following production run, wasting scheduled beam time. The beam time utilisation is vital in this experiment because the cross section of this reaction is in the order of μb (based on the ERNA data [DGK09]) therefore, production time was optimised in order to minimise the statistical error contributions. In addition, as it will be explained below, the catchers were sent to Israel where the γ-activity from the Cu catchers was measured using a specialised low-background γ counting setup.

In the 2009 experiment, each measurement was performed continuously and the target length was fixed at the beginning of each measurement. In the 2011 run, it was not possible to run the accelerator overnight and each measurement was divided in two or three different days in order to optimise the ^{7}Be implantation, fixing the target length in the first day of each measurement. In this case, after measuring during one day, the setup was remained without any changes except that the target was replaced with fresh supply the next day.

Some details of the measurements performed with the activation experiment are shown in Table 3.2. For the measurements taken during the 2011 experiment an effective implantation time was calculated according the procedure in reference [FM62].

$E_{^3\mathrm{He}}$ (keV)	T_{IMP} (hr)	Year
2106 ± 2	10.2	2011
2306 ± 2	9.9	2009
2507 ± 3	11.6	2011
2807 ± 3	10.9	2011
3208 ± 3	8.6	2009
4010 ± 4	16.1	2011
4410 ± 4	8.1	2009
4811 ± 4	5.1	2009
4811 ± 4	6.7	2011
5312 ± 4	6.6	2011

Table 3.2: *Details of the measurements performed in 2009 and 2011 using the Activation Method at CMAM (Madrid). The ^{3}He incoming beam energies within the error given by the accelerator are shown in the first column, the second column shows the implantation time for each energy, while the third column shows which experiment each measurement corresponds to.*

3.2.2.1 Experimental energy determination

The incoming beam energy is precisely estimated from the terminal voltage of the accelerator. In general, for a tandem accelerator, the energy of the beam, E^{beam}, is calculated from:

$$E^{beam} = E_{ext}+(n+1) \cdot V_T \tag{3.2}$$

where "E_{ext}" is the extraction energy of the beam from the ion source. For the case of ^{3}He, E_{ext}=18 keV. Although according to the manufacturer the error associated is $\pm$2%, it has been observed even smaller. In any case, it is negligibly small when comparing with the total beam energy. "n" is the charge state of the ^{3}He ion, which in our case was 1^+ and "V_T" is the actual terminal voltage. There is a calibration factor that relates the nominal terminal voltage that we introduce for setting the accelerator during the experiment, V_{nom}, and the actual terminal voltage:

$$V_T = A + B \cdot V_{nom} \tag{3.3}$$

where "A" and "B" are the relation coefficients, unique for every machine.

After the 2011 measurements, the accelerator was re-calibrated using, among others, the resonance reaction ^{27}Al(p,γ)^{28}Si at 992 keV. The measurements resulted in the coefficient values: A=4.4$\pm$ 0.4 kV and B=1.0173$\pm$0.0007.

The beam energies have been determined from the nominal terminal voltages considered during the 2009 and 2011 experiments. The errors associated with the beam energies are given by the uncertainties in the relation coefficients A and B. The energy values together with their errors are shown in the second column in Table 3.2.

3.2.2.2 Observables

As it can be seen from expression 3.1, in order to determine the reaction cross section and subsequently the S-factor, the total number of incoming particles, the number of recoils produced in the reaction, and the target areal density must be known:

• Two methods were simultaneously used for determining the **number of ^{3}He incoming number of particles**. As already mentioned, the chamber as a whole was acting as a Faraday cup and the accumulated charge in the chamber was measured as a number of *Pulses*, where each pulse corresponded to 10^{-10}C. The number of incoming particles could thus be estimated by using the following expression:

$$N_{^3\mathrm{He}} = \frac{Pulses \cdot 10^{-10}C}{q \cdot e^-} \tag{3.4}$$

here, q is the charge state of the incoming beam, which in this case was 1^+ and e^- is the electron charge in Coulombs. The average current can be obtained dividing the previous expression by the measurement time. The typical currents during our experiment were around 200 nA.

The second method was used to cross check the results for the number of incoming particles. This could be estimated using the ^{3}He beam particles scattered from the Ni foil and detected in the silicon detector. The Coulomb interaction between the beam particles and the Ni foil is given by:

$$V_c = 1.44(\mathrm{MeV \cdot fm}) \cdot \frac{q_1 \cdot q_2}{\mathrm{R_n}} \tag{3.5}$$

here, q_1=2 and q_2=28, and considering the approximation $R_n \approx 1.23(A_1^{1/3}+A_2^{1/3})$, V_c results in $\sim$12 MeV (for a more realistic square-well radius $R_n \sim 8$ fm and thus $V_C \simeq 9$ MeV). Thus, as the incoming beam energies are below this value, only Coulomb interaction plays a role and therefore detected particles at a given angle θ depends on the Rutherford cross section given by:

$$\frac{d\sigma}{d\Omega} = \left(\frac{zZe^2}{4\pi\epsilon_0}\right)^2 \left(\frac{1}{4T_a}\right) \frac{1}{\sin^4 \frac{\theta}{2}} \tag{3.6}$$

where z and Z are the atomic number of the beam and target ions, respectively, T_a is the incoming beam energy and θ is the scattered output angle with respect to the beam direction. Thus, as the elastic scattering cross section is known, the total number of incoming particles can be determined from the number of particles detected in the silicon detector and the areal density of the Ni foil.

• Due to the low gas pressures used in the reaction chamber, it can be assumed that the gas behaves as an ideal gas, thus the **gas target areal density** (N_t) is estimated using the expression:

$$N_t = 9.66 \cdot 10^{18} \frac{l \cdot P}{T_0 + T_C} (^4He/cm^2) \tag{3.7}$$

where l in cm is the distance between the Ni foil and the Cu catcher (for each measurement this length was kept constant by fixing the movable arm in which the Cu catcher was placed), P in Torr is the gas pressure, and T_0 and T_c in kelvin are the room temperature and the correction in temperature due to the beam heating, respectively.

• The **^{7}Be recoils** were deposited in the 50 mm diameter Cu catchers kept 11-12 cm downstream from the Ni foil. In order not to underestimate the cross section we need to guarantee that all the recoils are implanted in the copper catcher:

With this aim, the beam straggling was simulated using the TRIM code [SRI] for different beam energies and effective target lengths according to Table 5.3. In our simulations it was considered that the point-like mono energetic ^{3}He beam punch through a 1.03 μm Ni foil (see section 3.2.4.4) plus half of the gas length, based on the assumption that the reaction takes place at the centre of the target. The straggling for the maximum and minimum energies are shown in Figure 3.9. On the other hand, due to the kinematics of the reaction, the momentum of the ^{7}Be recoils is along the beam direction and therefore forward focused. The straggling of the ^{7}Be recoils passing through half of the target length before reaching the Cu catcher have also been simulated with TRIM. The monoenergetic recoil energies considered in the simulation correspond to the recoil ions created at the centre of the gas target and the prompt γ-ray emitted at 90º. Figure 3.10 shows the simulated straggling of the ^{7}Be nuclei for the maximum and minimum energies.

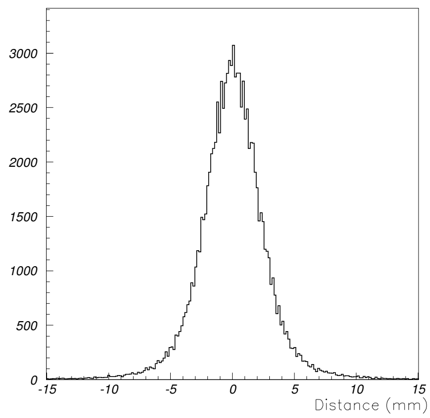

(a)

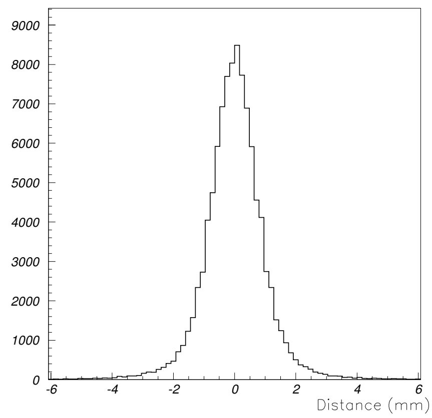

(b)

Figure 3.9: *Mono-energetic point-like ^{3}He beam straggling distribution using 10^5 particles crossing the 1.03 μm Ni foil plus half of the ^{4}He gas length. The simulations were run using the TRIM code [SRI]. (a) Incoming beam energy of 2106 keV corresponding to the lowest energy measured and gas target length of 13.29/2=6.65 cm. The FWHM of the distribution from a Gaussian fit results: 5.5 mm. (b) The same situation for a 5312 keV incoming beam energy (highest energy measured) and same gas target length. The FWHM in this case results in 1.9 mm*

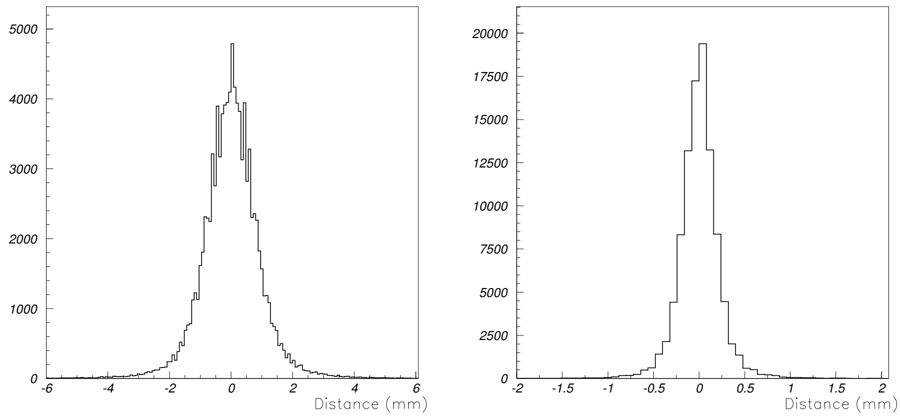

(a) (b)

Figure 3.10: *^{7}Be recoil straggling distribution for 10^5 ions crossing the remaining half of the gas length for (a) a 585.5 keV ^{7}Be energy corresponding to the 2015 keV ^{3}He incoming beam energy (FWHM of the distribution from a Gaussian fit results in 1.9 mm), and (b) a 2112.1 keV ^{7}Be recoil energy corresponding to the 5312 keV beam energy.*

The beam optimisation was done at the beginning of every experiment. To this purpose, the final downstream flange of the chamber was replaced by another flange with a quartz viewer and a metal grid. The beam was monitored on the quartz using a camera. This assured a good overlap of the beam axis and the chamber axis so that the beam passed throughout the centre of the Ni foil and the ^{3}He gas target. Beam path also got an additional cross check by the level of agreement between the number of beam particles estimated using the chamber as a Faraday cup and the scattered beam in the Silicon detector. Two pictures showing both how the beam is centred in the Ni foil and the beam direction are shown in Figure 3.11.

Therefore, by assuming a beam spot size of 1-2 mm, a maximum $\sim$5 mm straggling of the beam, $\sim$2 mm straggling of the recoils and a maximum recoil angle of 27 mrad for the lowest beam energy, we can guarantee that the recoils fall within a circle of 23 mm diameter centred on the 50 mm catcher.

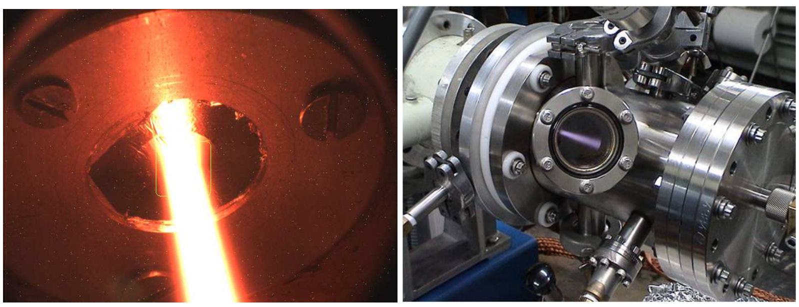

(a) (b)

Figure 3.11: *Photos taken during the production runs as beam is passing through the centre of the Ni foil (a) and the gas target (b). The violet colour is due to the light emission following the ionisation of the target ions upon the beam impact.*

3.2.3 Setup for the γ-activity measurements

After the recoil implantation the delayed 478 keV γ-activity from the catchers (one catcher was used for each measurement at a given energy) was measured off-line at the low-background detection station of Soreq Research Center, Yavne, Israel. A sketch of the station is shown in Figure 3.12.

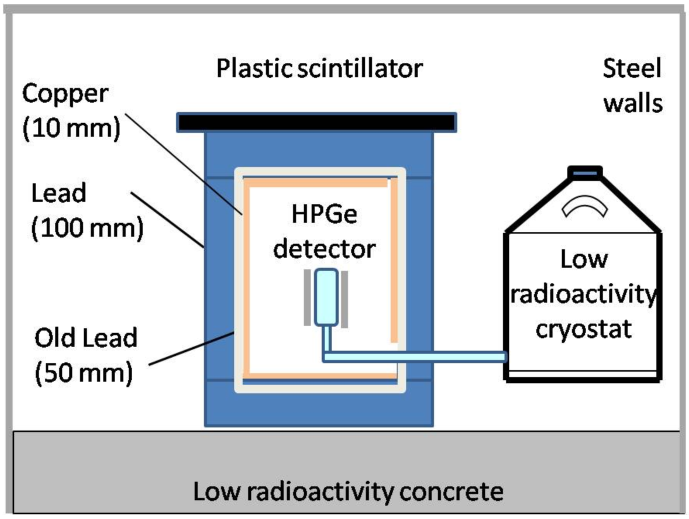

Figure 3.12: *A sketch of the HPGe low-background station at SOREQ. See text for more details.*

The γ-rays were measured by a p-type coaxial 70 mm diameter High-Purity-Germanium detector (HPGe, model 65-83, GEM series, ORTEC), having 70% relative efficiency and peak resolution of 1.7 keV at 1332 keV. The γ-rays were measured by placing the copper catchers at a distance of 20 mm from the HPGe detector. This well-established arrangement with an optimised solid angle and precisely known efficiency correction of 1.3% for the ^{7}Be spatial distribution over the catchers had an effective shielding to suppress the ambient background. The passive part of the shielding is 50 mm of mercury, 10 mm of copper, lead of 150 mm thickness (50 mm are radiologically ultra-clean) and the active part is a plastic detector of dimensions 1000 x 1000 x 50 mm^3 (BC408 plastic scintillator by Saint Gobain) placed on top of the lead shield and operated in anti-coincidence (veto detector) with the HPGe detector in order to discard events from the cosmic rays. Two pictures of the complete station (a) and a catcher in the measurement position (b) can be seen in Figure 3.13.

The activity spectra were collected for durations between 3-10 days, to minimise the statistical uncertainty in the γ counting. The absolute detection efficiency for the 478 keV γ-rays was (4.36$\pm$0.10)% for all catchers except for those at 4811, 2807, and 2106 keV in 2011 whose efficiency was (3.79$\pm$0.11)%.

The signals from the HPGe and the scintillator detectors were amplified and then fed into the signal and gate inputs (correspondingly) of an ADC module (model 927 by ORTEC), which was connected to a PC via USB cable and the software MAESTRO-32 was used for the spectra acquisition. Thus, the signal from the HPGe detector is gated in anti-coincidence with the scintillator detector reducing cosmic and ambient background. This assembly of the passive and active shielding provides a background radiation rate of 0.67 events/seconds over the energy range of 40-2800 keV.

The energy for the γ-ray to be detected from the ^{7}Be activity is 478 keV. In order to check possible background interfering in this energy region a spectrum was collected during 168 h without any Cu catcher, i.e. activity seen in the HPGe with the shield. The spectrum is shown in Figure 3.14.

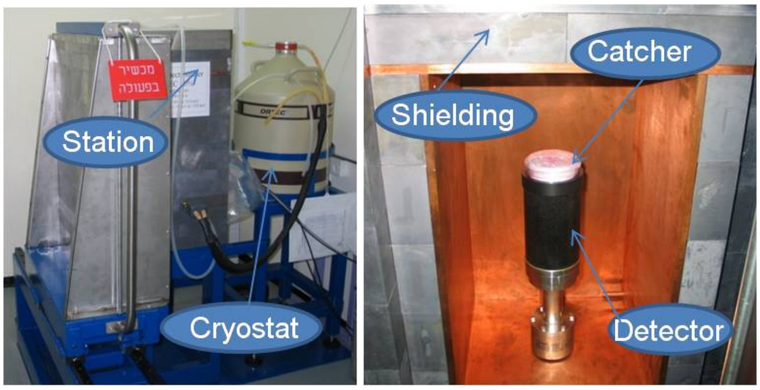

(a) (b)

Figure 3.13: *(a) Picture of the low-background HPGe detector station placed in a basement in SOREQ centre. (b) Copper catcher in the position to be measured.*

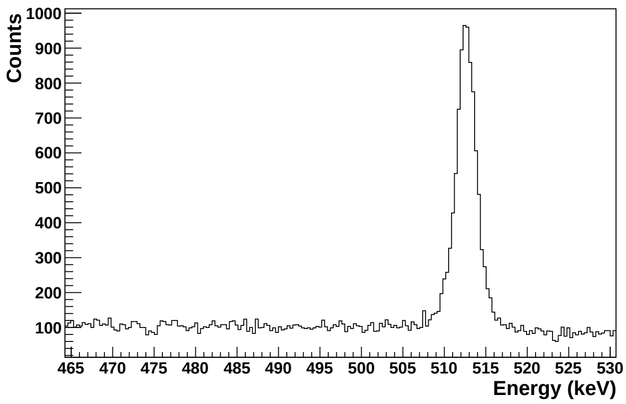

Figure 3.14: *Background γ-activity measured during 168 h in the HPGe in the low-background station at SOREQ centre in the week preceding the measurements of the Cu catchers of the 2009 experiment. The 511 keV peak is the γ radiation coming from the e^--e^+ background annihilation. The positrons (e+) are originated by pair production interaction of the γ-rays background with the surrounding materials.*

As can be seen the spectrum does not show any interfering peak around 478 keV and, a 0.025 counts/s background rate in the 450-500 keV region with a bin size of 0.35 keV is observed. Exactly the same spectrum was obtained for a Cu catcher prepared with no target gas but ^{3}He beam at an energy around 4 MeV. This confirms that there is no background contribution from the beam hitting the Cu catcher.

3.2.4 Additional measurements

In the following some of the complementary measurements performed that allowed a better control of the experimental setup and a better estimation of the experimental errors.

3.2.4.1 Energy calibration of the silicon detector

In order to know the energy of the ^{3}He ions reaching the detector, the energy calibration measurements for the silicon detector were performed. They were carried out at the beginning of each experiment using two standard alpha sources: ^{148}Gd, and a standard triple alpha source (^{239}Pu+ ^{241}Am+ ^{244}Cm). The energies of the alpha particles emitted by these sources are shown in Table 3.3.

α source	E_α (keV)	I_α (%)
^{148}Gd	3182.787(24)	100
	5156.59(14)	73.3(8)
^{239}Pu	5144.3(8)	15.1(8)
	5105.5(8)	11.5(8)
	5485.56(12)	84.5(10)
^{241}Am	5442.80(13)	13.0(6)
	5388.23(13)	1.6(2)
	5804.82(5)	76.4(2)
^{244}Cm	5762.70(3)	23.6(2)
	5664(3)	0.022(1)

Table 3.3: *Energies and intensities for alpha particles from ^{148}Gd and triple alpha (^{239}Pu,^{241}Am and ^{244}Cm) sources used for calibration of the silicon detector [Lun].*

For the calibration measurements, the collimator in the chamber was replaced first by the ^{148}Gd source and then by the triple alpha source. The air pressure inside the chamber for the two measurements was below $\sim 10^{-6}$mbar which guarantees no energy losses by the α particles before reaching the detector. The two calibration spectra are shown in Figure 3.15.

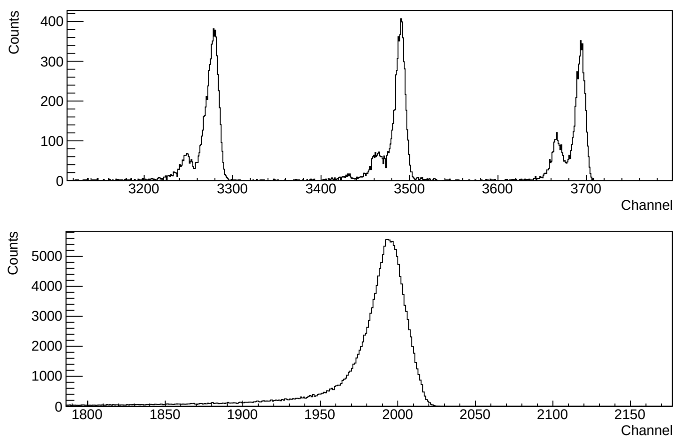

Figure 3.15: *Spectra taken with the triple alpha (top) and ^{148}Gd (botton) calibration sources in the silicon detector during a measurement time of 1000 and 300 s, respectively.*

It is worth noting that for this experiment the energy resolution is not a relevant parameter. The aim of using the detector lies on determining the number of scattered beam particles reaching the detector, and knowing the energy calibration is just a way of cross check the scattered particles.

The procedure to calibrate the detector was to perform a regression analysis between the values of the centroid from the ^{148}Gd source peak and the most intense peaks from triple alpha source shown in Figure 3.15 and their nominal values in Table 3.3. The values used are shown in the second and the third columns in Table 3.4.

α source	E_α (keV)	Centroid (ch)	FWHM (keV)
^{148}Gd	3182.787(24)	1994 (1)	36.23
^{239}Pu	5156.59(14)	3280 (1)	23.06
^{241}Am	5485.56(12)	3491(1)	19.11
^{244}Cm	5804.82(5)	3694(1)	18.94

Table 3.4: *Values used in the regression analysis performed for the energy calibration of the silicon detector. The second column shows the nominal values of the energies considered and the third column shows their corresponding centroids in channels taken from the fit of peaks shown Figure 3.15. The fourth column shows the FWHM after calibration.*

The regression analysis gives the value of the relation parameters between the histogram channel number and the alpha particle energies. In this case, this is expressed by:

$$\text{Energy (keV)} = 109.4\ (36) + \text{channel} \cdot 1.54\ (1) \tag{3.8}$$

3.2.4.2 Radius of the collimator

In order to estimate the number of incoming beam ions from the scattered particles, it is necessary to know the solid angle covered by the detector, i.e. to know exactly the area of the hole of the collimator. A small radius collimator was chosen in order not to cover a wide angle and thus better constrain the solid angle of the scattered particles. Due to the standard elements as caliper could not measure such small apertures, the radius was determined experimentally.

An alpha spectrum from a ^{148}Gd source placed before the collimator was taken during ~10 h together with a pulser of 10 Hz count rate in the system. Afterwards, another spectrum was collected by replacing the collimator with one of well-known 4 ± 0.05 mm diameter, during ~3 h. The unknown radius of the smallest collimator (R_s) is obtained from the expression below (eq. 3.9). In this expression the number of alpha particles detected in the collimator in both cases is normalised using the number of pulser counts in order to account for the differences in the collection times for the two spectra:

$$\frac{\pi R_s^2}{\pi R_b^2} = \frac{Peak_s/Pulser_s}{Peak_b/Pulser_b} \tag{3.9}$$

Here, the "s" subscript refers to the small unknown radius collimator and big "b" subscript refers to the big known radius collimator. *Peak* and *Pulser* refer to the integration of the ^{148}Gd source peak and the pulser peak in the spectra, respectively. The collimator radius was determined to be: $R_s = 0.270 \pm 0.003$ mm.

3.2.4.3 Aperture angle of the collimator

Continuing with the interest of determining the detector solid angle, the angle of the collimator respect to the Ni foil needs also to be known. To determine the collimated angle of the silicon detector with respect to the beam, the Ni foil (see Figure 3.6) was replaced by a C foil, and the same setup (including the same small collimator) without any mechanical changes was used. In this case, a ^{4}He beam at seven different energies (2, 2.5, 3, 3.5, 4, 4.5 and 5 MeV) impinged onto the chamber with no gas inside and air pressures in the order of $\sim 10^{-6}$ mbar. The seven spectra for the scattered particles in the C foil detected with the silicon detector were saved. Two examples corresponding to the cases with 3 MeV and 5 MeV incoming ^{4}He beam energies are shown in Figure 3.16. The wide energy spread in the peak is due to the different energy losses in the C foil thickness and where the reaction takes place: at the entrance, middle or the end of the foil.

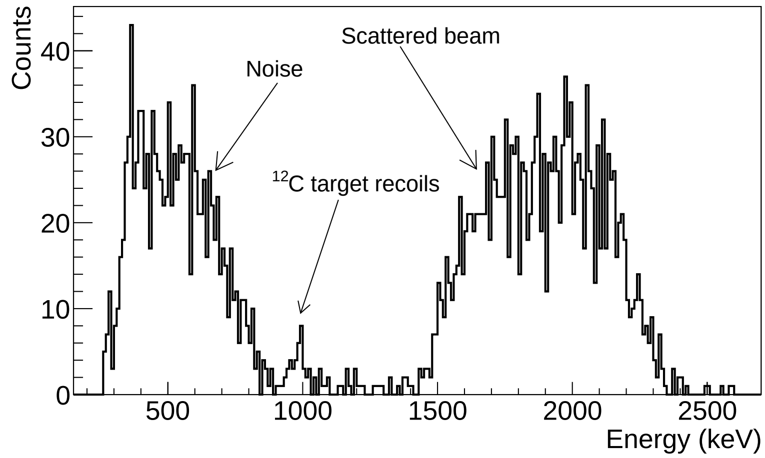

(a)

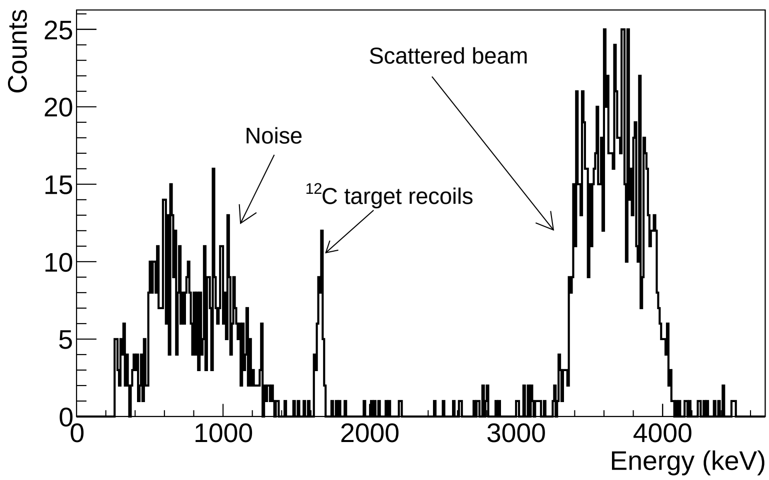

(b)

Figure 3.16: *Silicon spectra corresponding to 3 (a) and 5 (b) MeV ^{4}He beam particles scattered from a C foil. Peaks corresponding to noise, ^{4}He elastic scattered particles and ^{12}C target recoils are marked. The energy spread is related to the thickness of the foil. The deeper the scattering takes place in the C foil the larger is their energy deposited in the detector.*

The idea was to obtain the angle (ϑ) of the collimated detector by considering the particles scattered at the end of the C foil and taking into account the expression relating the energy of the elastically scattered particles (E_1) and the incoming beam energy after subtracting the energy loss in the C foil (E_0):

$$\frac{E_1}{E_0} = \frac{1 + 2\rho cos\Theta + \rho^2}{(1+\rho)^2} \tag{3.10}$$

here ρ is the mass ratio between the ion beam and the target, and Θ is the output angle in the centre of mass system.

Unfortunately, the carbon foil thickness was not known to sufficient accuracy therefore, the energy at the end of the foil (E_0) cannot be calculated and thus the angle cannot be directly obtained from expression 3.16. Moreover, the angle is very sensitive to minor changes, and with low statistics the highest energy of the peaks cannot be obtained precisely. Instead, a program using the minimisation MINUIT library has been created. Two variables, angle and thickness are optimised simultaneously using the experimental values. From the incoming energy, the program estimates the energy loss by interpolating the SRIM input values assuming a given C foil thickness, and estimates the angle utilising the expression 3.10. Then, it gives the optimised values of C foil thickness and the silicon detector angle that fit best the scattered particle spectra. Finally, the angle is transformed to the laboratory reference system using the expression:

$$cos\vartheta = \frac{cos\Theta + \rho}{\sqrt{1 + 2\rho cos\Theta + \rho^2}} \tag{3.11}$$

here, ϑ is the angle in the laboratory system. The resulting values for the thickness and ϑ are $(0.428 \pm 0.048)\mu m$ and $(44.9 \pm 0.4)°$, respectively. The corresponding solid angle covered by the collimator placed before the detector is: $(4.7 \pm 0.2) \cdot 10^{-6}$sr

3.2.4.4 Ni foil thickness

In order to calculate the energy at which the capture reaction takes place, the energy-loss of the ^{3}He beam particles in the Ni foil must be taken into account and thus the Ni foil thickness must be known. The Ni foil thickness was determined experimentally using standard energy loss techniques with a setup which consisted of another silicon barrier detector and the standard triple alpha source inside a vacuum chamber. Firstly, the alpha source was placed in front of the detector for calibration following the same procedure used to calibrate the other detector (cf. section 3.2.4.1). This corresponding spectrum is shown in Figure 3.17.

The Ni foil, dismounted after the 2009 experiment, was then placed between the alpha source and the detector. The corresponding spectrum was saved. The same measurement with a 2 mm radius collimator between the source and the Ni foil was also performed. Finally, in order to check possible foil damages because of the beam impact, a measurement replacing the used Ni foil by a new unused Ni foil, with similar characteristics to that used in the experiment, was also carried out. Various histograms corresponding to these measurements are shown in Figure 3.18. As it an be seen, all measurements performed agree for the energy of the alpha particles after crossing both the used and the new Ni foil confirming that no relevant damage has happened on the used Ni foil. The black spectrum shows the total number of counts after adding all of them. The Ni foil thickness was determined using the SRIM code and the energy loss by the alpha particles from the triple source crossing the Ni foil, which is ∼400 keV. The thickness resulted to be: $(1.03 \pm 0.02)\mu m$, which is close to the value given by the manufacturer of $1\mu m$.

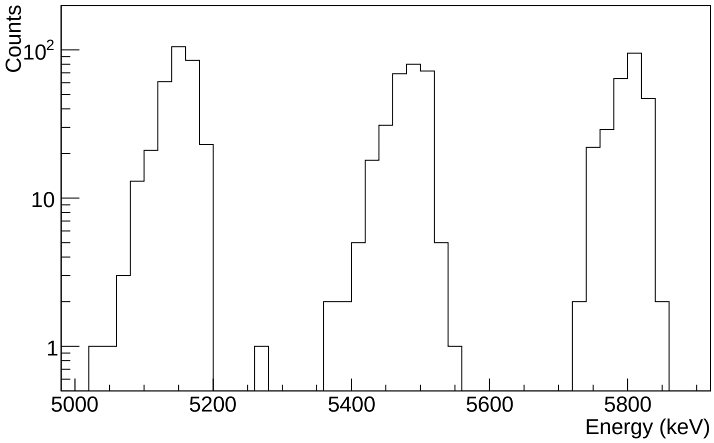

Figure 3.17: *Energy spectrum of alpha particles from a measurement using a triple alpha source taken with the silicon detector used to determine the Ni foil thickness.*

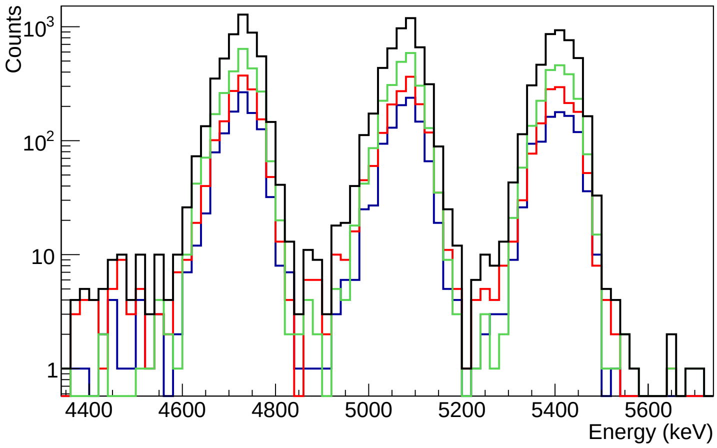

Figure 3.18: *Energy spectra of alpha particles from a triple alpha source after crossing a Ni foil. In red the spectrum taken with the Ni foil used in the experiment with a 2 mm radius collimator between the source and the foil. The blue one shows the same without collimator and the green spectrum shows the histogram taken with a new Ni foil. The black spectrum shows the sum of all of them, used for the energy loss calculations and foil thickness determination.*

The following sections will describe the complementary experiment using the direct recoil counting method. The data analysis and the results of the activation experiment will be detailed in Chapter 5.

3.3 Direct Recoil Counting Method @ DRAGON

The experiment using the *Direct Recoil Counting Method* was performed at TRIUMF (**TRI** -from three original founding members: University of British Columbia, University of Victoria, and Simon Fraser University- **U**niversity **M**eson **F**acility) laboratory in Vancouver, Canada. The laboratory is dedicated to Nuclear Physics and Particle Physics research. A general layout of the laboratory is shown in Figure 3.19. It houses a main cyclotron of ∼17.9 m diameter, which accelerate hydrogen ions, H^-, in a magnetic field of 5600 Gauss producing primary beams with currents up to ∼100 μA and energies up to 500 MeV. The proton beam is delivered to different beam lines depending upon the experiment to be performed. For nuclear physics experiments, the proton beam is let to impinge on targets such as tantalum or UC_x in the target stations, producing radioactive secondary beams which after mass selection in a mass separator are guided to the two main facilities, ISAC-I (Isotope Separator and Accelerator) and ISAC-II.

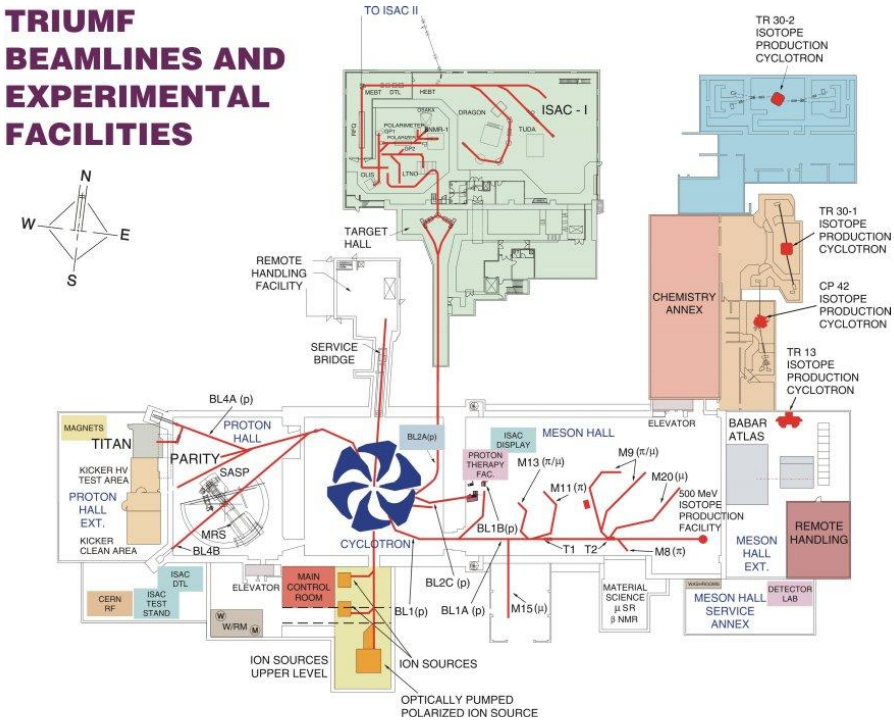

Figure 3.19: *Layout of the TRIUMF laboratory with the cyclotron and some of the facilities as ISAC-I where our experiment was performed.*

Furthermore, in the ISAC-I and ISAC-II facilities, apart from the radioactive beams, stable beams from the Off-Line Ion Source (OLIS) can be accelerated. As our beam in this case is ^{4}He, which can be obtained directly from a gas bottle, we only needed to use OLIS. The OLIS facility can produce most of stable ions beams from Z=1 to Z=87. It consists of a high voltage terminal containing a *surface ionising source*, a *ECR-multi-charge ion source (Supernanogam)* and a *microwave cusp ion source*. For our experiments in September 2011 and August 2013, the Supernanogam source [JWG10] and the Microwave Ion source [JAC08] were used, respectively, to produce the $^4He^+$ ion beams.

After the ion extraction from OLIS, the ions were accelerated in the ISAC-I facility. The first stage of acceleration happens in the radio-frequency quadrupole, where the ions can be accelerated from 2 keV/u to 150 keV/u. The second stage of acceleration happens in a Drift Tube Linac (DTL), which is divided into eight modules (five accelerating structures and three bunchers). The beam is firstly bunched in the DTL entrance by means of the Medium Energy Beam Transport Buncher (MEBT) and can be further bunched in time from 4 ns to 1 ns by means of the high energy beam transport (HEBT) located downstream the DTL. After the DTL, the beam was guided to the DRAGON (**D**etector of **R**ecoils **A**nd **G**ammas **O**f **N**uclear Reactions) separator, where the experiment was performed. A layout of the ISAC-I hall including the different accelerator stages and the DRAGON facility is shown in Figure 3.20.

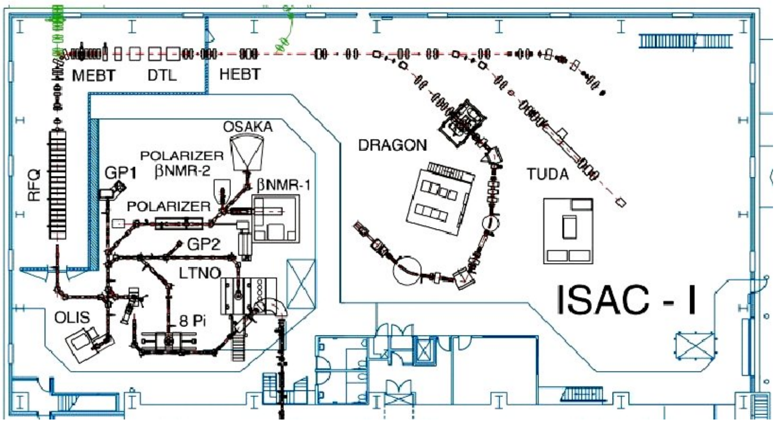

Figure 3.20: *Layout of the ISAC-I hall with the different acceleration elements and the DRAGON facility. The ^{4}He beam ions were produced in the Off-Line Ion Source (OLIS) and accelerated using the RFQ and DTL elements before reaching the DRAGON experimental area where the experiment was performed. Some other experimental setups in the ISAC-I hall such as 8π or TUDA are also marked.*

3.3.1 DRAGON setup

In order to count the ^{7}Be recoils directly, they must be separated from the unreacted beam particles before being counted in a detector. Recoil separators are devices which separate nuclear reaction products (recoils) leaving a target from the unreacted beam particles. In addition, some separators have the additional property that they can disperse the reaction products at the focal plane according to their mass/charge.

The recoil separators use electromagnetic elements such as electric dipoles, magnetic dipoles, Wien filters etc..., to do the separation. In addition, magnetic quadrupoles are used to focus the ions, and magnetic sextupoles and octupoles are used to correct higher order aberrations. Because heavy ions are routinely used as beams, high vacuum is necessary in recoil separators in order to avoid losses due to multiple scattering or charge-changing collisions.

Usually, the yield of recoils is peaked near 0° with respect to the beam direction, and thus the recoils are mixed with primary beam particles that have not reacted when both leave the target. To obtain the maximum suppression of beam, the beam particles are blocked at an early stage of the separator. The magnetic and electric fields in the dipoles are set to pass particles with energy E_o, mass M_o, and charge Q_o along the central trajectory, and the quadrupole lenses are set to focus the particles at the focal plane.

DRAGON, placed at TRIUMF's ISAC-I hall, is a recoil separator designed for measuring radiative capture reaction cross sections of astrophysical interest. DRAGON consist of four main components, a windowless recirculating gas target, a γ-detector array, an electromagnetic separator (EMS) and a heavy-ion recoil detection system [HBB03]. A diagram of the DRAGON facility with the main elements is shown in Figure 3.21 and the details of the different components will follow.

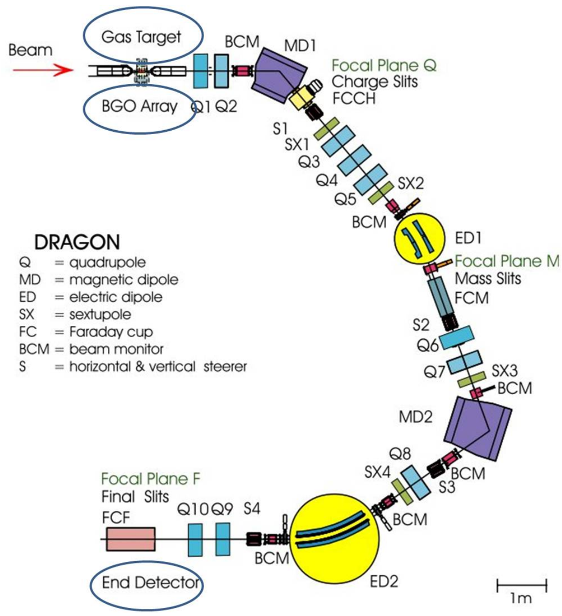

Figure 3.21: *Diagram of the DRAGON facility taken from Ref. [EHB05]. Radioactive and stable beams enter the windowless gas target which is usually filled with either hydrogen or helium gas at pressures between 0.2 to 10 Torr. The recoils produced emerge the target with different charge states and almost with the same momentum of the beam. The recoils are separated from the beam particles using the two magnetic dipoles, MD1 and MD2, and the two electrostatic dipoles, ED1 and ED2. Magnetic quadrupoles and sextupoles are used to focus the particles. Enclosed in circles are the three main components: Gas Target, BGO Array and End Detector.*

In our experiment, a ^{4}He beam impinged onto the ^{3}He gas target kept in the target cell. Eventually, they fuse producing the ^{7}Be recoils and prompt γ-rays. The latter are detected in the BGO detectors surrounding the target. The recoils are forward focused and exit the target with different charge states together with the unreacted beam particles. The first quadrupoles (Q1 and Q2) focus both the unreacted and recoil beams after exiting the target and before they enter to the rest of the separator. Then, the two magnetic and electric dipoles select the ^{7}Be recoils from the unreacted beam taking into account the different charge states and different kinetic energy between them. The ^{7}Be with the given charge state are then counted in the End Detector.

3.3.1.1 Gas target

The ^{3}He gas target was enclosed inside a windowless cell with an effective length of $\sim$11 cm, that was positioned inside an aluminium target box. Figure 3.22 shows a sketch of the cell position. A photo of the aluminium target box attached to the beam line is displayed in Figure 3.23, where a section of the BGO array and the vacuum pumps together with the pumping tubes can also be seen.

Inside the box and exiting the cell there are two "arms" which accommodate two collimated *Ion Implanted* silicon detector to monitor the scattered beam and target particles. The entrance and exit apertures of the cell are circle holes of 3 and 4 mm radius, respectively. The box is connected to the beam line through a series of differentially pumped tubes.

Although a windowless gas target maximise the transmission of the recoils through the target, it requires a differential pumping system both upstream and downstream of the target to maintain the beam line vacuum. The eight turbo pumps, three upstream and five downstream, maintain the vacuum out of the cell, e.g. 10^{-6} mbar was maintained at the entrance of the first quadrupole (Q1 in Figure 3.21). The

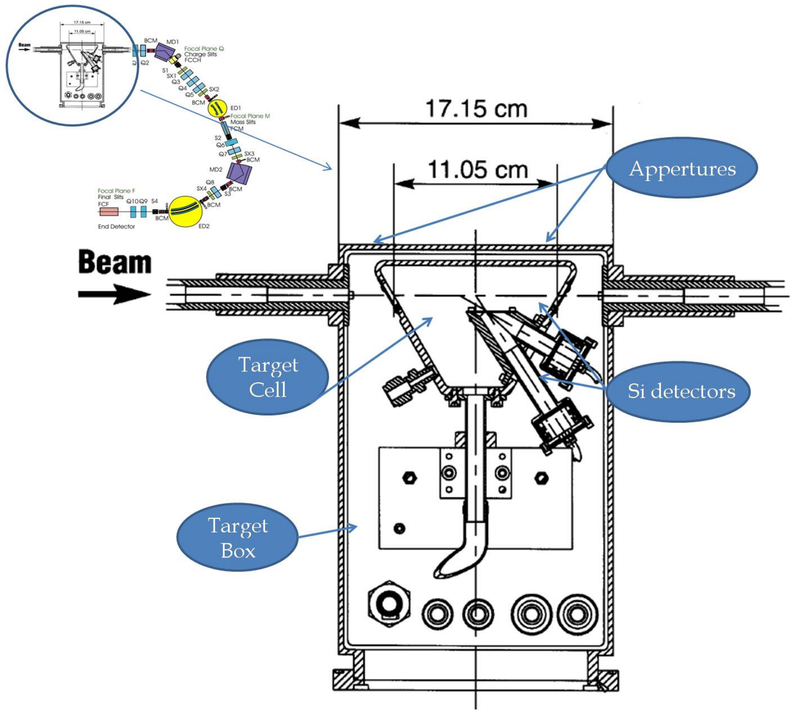

Figure 3.22: *A schematic view of the target cell, from Ref. [LIB03]. The target cell is fixed to one of the lids of the target box (see Figure 3.23). To detect the beam and target scattered particles, two collimated silicon detectors were placed at 30° and 57° with respect to the beam direction.*

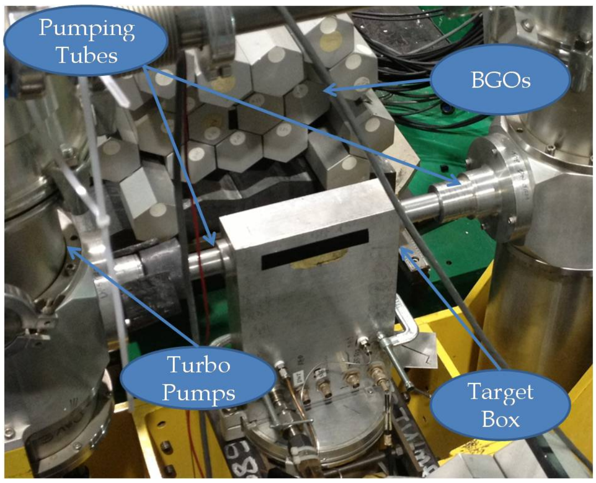

Figure 3.23: *Real picture of the box and the pumping tubes connected to the beam line. The face of the box showed is the one holding the target cell.*

^{3}He gas pressure range during our experiment varied from 4.9 to 6 Torr and a recirculating gas system using a liquid nitrogen ion trap guaranteed a constant pressure and purity of gas target inside the cell during the time of each individual measurement.

The complexity of the windowless gas target system is illustrated in Figure 3.24, where (a) shows the pumping tubes and the gas Al box in blue, where the target cell can also be seen; the vacuum pumps (rootsblowers and turbo pumps) are also shown in yellow; (b) shows the recirculating gas system. All valves and pumps are computer controlled in order to achieve a target gas-profile with a nearly constant density across its effective length.

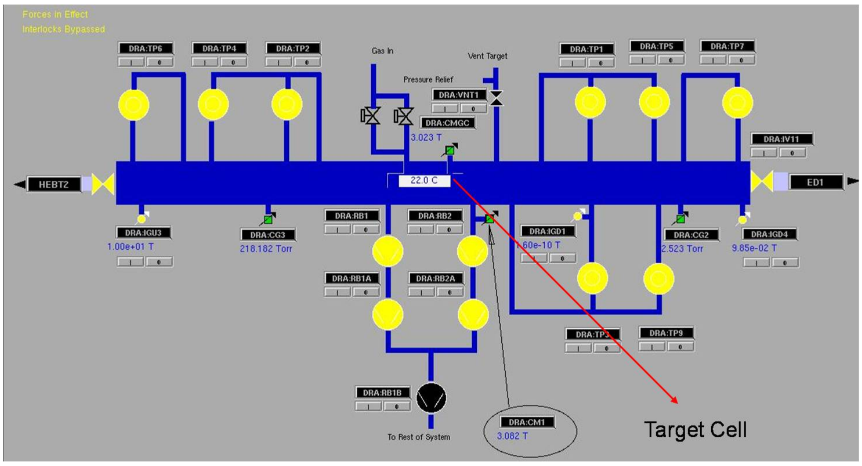

(a)

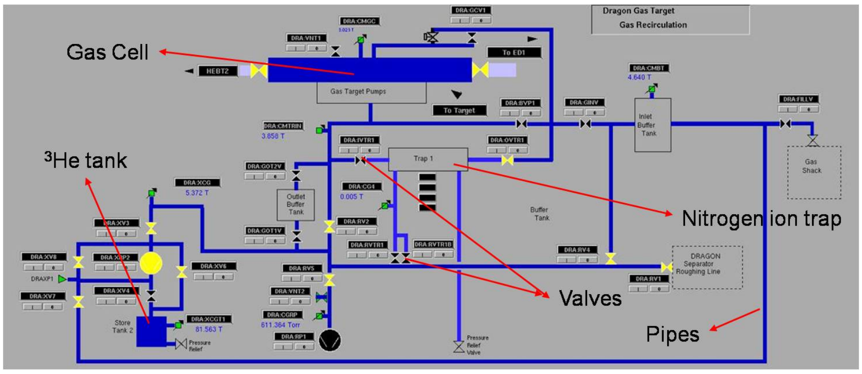

(b)

Figure 3.24: *Screen shots of the DRAGON target gas system which can be computer controlled remotely; (a) shows the target box and pumping tubes (blue rectangle) with the different pumps (in yellow) used to keep constant the gas pressure inside the cell. (b) shows the recirculating gas system. The* ^{3}*He gas tank and Nitrogen ion trap, several meters and valves are also marked.*

It should be pointed out that this DRAGON experiment was the first of its type using ^{3}He gas target, therefore, accurate information of the density profile was needed to obtain and the procedure will be detailed in the next section.

3.3.1.2 γ-detector array

In order to detect the prompt γ-rays from the reaction, a γ-detector array was surrounding the target box, consisting of 30 Bismuth Germanate Oxide scintillation (BGO) detectors of 76 mm length in a close packed configuration (see Figure 3.25). The scintillator detectors have the property of luminescence, that is, they absorb the incoming radiation and re-emit it in the form of light. Therefore, the scintillators are coupled to light sensing devices, photomultipliers, which absorb the light from the scintillator and produce electrons via the photoelectric effect. The resulting signal can then be processed using standard methods [Leo87].

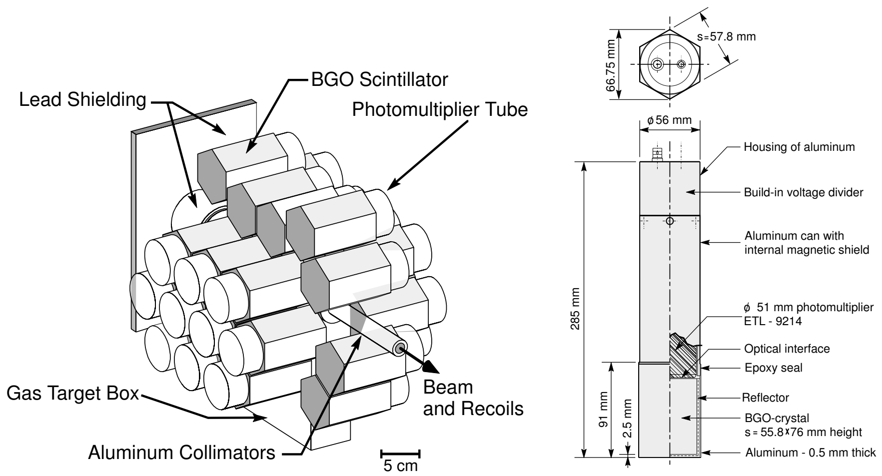

Figure 3.25: *The BGO γ-ray detector array surrounding the target box (left). It consists of 30 individual hexagonal detectors (right) coupled to cylindrical photomultiplier tubes [HBB03]*

The DRAGON BGO detectors have a hexagonal shape coupled to cylindrical 51 mm diameter photomultiplier tubes (PMT). Monte Carlo simulations predict a γ-ray efficiency from (45-60)% for the energy range 1-10 MeV over the 11 cm target cell and a FWHM of 7% at 6.13 MeV [HBB03].

A typical BGO spectrum of our experiment is shown in red in Figure 3.26. The same Figure shows in blue the spectrum obtained in coincidence with the ^{7}Be recoils detected in the DSSSD at the focal plane. A comparison between the two spectra reveals high background contribution in the BGO detectors. Remarkably high is the contribution from the de-excitation of ^{30}Si produced by the beam induced reaction with the Al present in the beam line components. The two peaks in the blue spectrum show the γ-ray from the "direct capture state" (DC) de-excitation to the ground sate (γ_0) and to the 429 keV first excited state (γ_1) in the ^{7}Be nucleus (see caption for more details).

3.3.1.3 Electromagnetic separator

The ^{7}Be recoils produced in the gas target enter the ElectroMagnetic Separator (EMS), where the recoils are separated from the ^{4}He beam particles. The latter are efficiently suppressed and only recoils reach the focal plane of the separator. The downstream pumping tubes and apertures limit the recoils accepted by the separator. This is influenced by where the reaction is produced along the target length. The separator was checked separately with dedicated tests to confirm that the recoils created in a angular cone of around 20 mrad were accepted.

Both beam and recoils particles emerge with almost the same momentum and with different charge states. The magnetic and electric elements are tuned in order to obtain the optimum beam suppres-

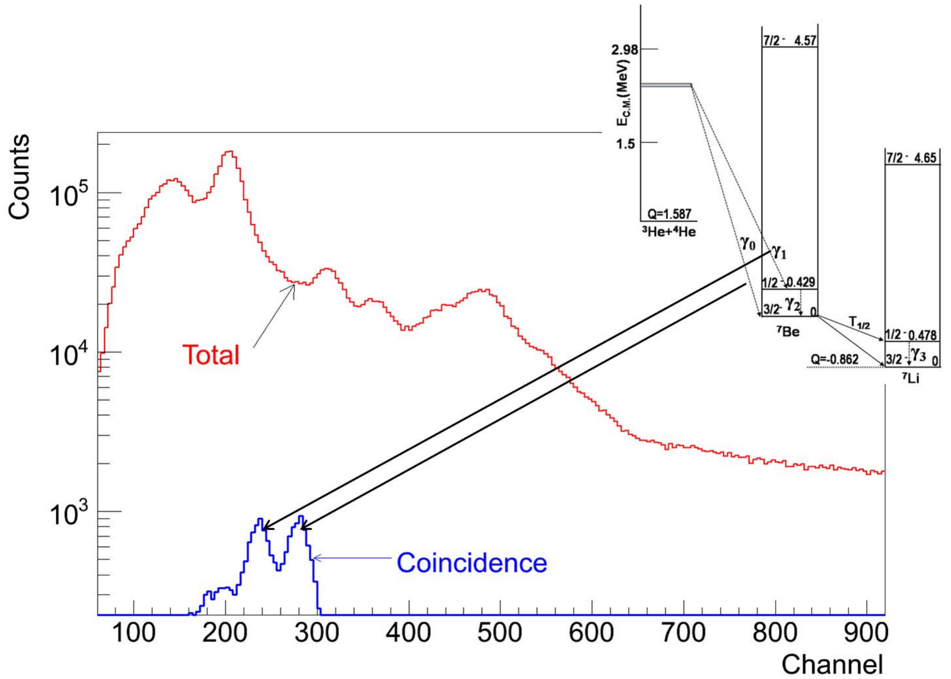

Figure 3.26: *The total γ-ray spectrum obtained with the BGO array detector is shown in red for the ^{3}He(α,γ)^{7}Be reaction with a ^{4}He beam energy of 3.521 MeV and ^{3}He target pressure of $\sim$6 Torr. The highest energy peak is due to the de-excitation of ^{30}Si produced by the beam induced reaction ^{27}Al(^{4}He,p)^{30}Si with the aluminium target box, pumping tubes and apertures. The same spectrum is shown in blue for coincidence events with the ^{7}Be recoils detected in the focal plane with the DSSSD detector. The two peaks correspond to γ-rays from the de-excitation between the direct capture state to the first excite state and to the ground state in the ^{7}Be nucleus. The subsequent 429 keV γ_2-ray is not seen because of the energy threshold set in the BGO due to the high level of background radiation.*

sion, recoil separation and acceptance. The first stage of the separation occurs in the first magnetic and electric dipoles (MD1 and ED1 in Figure 3.21). One of the charge states of the recoils is selected by MD1 and the particles are then separated by ED1 based on their kinetic energy. The magnetic dipole separates the particles based on their rigidity as:

$$B\rho = \frac{p}{q} \tag{3.12}$$

here B is the magnetic field, ρ is the gyroradius with respect to the beam direction, p is the momentum and q is the charge state of the particle. As the momentum p for both beam and recoil are very similar and the gyroradius ρ is constant for the dipole, setting a magnetic field B in the dipole leads to a selection of one of the charge states. Slits strategically placed after MD1 allow only particles with the selected charge state going towards the next step of the separator.

The field of the magnetic dipole is measured using a NMR probe located in the vacuum vessel. A recent calibration of the NMR probe using the ^{24}Mg(p,γ)^{24}Al reaction at centre of mass energy of 0.22 MeV has confirmed the relationship:

$$\frac{E}{A} = k\left(\frac{qB}{A}\right)^2 \tag{3.13}$$

with k=48.15(7) MeV/T^2 [HRF12]. Here, E, A and q are the kinetic energy, the mass in atomic units (u) and the charge state of the particle, respectively, while B corresponds to the magnetic field. The next phase of separation occurs in the first electric dipole (ED1 in Figure 3.21), which separates particles based on the kinetic energy per charge unit as:

$$\varepsilon\rho = \frac{pv}{q} \tag{3.14}$$

where ε is the electric field and v is the velocity of the particles. As well as with MD1, a set of slits is strategically positioned at the ED1 focus to stop the unwanted particles.

A second magnetic dipole (MD2) and electric dipole (ED2) follow the first separation stage and allow for further beam suppression. Magnetic quadrupoles and sextupoles are used to focus the particles. We used the standard procedure to set the separator for the ^{7}Be recoils (see section 3.3.2).

3.3.1.4 Double-Sided Silicon Strip Detector (DSSSD) at the focal plane

Once the recoils have been separated from the beam particles, they reach the final focus at the end of the separator. Different detectors are used in DRAGON, including a DSSSD, a Micro-Channel-Plate (MCP) and a *Ionisation Chamber*, to determine the final position, energy and mass of the recoils.

In our experiment, the ^{7}Be recoils were implanted and detected in the DSSSD consisting of a silicon wafer with 16 front strips with respect to the recoils impact, and 16 orthogonal back strips which collected the charge (see Figure 3.27).

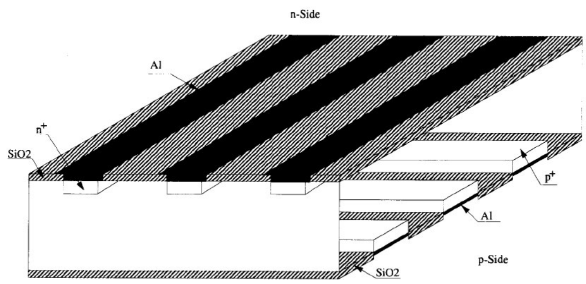

Figure 3.27: *Diagram of a Double-Sided Silicon Strip Detector. The p and n sides and the p+ and n+ corresponding strips as well as the Al contacts are marked.*

Each strip has 3 mm width providing an effective area of 256x9 mm^2 over the 5 cm^2 detector surface. The gap between the strips is 120 μm due to which a 3.85$\pm$0.10% of the incident ions on the detector's surface will not be detected with the correct energy at the detector (see reference [WHRD03]). Front strips are biased with negative voltage while back strips are kept at ground potential. When the ions hit the DSSSD, electron-hole pairs are created in the silicon (see section A.1) and guided to opposite strips inducing electric signals of opposite polarity on front and back sides. This allow us to determine the energy and identify the position of the particle hitting the detector.

3.3.1.5 Electronic setup

In the same way as in the Madrid experiment, an electronic setup is required in order to process the electronic signals from the detectors before being digitised and saved. This setup requires more electronic devices that the Madrid experiment. Apart from the detectors already mentioned here, a BGO array, silicon detectors and a DSSSD, other detection systems are likely to be used in DRAGON depending upon the kind of experiment to be performed (ionization chamber, Germanium detectors...). The electronic setup is designed to process the signals produced in all the detectors where the signal treatment for each individual detector follows the same scheme as CMAM experiment (cf. Figure 3.8). Between our experiments in 2011 and 2013 the data acquisition system (DAQ) was changed. In both experiments the data were saved and displayed on-line using the TRIUMF-MIDAS (Multi Instance Data Acquisition System) system.

The signals processing are separated in two parts: one for the "head" of the *DRAGON*, which includes the γ-ray detectors, and another for the "tail" of the *DRAGON*, including the DSSSD (or ionisation chamber, depending on the experiment), the MCPs, and also the silicon detectors.

In the old system used for the 2011 experiment an event on either the head or the tail side could activate the DAQ system and there was only one readout. Coincidence conditions between both sides were set entirely in the hardware. When there was an event trigger from either side, a time gate was opened up and a search for triggers in the other side was carried out during the time of the gate and thus acquiring the coincident events.

In the 2013 experiment, the DAQ system had been updated: it consisted of two separate and independent DAQ (two VME crates), one for the "head" and one for the "tail". Each crate was triggered and read out separately and was tagged with timestamps from a "master" clock that is part of the head electronics. In this case, the coincident events could be figured out in the analysis by looking at the timestamps. Any two events with triggers within 10 μs of each other are deemed a coincidence event. A summary diagram of the trigger electronic system for the 2013 experiment is shown in Figure 3.28.

3.3.1.6 Faraday cups

Other elements playing an important role in our experiment are the Faraday cups. A series of Faraday cups placed across the DRAGON separator are used for tuning. These are also important for determining the beam currents and some of the additional observables such as charge state distributions. In the following, the nomenclature of the DRAGON control program to describe their location across the DRAGON (see Figure 3.21 to identify the location):

- FC4: located just before the gas target, it measures the incoming current
- FC1: located after the target and before MD1, it measures the transmission throughout the target.
- FCCH: located after the MD1 charge slits, it measures the current of a selected charge state.
- FCM: located after ED1, it measures the current after the selection of a charge state and energy.
- FCF: located before the focal plane detector, it measures the current at the end of the separator.

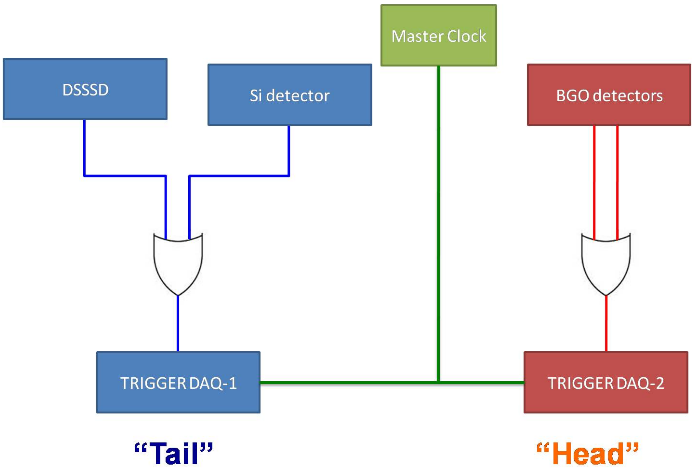

Figure 3.28: *A sketch of the trigger electronic setup for the 2013 experiment using DRAGON.*

3.3.2 Details of the measurements

The experiment was run in two different periods, in 2011 and 2013, carrying out studies at three and one incoming beam energies, respectively. Some of the corresponding parameters are shown in Table 3.5.

Run	$E_{^4He}$ (keV)	Time (hr)	^{7}Be Charge state	B (MD1) Gauss
2011	6553.88 ± 2.78	6.4	3+	2458.70
	5165.97 ± 2.19	14.1	3+	2186.61
	3521.61 ± 1.50	10.1	2+	2697.14
2013	4716.45 ± 2.00	4.2	2+	3102.419
2013 (Impl.)	4716.49 ± 2.00	27.8*	N/A	N/A

Table 3.5: *Some relevant details for the measurements performed in 2011 and 2013 at TRIUMF. The ^{4}He incoming beam energies within the error are shown in the second column, the third column shows the measurement time for each energy, the fourth column shows the ^{7}Be recoil charge state selected in the separator and the fifth one shows the averaged values for MD1 magnetic field B(MD1) at each energy. Errors in B(MD1) are negligible. The last row shows the measurement performed at TRIUMF using the activation method (see text for more details).*
(*)Effective implantation time.

3.3.2.1 Beam purity

In 2011, the supernanogam ion source was used while in 2013 it was the microwave ion source. In order to determine the beam purity, in both cases, a gold foil was placed after the DTL (see Figure 3.20) and a surface barrier silicon detector at 30º with respect to the beam axis detected the scattered beam ions. The on-line $^4He^+$ beam purity spectra taken with both sources are shown in Figure 3.29, from which the level of contaminants can be noted.

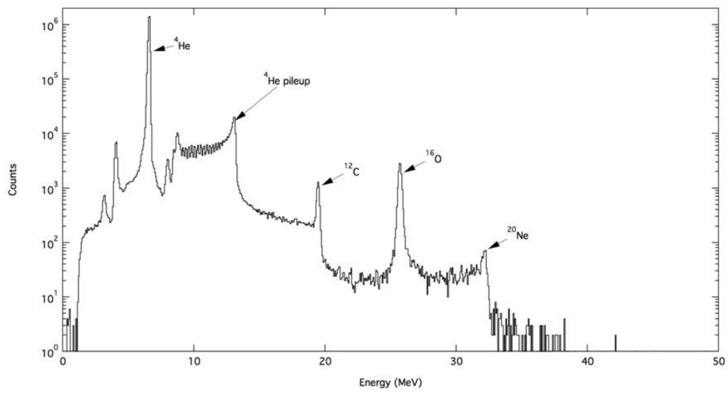

(a)

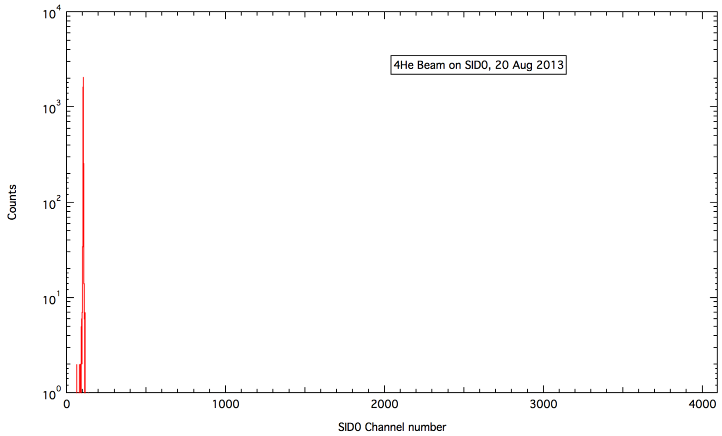

(b)

Figure 3.29: *On-line $^4He^+$ beam purities. The spectra of the beam scattered from a gold foil and detected in a surface silicon barrier detector placed at 30° after the DTL, corresponding to (a) the supernanogam ion source in the 2011 measurements and (b) the microwave ion source used in the 2013 run. It should be noted that both spectra are in logarithmic scale. The influence of the contaminants such as ^{12}C, ^{16}O and ^{20}Ne is negligible.*

3.3.2.2 Tuning procedure for the separator

The separator must be tuned in order to optimise the transmissions for the recoils from the gas target to the DSSSD. It must recalled here that the ^{7}Be recoils exit the target with different charge states and the separator is tuned to accept only one of the charge states using the standard procedure for DRAGON.

Following this procedure, we tuned the separator to achieve optimum transmission for an attenuated ^{4}He beam through the ^{3}He gas target . The first stage consists of centring the beam in the target cell. A **C**harge-**C**ouple **D**evice (CCD) camera is mounted on MD1 facing the gas cell. It is used for online monitoring the light from the ionisation of the gas particles due to the beam passing. This allowed us to centre the beam from ISAC-I in the target cell. A picture taken with the CCD camera during one of our measurement is shown in Figure 3.30. The inner and outer yellow circles represent the entrance and exit apertures of the target cell.

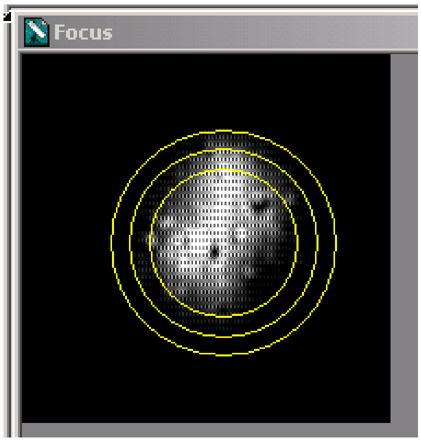

Figure 3.30: *On-line CCD camera image of the light produced upon the ^{4}He beam impact on a $\sim$6 Torr ^{3}He gas target taken during the 2011 measurements.*

Next, the beam is tuned step by step through the different elements, along which several devices such as slits, beam profile monitors, steers and Faraday cups have been installed to optimise the transmission to the DSSSD. Controlled adjustments of the magnetic fields, electric fields, and all devices along the separator could be made with the Experimental Physics and Industrial Control System (EPICS). EPICS is a set of software tools which allows for real time adjustments to the interfaced equipment [EPI]. Figure 3.31 shows the EPICS control software for half of the first separation stage. Different elements can be observed (see caption for the details). Finally, once the attenuated beam reaches the final Faraday cup, the mass and charge is changed to select the ^{7}Be recoils using EPICS control system. Here, the separator settings were automatically scaled, which we refer to change to "recoils mode". The change to recoils using EPICS does not take into account the differences in energy losses of beam and recoils in the gas target.

In our reaction, the most symmetric studied ever at DRAGON, the energy differences between the recoils created upstream and downstream are not negligible, in contrast to the typical reactions studied with DRAGON, e.g. (p,γ) reactions with heavier beam compared to ^{4}He. This very important aspect will influence the acceptance of the separator that is tuned to select one energy (above all in the electric dipoles). In the 2011 run, the standard procedure to change from attenuated beam to recoil mode was employed. In the 2013 experiment, a different manual procedure was used. It consisted of tuning the attenuated beam and changing the magnetic field manually to the corresponding recoil energy calculated utilising the expression 3.13. For the latter the energy of the recoils created at the centre of the gas target minus the energy loss in half of the gas effective length was considered. This procedure favours the selection of the recoils created at the centre of the target. This is in contrast to the standard method where

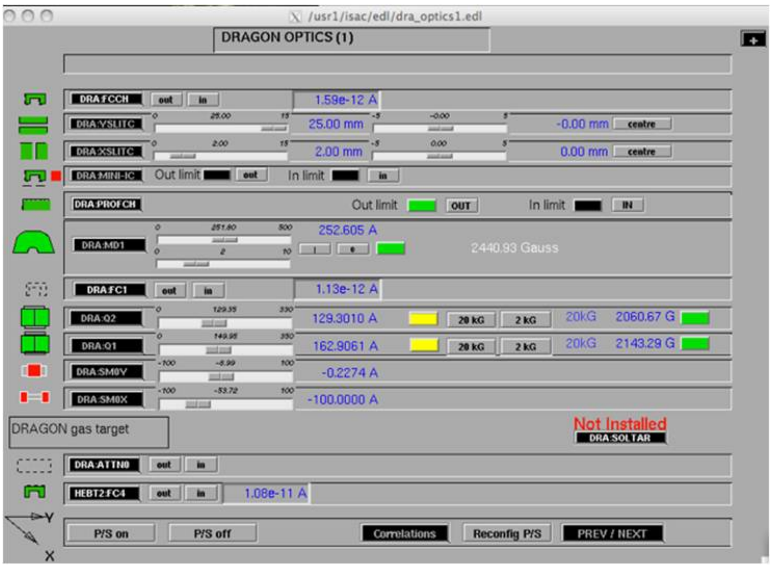

Figure 3.31: *EPICS control system for half of the first separation stage of DRAGON. The controlled elements are: FC4 (HEBT2:FC4), the gas target, quadrupoles (Q1,Q2), FC1 (DRA:FC1), the first magnetic dipole (DRA:MD1), slits (DRA:XSLITC and DRA:SLITC) and FFCH (DRA:FFCCH).*

recoils created at the end of the gas target were favoured. As it will be discussed in the next chapter, these differences in procedures had a strong influence on the acceptance of the recoils.

3.3.2.3 2011 measurements

Three beam energies were considered during the 2011 measurements (see Table 3.5). In principle, the separator should be tuned to select the 3^{+} charge state ($^{7}Be^{3+}$) based on our beam suppression studies (details given in section 3.3.3.2). However, for the lowest energy measured, MD1 and MD2 were in the lower limit of their range (they could not be locked) and this did not allow us to select the $^{7}Be^{3+}$ recoils. Therefore, the separator was tuned to select $^{7}Be^{2+}$ recoils. Some measurements were taken for the $^{7}Be^{3+}$ settings for the lowest energy but they will not be presented here, because the acceptance of the separator cannot be determined without knowing properly the MD1 and MD2 magnetic fields.

Two examples of the DSSSD spectra showing the $^{7}Be^{3+}$ and $^{7}Be^{2+}$ recoils are presented in Figure 3.32. It can be noted that for the 3+ charge state there is no peak corresponding to unreacted beam components close to the recoil peak as expected from the beam suppression studies. In contrast, for the $^{7}Be^{2+}$ case, the unreacted beam appears close to the recoil peak. Thus, we could not completely separate the recoils from the unreacted beam.

3.3.2.4 2013 measurements

In the 2013 run, a measurement was performed using $E^{beam}_{^{4}He} = 4717(2)$ keV (see Table 3.5). Based on the experience from the 2011 measurements, two issues were complementary treated in order to better understand our knowledge of the DRAGON separator for this reaction: the likely unreacted beam contribution in the recoil peak seen for the 2^{+} charge state during the 2011 measurements, and try to reduce the dependence of the transmission of the recoils throughout DRAGON.

• The MD1 and MD2 could not select the 3^{+} charge state ($^{7}Be^{3+}$) for this measurement, thus the separator was again tuned to accept the $^{7}Be^{2+}$ recoils. Figure 3.33 presents the problem due to the

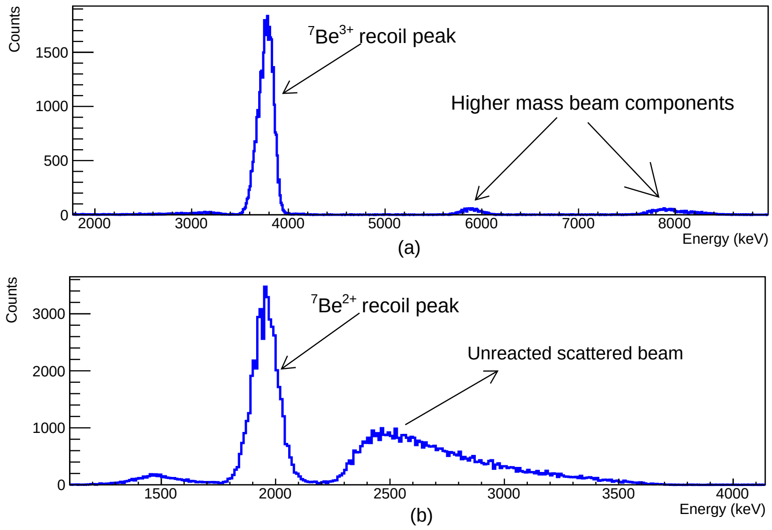

Figure 3.32: *The histograms show the ^{7}Be recoils detected in any of the 16 front strips of the DSSSD. Here, (a) and (b) correspond to the measurements with beam energies of 5166.01 keV and 3521.64 keV and the charge states of 3^{+} and 2^{+}, respectively.*

selection of the 2^{+} charge state, namely, the contribution of the unreacted beam to the recoil peak. The DRAGON MCPs placed before the DSSSD were used during some of the measurements to gauge this effect from the leaky beam.

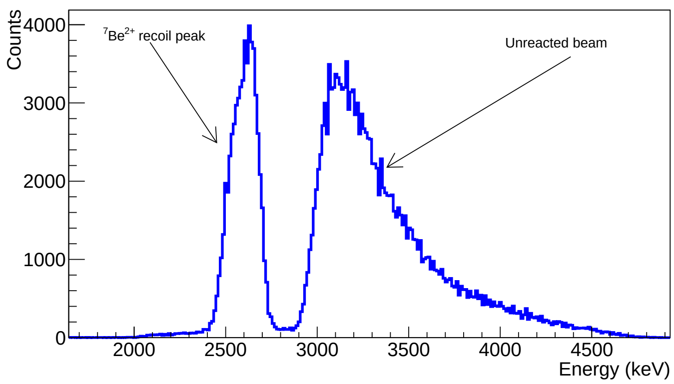

Figure 3.33: *DSSSD spectrum for the $^{7}Be^{2+}$ recoils taken during the 2013 run with $E^{beam}_{^4He} = 4717(2)$ keV*

The DRAGON MCP consists of two microchannel plates in chevron configuration, one behind the other [Lam01]. Ions crossing the devices deposit a small amount of energy. Secondary electrons escape from the foil and are accelerated by a first grid and deflected by a second one toward the MCP, where they are detected. The time of flight between the two different plates allow us to identify the mass of the ions. This allowed us to distinguish between ions with mass 4 and mass 7 corresponding to the leaky beam and recoils, respectively. Figure 3.34 shows where the MCP are located at DRAGON.

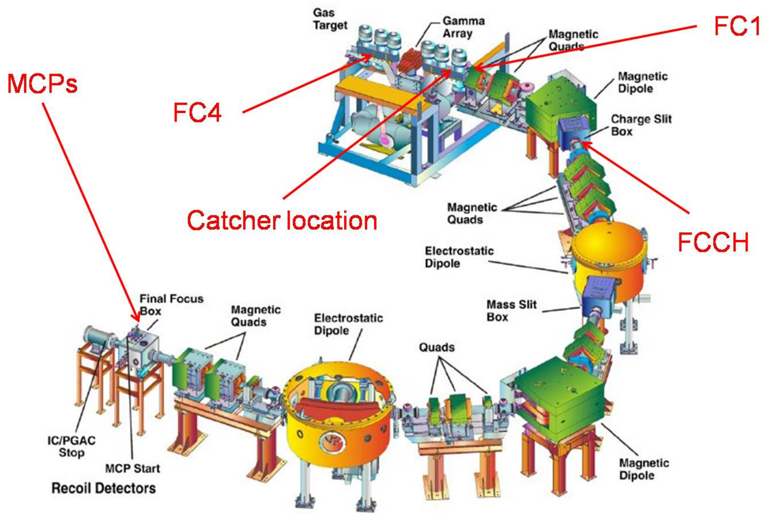

Figure 3.34: *DRAGON layout where the location of some key devices are labelled in red*

The MCPs were placed in and out of the beam path using a manual drive. It is important to move them as the recoil losses in MCPs could not be accurately estimated and thus the measurements taken with the MCPs in the beam path cannot be used to determine our reaction cross section. Nevertheless, measurements have been useful to analyse the effects of the leaky beam.

•As it will be discussed in the next Chapter, one of the key information required is the DRAGON acceptance of the recoils, that is, the fraction of the recoils which can reach the end detector without being stopped throughout the separator. Therefore, the separator was tuned manually in this case and simulation is the key in this respect.

We also performed an additional cross check by carrying out a complementary measurement at the same beam energy and gas target condition using the **activity** method at DRAGON ("implantation mode"). For that, we placed a Cu catcher 85 cm downstream of the gas target, i.e. before the first quadrupole of the separator (see Figure 3.34) and therefore the recoils do not cross the entire separator before being implanted.

As the implantation runs were only carried out during the nights, with breaks during the daylight an effective implantation time has been determined in the same way as for the Madrid experiment following the procedure of reference [FM62].

3.3.2.5 Data taking

In the recoils mode, the information from different detectors was saved in files which can be individually treated or added off-line. Unless there were some problems during the experiment, each file was automatically closed and saved every 60 minutes, and a new file started. At the beginning of each file, a set of readings with Faraday cups, FC4,FC1,FC4,FCCH,FC4 were automatically taken and saved to determine the beam currents. The pressure and the temperature in the target cell were saved automatically every five minutes together with the values of the electric and magnetic fields in the dipoles. See Table 3.5 for some details.

For the implantation mode (in 2013) the recoils were implanted in the Cu catcher and the cell temperature as well as the pressure were also saved each five minutes. None of the magnetic or electric fields were recorded as the separator was not used in this mode. A new file with the information related to the scattered particles detected in the silicon detectors and the γ-rays detected in the BGO array was opened every hour, after recording the FC4 reading. This FC4 reading allowed us to determine the total number of beam particles in the implantation mode. The FC1 and FCCH were placed downstream after the Cu catcher and thus were not relevant during the implantation mode, see Figure 3.34.

3.3.2.6 Experimental determination of the beam energy

Precise information of the incoming beam energy is required. Typical differences of a few keV were seen in previous experiments between the beam energy provided by the ISAC team and the one determined within the DRAGON setup. We used the standard procedure with DRAGON, based on the magnetic fields measured with the NMR probe placed in the first magnetic dipole.

As MD1 is not capable of bending the $^4He^{1+}$ ions, the beam was converted to the $^4He^{2+}$ ion in the target cell filled with ^3He gas at different pressures [MN67, AMHM65]. The $^4He^{2+}$ ions passed through MD1 and the magnetic field "B" was set so that the ions were centred in the 2 mm wide charge slits after MD1 (S1 in Figure 3.21). A regression analysis of the dependence of the magnetic fields with respect to the ^3He gas pressures was used to obtain the magnetic field with no target gas, which corresponds to the incoming beam energy. The kinetic energy is then obtained from the expression 3.13. An example of the extrapolation procedure to zero pressure (no gas condition) is shown in Figure 3.35; in this case the magnetic field for no gas inside the cell is 2705 Gauss, and the corresponding beam energy is 3.521 MeV.

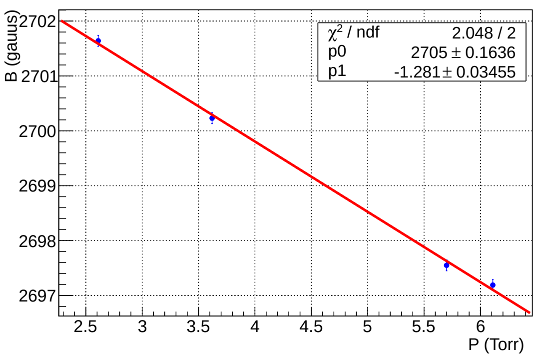

Figure 3.35: *Example of magnetic field values in MD1 for a $^4He^{1+}$ beam after crossing a ^3He gas target at different pressures for the beam energy of $\sim$3.5 MeV given by ISAC. The fields were read out once the beam was centred in the 2 mm width slits placed after MD1. The offset from the fit, 2704.93 Gauss, gives the extrapolated magnetic field value for the incoming beam without any gas in the target cell. The beam energy can be calculated by using the expression 3.13 where A=4.00154 and q=2. For the case of this graph the beam energy at 0 Torr gas pressure is 3.521 MeV.*

The associated beam energy dispersion is reported to be 0.1% FWHM at 1.5·A MeV by the ISAC-I website [GUI]. Therefore, the spread in the kinetic energy can be given by:

$$\Delta E = E\frac{0.1\%}{2\sqrt{2\ln 2}} \tag{3.15}$$

The four beam energies used in the experiments are listed in Table 3.5 within their errors.

3.3.2.7 Observables

As in the case of Madrid experiments, the three main observables to determine the ^{3}He(α,γ)^{7}Be reaction cross section are: the total incoming ^{4}He beam particles, the total number of ^{7}Be recoils produced and the ^{3}He gas target areal density:

• For this experiment the **number of beam particles** has been determined from the combination of two observables, namely, the scattered ions detected in the two silicon detectors placed at 30° and 57°, and the currents measured by the Faraday cups. Examples of the spectra taken with the collimated silicon detectors placed at 30° (a) and 57° (b) are shown in Figure 3.36 for the case of a ^{4}He beam at 5166 keV and a ^{3}He gas target at the pressure of $\sim$6 Torr. At this energy, two peaks originated from the beam and target scattered particles can be separated in the 30° detector, but they are merged in the case of the detector at 57°.

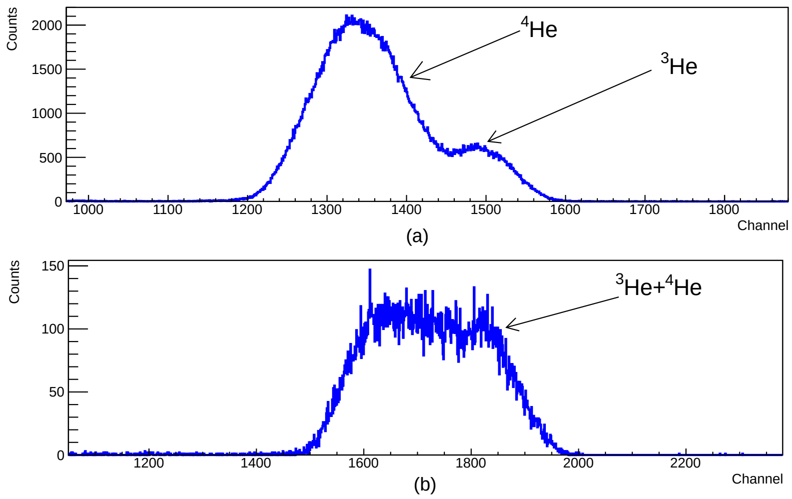

Figure 3.36: *Collimated silicon detector spectra at (a) 30º and (b) 57º taken for an incident ^{4}He beam at E^{beam}=5166 keV impinging onto a$\sim$6 Torr ^{3}He gas target.*

The scattering of ^{3}He by ^{4}He has been studied by, for example, R.J. Spieger and T.A Tombrello [ST67] showing (i) an energy dependence different from that given in equation 3.6 for the Rutherford scattered beam particles from the Ni foil and, (ii) the large energy dependence of the cross section for the elastic scattering channel. Thus, for each energy, we determine a normalisation factor between incoming particles measured via the Faraday cup readings and the total scattered particles in the silicon detector (^{3}He and ^{4}He peaks integrated together) and utilised them to determine the total number of incoming particles. It is worth noting that the correspondence between laboratory and centre of mass angles is different at each energy and thus the centre of mass angle subtended by the detector is different for the different energies.

• The total **number of ^{7}Be recoils** is derived from the total counts in the recoil peak of the DSSSD spectra i.e. Y_{DSSSD}. This yield corresponds to those ^{7}Be recoils with a particular charge state that managed to go through the separator, hit in the active area of the DSSSD and be accepted by the DAQ system. Therefore, the total number of recoils produced can be given by:

$$Y_{^{7}\text{Be}} = \frac{Y_{\text{DSSSD}}}{\text{t}_{\ell} \cdot q_{\text{f}} \cdot \epsilon_{\text{DRAGON}} \cdot \epsilon_{\text{DSSSD}}} \tag{3.16}$$

here t_{ℓ}, q_{f}, ϵ_{DRAGON} and ϵ_{DSSSD} refer to DAQ livetime, charge state fraction of the recoils for the selected charge in the separator, the recoil acceptance of DRAGON for this reaction and the DSSSD detection efficiency, respectively.

•The **gas target areal density** is calculated using the equation 3.7. In this case the pressure, P, and the total temperature, T_0, will be the average of all the values recorded each 5 minutes during the experiment. The temperature correction due to the beam heating of the target is negligible in this case. The effective target length, l, is considered to be 12.3 ± 0.5 cm.

3.3.3 Additional measurements

Some complementary and important measurements are required in order to extract the cross section from our measurements [NSD12]. As mentioned in the previous section, MD1 and MD2 separate particles based on their charge state (see expression 3.12) and only the recoils with the chosen charge state get through these dipoles. Therefore, we need to estimate the ^{7}Be$^{1+,2+,3+,4+}$ charge state fractions at the exit of the target in order to know the total number of ^{7}Be recoils produced in the capture reaction. On the other hand, in the energy range of interest, it can be safely assumed that the probability for the reaction to occur is the same throughout the effective length of the gas target. Therefore, the acceptance of the separator is influenced by the origin of the recoils and thus the experimental determination of the target density profile (TDP) is required. The details of the charge state distribution (CSD) and TDP measurements together with the DSSSD calibration and beam suppression measurements are given in the following subsections.

3.3.3.1 DSSSD calibration

The objective of our experiment is to determine the cross section of the ^{3}He(α,γ)^{7}Be reaction. Therefore, a clean identification of the ^{7}Be recoil is the key requirement, but a reasonable knowledge of their energies should be extracted. In fact, we can calculate the recoil energy rather well from the known beam energy and the effective target length. Moreover, we can precisely determine the ^{7}Be recoil energy accepted by the separator by using the expression 3.13 and the MD1 magnetic field values.

In this context, it is sufficient, but required to have the peak corresponding to a given ^{7}Be energy aligned between the spectra for the various DSSSD strips. These spectra can then be added in order to obtain the correct total number of recoils.

Firstly, the linear behaviour for all 32 strips was studied using a pulser at voltages of 0.5, 1, 1.5, 2 and 2.5 V. An example for one of the strips can be seen in Figure 3.37 where an regression analysis between the nominal voltage and the channel in the histogram is shown. The offset -$p0$- from the fit (25.5 for the example in Figure 3.37) is the value corresponding to no particle hitting the detector.

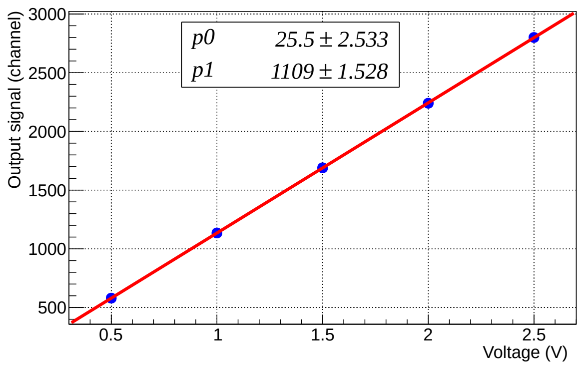

Figure 3.37: *Linearity check for one of the vertical strips. "X" and "Y" axes show the pulser voltage and the corresponding channel in the DSSSD histogram. P0 and P1 give the offset and slope for the linear fit, respectively. As can be seen, a clear linear behaviour is present for this strip.*

Complementary, a calibration measurement was performed by placing an standard triple alpha source in front of the DSSSD. As in the case of Madrid experiment a linear regression between the channel numbers and the values for the energy deposited in the DSSSD was done for each strip. The deposited energy for the alpha particles was slightly different from the standard triple alpha energies given in Table 3.3. These differences essentially come from the energy losses in the aluminium dead layer with effective thickness of 0.5 μm. The energy losses in the dead layer were estimated using the SRIM code [SRI] and added to the deposited energy event by event. Apart from the triple alpha energies, the offsets as presented in Figure 3.37 were used in the calibration process.

The comparison for the energy matching of the strips before and after the energy calibration is shown in Figure 3.38. As it can be seen, there is good energy matching for the alpha particle peaks among all strips after the calibration.

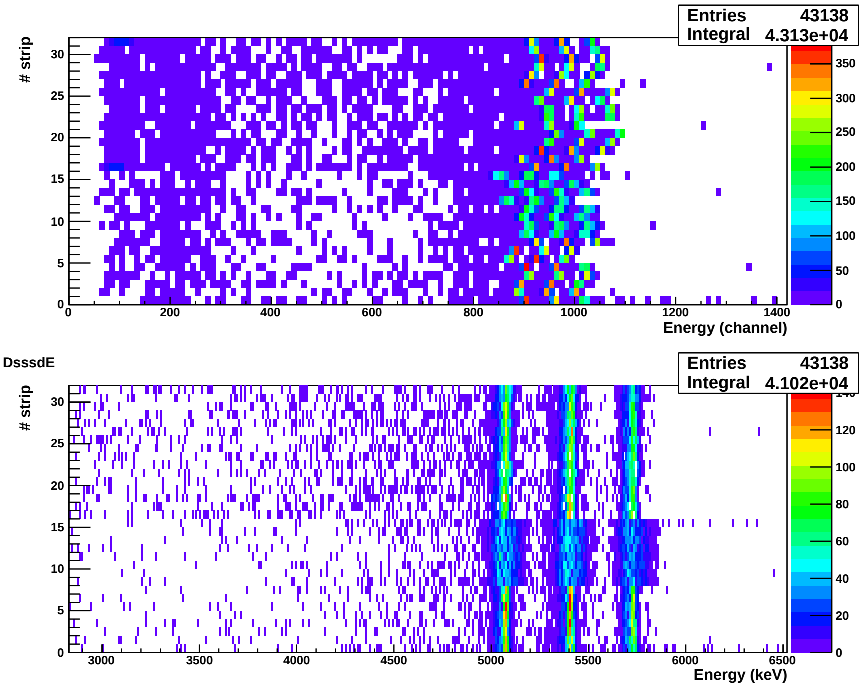

Figure 3.38: *The DSSSD strip number versus energy, before (upper) and after (lower) the energy calibration. A good matching for the alpha energy peaks among the different strips can be seen in the calibrated plot.*

3.3.3.2 Beam suppression

In contrast to other reactions studied using DRAGON, e.g. (p,γ) reactions using higher mass beams, the relative mass difference between the α beam particles and the ^{7}Be recoils is large. This is advantageous as DRAGON settings for the beam and recoils are very different, allowing a good beam suppression. In addition, for the case of the 3^+ charge state of the ^{7}Be recoils the beam suppression is even higher because there is no 3^+ charge state for the beam. Indeed, we performed separate tests to quantify the beam suppression for our reaction [SSA13].

The three overlayed spectra shown in Figure 3.39 were taken in order to study the ^{4}He beam contribution to the ^{7}Be^{3+} recoils at E$^{\text{beam}}$ $\sim$6.5 MeV. The red histogram, collected during 31345 s ($\sim$8.7 h) represents an attenuated 6.542 MeV ^{4}He beam detected in the DSSSD, when DRAGON was tuned to detect recoils and with no target gas in the cell. The events in channels between 1000 and 1100, represent events from the beam scattered by a foil in the microchannel plate detector placed before the DSSSD. The ^{7}Be^{3+} recoils spectrum shown in black was taken with a gas pressure of ~7 Torr inside the target cell, 1.95(6)x10^{16} incoming beam particles and the separator tuned to A/q=7/3 and 3.741 MeV energy. The latter corresponds to the recoil energy. Also a background spectrum with no beam taken during 20967 s (~6 h) is shown in blue.

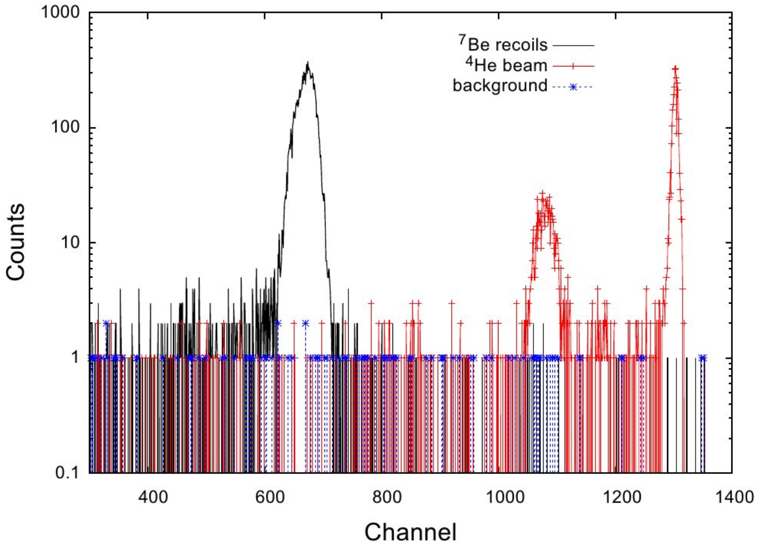

Figure 3.39: *Spectra taken froom reference [SSA13] highlighting the beam suppression for our reaction. The attenuated 6.542 MeV beam energy spectrum is shown in red. The recoils spectrum and the background spectra are shown in black and blue, respectively (see text for more details).*

The expected number of events in a considered range of channels for the background and recoils spectra are given by $\nu_b = R_b \Delta t_b$ and $\nu_s = (R_b + R_s)\Delta t_s$, respectively. Here R_b is the background event rate and R_s is the scattered ^{4}He event rate. Two constrains $\nu_s \geq 1.50\nu_b$ based on the duration of the runs and, $R_b \geq 0$ are also present. The probability for having *i* background counts and *j* beam scattered counts is given by: $P_{ij} = \left(\frac{\nu_b^i}{i!} exp(-\nu_b)\right) \cdot \left(\frac{\nu_s^j}{j!} exp(-\nu_s)\right)$ for an expectation-values [ν_b,ν_s]. The limiting probability is given by the data, $P_0 = P_{ij}[i = N_b, j = N_s]$ being N_b and N_s the number of background events and the scattered beam events in the region of interest. The 90% confident interval is defined for all [ν_b, ν_s] that satisfy the conditional sum:

$$\sum_{ij|P_{ij} \geq P_0} P_{ij} \leq 0.90. \tag{3.17}$$

Two ranges of channels were considered: 770-1320 and 300-400. From the study in this two ranges, the integrated beam suppression from channels 300 to 1320 is >1.2 $\cdot 10^{14}$ in terms of the total number of incident ions divided by the number of transmitted ions at 90% confident level (CL).

The beam suppression has been determined for the ^{7}Be^{3+} recoils at E$^{\text{beam}} = 6.542$ MeV, which is the highest energy in our experiment. As already mentioned, for the E$^{\text{beam}} = 3.521$ and 4.716 MeV the separator was tuned to 2^+ charge state instead of 3^+ charge state due to the limitations of the separator in bending the ^{7}Be^{3+} recoils at those energies. The contributions of the unreacted beam in the recoil energy region for the ^{7}Be^{2+} recoils at these energies were measured using the MCPs.

3.3.3.3 Charge state distributions

The ^{7}Be recoils produced along the length of the target interchange electrons with the ^{3}He gas atoms. Therefore, a distribution of ^{7}Be^{+1}, ^{7}Be^{+2}, ^{7}Be^{+3} and ^{7}Be^{+4} ions is present at the exit of the target cell. During the experiments, DRAGON was set to select either the 3^+ or 2^+ charge states, therefore the fraction of the these particular charge states (q_f) must be known in order to determine the absolute cross sections, as it determines the overall efficiency of our setup for ^{7}Be recoil detection.

Once the ions pass through a minimum effective gas thickness needed for the charge state distribution to reach an equilibrium, this charge fraction stays constant upon encountering further gas atoms. Previous measurements of the charge state distributions for ^{16}O and ^{24}Mg using DRAGON are shown in Figure 3.40 [LIB03]. As it can be seen, after some critical gas thickness the charge state equilibrium is reached.

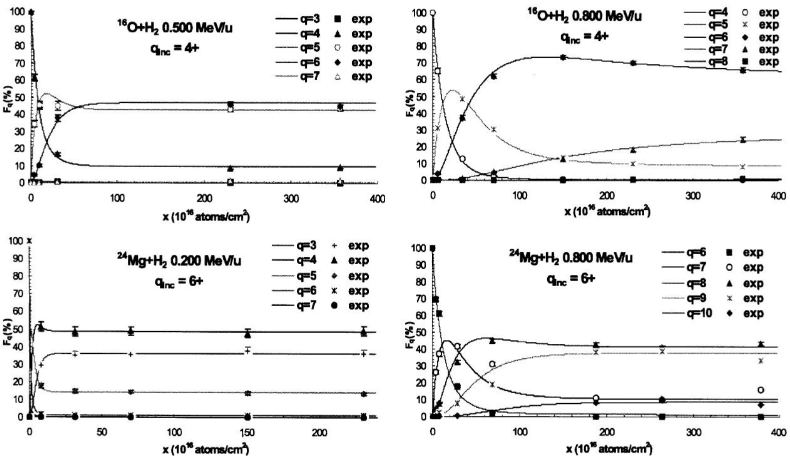

Figure 3.40: *Fractional charge state distributions measured using DRAGON taken from [LIB03]. The charge state fractions, denoted here by F_q, for the ^{16}O and ^{24}Mg ions are plotted as a function of the incoming energy and incident beam charge state. As can be observed, the charge state fraction do not change after a critical thickness.*

Some arguments are given in the paper based on the results for the charge state fractions using DRAGON, which fit the Gaussian distribution well (cf. Figure 3.41).

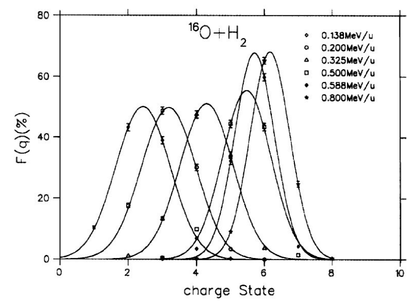

Figure 3.41: *Figure taken from [LIB03] which shows the equilibrium charge state distributions for a ^{16}O beam at different energies impinging onto a ^2H target. The charge state fractions are fitted using Gaussian functions.*

The average equilibrium distribution can be given semi-empirically by [Bet72]:

$$\bar{q} = Z_p \left[1 - exp \left(- \frac{A}{Z_p^{\gamma}} \sqrt{\frac{E}{E'}} + B \right) \right] \tag{3.18}$$

where A, B and γ are free parameters, Z_p is the atomic number of the projectile with energy E (MeV/u) and $E' = 0.067635$ MeV/u. Although some values for A, B and γ parameters are determined in reference [LIB03] these cannot be used in our analysis as this semi-empirical expression is not general and depends on each experiment itself. However, some observations can be made. For a given incident beam element, the charge state equilibrium is independent of the initial charge state or isotope. The cross section of capture and loss of electrons for an ion beam depends on the velocity of the projectiles, atomic number of the ion beam and nuclear charge of the target atoms.

Based on these qualitative observations we performed measurements in order to determine the charge state distribution of the ^{7}Be recoils. We used a ^{9}Be^{2+} beam at three different incoming energies onto a ^{3}He gas target at different pressures. The charge state fractions (q$_f$) are determined by obtaining the ratio between the incoming ^{9}Be^{2+} beam current measured using the FC4 Faraday cup placed before the gas target, and the number of ^{9}Be^q ions (being $q = 2^+, 3^+$ or 4^+) measured in FCCH. This cup is located downstream MD1, the magnetic dipole which selects charge sate of interest. Therefore, we have

$$q_f = \frac{N_{^9Be^q}}{N_{^9Be^{2+}_{incoming}}} = \frac{I_{FCCH} \cdot T/(q \cdot e^-)}{I_{FC4}/(2 \cdot e^-)} \tag{3.19}$$

here, I represents the currents measured in the Faraday cups in Ampere, e^- is the electron charge and q is the selected ^{9}Be charge state in MD1. The transmission, T, throughout the gas target was estimated by the ratio between the currents measured in FC4 and FC1 (placed just before Q1) without gas in the target cell.

Using a computer program called "Rosumn", the Faraday cup readings were taken in the following order FC4-FC1-FC4-FCCH-FC4. Each of these cup measurements takes 30 seconds. If there is gas inside the target cell, FC1 readings cannot be used to determine the transmissions due to the mixture of different charge states at that point. Therefore FC1 were considered with no gas target inside.

The charge state fractions measured using the ^{9}Be^{2+} ion beam and ^{3}He gas target are shown in Table 3.6. The I_{FC4} value was considered as the average of the three FC4 measurements taken during every cup reading sequence. In Chapter 5, a typical 30 seconds Faraday cup reading and how the information is extracted will be shown. For $E^{\mathrm{beam}}_{^9\mathrm{Be}}$= 533.78 keV/u and 420.54 keV/u, the charge state distributions were measured using two different gas pressures in order to prove that the charge state equilibrium is reached for a gas pressure >1 Torr. Figure 3.42 shows the example case of $E^{\mathrm{beam}}_{^9\mathrm{Be}}$=533.78 keV/u, and as can be seen the charge state equilibrium is reached. This means that all hte ^{7}Be recoils created via the ^{3}He(α,γ)^{7}Be reaction which pass through the gas of 1 Torr of effective pressure will exit the target with the same charge state distribution. Thus, the charge state selection in MD1 will affect in the same way to all the recoils independently of where they were created and we can infer the total number of recoils produced from just detecting one charge state and taking into account the charge state fraction (q$_f$) in Table 3.6.

$E^{incoming}/u$ (^{9}Be) (keV)	Transmission (%)	P (Torr)	q	q_f (%)
533.91	95	0.95	2	12.08± 2.17
			3	59.78± 1.85
			4	27.97± 0.91
		5.25	2	10.80± 2.32
			3	59.05± 1.87
			4	29.15± 1.21
420.64	96	5.3	2	22.88± 3.78
			3	61.87± 2.55
			4	12.59± 1.73
		1.1	2	23.42± 4.06
			3	60.07± 3.05
			4	13.28± 2.18
284.09	92	5.31	2	52.30± 3.33
			3	37.91± 2.37
			4	1.82± 0.98

Table 3.6: *Charge state distribution for a $^9Be^{2+}$ beam onto a ^3He gas target. The ^9Be electric charge after passing through the gas target is shown in the fourth column. The charge fractions in the fifth column were measured using three different incoming beam energies shown in the first column and determined as explained in section 3.3.2.6. For the first two energies, the CSD was measured at two different pressures shown in the third column in order to show that the charge state equilibrium was reached for pressures >1 Torr. The transmission between FC4 and FC1 is indicated in the second column and it was measured with no gas inside the target cell.*

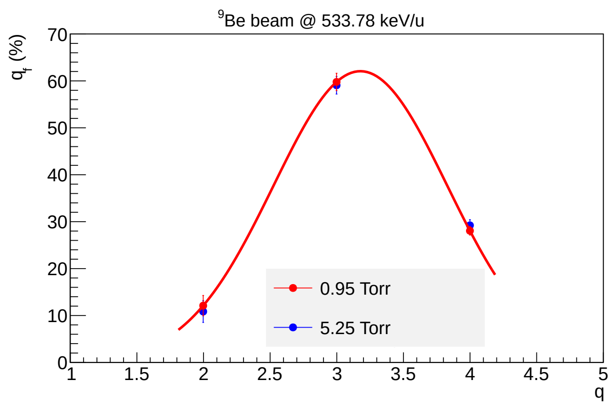

Figure 3.42: *Charge state distribution for a $^9Be^{2+}$ beam with incoming energy of 533.78 keV/u onto a ^3He gas target at two different pressures, 0.95 (red) and 5.25 Torr (blue). The values for the charge state fractions (q_f) for the different charges (q) are the same within the errors for the two values of ^3He gas pressure. This means that the charge state equilibrium is reached at and above the target gas pressure of 0.95 Torr.*

3.3.3.4 Target density profile

Kinematic calculations (see appendix B) for the ^{3}He(α,γ)^{7}Be reaction show that the maximum recoil cone angle is $\sim$ 20 mrad, which nearly corresponds to the separator geometrical acceptance. Moreover, a distinctive feature is that in our range of energy this is a non-resonant reaction. Thus, the probability of the reaction to occur is the same throughout the effective target length. This is in contrast to the most of reactions studied at DRAGON, which are usually resonant reactions. These two facts , namely, i) mass symmetry in the incoming reaction channel leading to a large cone angle, and ii) the position for ^{7}Be production anywhere in the target, limit the recoil acceptance of the separator.

If some other effects are considered as the ^{4}He beam and ^{7}Be recoil straggling in the gas along their path, variation on the beam direction, or the fact that the beam is not point- like, the recoil cone angle can be seen increased to 22 mrad [Ree12], which is above the 20 mrad of geometrical acceptance. It should be noted that in this case we assumed that the reaction takes place upstream the target centre. Such effects will be treated in the next chapter using simulations to estimate the DRAGON ^{7}Be recoil acceptance from the ^{3}He(α,γ) reaction, where the experimental target density profile must be included. Moreover, this was the first time using a ^{3}He gas target in DRAGON, and this measurements served as cross checks on the previously measured effective target length using ^{2}H and ^{4}He targets.

The target density profile (TDP) was experimentally determined using the ^{3}He(^{12}C,^{14}Nγ)p resonant reaction. The experiment was performed using a ^{12}C^{2+} ion beam impinging onto a $\sim$6 Torr ^{3}He gas in the target cell. Half of the BGO detector array surrounding the gas box was removed from the surroundings and a single lead shielding BGO detector was used to detect the γ-rays from the ^{12}C+^{3}He reaction. The shielded detector was placed on top of a movable platform, which allowed us to move it along the length of the gas box. Figure 3.43 shows two photographs of the shielded BGO detector in front of the target box as it was used during the experiment.

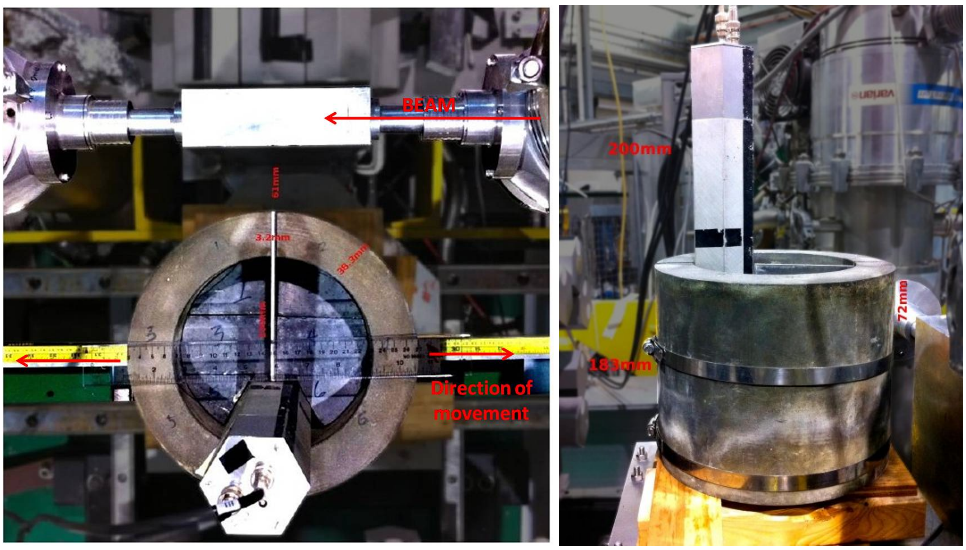

(a) (b)

Figure 3.43: *Setup used for the measurements of the target density profile. (a) An upper view of the setup is shown together with the target cell and the shielded BGO detector placed in front. The 3.2 mm length is the slit aperture in the shielding through which the γ-rays from the reaction in the cell are viewed by the BGO detector. (b) A side view of the setup is shown.*

Based on the results from reference [KBR64], in which the ^{3}He(^{12}C,^{14}Nγ)p reaction was studied using direct kinematics, i.e. ^{3}He beam onto a ^{12}C target, there is a known broad resonance centred at 2.99 MeV ^{3}He beam energy for the ^{12}C(^{3}He,^{14}Nγ)p reaction (6.44 MeV state in ^{14}N). This was observed by the detection of the 6.44 MeV γ-rays at this particular 2.99 MeV beam energy and not above (3.46 MeV) or below (2.62 MeV). This broad resonance was chosen in order to have a low energy dependence across the target length. The goal of our measurements was to populate the same resonance state using inverse kinematics (we need to use the ^{3}He as target due to our interest of determining the TDP for ^{3}He) and detect the 6.44 MeV γ-ray. The target density profile could be determined by comparing the number of γ-rays detected by the BGO, collimated using a 3.2 mm slit, placed at different positions across the target box (see Figure 3.43(a)).

A part of the energy level diagram relevant for the reaction with p+^{14}N in the exit channel is shown in Figure 3.44. Some other open reaction channels e.g. ^{3}He(^{12}C,^{11}C)α are not denoted. By selecting the optimum ^{12}C beam energy, the 14.46 MeV state in ^{15}O is populated. This state decays by proton emission populating the 6.44 MeV state in ^{14}N, which de-excites by the emission of one of the four possible γ-rays with the relative intensities shown in the figure. The incoming beam energy of 12.088 MeV for our measurements was determined using the same procedure described in section 3.3.2.6, using the MD1 tuned to select the 5$^+$ charge state of ^{12}C.

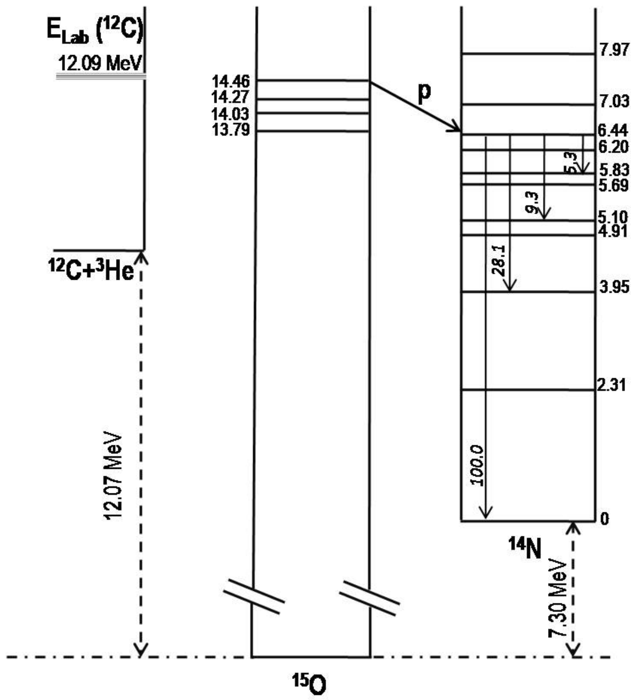

Figure 3.44: *A relevant part of the energy level diagram for the ^{12}C+^{3}He reaction showing the excited states in ^{14}N and ^{15}O nuclei that play an important role in our analysis. The levels are marked with their energies in MeV (from [Nuc]). All the γ-rays from the 6.44 MeV state in ^{14}N, to the ground, 3.95, 5.10 and 5.83 MeV states, are also shown with their relative intensities written down in italic. Using a 12.09 MeV ^{12}C beam, we populated the 14.46 MeV state in ^{15}O, which decays mainly via proton emission to the 6.44 MeV state in ^{14}N. Some other channels are opened for this energy, such as the ^{3}He(^{12}C,^{11}C)α reaction, but they are not shown in the figure as these are irrelevant for the TDP determination.*

In order to check the $^{12}C^{2+}$ beam purity, the beam was scattered using a gold foil located just after the DTL. Figure 3.45 shows an on-line calibrated spectrum of the Rutherford scattered particles detected in a silicon detector kept at 30º with respect to the beam direction taken during a short measurement. The yield in the peaks implies that the ^{18}O contaminant is present at a level of 0.5% in the ^{12}C beam.

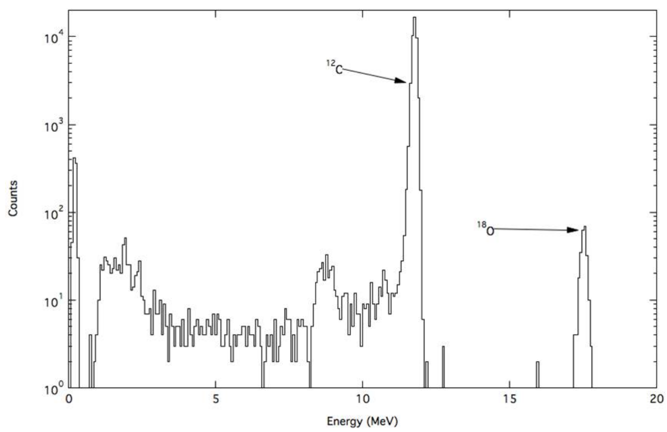

Figure 3.45: *An on-line spectrum of ^{12}C beam scattered from a gold foil placed after the DTL (see text for details).*

An example of the BGO spectrum showing the γ-rays from the $^3He(^{12}C,^{14}N\gamma)p$ reaction is shown in Figure 3.46 for the BGO detector placed at the centre of the target cell. Thirty-seven measurements were performed covering a range between -11 cm upstream and 9 cm downstream with respect to this position with an average time for each measurement of $\sim$2500 s and a livetime percentage of $\sim$99%. It should also be noted that the distance between the beam line and the BGO detector was kept constant as we moved the shielded BGO along the target box.

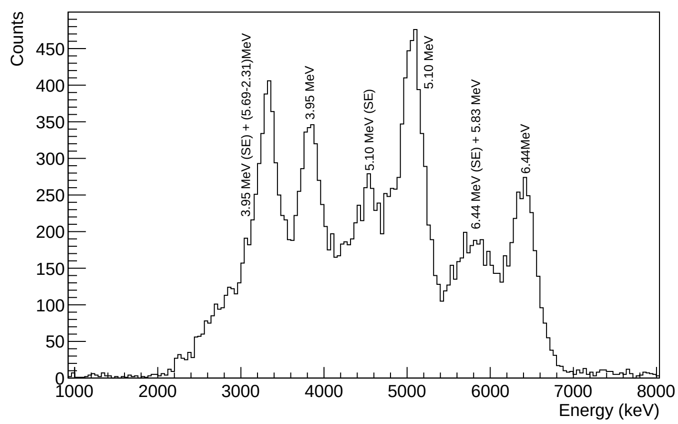

Figure 3.46: *BGO spectrum for the $^3He(^{12}C,^{14}N\gamma)p$ reaction with the BGO detector viewing the centre of the gas cell. The main peaks are labelled with their energy in MeV. SE refers to the single escape peak of the corresponding energy.*

The TDP is related to the yield of the 6.44 MeV γ-peak in each of the BGO position. The yield for each position is given by:

$$Yield = \frac{BGO^{6.44\gamma}/Livetime \cdot 8.02 \cdot 10^{-8}}{SB0 \cdot P} \tag{3.20}$$

where $BGO^{6.44\gamma}$ is the 6.44 MeV integrated peak, $livetime$ is the correction due to the dead time of the acquisition system, P is the pressure in the target cell included as the correction related to the different number of ^{3}He gas particles for each run, and *SB0* is the normalisation factor related to the ^{12}C beam particles for each run.

During each measurement, the scattered beam ions with the gas were detected in the silicon detector mounted on the arm of the gas cell at 30º with respect to the beam direction (see Figure 3.22). Figure 3.47 shows a calibrated spectrum of scattered particles detected in the silicon detector for a ^{12}C beam at 12.09 MeV impinging onto the ^{3}He gas target at 5.9 Torr.

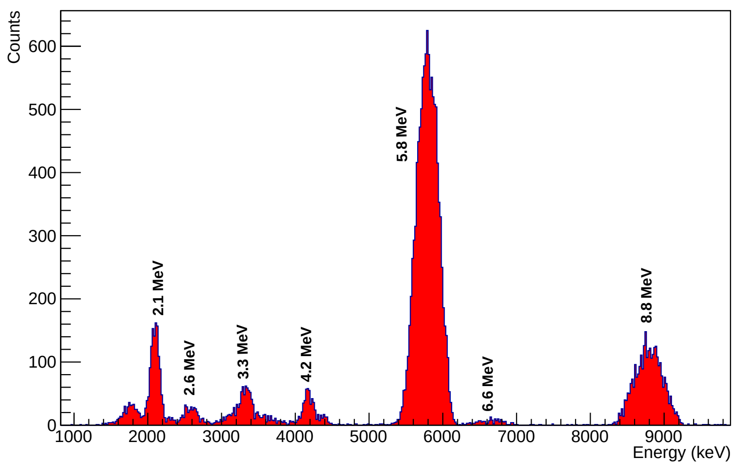

Figure 3.47: *A scattered particles spectrum detected with the silicon detector placed at 30°with respect to the beam for a 12.088 MeV ^{12}C beam impinging onto the ^{3}He target at 6 Torr. Some of the peaks are labelled with their corresponding energy, see text for the details of the origin of each peak. The peak of interest for the the TDP measurements is the 5.8 MeV corresponding to the scattered ^{3}He from ^{12}C.*

Energies corresponding to the peaks and their origin are:

- 8.8 MeV: α particles from the ^{3}He(^{12}C,^{11}C)α reaction
- 6.6 MeV: ^{3}He elastically scattered from the ^{18}O beam component
- 5.8 MeV: ^{3}He elastic scattered from ^{12}C
- 2.1 MeV: protons for the ^{3}He(^{12}C,^{14}N*)p reaction

In order to normalise the yield with the number of incoming ^{12}C beam particles, *SB0* factor in expression 3.20 is considered as the 5.8 MeV peak integration. The gas pressure for each run has been calculated as the average of the pressure readings saved each five minutes during the measurements. $BGO^{6.44\gamma}$ is the area under the 6.44 MeV peak, which is deduced by fitting the 6.44 and 5.83 MeV peaks in Figure 3.46 to two Gaussian distributions simultaneously and then taking the area of the 6.44 MeV peak. A background spectrum was subtracted for all BGO spectra, however, no influence was seen in the 6.44 MeV peak region.

Figure 3.48 shows the target density profile obtained using the expression 3.20. It is worth noting that there are two unwanted features in the profile which should be corrected. These are, (i) the asymmetry of the profile between the downstream and upstream ends of the target cell, and in the region corresponding to the target cell, between ∼ -50 mm and ∼ 50 mm (see Figure 3.22), and (ii) the yield is non- zero in the extremes, i.e. at +100 mm. The latter would mean that there is gas far away from the centre of the target cell, which would alter the acceptance significantly.

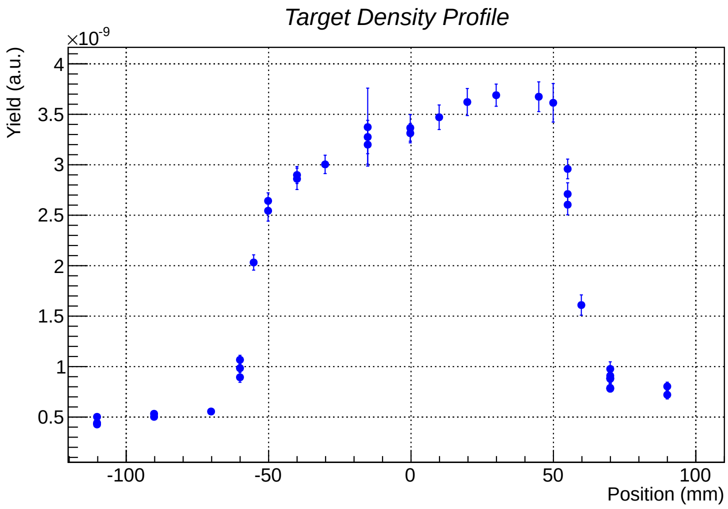

Figure 3.48: *The measured target density profile obtained using the expression 3.20. The X axis shows the different positions of the BGO detector parallel to the beam axis. The yield between -50 and 50 mm is not flat as it would be expected for our recirculating gas system.*

In order to correct for the asymmetry and the sloped-profile in the gas cell, we considered the energy loss by the beam throughout the gas target and the energy dependence of the resonance reaction. The ^{12}C beam energies at the entrance and exit of the target are 12.09 and 11.96 MeV, respectively. The latter is extracted directly from the MD1 reading (3452.92 G) tuned for the $^{12}C^{+5}$ beam, after crossing the ^{3}He gas target at 5.8 Torr pressure. On the other hand, the resonance reaction populates an unstable excited state of ^{15}O, the decay of which has the Breit-Wigner distribution with respect to the energy:

$$w(E) \propto \frac{(\Gamma/2)^2}{(E - E_0)^2 + (\Gamma/2)^2} \tag{3.21}$$

here, Γ is the level width and is inversely proportional to the lifetime. The values of $E_0 = 14.46$ MeV and $\Gamma = 100$ keV are taken from [Nuc]. Figure 3.49 shows in blue a representation of the Breit-Wigner expression for the population of the 14.46 MeV state in ^{15}O using a ^{12}C beam on a ^{3}He target. E_0 and Γ have been converted to consider a ^{12}C beam and the proportional factor has been considered as $w(E_0) = 1$, for simplicity for our purposes. The red area shows the beam energy region between 11.96 and 12.09 MeV, and it can be observed that the probability for the decay varies significantly. Thus, a correction factor in the expression 3.20 has been included in order to account for this variation.

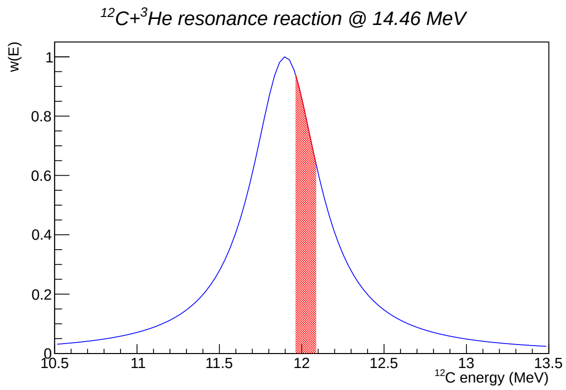

Figure 3.49: *The blue curve shows the probability decay ($w(E)$) of the $^{12}C+^{3}He$ resonance corresponding to the 14.46 MeV state in ^{15}O. The "x"-axis shows the energy of a ^{12}C beam. The red shaded region represents the beam energy loss in the gas cell and thus the variation in the probability for te reaction to occur in this energy range.*

Assuming an effective length of ∼12.3 cm estimated from the energy loss (12.09-11.96 MeV) by the beam crossing the 5.8 Torr of ^{3}He gas and the SRIM code [SRI], the beam energy at each position (E_p) has been determined by linear extrapolation. Considering E_p, the expression 3.20 has been multiplied at each position by the factor $w(E_p)$. This account for the difference in probabilities of the reaction to occur due to the variation of the beam energy across the target cell.

The new TDP, corrected for different reaction probabilities at each position, is shown in Figure 3.50. Clearly, this profile does not have a slope in the region corresponding to the target cell and is rather symmetric outside, in line with our expectation for the configuration of the cell and the differentially pumping system.

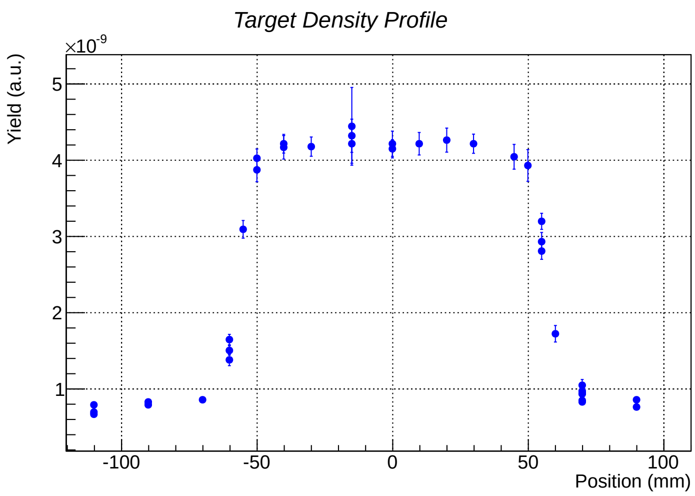

Figure 3.50: *A corrected target density profile obtained after considering the different beam energy at each position and the variations in the probability of the resonance reaction to occur. For each position in the x-axis, the y-axis shows the yield calculated using the expression 3.20 multiplied by the $w(E_p)$ factor, where E_p is the energy at each position.*

As it can be observed in Figure 3.50 the non-zero γ-yield is still persistent but now is symmetric at both extremes. This is against the expectations from the differentially pumped system with our particular arrangements, which creates a profile with a rapid decrease in pressure at the extremes of the cell, beyond which, the pressure should go to zero rapidly, and thus no reactions should occur. Therefore, we claim that the non-zero γ-yield effect is due to the non 100% shielding of the BGO and a constant background should be subtracted from the whole profile.

In order to probe this argument let us compare the situation at two different positions of the BGO detector, the extreme at z=-11 cm and the centre at z=0 cm. The ratio between the yields at this positions is 0.17 (cf. Figure 3.50), and Figure 3.51 shows the two cases considered.

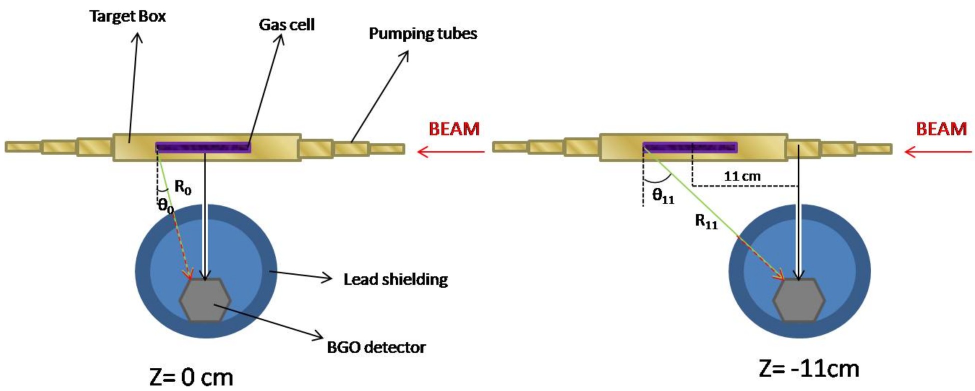

Figure 3.51: *The two different BGO detector positions (z=0 and z=-11 cm) used to analyse the effect of the shielding and the subtended solid angle by the BGO detector. In green are shown the γ rays created at the exit of the target cell, and in red the part of the rays inside the shielding.*

In these two positions, the γ-rays produced at the left extreme of the gas cell can in principle go through the shielding along the green lines, where R_0 and R_{11} indicate the distances to reach the detector. For these two scenarios, the subtended solid angles and the γ attenuation through the shield need to be considered. The ratio between the two solid angles can be given by: $d\Omega_{z=-11}/d\Omega_{z=0} = \frac{cos\theta_{11} \cdot R_0}{cos\theta_0 \cdot R_{11}} = 0.55$ based on the measured distances and simple trigonometric relations. Now, the relative γ intensity at any distance in one material can be expressed as: $I/I_0 = e^{-\mu \cdot x}$, where μ is the linear attenuation coefficient and I_0 and I are the γ intensities before and after crossing a "x" distance in the material, respectively. Taking into account that $\mu_{(lead)} = 0.505/cm$ and the different distances crossed by the beam through the lead (red dashed line in Figure 3.51), the ratio $e^{-\mu \cdot s}_{z=0}/e^{-\mu \cdot s}_{z=-11}$ results in 0.57. Thus, although the solid angle is smaller for further distances it gets compensated by the γ attenuation effects and a constant yield, at first order approximation, could be expected for all the measurements at the different positions. It should be noted that we had a reasonable assumption that γ-rays are emitted isotropically based on the symmetry seen in the extremes of our target density profile.

In principle, a Montecarlo simulation could be performed to determine the effect of the shielding, taking into account effects such as the non equal probability of producing the reaction at the different positions in the target or corrections for the Doppler effect of the different γ-rays, etc... However, the present method already constitutes a very good estimation. Therefore we will consider a constant "yield background" which is assumed to be the yield value at z=-11 cm. In Figure 3.52, the blue points show the final experimental target density profile with the first order "background yield" subtraction correction.

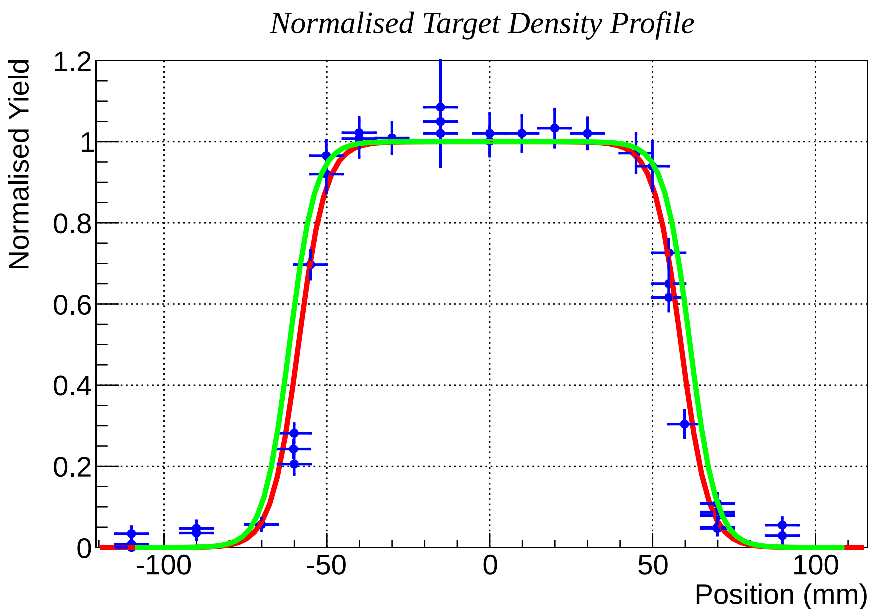

Figure 3.52: *Final normalised target density profile. The blue points show the normalised yield corrected with the energy dependence given by the expression 3.21 and after subtraction of a constant background. The red fit shows the "best" fit to the points with a Fermi function obtained using ROOT package and the green curve shows the same fit constraining that the effective length is 12.3 cm.*

The red and green curves in Figure 3.52 show two fits to the data points using the Fermi function given by [Hut02]:

$$\text{Yield}^{\text{Norm}} = \frac{1}{1 + e^{(|z|-R)/a}} \tag{3.22}$$

where R and a are the two free parameters. The red curve shows the "best" fit to the data points using the ROOT package [ROO] and the green curve shows the fit constraining that the effective length is 12.3 cm. This length is obtained from the energy losses of the ^{12}C passing through the ^{3}He gas target and estimated from the MD1 magnetic fields. In the next chapter, the influences due to different slopes and effective lengths in the profile will be discussed.

3.4 Conclusion

Two experimental techniques have been used to determine the cross section of the ^{3}He(α,γ)^{7}Be reaction in the range of E_{CM} 1-3 MeV. The details of the two experiments and setups have been given in this chapter.

The *Activation Method* was performed at CMAM using a tandetron accelerator. The reaction was produced using a ^{3}He beam at nine different energies on a ^{4}He gas target. The total number of ^{7}Be recoils produced are deduced by measuring the γ activity arising from the de-excitation of the ^{7}Li produced by the electron capture decay of the ^{7}Be. The γ measurements were performed at the SOREQ low-background HPGe detector station. The careful control and good knowledge of various parameters such as the solid angle subtended by the silicon detector, the Ni foil thickness or the silicon detector energy calibrations have been discussed in this chapter.

The *Direct Recoil Counting Method* was performed using the DRAGON spectrometer at TRIUMF. The reaction was carried out using inverse kinematics, i.e. ^{4}He beam at four different energies on a ^{3}He gas target. One measurement using the *Activation Method* was also performed at one of the energies at which data was already obtained in direct recoil counting method. The total number of recoils produced is inferred by detecting one of the charge states in a DSSSD placed at the focal plane at the end of the separator. The necessary charge state distribution measurements were carried out using a ^{9}Be beam. The density profile of the windowless gas target is a crucial parameter that was experimentally determined to be used in the simulations to obtain the acceptance of the separator (see next chapter). Other details concerning the beam energy determination, the DSSSD calibration and the separator tuning have also been discussed. The analysis of the data from both experiments will be presented in Chapter 5.

"We cannot solve our problems with the same thinking we used when we created them".

Albert Einstein

CHAPTER 4

GEANT SIMULATIONS OF DRAGON

Abstract: *In this chapter I will discuss the Monte Carlo simulations performed in order to obtain the acceptance of the DRAGON separator for the recoils created in our $^{3}He(\alpha,\gamma)^{7}Be$ reaction. Firstly, different input parameters considered in order to define the experimental conditions are detailed. In what follows I will present the results from the simulations carried out for the different beam energies, as well as the estimated uncertainties in the acceptance due to the possible changes in the input parameters.*

In the previous Chapter the two experimental techniques used in this work to determine the astrophysical S-factor were detailed. Additional essential measurements were also presented. Some of these measurements are needed in order to get the astrophysical S-factor precisely, e.g. the experimental determination of the collimated silicon detector angle in Madrid experiment, and some of them are even necessary in order to determine the absolute cross section, e.g. the charge state distribution using the DRAGON separator.

On the other hand, simulating experimental conditions using Monte Carlo codes have become common in designing experiments as well as in understanding measured quantities. In the case of Madrid experiment, thanks to the simplicity and good experimental knowledge and control of the parameters of the setup, no detailed simulations were necessary. By contrast, the DRAGON setup needed extensive simulations as the separator acceptance is such that there is a scope for losing ^{7}Be recoils between the production points in the target and the detection in the DSSSD.

The loss of these recoils depends on various parameters, an experimental control of which is very difficult, if not impossible. Therefore, we resorted to simulations to obtain additional information on the acceptance of the setup to obtain the final results from TRIUMF work. It is worth pointing out that the acceptance of the DRAGON separator has high influence on the S_{34}(E) data. The influence of possible variations in many parameters, such as the beam spot size or the magnetic fields in the dipoles must be precisely studied as they can change the acceptance significantly. Therefore, an extended discussion about the transmissions of the ^{7}Be recoils generated via the ^{3}He(α,γ) reaction will presented in this chapter.

4.1 Introduction

As it has been already mentioned throughout this text, one of the main concerns to be taken into account for studying the ^{3}He(α,γ)^{7}Be reaction at DRAGON is the separator acceptance or transmission for the recoils produced in this reaction ($\epsilon_{\mathbf{DRAGON}}$). **For a given charge state** the acceptance is defined as the ratio of the recoils detected in the DSSSD and the total recoils created in the gas target ($\epsilon_{\mathbf{DRAGON}}=\frac{^{7}\mathrm{Be}^{\mathrm{DSSSD}}}{^{7}\mathrm{Be}^{\mathrm{produced}}}$). In order to estimate the DRAGON acceptance for our reaction, the GEANT 3-DRAGON simulation code has been adapted to recreate our experimental conditions and obtain the $\epsilon_{\mathbf{DRAGON}}$ parameter.

GEANT (GEometry And Tracking) 3 is a FORTRAN software which allows the construction of different geometrical setups, the interaction between particles, the tracking of particles in different media and the use of electromagnetic fields using Monte Carlo techniques [GEA]. Any GEANT simulation consists of three main stages: initialisation, event processing and termination. In the three stages the user can incorporate his own codes. In the first stage the user defines the different geometrical volumes of the setup and the materials, the sensitive volumes are specified. During the processing phase the events are firstly created, the kinematics is defined and the particle's path through the different volumes is tracked, interactions with the different media are simulated and secondary events, such as likely γ-rays, are tracked. The response of the detectors to the particle hits is also considered at this stage. During the termination phase the statistical information is computed. The information is saved event by event as ntuples in files (files with one row an n-columns of information per event) and are also histogrammed into frequency distributions by the software package HBOOK [HBO]. A detailed information about the GEANT structure can be found in reference [GEA].

The GEANT 3-DRAGON code was designed using the version 3.2.1 of GEANT and it consists of two main geometrical parts. The first includes the target box, the cell, BGO detectors and the pumping tubes placed before the first quadrupole (Q1 in Figure 4.1(b)). The second part concerns the separator and includes all the components after the first quadrupole. The magnetic and electrostatic elements of the separator are scaled (i.e. magnetic and electric field are set to let the recoils go through) to the corresponding recoils created in the reaction by using an input RAYTRACE file read at the initialisation stage. Figure 4.1 shows the two main geometrical areas discussed in the context of the simulation, (a) the target region and (b) the separator.

This code has previously been used and tested for other reactions studied with DRAGON for example the ^{17}O(α,γ)^{21}Ne or ^{12}C(α,γ)^{16}O reactions [MBH06]. The code has been adapted in this work in order to determine the overall acceptance of the ^{3}He(α,γ)^{7}Be reaction.

4.2 Input Parameters for the Code

To estimate the acceptance of DRAGON for a given reaction, the experimental conditions must be recreated as closely as possible in the simulations. In contrast to the previous reactions studied, the recoil cone angle of our reaction is beyond the geometrical acceptance of the separator, thus all input parameters can play a determining role in the transmission of the recoils through the separator. The following subsections describe the realistic input parameters used in the simulations.

4.2.1 The gas target

As the gas target is kept in a windowless cell differentially pumped, it is important to include accurate knowledge of the density profile as this will determine the probability for the ^{7}Be production and their acceptance by the separator. The target density profile was studied using the ^{3}He(^{12}C,^{14}Nγ)p reaction, and the details and results are explained in section 3.3.3.4. As whatever volume defined with GEANT 3 can only be filled with one material, i.e. gas with a constant pressure and temperature, the target density profile (TDP) function shown in Figure 3.52 must be adapted to our defined GEANT volumes.

Figure 4.2 is a detail of the target area as simulated with the GEANT 3-DRAGON package. It shows the volumes with different colours for the target cell where most of the gas is contained, and for the pumping tubes where there could be residual gas. The target cell, target box, downstream aperture and

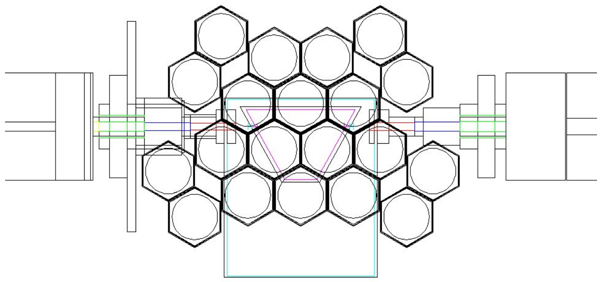

(a)

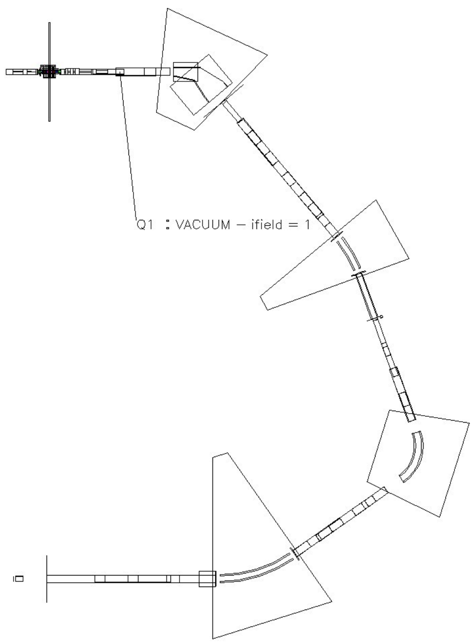

(b)

Figure 4.1: *Two geometrical areas from the GEANT 3-DRAGON simulation. (a)Target side with the target box, target cell pumping tubes and BGO detectors and (b) separator.*

pumping tubes are labelled, followed by the materials which they are filled in (e.g. *"CELG: Gas target"*, where the volume "CELG" refers to the target cell which is filled with a material called "Gas Target"). Some volumes, like the cell apertures have been split into two pieces (XAPG and XAP2) in order to let two different materials to be used.

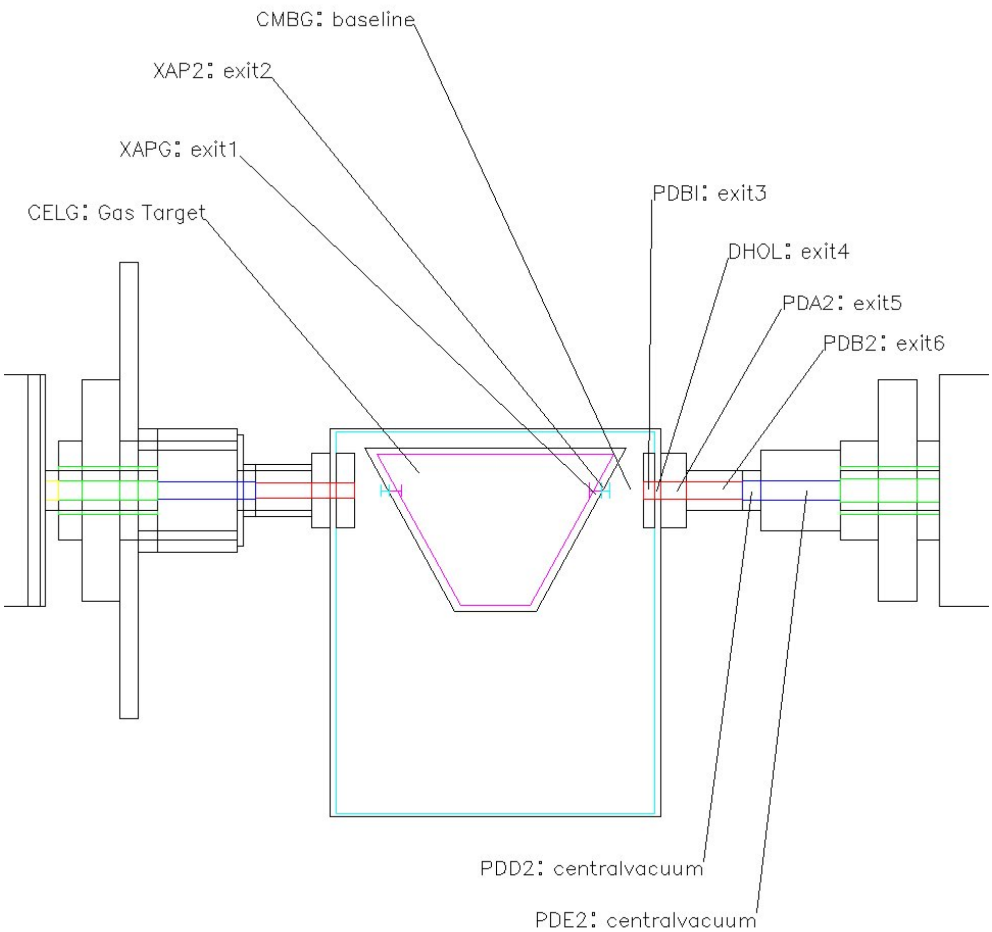

Figure 4.2: *Some of the target volumes defined in GEANT 3-DRAGON. The target box (CMBG), target cell (CELG), exiting aperture (XAPG,XAP2) and downstream pumping tubes (PDI,DHOL,PDA2,PDB2,PDD2,PDE2) are marked. The volume names are followed with their defined materials.*

A central ^{4}He gas target material for the target cell is defined for every energy using the experimental gas target pressures and temperatures shown in Table 5.7. This material is named as "Gas target". The other materials are defined with a fraction of the density of the "Gas Target". In order to determine this fraction, the measured TDP has been fitted to a step-function as shown in Figure 4.3. The density of a given material is obtained by multiplying the "Gas Target" density by the coefficient (Coeff) from the fit.

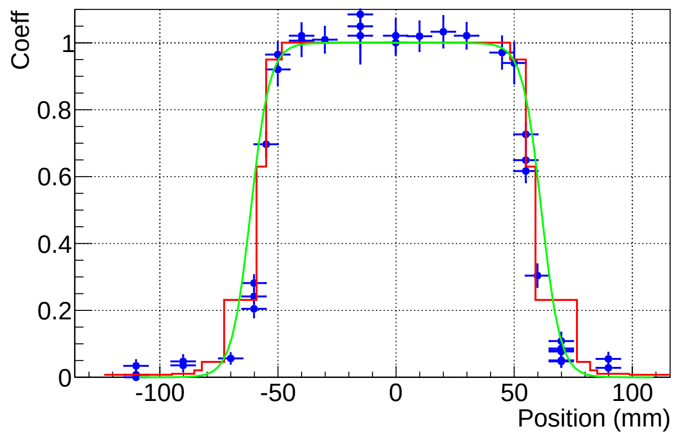

Figure 4.3: *Same TDP as the one shown in Figure 3.52 where a step function in red is included. Every step represents a different volume in GEANT as defined in Figure 4.2. The corresponding coefficient (Coeff) shows the density ratio with respect to the "Gas Target" material in the cell.*

Changes in the step function and its influence on the acceptance will be studied in section 4.5 in order to determine the uncertainty associated to the transmissions.

4.2.2 The beam energy

The ^{4}He mean beam energies (Table 3.5) are given as input parameters to the programme. The programme creates a Gaussian distribution with the given mean value and with a FWHM of 0.1% according to ISAC-I specifications. For each event, the beam energy is then randomly selected from the distribution and the corresponding momentum vector is calculated. Figure 4.4 shows an example of 10^5 simulated particles with 3521.6 keV mean beam energy.

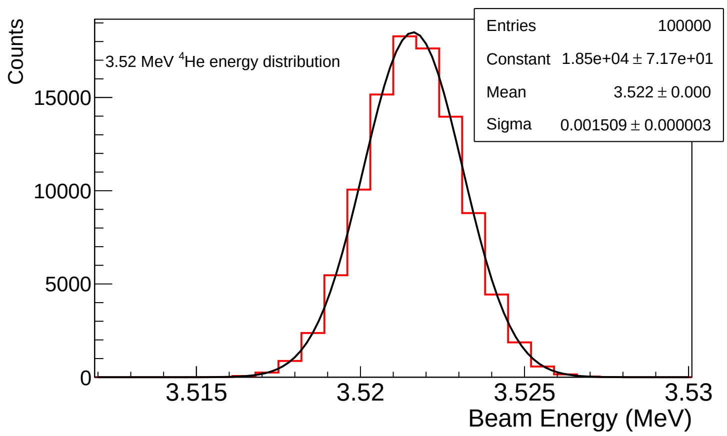

Figure 4.4: *Simulated energy distribution for 10^5 ^{4}He beam particles at the mean energy of 3521.6 keV. The black curve represents a Gaussian fit whose parameters are given in the box.*

4.2.3 The beam spot size and divergence

It is necessary to take into account the finite spot size and divergence of the beam as these will have influence on the separator acceptance. The simulated beam spot size is based on the experimental transmissions of the beam through the gas target. The beam transmissions are calculated for the runs of each energy as the ratio of the FC1 and FC4 readings and a mean value is calculated by averaging those values.

Due to the beam spot that enters the cell has a Gaussian profile in both x and y directions, the experimental beam transmissions represents the volume of the two Gaussians cut off at the 6 mm diameter entrance aperture compared to the full Gaussians integrated over x and y to infinity. This gives us the widths $\sigma_{x/y}$ of both X and Y Gaussian distributions, i.e. the beam spot size. Then, the emittance in the angular direction can be determined from the ISAC equations and so the beam divergence. According to ISAC-I specifications the normalised emittance for 2 rms is 0.2 μm thus:

$$\text{Emittance} = \frac{0.2}{\beta\gamma} \tag{4.1}$$

$$2\Delta\theta_{x/y} = \frac{\text{Emittance}}{2\sigma_{x/y}} \tag{4.2}$$

where $\beta = \frac{\mathrm{v}}{c}$, $\gamma = \frac{1}{\sqrt{1-\frac{\mathrm{v}^2}{c^2}}}$ and $\Delta\theta_{x/y}$ is the divergence Gaussian width in the X/Y axes. Table 4.1 shows the experimental transmissions, $\sigma_{x/y}$ and $\Delta\theta_{x/y}$ for the four experimental beam energies.

$\sim E_{^4\mathrm{He}}$ (MeV)	Transmission (%)	$\sigma_{x/y}$ (mm)	$\Delta\theta_{x/y}$ (mrad)
6.5	89.30±1.68	1.41868(*)	0.562
5.2	96.97±1.29	1.13444	0.836
4.7	94.09±1.51	1.26132	0.783
3.5	93.91±2.95	1.26807	0.911

Table 4.1: *Beam characteristics for the four beam energies studied. The experimental transmissions for the ^{4}He beam are shown in the second column. From the transmissions, the beam standard deviations in the X and Y directions are estimated and are shown in the third column. The standard deviations of the divergence beam distributions are shown in the fourth column.*
(*)The real value considered in the simulations is 1.50 mm as it reproduces more fairly the 89.30% experimental transmission.

In GEANT, the $\sigma_{x/y}$ values are introduced in the input files, the programme determines the $\Delta\theta_{x/y}$ divergence standard deviations from the nominal mean beam energies and ISAC equations. For each event GEANT selects randomly the offset in the X and Y direction from the Gaussian distributions of standard deviation $\sigma_{x/y}$ and the divergence from the Gaussian distributions of $\Delta\theta_{x/y}$ standard deviations. Figure 4.5 shows an example of the simulated beam spot and X-divergence for the 3.522 MeV beam energy.

Changes in the beam spot and divergence due to the errors in the transmissions will also be studied in section 4.5.

4.2.4 The reaction probability and reaction location

For a given energy, another parameter that determines the transmission of DRAGON is the reaction point, in other words, where the reaction occurs in the gas target. In our beam energy range, even

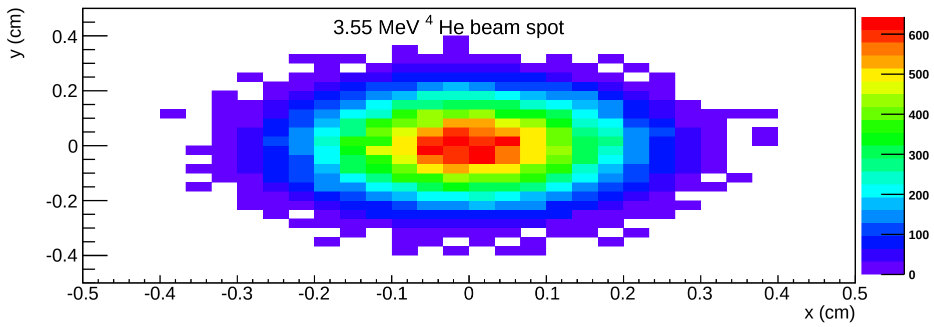

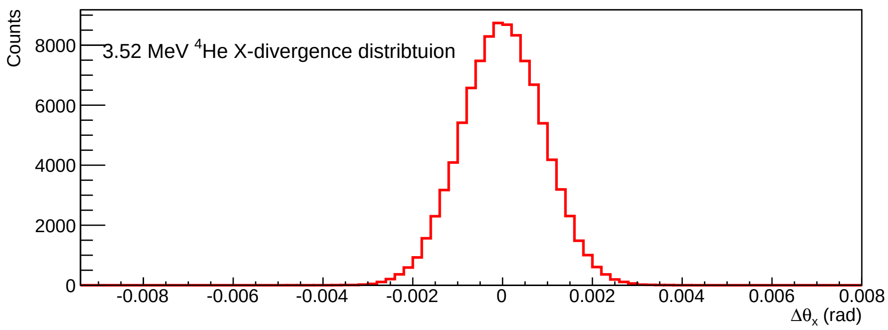

Figure 4.5: *Simulated 10^5 ^{4}He beam particles at ∼3.52 MeV. (a) shows the beam spot and (b) the X-divergence of the beam.*

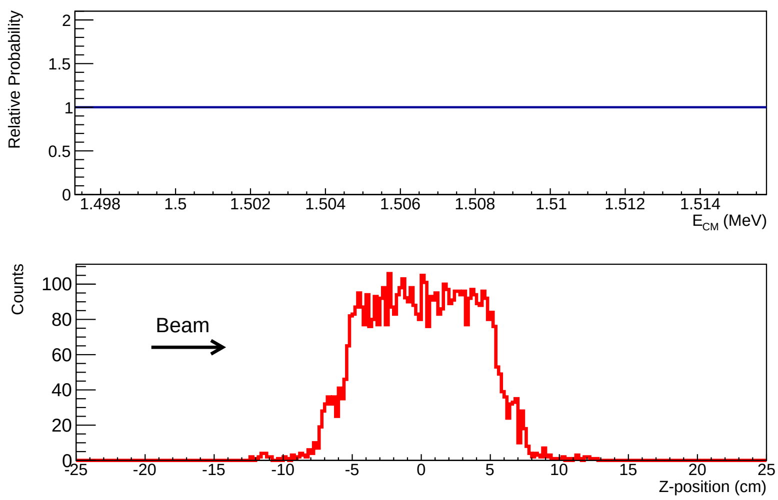

Figure 4.6: *Reaction probability for 10^5 beam particles for the case of E_{CM} ∼1.5 MeV (beam energy ∼3.5). (a) shows the relative reaction probability ≡ 1 for the E_{CM} across the target length. For each event, GEANT code selects a random "goal-energy" from this distribution (same probability for the different energies). In case that the centre of mass energy at any point equals the random energy the reaction will occur. (b) shows where the 55383 reactions are produced throughout the gas target being z=0 cm placed at the centre of the cell.*

after including the energy loss in the target (<20 keV), no resonances are present and thus the cross section can be assumed to be constant. For example, a relative distribution shown in Figure 4.6 (top) is assumed for σ_{34}(E) for the case of ∼3.5 MeV beam energy (corresponding to E_{CM} ∼1.5 MeV). GEANT uses this input function as a probability distribution between the outcoming and incoming centre of mass energy region. For each event, a "goal-energy" is randomly selected from the distribution. If during the beam tracking the centre of mass energy at any point is equal to the random "goal-energy" the reaction will be triggered and the ^{7}Be recoil will be created. Clearly, the probability for the ^{7}Be production depends only on the target density profile, therefore as shown in Figure 4.6 (bottom) the production profile of ^{7}Be recoils follows the TDP.

4.2.5 The S_1/S_0 branching ratio and the γ-rays angular distribution

The ^{7}Be recoil angle and the prompt γ-ray emission angle depend on each other in the capture reaction. Moreover two different capture γ-rays corresponding to the decay to the ground state (γ_0) or the first excited state (γ_1) are present. For the latter, a 429 keV γ-ray is subsequently emanated from the de-excitation of the first excited state to the ground state in ^{7}Be. Therefore assumptions related to prompt γ-ray angular distributions as well as to the ratio between the population of the first excited and ground state (S_1/S_0) must be made.

As initial first order approximation, the values for (S_1/S_0) has been determined from a linear extrapolation of Figure 4.7 taken from reference [CD08], while changes in this ratio will be studied in the section 4.5. For each reaction GEANT will create a prompt γ_1 or γ_0 rays and the corresponding ^{7}Be state with relative ratios (S_1/S_0) shown in Table 4.2.

Concerning the angular γ-ray distributions, isotropic angular distributions for both γ_0 and γ_1 rays are assumed based on the results in reference [DGK09]. In GEANT 3-DRAGON code this is done by introducing a uniform distribution for the values of cos(Θ), where Θ is the centre of mass polar angle in the spherical coordinate system. The 429 keV γ-ray distribution is always isotropic as it comes from a J=1/2 state.

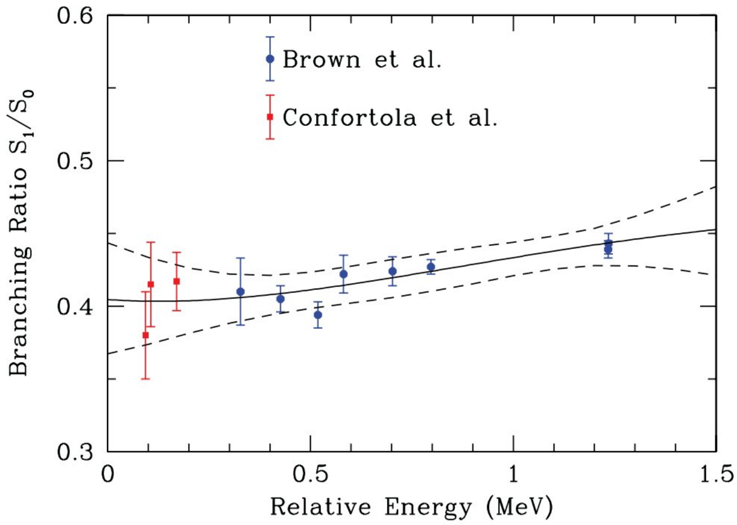

Figure 4.7: *The S_1/S_0 branching ratio. A fit to the data (solid line) of [BBS07, CBC07] as calculated by Cyburt and Davids [CD08]. For the simulations, a linear extrapolation of the fit up to 2.8 MeV centre of mass energy has been considered in order to determine the S_1/S_0 branching ratio.*

$\sim E_{^4He}$ (MeV)	E_{CM} (MeV)	S_1/S_0
6.5	2.81	0.5077
5.2	5.16	0.4829
4.7	2.02	0.4755
3.5	1.51 1	0.4545

Table 4.2: *The S_1/S_0 branching ratios considered in the simulations.*

4.2.6 The separator settings

The most determining parameters for the DRAGON acceptance are the separator settings. Therefore the electrostatic and magnetic fields used for the simulations play a key role.

As already explained, the experimental procedure consists of tuning the separator for the optimal transmission of the beam through the gas target and centre the beam throughout the different elements of the separator. The separator is then rescaled to the charge and mass of the recoils. This procedure is essential as the low recoil yield does not allow to adjust the separator settings in order to optimise recoil transmissions. An important issue to be considered here is that the potential energy loss differences between the beam and the recoils in the gas target are not taken into account by the rescaling programme automatically. This will have some influence on the mean accepted recoil energy ($\overline{\mathrm{E}}$) and thus on the overall acceptance. Indeed, during the 2011 run the separator was automatically tuned to the recoils following the usual procedure. Clearly this was not optimal. In the 2013 experiment an improvement was made by tuning the separator manually to obtain optimal transmission for the energy of the recoils created at the centre of the target taking into account the energy losses before exiting the target.

In GEANT simulations, the settings of the separator are usually adjusted based on parameters of the reaction. The code determines the scaling values of the magnetic and electric fields from the kinetic energy and momentum of the recoils created at the centre of the target after crossing half of the target length , eventually obtaining the optimal settings for the separator. Nevertheless, in order to guarantee the consistency between the experimental and GEANT settings, the tuning energies in GEANT have been manually set to those corresponding to the experimental ones. Table 4.3 gives the experimental tuning energies (column three) used in the simulations, that correspond to the MD1 magnetic fields during the experiment (Table 3.5). The fourth column shows the calculated mean energies at the exit of the gas target of the recoils that are created at the centre. The fifth column shows the relative difference between them.

Run	$\sim$E$_{^4\mathrm{He}}$ (MeV)	$\mathrm{E}^{\mathrm{simu}}_{^7\mathrm{Be}}$ (keV)	$\overline{\mathrm{E}}^{\mathrm{calcu}}_{^7\mathrm{Be}}$ (keV)	Relative Difference $\frac{\lvert E^{\mathrm{simu}}_{^7\mathrm{Be}} - \overline{\mathrm{E}}^{\mathrm{calcu}}_{^7\mathrm{Be}}\rvert}{\overline{\mathrm{E}}^{\mathrm{calcu}}_{^7\mathrm{Be}}}$ (%)
2011	6.5	3734.51	3696.02	1.04
	5.2	2940.21	2898.33	1.44
	3.5	1997.32	1955.01	2.16
2013	4.7	2642.67	2647.71	0.20

Table 4.3: *The third column shows the experimental ^{7}Be energies used in the simulations for the tuning conditions. Whilst the MD1 values during the 2011 campaign were automatically determined by the programme by scaling the settings for the beam, for the 2013 measurements the MD1 value was set manually for the energy corresponding to the recoils created at the centre of the target. The fourth column shows the calculated energies for the exiting recoils created in the centre of the gas target, and the fifth column shows the relative difference between the two energies.*

As it can be observed for the 2011 measurements, when the separator was tuned automatically to "recoils mode", the relative differences between the real tuning energies, $\mathrm{E}^{\mathrm{simu}}_{^7\mathrm{Be}}$, and the optimum energies, $\overline{\mathrm{E}}^{\mathrm{calcu}}_{^7\mathrm{Be}}$, which would maximise the transmissions of the recoils created at the centre, are relatively high. For the 2013 measurement, the separator was tuned manually and therefore, the relative energy difference for this case is remarkably smaller compared to the measurements in 2011, maximising the transmission of the recoils created in the centre of the gas target.

Looking at the relative differences among the 2011 energies in Table 4.3, the trend is consistent with the stopping power of a ^{7}Be nucleus crossing a ^{3}He gas target. Figure 4.8 shows the stopping power of ^{7}Be ions crossing a ^{3}He gas target calculated using the SRIM code[SRI]. One can observe that in the range of interest, i.e. $\sim$2000 - $\sim$3700 keV for the ^{7}Be recoils, the higher the energy is the lower is the amount of energy loss. Therefore, for the highest energy case the relative difference between the mean energy and the automatically tuned energy must be lower as seen in Table 4.3.

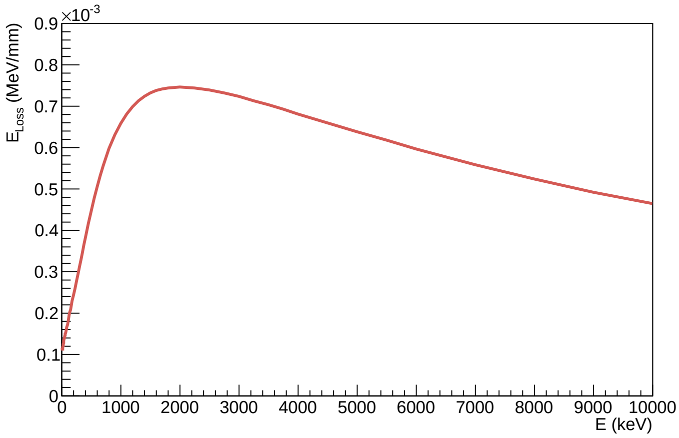

Figure 4.8: *Stopping power for ^{7}Be recoils crossing a 9.327·10^{-7} g/cm^3 density ^{3}He gas target.*

4.3 First Simulations and Analysis

Taking into account the conditions and parameters defined above, the recoil transmissions through the separator for each energy are calculated as the ratio between the recoils reaching the end detector and the total recoils created in the gas target. From now on, unless otherwise specified, the simulations will be carried out assuming 10^5 beam particles.

Figure 4.9 shows some output spectra from the first series of simulations with the given input parameters. In the left column the kinematic curves representing the output recoil angle after emitting the γ-ray versus the kinetic energy are shown. In blue we can see the recoils reaching the DSSSD and in green those lost throughout the separator, i.e. not reaching the focal plane. The second and third column show the projections of the previous spectra where, in red, one can see the total recoils created, in blue the detected ones, and in green those stopped before reaching the DSSSD. As it can be observed the acceptance-dependence is stronger on the recoil energy compared to the angle (e.g. for the highest energy, the second column shows the different energy between detected recoils (blue) and not-detected (green), while this effect in not seen for the angles shown in the third column).

In the second column, it can be seen that, for the first three histograms corresponding to beam energies of 6.5, 5.2, and 3.5 MeV of 2011 measurements, the recoils created with the higher energies are more likely to be detected. These correspond mostly with those recoils created at the end of the gas target according to Figure 4.10, which represent the positions where the recoils are created. This is in concordance with the fact that during the 2011 run the separator was tuned automatically from the beam tuning without taking into account the different energy losses between recoils and beam particles. For the last case, 4.7 MeV energy, the separator was tuned manually setting the magnetic field to the exiting energy of the recoils created at the centre of the gas target and as can be observed the detected histogram is more symmetric on the detected energy.

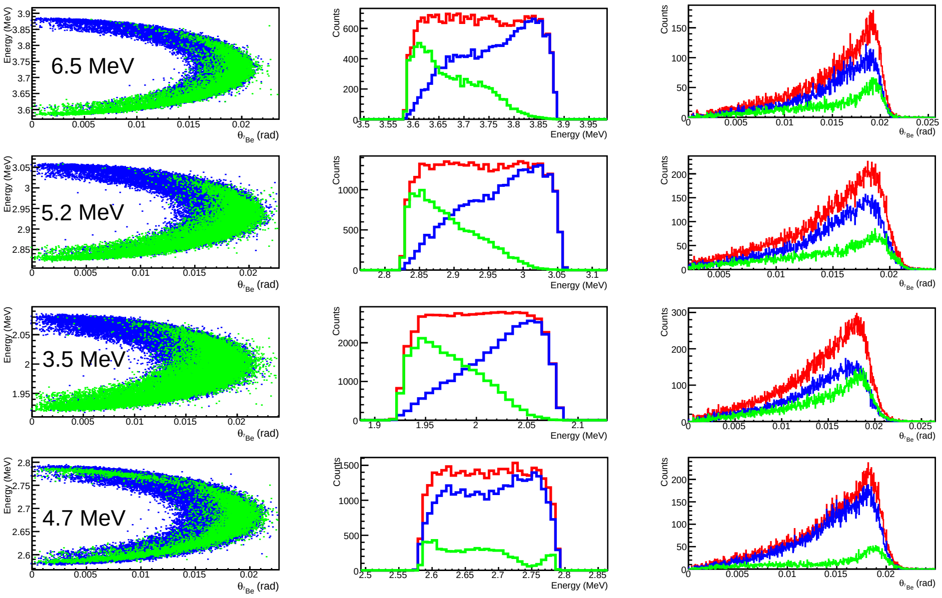

Figure 4.9: *Outputs for 10^5 beam particles simulated at the different beam energies. The left column shows the kinematic curves and the middle and right columns show the projections for the recoil energy and the output recoil angle. In red, all recoils created for each energy are shown, in blue, those reaching the end detector and in green, those stopped throughout the separator. As it can be seen from the second and third columns, when the separator is optimised for the recoils created at the centre of the gas target (last row), the acceptance is optimal and the area under the green curve corresponding to the recoils stopped within the separator is minimal.*

The first results for the acceptance at the different beam energies are shown in Table 4.4.

Run	$E_{^4He}$ (keV)	^{7}Be recoils created	^{7}Be recoils detected	Transmission (%)
2011	6553.88	26365	17617	66.8±0.6
	5165.97	39790	26374	66.3±0.5
	3521.61	55535	32282	58.1±0.4
2013	4716.45	38842	31863	82.0±0.6

Table 4.4: *DRAGON transmission for the ^{3}He(α,γ)^{7}Be reaction. Only statistical errors are shown here.*

Specific knowledge of the DRAGON's transmission efficiency for the ^{3}He(α,γ)^{7}Be is gained by examining where in the separator the recoils are stopped. The location of different components where recoils stop are labelled in the schematic DRAGON layout shown in Figure 4.11, and Figure 4.12 shows the fraction of the recoils stopped by the given components. It can be clearly seen that the majority of the recoils are stopped at the charge slits for all energy cases, being the relative percentage small for the 4.7 MeV (2013 experiment with manually separator tuning), in agreement with the effect discussed above.

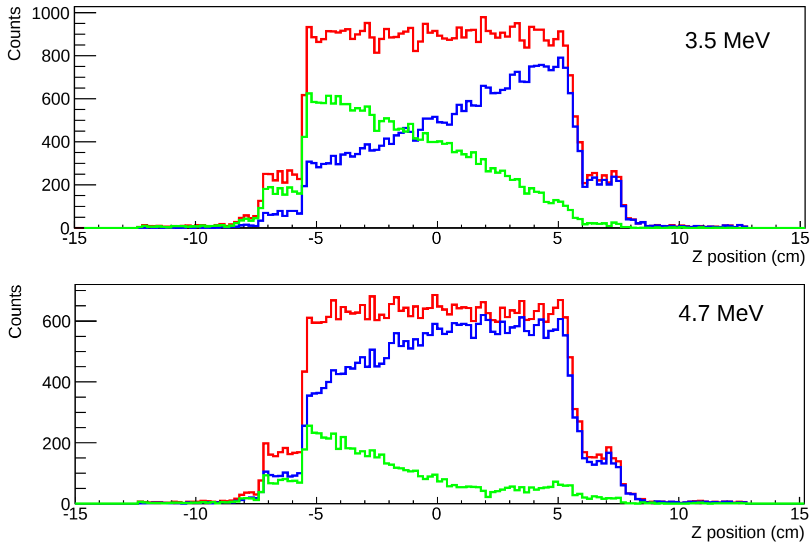

Figure 4.10: *Positions of the recoils created in the gas target. The colours have the same meaning than Figure 4.9. The top panel shows the ∼3.5 MeV beam energy case and the bottom panel the ∼4.7 MeV.*

Figure 4.11: *Layout of DRAGON. The red labels point at different components where the recoils are stopped*

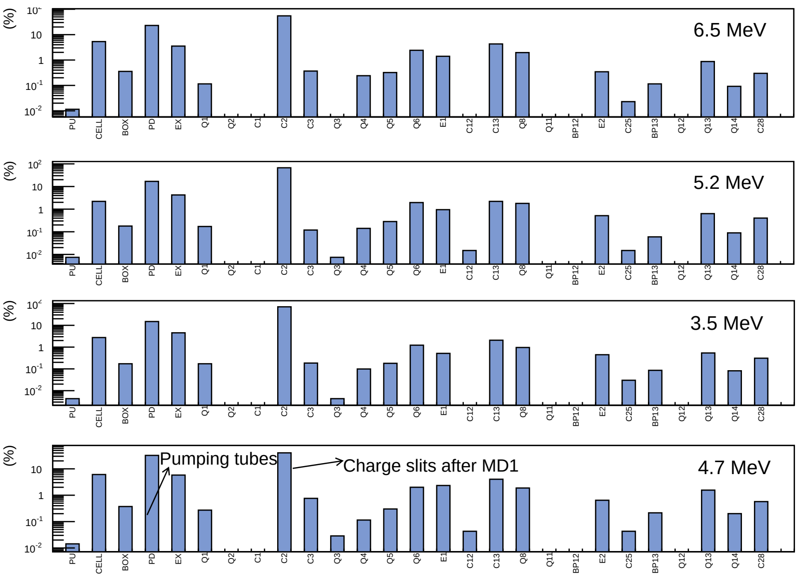

Figure 4.12: *Percentage of the recoils stopped in the different volumes throughout the separator. PU refers to the pumping tubes upstream the target box, PD refers to the first pumping tubes downstream the target cell (up to ∼15 cm) and EX indicates the different tubes up to the first quadrupole (from 15 to ∼85 cm). The other volumes are labeled in Figure 4.11.*

4.3.1 Tests on the DRAGON recoil energy selection procedure

The transmissions shown in Table 4.4 are much lower than the originally predicted, specifically for the 2011 runs. This should be in line with the discussion about the tuning energies. In order to further examine the effect of the automatic settings for the 2011 runs, 20000 beam particles have been simulated using as tuning energy the corresponding to the recoils created at the centre of the target cell. The results, displayed in Table 4.5, show a big improvement in the transmission when the mean ^{7}Be energy is used to tune the separator.

Run	$E_{^4He}$	$E^{simu}_{^7Be}$	$\overline{E}^{calcu}_{^7Be}$	Transmission	Relative Difference
	MeV	keV	keV	%	%
	∼6.5	3696.02	3696.02	78.9±1.6	18.1
2011	∼5.2	2898.33	2898.33	81.1±1.3	22.3
	∼3.5	1955.01	1955.01	75.7±1.6	30.3

Table 4.5: *Simulated transmissions for the tuning energies matching the mean exiting recoil energy. The relative differences respect to the results in Table 4.4 are also shown in the last column.*

This proves that the differences in the ^{7}Be recoil energy due to the energy loss in the target plays an important role in the transmissions of the recoils throughout the separator for the ^{3}He(α,γ)^{7}Be reaction. The last column in Table 4.5 shows the relative transmission differences comparing to those shown in Table 4.4 for the automatically separator tuning. As expected, for the highest energy the difference is less significant because the energy losses are smaller.

At this stage, I would like to reiterate the fact that DRAGON should be tuned to the recoils created at the centre of the target, which was also concluded in Figure 4.9. The corresponding kinematics curves, displayed in Figure 4.13(a), do not show the previous asymmetries in the energy acceptance and even for the highest energy the percentage of recoils stopped in charge slits shown in Figure 4.13(b) are not dominant anymore. Therefore, it is evident again that the limiting factor in determining the transmission is the kinetic energy of the recoils.

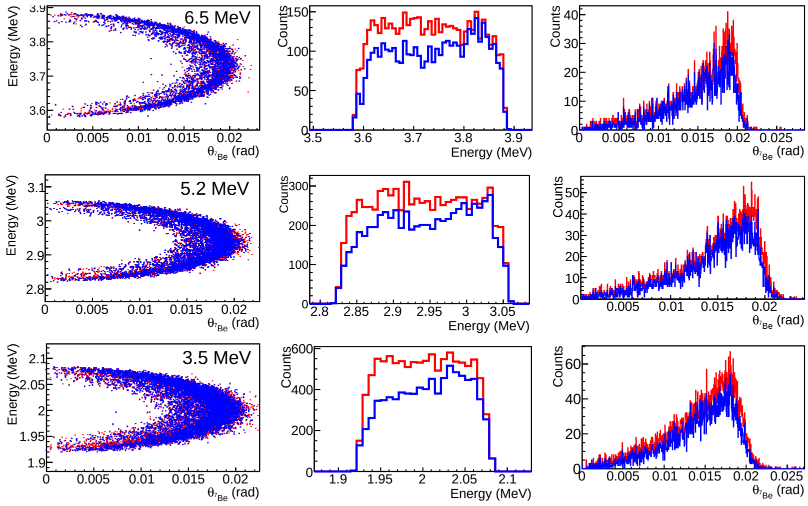

(a)

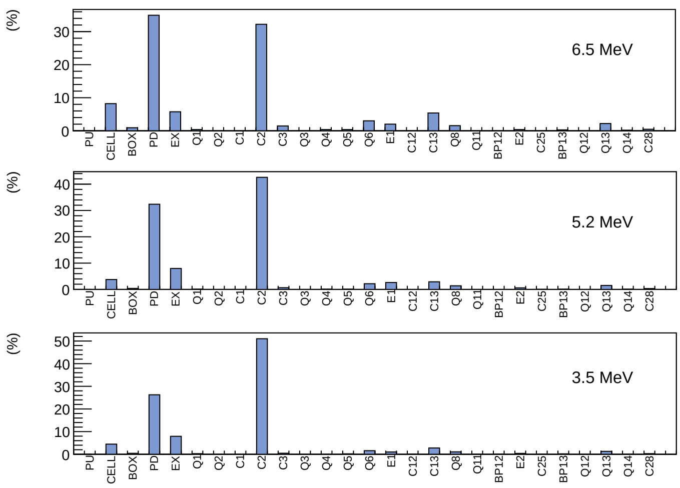

(b)

Figure 4.13: *Simulation outputs when the tuned separator energy is set to the mean exiting recoil energy. (a) shows the kinematic curves and projections. Red colour shows the recoils created and blue colour shows the detected ones; (b) shows the percentage recoils stopped in the different volumes.*

4.4 Final Simulations using the Measured Tubes Displacements

As it can be observed from the previous plots (e.g. Figure 4.12) some of the recoils are stopped in the exiting pumping tubes before the first magnetic quadrupole Q1 (z=85 cm). For this reason a careful determination of a likely displacement of the tubes was done using a theodolite [Vuj14]. Some displacements were observed in both vertical and horizontal direction at different positions as shown in Figure 4.14.

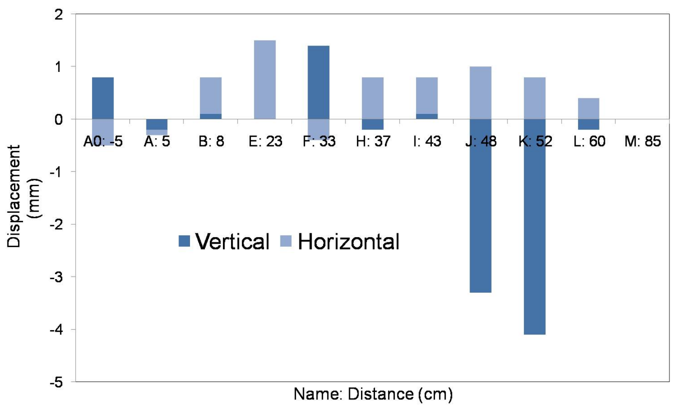

Figure 4.14: *Horizontal and vertical DRAGON tubes displacements measured using a theodolite. Each pumping tube is labelled with a letter in order to be identified, followed by the end distance of the tube in cm.*

The displacements have been introduced in the code in order to extract the correct values for transmissions. It should be pointed out that the two first displacements corresponding to the entrance and exit cell apertures (at -5 and 5 cm of the centre of the target, respectively) were a consequence of the setup for the 2013 experiment so these two are added only to the 4.7 MeV simulation. A new series of simulations were performed for each energy with the new geometry including the displacements of the tubes. The other parameters such as γ-ray angular distributions or tuning energies are the same as the original values. Table 4.6 shows the results of the transmissions in the fifth column while the sixth column displays the relative differences when comparing with transmissions shown in Table 4.4.

Run	$\sim E_{^4He}$ (MeV)	^{7}Be recoils created	^{7}Be recoils detected	Transmission (%)	Relative Difference (%)
2011	6.5	25931	14873	**57.4±0.6**	14.1±1.2
	5.2	39694	22907	**57.7±0.5**	12.9±1.0
	3.5	55383	28392	**51.3±0.3**	11.8±0.9
2013	4.7	38554	27627	**71.7±0.6**	12.6±0.9

Table 4.6: *DRAGON transmissions after considering the displacements of the pumping tubes shown in Figure 4.14. The last column shows the relative differences respect to the results shown in Table 4.4.*

As it can be seen, the higher the energy, the higher the effect of the displacements; this is in line with the fact that output recoil angles are slowly increasing with energy (see Appendix B for the kinematics of this reaction). Figure 4.15 shows in black the maximum recoil angle for our centre of mass energies whilst the red dots just indicate the trend. Therefore, the effect of the tube displacements will also increase with energy.

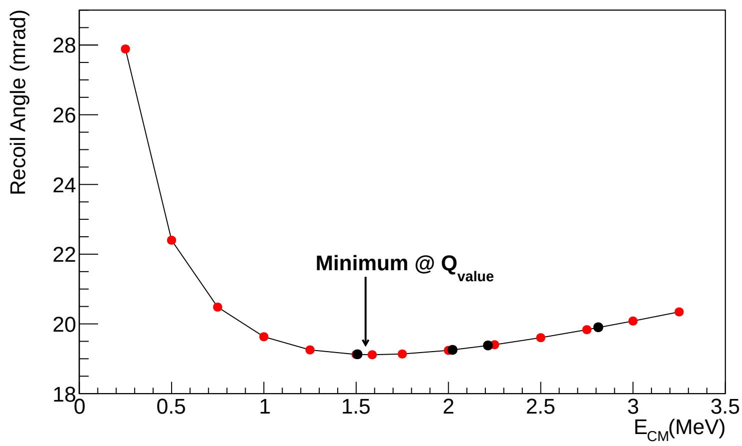

Figure 4.15: *Maximum output recoil angle distribution for different centre of mass energies. In black colour one can see the centre of mass energies corresponding to our beam energies*

The effect of each pumping tube displacement can be observed for example in Figure 4.16. Here, the number of recoils stopped in the different volumes is displayed for the 3.5 MeV energy. The number of stopped recoils before Q1 is increased from 5199 for no displacements (a), to 10420 with displacement (b).

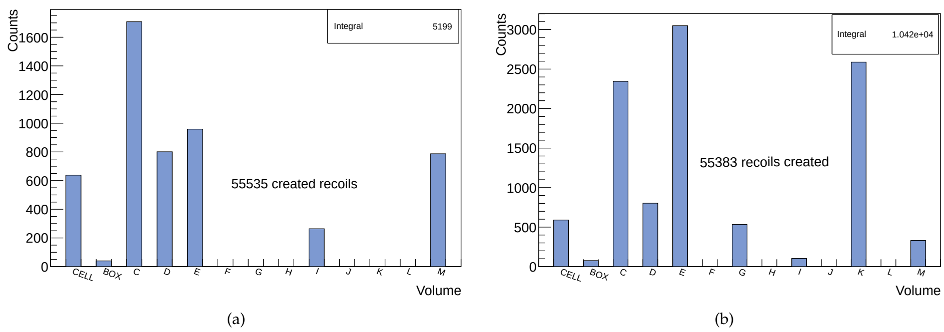

Figure 4.16: *Simulated recoils stopped in the DRAGON pumping tubes at 3.5 MeV beam energy. The volumes are named according to Figure 4.14. (a) with no displacements and (b) with the displacements shown in Figure 4.14*

Clearly, the displacement of the volume labelled as "K", placed just before the first quadrupole Q1, has a crucial effect on the acceptance. As it can be seen the displacement of volumes "E" and "C" are also significant. The new kinematic curves after considering the effect of the tubes displacements are shown in Figure 4.17.

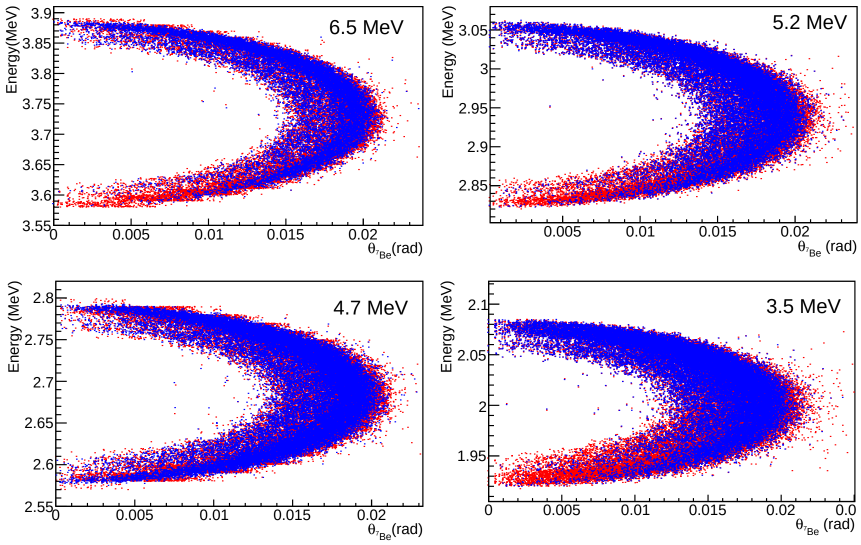

Figure 4.17: *Kinematic curves after introducing the pumping tubes displacements. The red dots show the recoils produced and the blue ones corresponds to those detected in the DSSSD.*

Unless otherwise specified, the transmission values $\epsilon_{\mathrm{DRAGON}}$ shown in Table 4.6 which also include the effect of the displacements in the pumping tubes will be considered as the final transmissions of DRAGON for our reaction.

4.4.1 The DSSSD and the BGO spectra: simulations and data

Here, several tests will be discussed to determine the reliability of the simulations. Figure 4.18 shows a comparison between the simulated (in red) and real (in blue) DSSSD spectra for the ~3.5 MeV and ~5.2 MeV beam energy cases. For the 3.5 MeV case, the tiny differences between the two spectra are due to two effects. Firstly, for the DSSSD calibration a 0.5μm dead layer has been considered to calibrate the detector, however, this is not accurate enough and moreover, the triple alpha energies used to calibrate the detector are not close to this recoil energy. This implies an offset in the calibrated DSSSD energy. Secondly, the real DSSSD resolution is not considered in the simulation, which would increase the width of the simulated recoil peak.

An example comparing the experimental and simulated DSSSD hit-maps is displayed in Figure 4.19, where, in the left column, we see the simulated hit-maps for the ~5.2 and ~3.5 MeV beam energy cases and, on the right side, the corresponding simulated hit-maps. Whereas for the 3.5 MeV case the recoil spots are more or less centre in the DSSSD in both the simulated and experimental hit-maps, for the 5.2 MeV different recoil spot displacements can be observed. In order to account for these differences, the different input parameters are varied and the resulting effects are considered to determine systematic uncertainties in the transmissions shown in Table 4.6.

For the BGO detectors, two examples of the spectra comparing the simulations and experimental data are shown in Figure 4.20. Both, experimental and simulated spectra display the energy of the BGO whose recorded energy for the given event is the maximum among the thirty BGO detectors. Only the events that are in coincidence with recoils measured in the DSSSD have been considered in both experimental and simulated histograms. As it was discussed in Chapter 3, it is not possible to identify the prompt γ-ray peaks in the total single BGO spectra (without coincide with the DSSSD) due to the high background contamination including some beam induced background (see Figure 3.26).

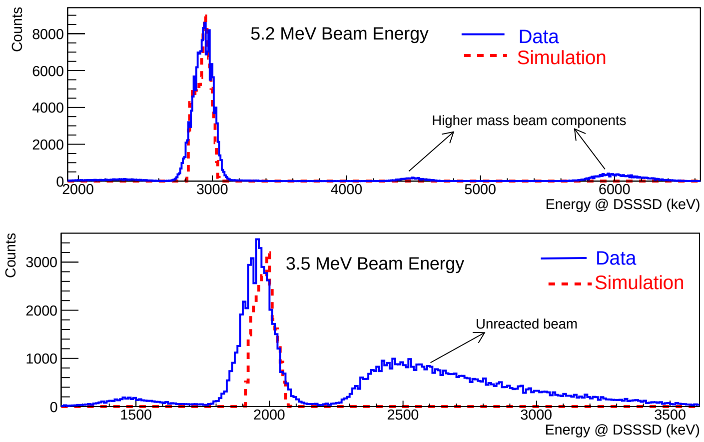

Figure 4.18: *Comparison between the simulated DSSSD spectra (red dash line) with the measurements (in blue) for beam energy of 5.2 MeV (top) and 3.5 MeV (bottom). The highest peaks show the recoiling ^{7}Be nucleus in the DSSSD.*

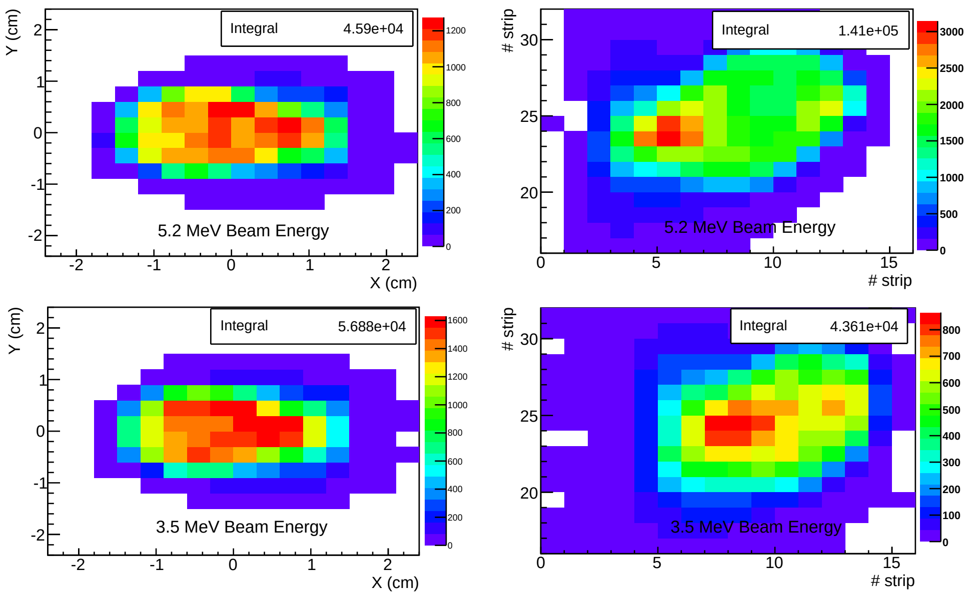

Figure 4.19: *DSSSD hit-maps for beam energies of ∼5.2 MeV and ∼3.5 MeV. For simulations (left) X and Y are shown in cm and from measurements (right) with the X and Y axis indicates the strip number. In order to increase the statistics for the hit-maps in these plots $2{\cdot}10^5$ beam particles were simulated. The apparent difference between simulation and measurements could be due to the lack of an accurate knowledge of all DRAGON parameters or the exact DSSSD position and eventual angle.*

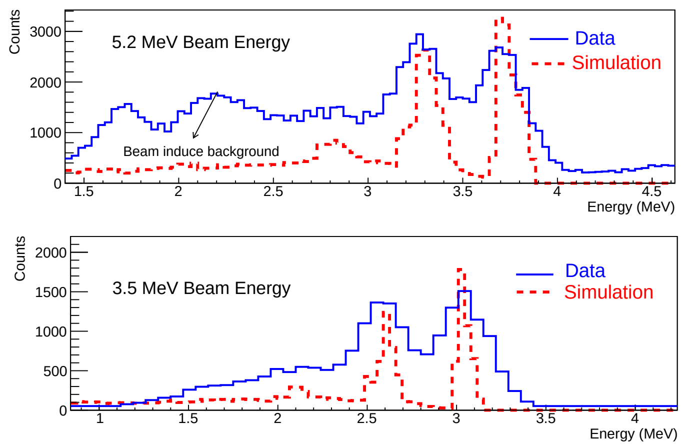

Figure 4.20: *Comparison between the simulated BGO spectra (in red) and the experimental (in blue) in coincide with the ^{7}Be recoils. The two highest energy peaks correspond to the γ-rays from the de-excitation of the capture state to the ground and first excited states. It must be pointed out that for the 5.2 MeV, the real simulated spectrum has been multiplied by four in order to have comparative number of counts in the γ peaks comparing to the experimental one.*

The peak width differs between the simulated and experimental spectra as the proper resolutions of the BGO detectors are not included in the simulations. The relative intensity of the two peaks seems to be different between experimental data and simulations, this is due to the assumed S_1/S_0 ratio in the simulations and further analysis on that will be performed in the following sections.

The BGO hit-maps patterns have been simulated independently for each γ peak that are selected by placing the corresponding coincidence gates in energy (see Figure 4.21 for the 3.5 MeV case).

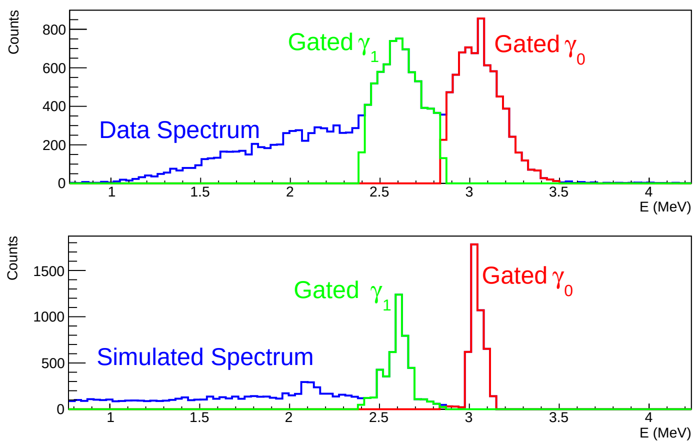

Figure 4.21: *Energy gates performed in the experimental data spectrum (top panel) and the simulated one (bottom panel) for the 3.5 MeV beam energy case.*

Figures 4.22 and 4.23 shows the BGO hit-maps for the γ_0 and γ_1 rays at the different beam energies that are obtained by placing the corresponding energy gates.

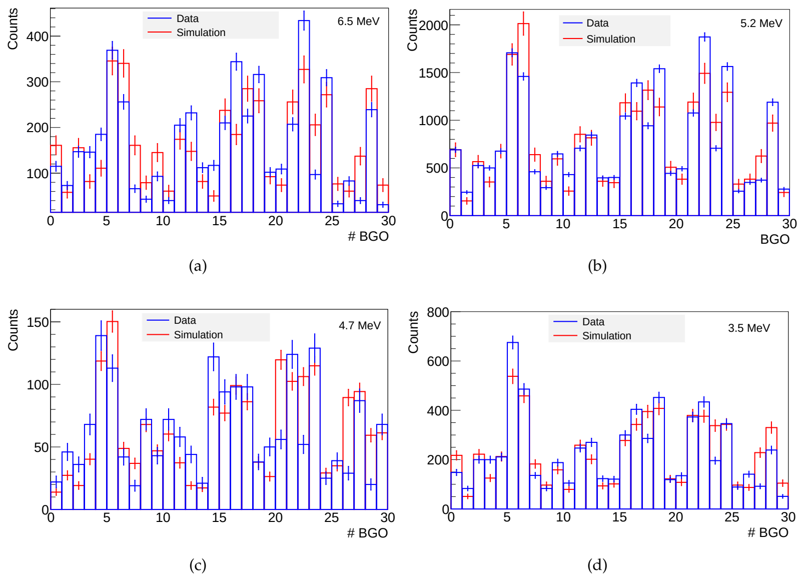

Figure 4.22: *BGO hit-maps corresponding to γ_0. The simulated histograms are normalised to the total number of hits in the experimental data. Each panel is tagged with E^{beam}.*

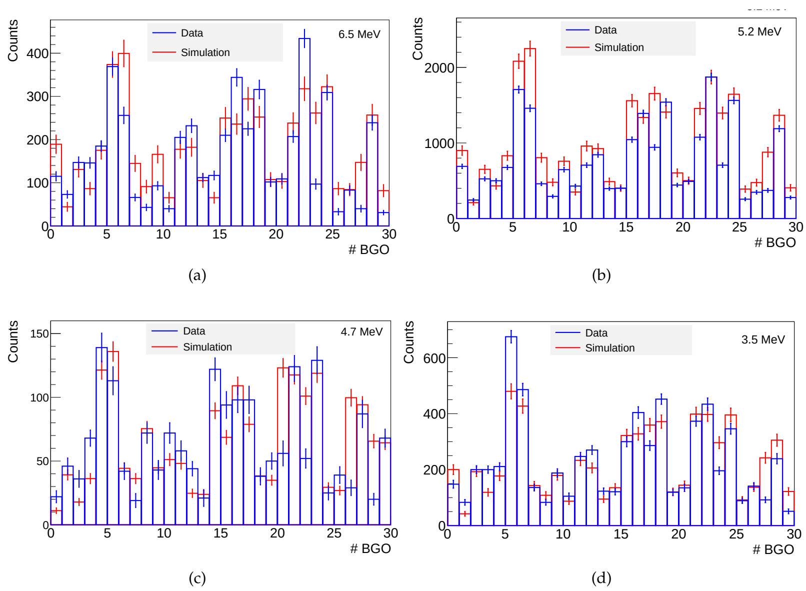

Figure 4.23: *Same as Figure 4.22 but for γ_1.*

Further investigations of the influence of the γ angular distribution assumptions will be made in the following section. In order to quantify the dispersion between simulated and experimental data, I will use $\chi^2_{\nu-1}$ value defined as:

$$\chi^2_{\nu-1} = (\sum_{i=1}^{30} \frac{(N_i^{\text{data}} - N_i^{\text{simu}})^2}{\sigma^2_{N_i^{\text{data}}} + \sigma^2_{N_i^{\text{simu}}}})/29 \tag{4.3}$$

where N_i^{data} and N_i^{simu} are the number of γ-counts in a given BGO detector and $\sigma_{N_i^{\text{data}}}$ and $\sigma_{N_i^{\text{simu}}}$ are the associated errors, respectively. The results are shown in Table 4.7.

$E_{^4\text{He}}$ (MeV)	$\sim$6.5	$\sim$5.2	$\sim$4.7	$\sim$3.5
$\chi^2_{\nu-1}(\gamma_0)$	7.5	5.3	1.1	6.7
$\chi^2_{\nu-1}(\gamma_1)$	8.2	11.1	6.4	5.6

Table 4.7: *$\chi^2_{\nu-1}$ as defined in expression 4.3 for the comparison of the simulated and experimental BGO hit-map.*

4.5 Simulations for Estimating Uncertainties in ϵ_{DRAGON}

In the previous section some discrepancies have been observed when comparing the simulated and the experimental data. Furthermore, differences between the simulated mean recoil energies and those used for setting up the DRAGON separator have been observed. These are originated because the DRAGON programme considers only the change in mass of the nuclei without taking into account the differences in energy loss between beam and recoils. An analysis of the output mean energies shows agreement with those calculated using SRIM, which suggests that the ^{7}Be recoils lose approximately seven times more energy than an alpha particle crossing the same distance for a given energy. Indeed, it has been proved that the transmissions increase notably by considering the mean energies to scale DRAGON. However, the range of mass and energy for the reaction partners is one in which energy loss is poorly described by theory [Ili07].

Therefore, with a better understanding of the results from the original series of simulations, a number of additional tests have been carried out to determine the sensitivity of DRAGON to several parameters. The central values of the transmissions are those shown in Table 4.6 and their sensitivity to the parameters are considered when determining the uncertainties. In the following, only information differing from what already presented will be detailed and it will always be considered that the number of beam particles simulated is 10^5.

4.5.1 Gas target density profile

The density profile of the windowless gas target was determined experimentally using the method explained in section 3.3.3.4. In the simulation, a step function fit of the experimental data was used (Figure 4.3). In order to account for both the uncertainties in the experimental data and those related to the fit, variations in the width and steepness of the profile are considered as possible sources of systematic error in the results of the transmissions.

Effective length of the gas target

In order to estimate the error in the transmission related to the target length, the actual effective target length of 12.3 cm is varied $\sim$ -0.5 cm, according to the red fit in Figure 3.52. The new step function is shown in purple in Figure 4.24.

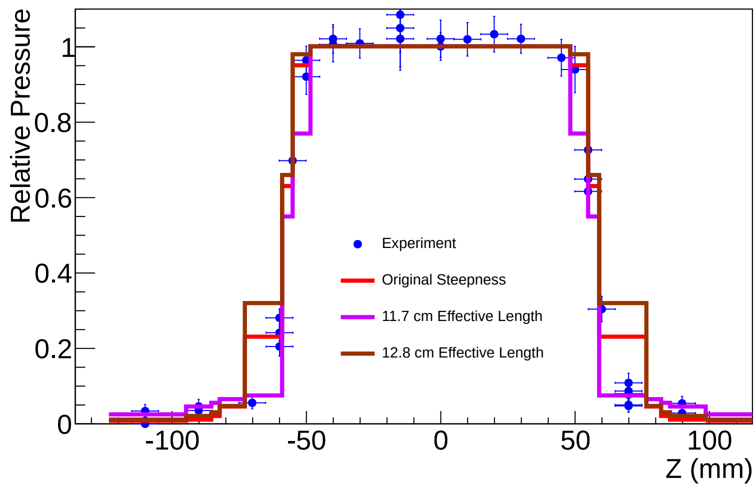

Figure 4.24: *Step target density profiles for the effective lengths of, original 12.3 cm (red) 11.75 cm (purple) and 12.8 cm (brown) compared the experiments (blue dots).*

The results are shown in Table 4.8 where the last column indicates the relative differences comparing with the final transmissions shown in Table 4.6.

Run	$E_{^4He}$ (MeV)	^{7}Be recoils created	^{7}Be recoils detected	Transmission (%)	Relative Difference (%)
2011	∼6.5	25383	14624	57.6±0.6	+0.45±1.47
	∼5.2	38825	22710	58.5±0.5	+1.36±1.19
	∼3.5	54010	28191	52.2±0.4	+1.82±1.05
2013	∼4.7	36921	26625	72.1±0.6	+0.64±1.13

Table 4.8: *DRAGON transmissions when the target effective length is 11.75 cm (see Figure 4.24). The last column displays the relative differences between the transmissions obtained here and those shown in Table 4.6.*

As observed, reducing the effective length of the gas target does not have a large effect on the transmission. As expected, the maximum relative difference is for the the lowest energy because the energy losses (i.e. the gas quantities) play a more determining role for lower energies.

Even though the effect of considering a change in the effective length does not play a very influential role, the opposite case in which the width of the profile is increased must be investigated. The corresponding step function is shown in brown in Figure 4.24 and the resulting transmissions are displayed in Table 4.9.

Run	$E_{^4He}$ (MeV)	^{7}Be recoils created	^{7}Be recoils detected	Transmission (%)	Relative Difference (%)
	∼6.5	14784	26691	55.4±0.6	-3.43±1.15
2011	∼5.2	23532	41397	56.8±0.5	-1.50±0.89
	∼3.5	28745	56660	50.7±0.4	-1.04±0.77
2013	∼4.7	27945	39466	70.8±0.6	-1.19±0.89

Table 4.9: *DRAGON transmissions when the effective length is 12.8 cm (see Figure 4.24). TheThe last column displays the relative differences between the transmissions obtained here and those shown in Table 4.6.*

In this case, for the three lowest energies the relative differences are similar to the ones obtained in Table 4.8 for the 11.7 cm effective length. However, a significant relative difference is observed for the highest energy. A possible explanation could be related to highest influence of the tube displacements for the higher energy (see Table 4.6).

Steepness of the gas profile

Although from the previous analysis it is not expected a high effect from changing slightly the target density profile, it is necessary to examine the effect of modifying the steepness of the step function by considering that the pressure decrease more rapidly and thus the pressure is higher in the extremes. The new step function is displayed in purple in Figure 4.25 where it can be observed that in the two first steps out of the centre (cell apertures) the pressure decrease more rapidly than in the original one (red).

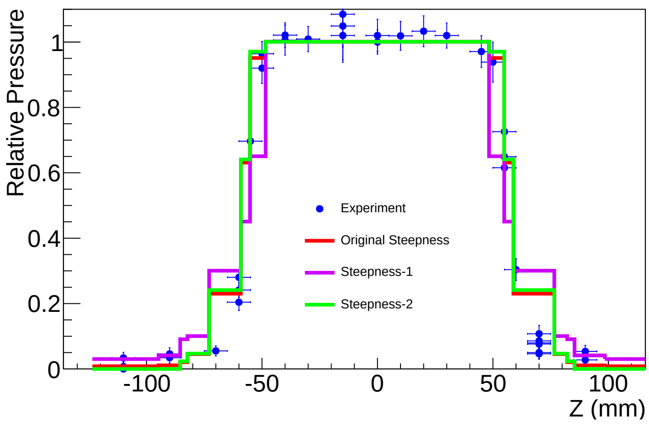

Figure 4.25: *New step functions in purple (and green) where the pressure decreases (increases) more rapidly than in the original one (red).*

The transmissions obtained with the modified step function are displayed in Table 4.10. As expected, the relative differences are negative because the proportion of the gas further upstream is higher and as expected from Figure 4.10 the recoils created further upstream are more likely to be stopped. The relative differences are similar to those obtained by changing the effective target length in Table 4.9.

Run	$E_{^4He}$ (MeV)	^{7}Be recoils created	^{7}Be recoils detected	Transmission (%)	Relative Difference (%)
2011	∼6.5	26575	14758	55.5±0.6	-3.18±1.15
	∼5.2	40612	23092	56.9±0.5	-1.47±0.90
	∼3.5	56766	28561	50.3±0.4	-1.86±0.76
2013	∼4.7	39263	27914	71.1±0.6	-0.79 ±0.89

Table 4.10: *DRAGON transmissions when the profile step function is changed to this in purple in Figure 4.24. The last column displays the relative differences in the transmission values between the results here and those shown in Table 4.6.*

The same study has been made considering that the pressures decreases more smoothly in the cell apertures. The step function is shown in green in Figure 4.25 and the corresponding transmissions are given in the Table 4.11. The relative differences are also smaller due to the lower proportion of gas downstream.

Run	$E_{^4He}$ (MeV)	^{7}Be recoils created	^{7}Be recoils detected	Transmission (%)	Relative Difference (%)
2011	∼6.5	14687	26184	56.1±0.6	-2.20±1.17
	∼5.2	22995	39870	57.7±0.5	-0.06±0.92
	∼3.5	28298	55244	51.2±0.4	-0.08±0.78
2013	∼4.7	27409	38322	71.5±0.6	-0.19±0.91

Table 4.11: *Transmissions when the profile step function is changed to this shown in green in Figure 4.24. The last column displays the relative differences in the transmission values between the results here and those shown in Table 4.6.*

The final error contributions associated to the target density profile are given in Table 4.12. The introduced uncertainties are smaller than 2% except for the highest energy, where in line with the observed effect of the tube displacement, the introduced uncertainties are considerable higher.

Run	$E_{^4He}$ (MeV)	Original Transmission (%)	Uncertainty associated to the effective length	Uncertainty associated to the steepness
2011	∼6.5	57.4±0.6	$^{+0.3}_{-2.0}$	$^{-1.8}_{-1.3}$
	∼5.2	57.7±0.5	$^{+0.8}_{-0.9}$	$^{-0.8}_{+0.0}$
	∼3.5	51.3±0.3	$^{+0.9}_{-0.5}$	$^{-1.0}_{+0.0}$
2013	∼4.7	71.7±0.6	$^{+0.5}_{-0.9}$	$^{-0.6}_{-0.1}$

Table 4.12: *Systematic errors introduced to the final transmission efficiencies due to the assumptions made on the target density profile. For the given energy, the fourth column gives error for considering a 11.7 cm effective target length (top) and 12.8 cm (bottom). The fifth column shows the error from a rapid pressure decrease in the apertures (up) and a more smoothly pressure decrease (bottom).*

4.5.2 Beam offset

The beam from ISAC facility can vary in transverse emittance and in central location. During the experiment, the central location of the beam is monitored with the CCD camera inside an alignment port of the first magnetic dipole. However, there is a possibility that the beam can drift in the transverse directions to the beam direction during a period of time. Thus, the next step will be to analyse the effect on the transmission from transverse offset beam displacements of ±1mm in both x and y directions.

X-axis

The transmissions obtained by considering ±1 mm displacement in the x direction are given in Table 4.13.

Run	$E_{^4He}$ (MeV)	Transmission +1mm-X(%)	Relative Difference (%)	Transmission -1mm-X(%)	Relative Difference (%)
2011	~6.5	57.6±0.6	+0.36±1.48	54.6±0.6	-4.87 ±1.18
	~5.2	58.9±0.5	+2.05±1.20	54.4±0.5	-5.65±0.90
	~3.5	51.9±0.4	+1.28±1.06	49.3±0.4	-3.86±0.78
2013	~4.7	73.9±0.6	+3.07±1.18	66.7±0.5	-6.93 ±0.86

Table 4.13: *DRAGON transmissions with beam displacements of ±1 mm in the x direction. Columns titled with "Relative Difference" show the relative difference comparing to the transmissions shown in Table 4.6.*

A significant difference is observed respect to the simulations shown in Table 4.6. According to the results, a displacement in the negative direction produces higher change in the transmission than a displacement in the positive direction. The relative differences are higher for the 2013 run, and Figure 4.26 shows that pumping tubes placed downstream the target cell are the responsible for the significant increase in the number of stopped recoils for a displacement of -1 mm in the x direction.

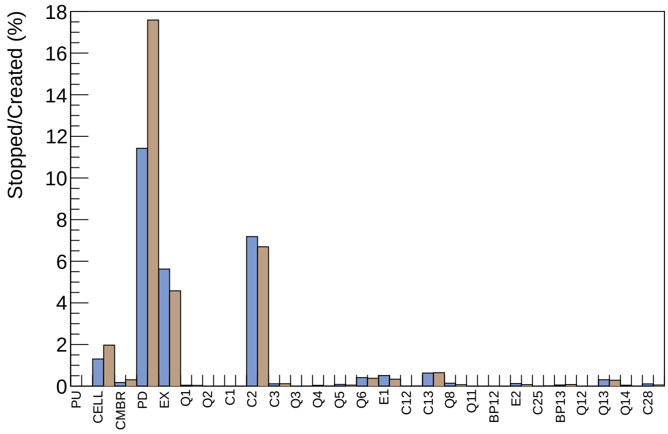

Figure 4.26: *For the 4.7 MeV beam energy case, the blue bars show the volumes where the recoils are stopped without any beam offset (Table 4.6), and in brown where the recoils stop with a -1 mm displacement in the x axis. The numbers are given as the ratio of the number of recoils stopped in a given volume to the total number of recoils created.*

Y-axis

The same type of analysis has been performed to see the influence of a displacement in the y direction. The results for both +1 mm and -1 mm offsets are displayed in Table 4.14.

Run	$E_{^4He}$ (MeV)	Transmission +1mm-Y(%)	Relative Difference (%)	Transmission -1mm-Y(%)	Relative Difference (%)
2011	∼6.5	55.2±0.6	-3.83±1.19	56.5±0.6	-1.55 ±1.20
	∼5.2	55.2±0.5	-4.35±0.91	56.7±0.5	-1.81±0.92
	∼3.5	49.3±0.4	-3.91±0.78	50.6±0.4	-1.23±0.79
2013	∼4.7	68.2±0.6	-4.85±0.89	70.6±0.6	-1.45 ±0.92

Table 4.14: *DRAGON transmissions with beam displacements of ±1 mm in the y direction. Columns titled with "Relative Difference" show the difference with the transmissions shown in Table 4.6*

In this case a significant decrease in the transmission is observed for both displacements, being clearly higher when the displacement is in the positive direction.
The uncertainties introduced to the final transmissions as a consequence of the beam location in the x and y axis are summarised in Table 4.15.

Run	$E_{^4He}$ (MeV)	Original Transmission (%)	Uncertainty associated to x-axis displacement	Uncertainty associated to y-axis displacement
2011	∼6.5	57.4±0.6	$^{+0.2}_{-2.8}$	$^{-2.2}_{-0.9}$
	∼5.2	57.7±0.5	$^{+1.2}_{-3.3}$	$^{-2.5}_{-1.0}$
	∼3.5	51.3±0.3	$^{+0.7}_{-2.0}$	$^{-2.0}_{-0.6}$
2013	∼4.7	71.7±0.6	$^{+2.2}_{-5.0}$	$^{-3.5}_{-1.0}$

Table 4.15: *Error introduced to the transmission efficiencies from the uncertainty in the beam location along with the x and y axes.*

4.5.3 Beam emittance

As described in section 4.2.3 the beam emittance is introduced in GEANT by defining a Gaussian beam spot distributions obtained from the experimental beam transmissions and Gaussian divergence distributions calculated from the normalised beam emittance from ISAC-I. In order to account for the effect of changes in the beam emittance on the acceptance, the beam transmission and beam divergence have been varied according to the experimental uncertainties.

Beam transmission

Here $\sigma\uparrow$ and $\sigma\downarrow$ correspond to the changed beam transmission by ±3 units with respect to those given in Table 4.1. The values of $\Delta\theta_{x/y}$ are changed accordingly. Table 4.16 shows the values considered for the modified $\sigma_{x/y}$ together with the DRAGON transmissions and relative differences respect to the values in Table 4.6. The associated uncertainties to the transmissions are shown in Table 4.17.

Run	$E_{^4\mathrm{He}}$ (MeV)	$\sigma_{x/y}\uparrow$ (mm)	Transmission (%)	R. Difference (%)	$\sigma_{x/y}\downarrow$ (mm)	Transmission (%)	R. Difference (%)
2011	~6.5	1.60	56.5±0.6	-1.47±1.20	1.40	57.2±0.6	-0.32±1.16
	~5.2	1.26	56.9±0.5	-1.34±0.92	0.75	60.3±0.5	-4.51±1.21
	~3.5	1.37	50.5±0.4	-1.41±0.79	1.14	52.0±0.4	1.34±1.04
2013	~4.7	1.36	70.4±0.6	-1.80±0.90	1.13	71.9±0.6	0.30±1.11

Table 4.16: *DRAGON transmissions when there is an increase ($\sigma_{x/y}\uparrow$)/decrease ($\sigma_{x/y}\downarrow$) in the beam transmission. Columns titled with "R. Difference" show the relative difference comparing to the transmissions shown in Table 4.6*

Beam divergence offset

Following the systematic procedure so far, in which an offset has been introduced in the beam spot, and the beam spot distribution and beam divergence were changed simultaneously to fit the beam transmissions, the next step is to study the influence of a likely offset in the beam divergence itself. For that, a ±0.5 mrad offset has been introduced in both $\Delta\theta_x$ and $\Delta\theta_y$. In the programme the particles are randomly selected with the divergence detailed in the section 4.2.3, and after that 0.5 mrad are added to the divergence in the selected direction for each event (see Figure 4.27).

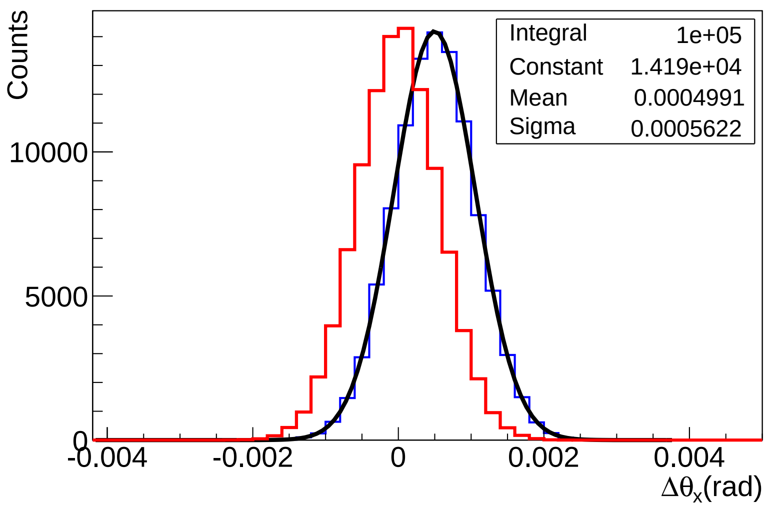

Figure 4.27: *An offset of +0.5 mrad in the divergence in the x direction, $\Delta\theta_x$, for the 6.5 MeV beam energy. Red histogram corresponds to the original x divergence distribution, $\Delta\theta_x$=0.56 mrad. Events are randomly selected from this distribution. Later, a displacement of 0.5 mrad is added to the events (blue distribution). The black curve shows a fit to the distribution, and the parameters show the same width (0.56 mrad) but a displacement of 0.499 mrad.*

The errors introduced in the transmissions due to the offsets in the beam divergences are displayed in Table 4.17.

Run	$E_{^4\mathrm{He}}$ (MeV)	Original Trans. (%)	Uncertainty from beam transmission	Uncertainty from $\Delta\theta_x$ displacement	Uncertainty from $\Delta\theta_y$ displacement
2011	~6.5	57.4±0.6	$^{-0.2}_{-0.8}$	$^{-1.1}_{-1.0}$	$^{-0.8}_{-0.8}$
	~5.2	57.7±0.5	$^{+2.6}_{-0.8}$	$^{+0.0}_{+0.1}$	$^{+0.0}_{+0.3}$
	~3.5	51.3±0.3	$^{+0.7}_{-0.7}$	$^{-0.6}_{-0.1}$	$^{-0.2}_{+0.4}$
2013	~4.7	71.7±0.6	$^{+0.2}_{-1.3}$	$^{-0.3}_{-0.3}$	$^{-1.2}_{+0.1}$

Table 4.17: *Error introduced to the final transmission efficiencies from the uncertainty in the beam divergence along the x and y axes. The top values show the uncertainties when the offsets are in the positive direction (+0.5 mrad) and the bottom ones show the relative to -0.5 mrad.*

4.5.4 Beam energy

The next parameter to be examined is the ^{4}He beam energy from the ISAC-I facility. To account for the uncertainties in the central beam energy, the simulations were run considering central energies of ±0.17% comparing to the original simulations and considering the same Gaussian widths ([HRF12]). Table 4.18 shows the new simulated beam energies (higher and lower) in the second column and the associated uncertainties in the fourth column.

Run	$E_{^4\mathrm{He}}$ (keV)	Original Transmission (%)	Uncertainty associated to mean beam energy
2011	$^{6586}_{6521}$	57.4±0.6	$^{+1.3}_{-3.1}$
	$^{5192}_{5140}$	57.7±0.5	$^{+1.8}_{-1.6}$
	$^{3539}_{3504}$	51.3±0.3	$^{+1.8}_{-1.7}$
2013	$^{4704}_{4693}$	71.7±0.6	$^{+0.4}_{-0.9}$

Table 4.18: *Error introduced to the final transmission efficiencies from the uncertainty in the mean beam energies. The new beam energies are shown in the second column where the top value represents a 0.17% increase from the original values and the bottom one represents a 0.17% decrease. The associated uncertainties are shown in the fourth column.*

As it can be observed a variation in the mean energy results in a relatively big change in the recoil transmissions. This is not an unexpected result because as it was presented above the energy plays the more determining role in the DRAGON transmission.

An increase in the beam energy leads to an increase in the energy of the recoil and a mean output energy closer to the value that the separator was tuned for, thus an increase in the transmission. For the 2013 run, the tuning energy was set manually closer to the real mean output energy, thus an increase in the tuning energy does not have a big effect in the transmission. A decrease in the beam energy leads to a decrease in the transmission because of the same reasons.

4.5.5 The branching ratio S_1/S_0

The next investigation is to check the influence of the S_1/S_0 ratio for the population of the first excited and ground states of the ^{7}Be recoils. The values adopted so far are those shown in Table 4.2 based on the extrapolations in reference [CD08]. However, the simulated BGO spectra (see Figure 4.20) show that the γ_1/γ_0 ratio (being γ_1 and γ_0 the areas under the corresponding γ peaks) is different when comparing to the experimental data.

In order to double check the influence in the DRAGON transmission of the assumptions made about the S_1/S_0 ratio and try to reproduce the experimental γ_1/γ_0 ratio, a first series of simulations have been performed. Based on the same area of the γ_0 and γ_1 experimental peaks (cf. Figure 4.20), the first assumption is to employ a S_1/S_0 ratio equal to 1. The transmissions obtained are shown in the third column in Table 4.19. Whereas the relative differences shown in the fourth column are similar to those obtained by varying other parameters as divergence, the relative S_1/S_0 ratios are clearly larger than those obtained with the experimental data (see Figure 4.28). This effect is due to the contribution from the escape peak corresponding to the γ_0 rays (γ_0-511 keV) to the γ_1 peak.

Run	$E_{^4He}$ (MeV)	Transmission (S_1/S_0=1) (%)	R. Difference (%)	S_1/S_0	Transmission (%)	R. Difference (%)
2011	∼6.5	58.4±0.6	1.74±1.47	0.393	56.0±0.6	-2.42±1.17
	∼5.2	59.6±0.5	3.35±1.21	0.495	58.0±0.5	+0.55±1.18
	∼3.5	53.0±0.4	3.32±1.06	0.420	51.3±0.4	+0.04±1.03
2013	∼4.7	73.5±0.6	2.58±1.14	0.423	70.8±0.6	-1.14±0.9

Table 4.19: *Transmissions obtained with different S_1/S_0 ratios. The third column shows the transmissions associated with S_1/S_0=1. The sixth column shows the transmissions with the S_1/S_0 ratios displayed in the fifth column. The relative differences are calculated with respect to the transmissions in Table 4.6.*

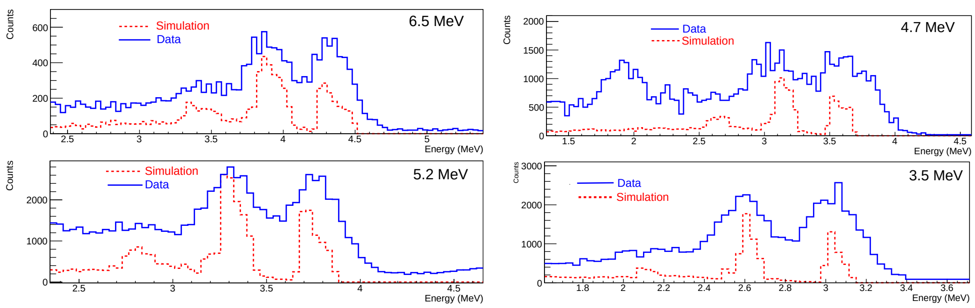

Figure 4.28: *BGO spectra comparison between the experimental data and simulation with S_1/S_0=1. Both simulated and experimental spectra are shown in coincide with a ^7Be in the DSSSD.*

Further simulations have been carried out to get closer values to the experimental γ_1/γ_0 data. The fifth column in Table 4.19 shows the final ratios which better reproduce the experimental values. Columns sixth and seventh show the associated transmissions and relative differences, respectively. In order to be conservative the maximum errors among the different tested S_1/S_0 ratios will be considered and are given in the fourth column in Table 4.20. A good agreement can be seen between the experimental and simulated γ_1/γ_0 ratios shown in fifth and sixth column in the same table, respectively.

Run	$E_{^4He}$ (MeV)	Original Transmission	Uncertainty from S_1/S_0	γ_1/γ_0 Experimental	γ_1/γ_0 simulation(*)
2011	∼6.5	57.4±0.6	$^{+1.0}_{-1.7}$	1.09±0.02	1.13±0.03
	∼5.2	57.7±0.5	$^{+1.9}_{-0.8}$	1.25±0.01	1.26±0.03
	∼3.5	51.3±0.3	$^{+1.7}_{-0.3}$	0.99±0.02	1.03±0.02
2013	∼4.7	71.7±0.6	$^{+1.8}_{-1.4}$	1.02±0.03	1.01±0.02

Table 4.20: *Errors introduced in the simulations due to the variation of the S_1/S_0 ratios (fourth column). The fifth and sixth columns show the γ_1/γ_0 experimental and simulated ratios, respectively. It is worth noting that the peak intensities are taken from the γ spectra in coincidence with recoils in the DSSSD.*
(*) Corresponding to simulations with the S_1/S_0 ratios shown in the fifth column in Table 4.19.

4.5.6 γ-rays angular distributions

So far in the simulations the prompt γ-ray angular distributions emitted in the ^{3}He(α,γ)^{7}Be reaction are considered isotropic. This assumption would be experimentally justified at energies below E_{CM}=1.23 MeV [DGK09, BBS07]. However, our measurements have been carried out at energies above E_{CM}=1.23 MeV. Therefore error contribution from γ anisotropy should be considered, for which the simulations have been done. For that, the γ angular distribution from reference [TP63a] has been considered. They calculated the prompt γ-rays of the ^{3}He(α,γ)^{7}Be reaction using the ^{3}He+^{4}He scattering phase shift and expressed the differential cross section as a function of the angular momentum of the final state of ^{7}Be (ground state or first excited state) as:

$$\frac{d\sigma}{d\Omega} = \sigma_0(J_f)[1 + a_1(J_f)cos\Theta + a_2(J_f)cos^2\Theta + a_3(J_f)cos^3\Theta + a_4(J_f)cos^4\Theta] \tag{4.4}$$

where J_f is the angular momentum of the ^{7}Be final state, Θ is the polar angle of the gamma ray in the centre of mass system with respect to the beam axis, and a_1, a_2, a_3 and a_4 are energy dependent coefficients and vary depending on the final state populated in the ^{7}Be. For our beam energies, the coefficients for both ground state and first excited state have been extracted from their energy dependent coefficient plots, and the differential cross section are given by:

$$\text{6.5 MeV: } \frac{d\sigma}{d\Omega} = \begin{cases} \sigma_0(J_f)[1 - 0.66cos\Theta - 0.034cos^2\Theta + 0.51cos^3\Theta - 0.043cos^4\Theta, \text{for ground state} \\ \sigma_0(J_f)[1 - 0.09cos\Theta - 0.2cos^2\Theta + 0.03cos^3\Theta + 0.0cos^4\Theta, \text{for first state} \end{cases}$$

$$\text{5.2 MeV: } \frac{d\sigma}{d\Omega} = \begin{cases} \sigma_0(J_f)[1 - 0.226cos\Theta - 0.02cos^2\Theta - 0.02cos^3\Theta + 0.017cos^4\Theta, \text{for ground state} \\ \sigma_0(J_f)[1 - 0.034cos\Theta - 0.08cos^2\Theta - 0.03cos^3\Theta + 0.0cos^4\Theta, \text{for first state} \end{cases}$$

$$\text{4.7 MeV: } \frac{d\sigma}{d\Omega} = \begin{cases} \sigma_0(J_f)[1 - 0.173cos\Theta + 0.025cos^2\Theta + 0.00cos^3\Theta + 0.017cos^4\Theta, \text{for ground state} \\ \sigma_0(J_f)[1 - 0.033cos\Theta - 0.02cos^2\Theta - 0.02cos^3\Theta + 0.0cos^4\Theta, \text{for first state} \end{cases}$$

$$\text{3.5 MeV: } \frac{d\sigma}{d\Omega} = \begin{cases} \sigma_0(J_f)[1 - 0.036cos\Theta + 0.109cos^2\Theta - 0.047cos^3\Theta + 0.017cos^4\Theta, \text{for ground state} \\ \sigma_0(J_f)[1 - 0.066cos\Theta + 0.097cos^2\Theta - 0.047cos^3\Theta + 0.0cos^4\Theta, \text{for first state} \end{cases}$$

Using these expressions, the relative probabilities for the direction of the γ rays are introduced in the simulations as a function of cosΘ. Thus, the relative probabilities of the direction of the γ rays are randomly selected from those shown in Figure 4.29.

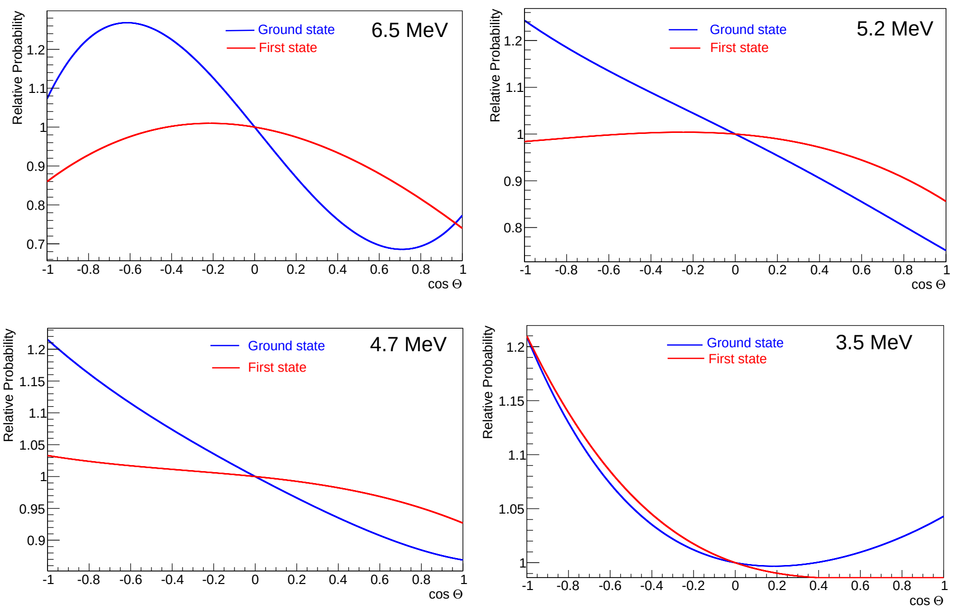

Figure 4.29: *Relative probabilities for the direction of the prompt γ rays populating the ground state (blue) and the first excited state (red) at E^{beam}=6.5, 5.2, 4.7 and 3.5 MeV that are introduced in the GEANT 3 code.*

Table 4.21 shows the transmissions obtained with Tombrello and Parker's distributions, together with the relative differences comparing to those in Table 4.6 and the associated errors introduced to the acceptance.

Run	$E_{^4\mathrm{He}}$ (MeV)	Transmission (%)	R. Difference (%)	Uncertainty from Angular Distribution
2011	∼6.5	58.9±0.6	2.71±1.49	±1.6
	∼5.2	60.6±0.5	5.07±1.22	±2.9
	∼3.5	52.4±0.3	2.20±1.05	±1.1
2013	∼4.7	72.1±0.6	0.62±1.12	±0.4

Table 4.21: *DRAGON transmissions for the $^3He(\alpha,\gamma)^7Be$ reaction when the gamma angular distributions are the calculated for Trombello and Parker in reference [TP63a].*

In order to compare with the isotropic distribution, Table 4.22 shows the $\chi^2_{\nu-1}$ values calculated using the expression 4.3.

$\sim$E$_{^4\mathrm{He}}$ (MeV)	6.5	5.2	4.7	3.5
$\chi^2_{\nu-1}(\gamma_0)$	5.7	7.7	7.0	5.5
$\chi^2_{\nu-1}(\gamma_1)$	10.3	8.2	5.5	4.7

Table 4.22: *$\chi^2_{\nu-1}$ as defined in expression 4.3 for the comparison of the BGO hit-maps between the simulations and the experimental data when the Tombrello and Parker distributions are assumed in the simulations.*

Observing the Tables 4.7 and 4.22 for the two angular distribution we believe that, with more extensive simulations, we will be able to reduce the $\chi^2_{\nu-1}$ by varying from a_0 to a_4. For now, the changes observed in varying the angular distribution will be considered as an uncertainty introduced in the final transmissions.

4.6 $\epsilon_{\mathbf{DRAGON}}$ Values and Uncertainties

The total systematic error contribution to the acceptance must be calculated from the estimated uncertainties. Conservative values of the uncertainties in each parameter previously described were used. The correlation between the parameters could have been accounted for, however, due to the lack of precise knowledge for the correlation between the variables, the total systematic errors in the acceptance can be considered as an upper limit. To calculate the total systematic errors introduced in the transmissions, both positive and negative contributions were treated independently. Therefore the total positive systematic error is given by:

$$\mathrm{Error}^{+}_{\mathrm{sys}} = \sqrt{\sum_{i=1}^{n} (x_i^+)^2} \tag{4.5}$$

being the x_i^+ the positive uncertainties associated to the different experimental parameters tested in the simulations. In the same way, the total negative error is given by:

$$\mathrm{Error}^{-}_{\mathrm{sys}} = \sqrt{\sum_{i=1}^{n} (x_i^-)^2} \tag{4.6}$$

The final values of the transmissions and associated statistical and systematic errors are shown in Table 4.23, whilst a list with all tested parameters and their associated systematic uncertainty contributions to the transmission is given in Table 4.24.

Run	E$_{^4\mathrm{He}}$ (keV)	Transmission (%)	Statistical Error	Systematic Error
2011	6553.88	57.4	$\pm$0.6	$^{+2.3}_{-6.4}$
	5165.97	57.7	$\pm$0.5	$^{+5.0}_{-5.6}$
	3521.61	51.3	$\pm$0.3	$^{+3.0}_{-3.8}$
2013	4716.45	71.7	$\pm$0.6	$^{+3.0}_{-6.7}$

Table 4.23: *Final DRAGON transmissions ϵ_{DRAGON} and associated statistical and systematic errors.*

Parameter	Run	$E_{^4\mathrm{He}}$ (MeV)	Systematic Error (%)
TDP Effective Length	2011	∼6.5	$^{+0.3}_{-2.0}$
		∼5.2	$^{+0.8}_{-0.9}$
		∼3.5	$^{+0.9}_{-0.5}$
	2013	∼4.7	$^{+0.5}_{-0.9}$
TDP Steepness	2011	∼6.5	$^{-1.8}_{-1.3}$
		∼5.2	$^{-0.8}_{+0.0}$
		∼3.5	$^{-1.0}_{+0.0}$
	2013	∼4.7	$^{-0.6}_{-0.1}$
x Beam Offset	2011	∼6.5	$^{+0.2}_{-2.8}$
		∼5.2	$^{+1.2}_{-3.3}$
		∼3.5	$^{+0.7}_{-2.0}$
	2013	∼4.7	$^{+2.2}_{-5.0}$
y Beam Offset	2011	∼6.5	$^{-2.2}_{-0.9}$
		∼5.2	$^{-2.5}_{-1.0}$
		∼3.5	$^{-2.0}_{-0.6}$
	2013	∼4.7	$^{-3.5}_{-1.0}$
Beam Transmission	2011	∼6.5	$^{-0.2}_{-0.8}$
		∼5.2	$^{+2.6}_{-0.8}$
		∼3.5	$^{+0.7}_{-0.7}$
	2013	∼4.7	$^{+0.2}_{-1.3}$
$\Delta\theta_x$ Beam Offset	2011	∼6.5	$^{-1.1}_{-1.0}$
		∼5.2	$^{+0.0}_{+0.1}$
		∼3.5	$^{-0.6}_{-0.1}$
	2013	∼4.7	$^{-0.3}_{-0.3}$
$\Delta\theta_y$ Beam Offset	2011	∼6.5	$^{-0.8}_{-0.8}$
		∼5.2	$^{+0.0}_{+0.3}$
		∼3.5	$^{-0.2}_{+0.4}$
	2013	∼4.7	$^{-1.2}_{+0.1}$
Beam Energy	2011	∼6.5	$^{+1.3}_{-3.1}$
		∼5.2	$^{+1.8}_{-1.6}$
		∼3.5	$^{+1.8}_{-1.7}$
	2013	∼4.7	$^{+0.4}_{-0.9}$
S_1/S_0	2011	∼6.5	$^{+1.0}_{-1.7}$
		∼5.2	$^{+1.9}_{-0.8}$
		∼3.5	$^{+1.7}_{-0.3}$
	2013	∼4.7	$^{+1.8}_{-1.4}$
γ Angular Distribution	2011	∼6.5	$^{+1.6}_{-1.6}$
		∼5.2	$^{+2.9}_{-2.9}$
		∼3.5	$^{+1.1}_{-1.1}$
	2013	∼4.7	$^{+0.4}_{-0.4}$

Table 4.24: *Experimental parameter tested in the transmissions simulations and their systematic errors.*

"Physicists like to think that all you have to do is say, these are the conditions, now what happens next?."

Richard P. Feynman

CHAPTER 5

ANALYSIS AND RESULTS

Abstract: *In this chapter the analysis techniques, calculations and procedures to treat the data from the two experiments are detailed and the final results are presented in two main parts corresponding to the two experiments. The chapter begins with the analysis of the Activation Experiment and follows with the one for the Direct Recoil Counting Experiment, focusing on the different observables and final results for the S-factor of the* $^{3}He(\alpha,\gamma)^{7}Be$ *reaction at the energies of our investigations.*

Experiments are the keys to determine properties such as nuclear radius, spin and parities or cross sections. Following an experiment the more tricky task of data analysis starts which is crucial in obtaining meaningful results. Eventually, this allows for progress in understanding various processes, e.g. the formation of primordial elements in the Universe.

Different nuclear physics experiments are performed in order to obtain the same information, usually in order to reduce errors in the measurements and to provide consistent results that makes possible to explain different phenomena and understand the underlying physics. In addition, the development of new systems, such as detectors and advanced electronics takes place benefiting the society and improving the results of the experiments.

Experiments devoted to measure the cross section of astrophysical reactions aim at precise measurements. Theoretical models are used to extrapolate the experimental values down to the astrophysical relevant energies that are unreachable with current experimental systems. Therefore, constraining models using different measurements and complementary methods are required. This demands fool-proof analysis procedures that provides a very good understanding of all possible sources of errors in the data that allows for a reliable evaluation of the observables.

It should be noted here that this is a high precision measurement where each parameter of the experiment has to be treated with specific care and thus I dedicate this chapter to the data treatment.

5.1 Analysis I: Measurements using the Activation Method

Based on the expression 1.7, the astrophysical S-factor for the ^{3}He(α,γ)^{7}Be reaction, $S_{34}(E)$ is expressed by:

$$S_{34}(E) = \sigma_{34}(E) \cdot E \cdot e^{2\pi\eta(E)} \tag{5.1}$$

where E is the centre of mass energy (E_{CM}) and σ_{34} the cross section of the reaction.

The reaction centre of mass energy is given in this case by (see appendix B):

$$E_{CM} = \frac{m^{T}_{^4He}}{m^{T}_{^4He} + m^{B}_{^3He}} \cdot E^{beam}_{^3He} \tag{5.2}$$

where the different *m* are the nuclear masses in atomic units. In the following, *T* will refer to the **T**arget and *B* to the **B**eam. $E^{beam}_{^3He}$ is the beam energy at the moment that the reaction happens.

The reaction cross section is given as:

$$\sigma_{34} = \frac{Y_{^7Be}}{N^{\circ T}_{^4He} \cdot N^{\circ B}_{^3He}} \tag{5.3}$$

where $Y_{^7Be}$, $N^{\circ T}_{^4He}$ and $N^{\circ B}_{^3He}$ are the total yield of recoils produced, the gas target areal density and the total number of incoming beam particles, respectively. In the diagram of the *activation* setup shown in Figure 5.1 the different observables required to determine the cross section are indicated.

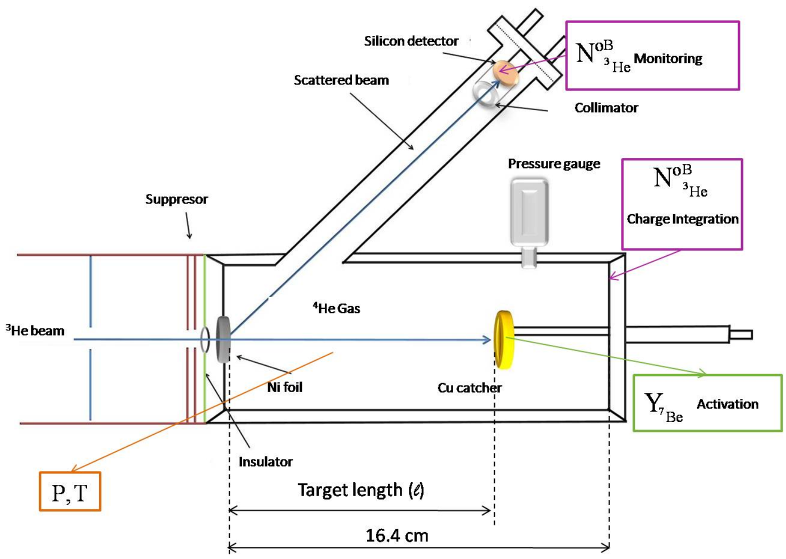

Figure 5.1: *Scheme of the experimental setup used for the activation method in Madrid. The positions at which the different observables for determining the cross section are indicated: the ^{7}Be yield from the deposited recoils in the Cu catcher, the ^{4}He gas target areal density (assuming an ideal gas behaviour) and the ^{3}He beam from the charge integration and the silicon detector monitoring the scattered beam.*

In the following, details of the analysis performed in order to obtain the number of beam particles, the target density parameters, the number of recoils produced and the reaction centre of mass energy are presented.

5.1.1 The number of ^{3}He beam particles: $N^{\circ}B_{^3He}$

The number of incoming beam particles are determined by using two methods simultaneously: (1) by measuring the incoming current using the target chamber as Faraday cup, and (2) by counting the scattered beam particles into a collimated silicon detector positioned at 44.9°.

During the experiment, every 30 minutes the accumulated number of pulses corresponding to the integrated electric charge in the chamber and the online scattered peak integration in the silicon detector were noted down. This allowed us to have control over the beam stability during the measurements. Aiming to the same offline beam stability checks, the silicon spectrum was periodically saved as a new file and cleared, and the same was done with the scaler information. As an example, the comparison of the different files taken for the ∼2.5 MeV beam energy is shown in Figure 5.2. For each file, the charge integration method consisted of obtaining the number of particles using the expression 3.4. In the case of the silicon spectra, the scattered beam peak is integrated and the number of incoming particles is estimated using the expression 3.6.

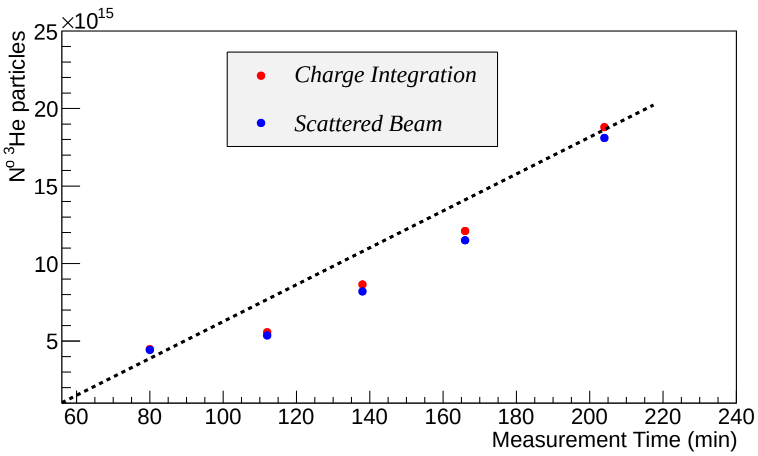

Figure 5.2: *Comparison of the calculated number of beam particles for different files taken for a ^{3}He beam at ∼2.5 MeV impinging onto a ^{4}He gas target at ∼60 Torr. The estimated number of beam particles (y axis) is shown as a function of the time for each measurement (x axis). The red and blue dots correspond to estimation using the charge integration and particles scattered from the Ni foil methods, respectively. The black line is just to guide the eye.*

As it can be seen, there is an excellent agreement between both methods for all files. The fluctuations in the number of beam particles, apart from the time of each file, is due to the oscillations in the beam current during the experiment. Nevertheless, this does not have influence in the estimation of the total number of beam particles, because even though the current were increased or decreased there is always agreement between the two methods. The same kind of agreement has been observed for all the measurements with different energies.

Thus, for each energy, the total number of beam particles estimated with the scattered beam method has been obtained by adding offline the individual spectra (see for example Figure 5.3), integrating the elastic scattered peak and applying the expression 3.6 assuming a kinetic energy corresponding to the beam energy at the centre of the Ni foil. A cross-check using the LISE++ code[LIS] has also been done. In this case, the number of particles has been obtained by averaging the number of particles obtained by assuming that the reaction takes place at the beginning, centre and the end of the foil.

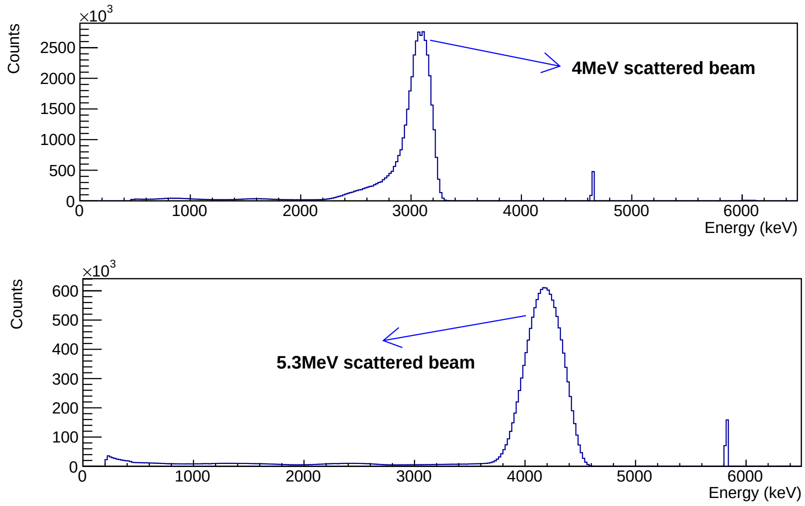

Figure 5.3: *Spectra taken with the silicon detector for the ^3He beam impinging onto a ^4He gas target. For ∼4 MeV beam energy and ∼60 Torr target pressure (top), and for 5.3 MeV in and ∼50.8 Torr (bottom). The most intense peaks correspond to the scattered beam with the Ni foil window.*

For the charge integration method, the number of pulses associated with each file has been added and the current estimated using the expression 3.4 where one pulse corresponds to 10^{-10} C. The total number of beam particles for all the energies is shown in Figure 5.4 for both, charge integration and scattered beam particles methods and the values with the errors are shown in Table 5.6. Perfect agreement between the two methods can be observed.

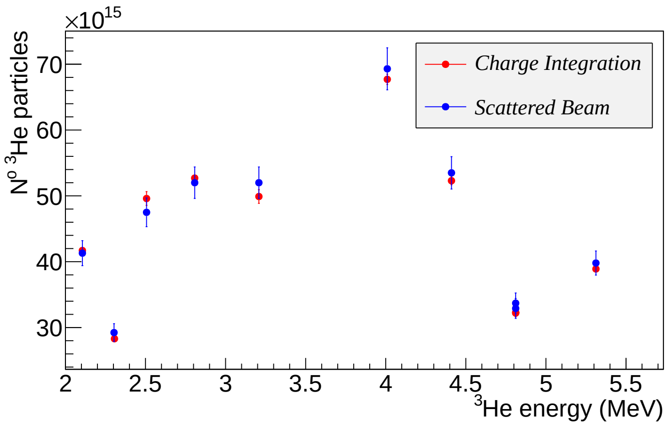

Figure 5.4: *Total number of ^3He beam particles for different energies measured at CMAM. The number of particles estimated from the electric charge deposited in the chamber are shown in red, and the estimated using the beam particles scattered from the Ni foil window are shown in blue.*

5.1.1.1 Error estimations

Taking into account all sources of error as shown in Table 5.1, a 4.6% relative error has been estimated by using standard error propagation of the number of beam particles estimated with the scattered particles.

Parameter value	Error Contribution
Collimator radius (0.27±0.03) mm	2.22%
Distance Ni foil-collimator (22.13±0.11) cm	0.99%
Collimator angle (44.9±0.4)°	3.38%
Ni foil thickness (1.03±0.02) μm	1.94%
Error Beam Energy (0.02-0.003) MeV	0.18%
Error Particles Detected ($\sqrt{\text{Particles}}$)	0.02%

Table 5.1: *Error contribution from the different parameters to the number of beam particles obtained using the scattered beam in the silicon detector.*

For the case of the charge integration method the errors have been estimated by considering the relative difference between the number of beam particles calculated with both methods divided by two:

$$\text{Relative Error (\%)} = \left(1 - \frac{N_{^3He}^{Scattering}}{N_{^3He}^{Integration}}\right) * 100/2 \tag{5.4}$$

The errors associated to the number of particles estimated with the charge integration method oscillate between 0.42%-2.12%.

5.1.2 The ^{4}He gas target areal density: $\mathbf{N^{o}T_{^4He}}$

The number of ^{4}He gas particles per square centimetre is given by the expression 3.7 ($N_t = 9.66 \cdot 10^{18} \frac{\ell \cdot P}{T_0 + T_C}$). Here, ℓ, P and T+T_0 are the target length in cm, the pressure in Torr, and the gas temperature in kelvin, respectively.

Target length

The distance between the Ni foil and the front face of each Cu catcher (see Figure 5.1), i.e. ℓ, was determined at the beginning and the end of each run by measuring with a caliper the distance between the front face of the Cu catcher and the inner face of the final chamber flange and subtracting it from the 16.4 cm distance between the Ni foil and the end of the chamber. The errors associated to ℓ are obtained by propagating the caliper error (0.005 cm) for all the measurements performed.

Target pressure

With a continuous gas flow, the pressure inside the chamber was continuously monitored and the value was noted each 30 minutes, approximately. The difference between the maximum and the minimum pressure values for all the runs was always lower than 2%, and lower than 0.16% for all the runs taken in 2011. The associated errors have been determined from the error in the pressure gauge, considered as 0.10 Torr, and the standard deviation of the pressure readings. An example of pressure stability is shown in Figure 5.5 where the red dots are the ^{4}He gas pressure when the ^{3}He beam impinged onto the gas with an energy of 4010 keV. The blue line shows the average pressure and the marked blue region indicates the error associated to the average.

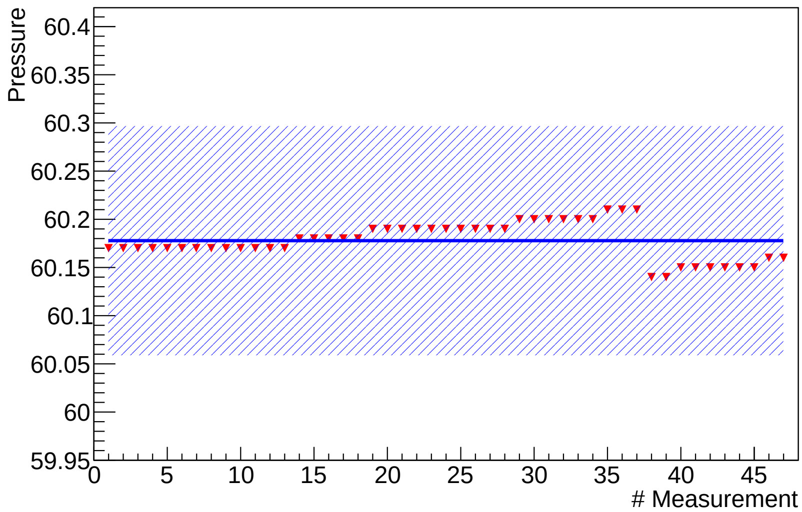

Figure 5.5: *An example of the pressure stability in the activation experiment. The red dots give the ^{4}He gas pressure readings performed during the measurement with the ^{3}He beam at an energy of 4010 keV. The blue line indicates the average pressure and the shaded region represents the associated error.*

Temperature

The gas temperature inside the chamber has been considered as the accelerator hall room temperature (T_0) plus the rising temperature due to the beam heating (T_C). The room temperature at the accelerator hall was 22.5°C and it was known to be very stable, indeed an automatic alarm goes off when a difference of $\pm$ 1.5°C is observed, considered as the error for T_0. As our setup is the same as the one used in [NHNEH04] to determine the cross section of the same reaction at lower energies, T_C has been estimated by extrapolating the values reported there.

They measured the temperature correction (T_C) by using the resonance reaction ^{10}B(α,p)^{13}C with a solid ^{10}B placed in the Cu catcher position and an α beam, populating the 12.70 MeV state in ^{14}N [AL55]. Subsequently, the state decays by different channels emitting particles as shown in Table 5.2. For example, with a cross section of 42 mb the 12.7 MeV state in ^{14}N* decays by emitting a proton, p_3, and populating the 3.85 MeV state in ^{13}C*. Subsequent γ-rays are emitted due to the de-excitation of the ^{13}C* nucleus.

E_α (MeV±keV)	$\Gamma_{c.m.}$ (keV)	$^{14}N^*$ (MeV)	Outgoing Particle (x)	σ_x (mb)	Γ_x (keV)
1518± 4	14±4	12.7	α		1.7
			p_0	4.7	0.62
			p_1	1.3	0.17
			p_2	5.3	0.70
			p_3	42	5.6
			d	7.0	0.93
			n	32	4.3

Table 5.2: *Resonance in ^{10}B+α at 1.518 MeV taken from [AL55]. Here, p_0, p_1, p_2 and p_3 correspond to the ground and the 3.09, 3.68 and 3.85 MeV states of ^{13}C. γ-rays are subsequently emitted in the de-excitation of the excited states in the $^{13}C^*$ nucleus.*

Basically, the procedure followed at the Weizmann Institute consisted of using a NaI detector placed close to the target chamber at 90º with respect to the beam direction. The chamber was filled with ^{4}He gas target at different pressures. The energy of the ^{4}He beam was increased for each pressure in order to maximise the statistic in the γ-ray NaI detector spectrum from the de-excitation of the 3.85 MeV state in the ^{13}C. The temperature correction is calculated from the energy loss in the gas target as the difference between the incoming energy and the resonance energy. For a beam power of 1 W (500 nA current of 2 MeV beam) they report a temperature correction of T_C=17 K.

The beam power for our measurements is given by:

$$\text{Beam Power} = \frac{N^o_{^3He} \cdot E(MeV) \cdot 10^6 \cdot e^-}{T_{IMP}} \tag{5.5}$$

and the temperature correction is determined using a linear dependence of T_C with the beam power from the values given in Ref. [NHNEH04]. The associated errors to T_C are given by the fluctuations in the beam current between the different files for each energy (i.e. see Figure 5.2). The total error associated with the temperature is given by 1.5ºC plus the error due to T_C. It is worth noting that the temperature correction T_C has been calculated using the beam currents from the two methods used (charge integration and elastic scattering), being the differences between the T_C values the same compared to the currents estimated with both methods (see Figure 5.2).

The values for pressure P, temperature $(T_0 + T_C)$ and target length ℓ are shown in Table 5.3. The results for the gas target areal density are shown in Table 5.6. The errors in the target density are calculated by standard error propagation from the errors in P, $T_0 + T_C$ and ℓ shown in Table 5.3.

5.1.3 The ^{7}Be recoils produced in the Activation Method: $Y_{^7Be}$

The ^{7}Be recoils were implanted in the copper catchers. The delayed 478 keV γ-activity from the catchers was measured off-line by placing them at a distance of 20 mm from a HPGe detector at the low-background detection station at Soreq Research Center (see Figure 3.12). This well-established arrangement with an optimised solid angle had an effective shielding to suppress the ambient background.

Figure 5.6 shows in the upper panel the total spectrum of the ^{7}Be catcher collected using a ~4 MeV beam energy and in the lower panel a zoom view of the energy region of interest (478 keV) in blue for

Year	$E_{^3\mathrm{He}}$ (keV)	T_0+T_C(*) (K)	Pressure (P) (Torr)	Target Length (ℓ) (cm)
	2306.28 ± 2.37	300.28 ± 2.25	54.68 ± 0.07	13.29 ± 0.02
	3208.05 ± 2.99	309.26 ± 2.19	63.77 ± 0.08	13.29 ± 0.02
2009	4410.42 ± 3.82	316.56 ± 9.83	50.66 ± 0.01	10.82 ± 0.02
	4811.20 ± 4.09	318.49 ± 7.92	50.83 ± 0.03	10.92 ± 0.02
	5312.19 ± 4.44	319.09 ± 2.25	56.68 ± 0.07	13.29 ± 0.02
	2105.89 ± 2.23	301.64 ± 2.11	60.14 ± 0.01	12.47 ± 0.02
	2506.67 ± 2.51	303.22 ± 2.20	60.16 ± 0.01	11.64 ± 0.02
2011	2807.26 ± 2.71	305.44 ± 2.15	60.08 ± 0.01	12.00 ± 0.02
	4009.63 ± 3.54	307.81 ± 2.45	60.18 ± 0.01	13.11 ± 0.02
	4811.20 ± 4.09	312.71 ± 3.63	51.16 ± 0.01	11.09 ± 0.02

Table 5.3: *Values of the T_0+T_C, P and L parameters considered to determine the areal target density. See text for more details.*
(*) The values shown here include the T_C calculated using the beam currents from the charge integration.

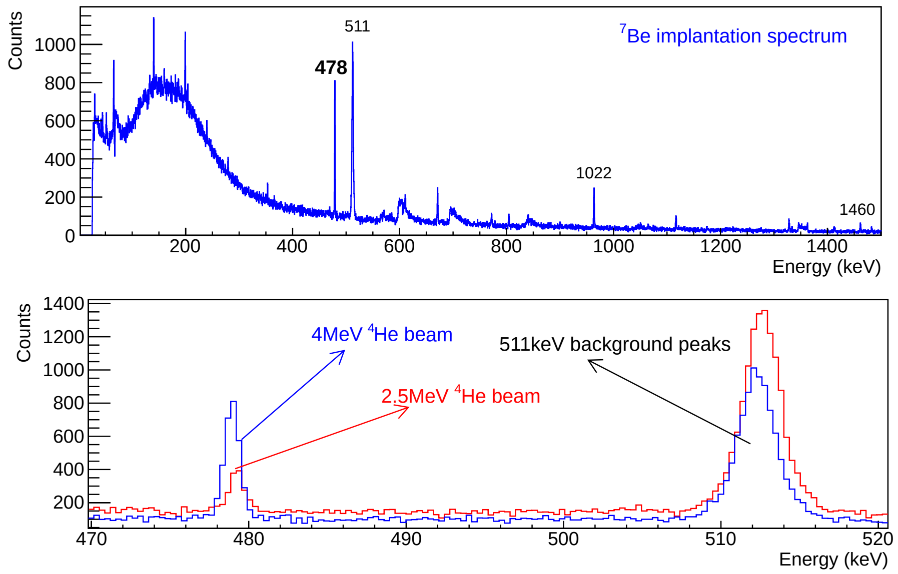

Figure 5.6: *Spectra for the γ-rays from the catchers having implanted ^{7}Be. In the upper panel a total spectrum for the ^{7}Be catcher at $\sim$4 MeV beam energy is shown. Some relevant peak energies are labelled. In the lower panel a zoom view of the region of interest is shown for the measurement at 4 MeV beam energy (blue) and $\sim$2.5 MeV (red).*

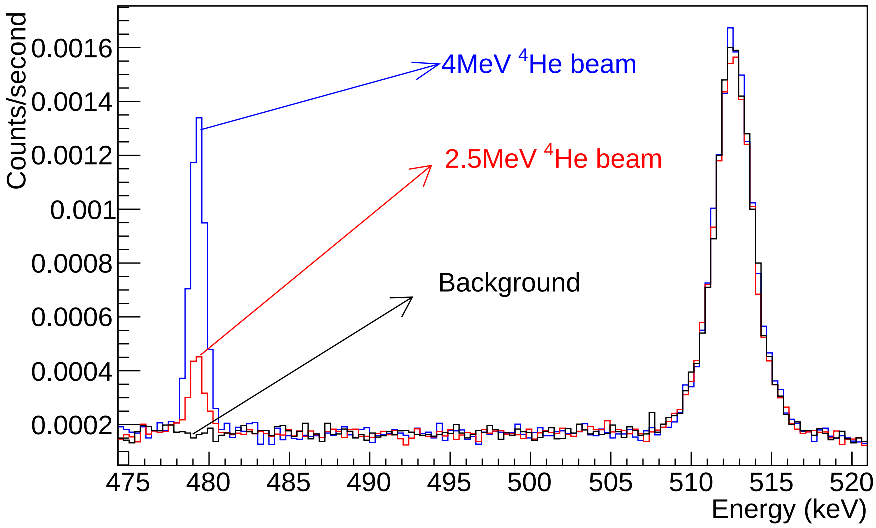

Figure 5.7: *Spectra showing the γ count rates for the catchers prepared with $\sim$2.5 and $\sim$4 MeV ^{4}He beams in red and blue, respectively. The γ count rate for the background radiation is shown in black. Note that the levels of the Compton continuum bases are equal, as well as the heights of the 511.0 keV peaks.*

$\sim$4 MeV and in red for $\sim$2.5 MeV. These spectra were collected for durations of 241.1 and 168.0 hours respectively, to minimize the statistical uncertainty in counting.

For comparison, Figure 5.7 shows the count rate spectra for the $\sim$2.5 and $\sim$4 MeV together with the count rate spectrum for the background measurement shown in Figure 3.14. Apart from not observing any interference between the 478 keV and the 511 keV peaks, the height of the 511.0 keV peak in the background is equal to the heights of this peak in the ^{7}Be catchers and the baselines of the three spectra are the same. This is a clear indication that the annihilation γ-rays of 511.0 keV are not coming from the catchers but from the ambient background.

5.1.3.1 478 keV peak integration

In order to determine the net number of counts under the 478 keV peak, we have used the procedure followed in reference [NEHY07]. In the case of a non symmetric 478 keV peak, the peak is divided in three regions, a central top region with g counts and two regions with G_1 and G_2 counts in the left and right sides, respectively. Two extra regions, one in the left side with B_1 number of counts and one in the right side with B_2 are considered in order to estimate the background under the peak (see Figure 5.8 for the case of non symmetric peak where the top channel is taken as just one channel).

The total number of counts under the peak is given by: $G=G_1+G_2+g$, and the baseline to be subtracted assuming that the top region is just one channel is [NEHY07]:

$$B = \frac{m_1+0.5}{n_1}B_1 + \frac{m_2+0.5}{n_2}B_2 \tag{5.6}$$

Thus, the net number of counts under the peak is given by: N=G-B and the associated uncertainty is

$$\sigma(N) = \left[G + \sigma^2(B)\right]^{0.5} \tag{5.7}$$

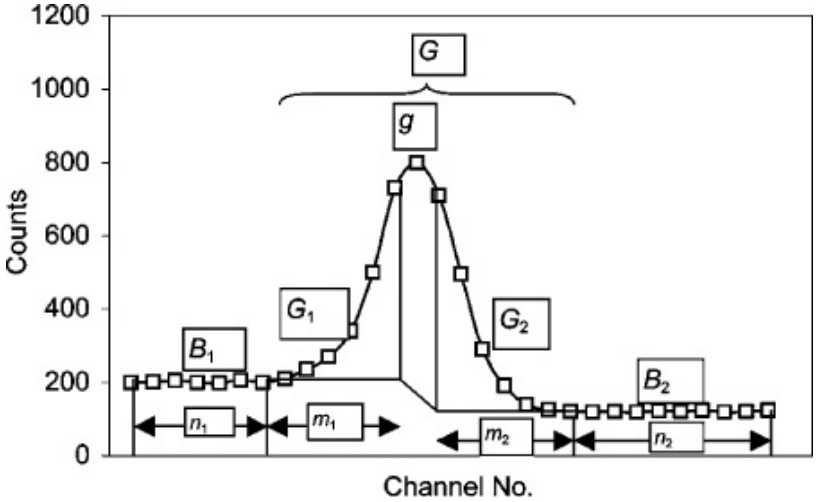

Figure 5.8: *Peak regions defined in order to determine the net area under the 478 keV peak. The widths are n_1, m_1, n_2 and m_2 and the number of counts of the different regions are B_1,G_1, G_2 and B_2 respectively. g indicates the counts under the single top channel. Figure taken from [NEHY07].*

with σ^2(B) the variance of the baseline:

$$\sigma^2(\mathrm{B}) = \left(\frac{\mathrm{m_1}+0.5}{\mathrm{n_1}}\right)^2 \mathrm{B_1} + \left(\frac{\mathrm{m_2}+0.5}{\mathrm{n_2}}\right)^2 \mathrm{B_2} \tag{5.8}$$

In case of getting a symmetric peak, i.e. two channels with the highest number of counts, g=0 and 0.5 must be removed in expression 5.8. Table 5.4 shows the net number of counts N under the 478 keV peak for the different energies within their statistical errors.

5.1.3.2 Determination of the total number of ^{7}Be recoils produced

After obtaining the number of net counts under the 478 keV γ peak (N) the next step is to determine the total number of ^{7}Be recoils produced for each beam energy.

Being N the number of counts in the 478 keV γ peak measured during the decay time T_d, ε_A the absolute detection efficiency of the HPGe detector, and $B.R.$ the branching ratio populating the first excited state in ^{7}Li (see Figure 1.12), we can establish the total number of decayed ^{7}Be nuclei (N_{DEC}) during the time T$_d$ by:

$$N_{\mathrm{DEC}} = \frac{N}{\varepsilon_A \cdot B.R.} \tag{5.9}$$

A γ detection efficiency of 0.0436±0.0010 (systematic uncertainty ±2.29%) was obtained experimentally using a ^{7}Be point source placed at the same distance of 2 cm from the HPGe detector and different transverse positions.

On the other hand, denoting by N_{A} and N_0 the number of ^{7}Be nuclei in the catcher at the end and at the beginning of the decay measurement at SOREQ, respectively, and T_d to the decay time, we can write the *Universal Law of Radioactive Decay* for our case as follows:

$$N_{\mathrm{A}}(T_d) = N_0 \cdot e^{-\lambda \cdot T_d} \tag{5.10}$$

Thus:

$$N_0 - N_{\mathrm{A}}(T_d) = N_{\mathrm{DEC}} \tag{5.11}$$

$$N_0 = \frac{N_{\mathrm{DEC}}}{1 - e^{-\lambda \cdot T_d}} \tag{5.12}$$

where λ is the decay constant expressed by $\lambda = \frac{\mathrm{Ln}\,2}{\mathrm{t}_{1/2}}$. The half life $\mathrm{t}_{1/2}$ of the ^{7}Be hosted in a copper material is 53.353(50) days. More details can be found in reference [NEHY07] for the measurement of the decay rate of ^{7}Be in Cu.

Being T_l the lost time since the implantation at CMAM finishes until the measurement of the decay starts, it can stated that:

$$N_0 = N_{\mathrm{IMP}} \cdot e^{-\lambda \cdot T_l} \rightarrow \tag{5.13}$$

$$N_{\mathrm{IMP}} = N_0 \cdot e^{+\lambda \cdot T_l} \tag{5.14}$$

where $\mathrm{N}_{\mathrm{IMP}}$ is the number of ^{7}Be nuclei at the time when the implantation finishes.

Moreover, due to the fact that the ^{7}Be recoils are unstable nuclei, in order to determine the total number of ^{7}Be produced we need to take into account the production of the recoils as well as their decay. Generally we can assume that for a given implantation time t, the number of ^{7}Be nuclei present in the catcher is denoted by:

$$dN_1(t) = R \cdot dt - \lambda \cdot N_1 \cdot dt \tag{5.15}$$

being R the reaction rate for the formation of the ^{7}Be nuclei, expressed by:

$$R = N_b \cdot \sigma \cdot I \tag{5.16}$$

where N_b is the areal number of nuclei in the target, σ is the cross section, and I is the intensity of the incident beam nuclei. Integrating the equation 5.15, the number of ^{7}Be nuclei for a given time $N_1(t)$ is given by:

$$N_1(t) = \frac{R}{\lambda} \cdot (1 - e^{-\lambda \cdot t}) \tag{5.17}$$

and thus, clearing R up:

$$R = \frac{N_1(t) \cdot \lambda}{1 - e^{-\lambda \cdot t}} \tag{5.18}$$

Denoting as T_{IMP} the total implantation time shown in Table 3.2, the reaction rate R during the experiment is:

$$R = \frac{N_{\mathrm{IMP}} \cdot \lambda}{1 - e^{-\lambda \cdot T_{\mathrm{IMP}}}} \tag{5.19}$$

where N_{IMP} is the number of nuclei in the catcher at end of the implantation as shown in equation 5.14. Therefore, the total number of ^{7}Be nuclei produced will be given by:

$$N_{^7Be} = R \cdot T_{\mathrm{IMP}} \tag{5.20}$$

The values for the implantation times were given in Table 3.2, while the net counts under the 478 keV peak, the decay times T_d the lost times T_l are shown in Table 5.4.

Year	$E_{^3\mathrm{He}}$ (keV)	N (counts)	T_d (d)	T_l (d)
2009	2306.28 ± 2.37	399±77	0.411	19.848
	3208.05 ± 2.99	1094.8± 82.2	0.356	36.843
	4410.42 ± 3.82	541.97±52.6	0.336	48.845
	4811.20 ± 4.09	845.72±80.3	0.213	30.567
	5312.19 ± 4.44	1938.8±84.0	0.274	16.225
2011	2105.89 ± 2.23	538.0±78.1	0.426	29.398
	2506.67 ± 2.51	934.9±64.4	0.485	22.792
	2807.26 ± 2.71	911.0±72.5	0.452	23.573
	4009.63 ± 3.54	2488.0±66.1	0.673	16.965
	4811.20 ± 4.09	1487.3±86.6	0.279	13.795

Table 5.4: *Variables for the determination of the number of ^{7}Be recoils produced during the activation experiment at CMAM in Madrid. For the different energies shown in the second column, the net number of counts under the 478 keV γ peak are shown in the third column. The fourth column shows the decay times while the fifth ones shows the lost time since the implantation finishes until the decay time starts.*

5.1.3.3 Error contributions

The errors associated to the total number of ^{7}Be recoils have statistical and systematic contributions. The relative (percentage) statistical errors for the produced ^{7}Be recoils are the same as those given for the net number of counts under the 478 keV peak as defined by the expression 5.7. A 2.33% systematic contribution is quoted based on the uncertainties of the different parameters shown in Table 5.5.

Parameter value	Error Contribution
$T_{1/2}$ (53.353±0.05) days	0.18%
B.R. 1st state in ^{7}Li (10.44±0.04)%	0.38%
HPGe efficiency (4.36±0.10)%	2.29% (*)

Table 5.5: *Systematic contribution to the uncertainty in the number of ^{7}Be recoils.*
(*) For the catchers implanted with beam energies of ∼2.10, ∼2.8 and ∼3.8 MeV, the HPGe detector was replaced with another one with $\varepsilon = (3.79 \pm 0.001)$% and thus a total error contribution raised to 2.90%.

5.1.4 Estimation of the reaction energy at the centre of mass system

In order to estimate the astrophysical S-factor as defined in the expression 1.7 the energy of the reaction in the centre of mass system is required. In reference [NHNEH04] where the same setup was used, the authors compare E_{CM} calculated assuming that the reaction takes place at the centre of the target and $\overline{E}_{CM}$ by the effect of considering a target of finite energy width (ΔE_T). For E_{CM}=420 keV they compute only a difference of 0.3 keV (0.1%); in our case, where the energies are even larger, this difference is even lower. Thus, we can consider that, on average, the reaction occurs at the centre of the gas target including a negligible error and therefore, the expression 5.2 becomes:

$$E_{CM} = \frac{m_{^4He}}{m_{^4He} + m_{^3He}} \cdot \left(E^{beam}_{^3He} - \Delta E_{Ni} - \frac{\Delta E_{^4He}}{2} \right) \tag{5.21}$$

where $m_{^4He}$ and $m_{^4He}$ are the target and beam nuclei masses in mass units respectively. $E^{beam}_{^3He}$ is the incoming beam energy as shown in Table 5.4 and ΔE_{Ni} and $\Delta E_{^4He}$ are the energy losses in the Ni foil and the whole gas target length respectively.

The energy lost by the beam when crossing the Ni foil and half of the gas length, $\Delta E_{Ni} + \frac{\Delta E_{^4He}}{2}$, is obtained by simulating 10^5 ^{3}He beam particles at the corresponding energies using the TRIM code [SRI]. The ^{3}He nuclei impinge onto a target composed of two layers: 1) 1.03 μm of a solid Ni foil and 2) ^{4}He gas target with densities calculated using the pressures and temperatures shown in Table 5.3 and lengths half of those shown in the same table. An example for the simulated output energy spectrum using a ~4 MeV beam energy and the corresponding target layers is displayed in Figure 5.9.

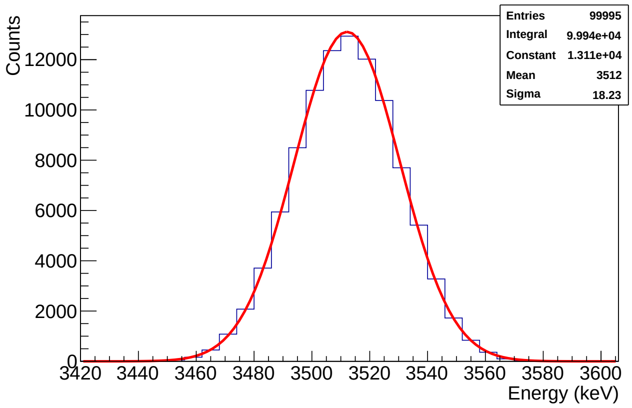

Figure 5.9: *Energy spectrum from a TRIM simulation for a ^{3}He beam at 4009.63 keV crossing a 1.03 μm Ni foil and a 6.55 cm long ^{4}He gas target at 60.18 Torr and 307.81 K. The red curve shows a Gaussian fit to the spectrum and the numbers enclosed in the box show the value of the fit parameters.*

The output energies are fitted to Gaussian functions and the mean of the fit (3512 keV for the example in Figure 5.9) represents the beam energies at the centre of the target that is, the value for all the terms enclosed in the brackets in expression 5.21. The centre of mass energy is then calculated by multiplying this mean energy by $\frac{m_{^4He}}{m_{^4He}+m_{^3He}}$.

The uncertainty associated to the centre of mass energy has been estimated by:

$$\Delta E_{CM} = \frac{m_{^4He}}{m_{^4He} + m_{^3He}} \cdot \Delta E \tag{5.22}$$

where ΔE is the error associated to the energy at the centre of the target, calculated by properly adding to the uncertainty of the beam energy (Table 3.2) the σ value from the Gaussian fit.

5.2 Astrophysical S-factors I: Measurements using the Activation Method

The results for the Activation experiment performed at CMAM are shown in the last two columns in Table 5.6. For the different beam energies displayed in the first column, the second column shows the corresponding centre of mass energies calculated as detailed above. The third column shows the number of beam particles estimated using the charge integration method. The fourth and fifth columns show the total number of target and recoil nuclei for each energy. The cross section is shown in the sixth column and the astrophysical S-factor for the different energies calculated by using the expression 5.1 is shown in the last column. The uncertainties of the different parameters are shown between brackets. The errors for the cross section and astrophysical factor have been obtained by standard error propagation. For the values of $N^{beam}_{^3He}$ and $N^{target}_{^4He}$ the uncertainties refer the systematic contribution while the statistical contribution is negligible. For the case of $N^{recoils}_{^7Be}$, σ_{34}(E) and S_{34}(E) the uncertainties are divided into statistical (first) and systematic (second).

$E^{beam}_{^3He}$ (keV)	E_{CM} (keV)	$N^{beam}_{^3He}$ ($\cdot 10^{16}$)	$N^{target}_{^4He}$ ($\cdot 10^{19}/cm^2$)	$N^{recoils}_{^7Be}$ ($\cdot 10^6$)	σ_{34}(E) (μb)	S_{34}(E) (keV$\cdot$ b)
2306.28±2.37	915.78±12.21	2.83(5)	2.34(2)	1.31(25)(3)	1.98(38)(6)	0.411(79)(15)
3208.05±2.99	1498.91±12.56	4.99(10)	2.65(2)	4.05(30)(9)	3.06(23)(10)	0.318(24)(11)
4410.42±3.82	2267.71±12.47	5.23(6)	1.67(5)	4.74(46)(11)	5.43(53)(22)	0.386(37)(16)
4811.20±4.09	2511.12±12.62	3.22(3)	1.68(4)	3.19(30)(7)	5.88(56)(21)	0.391(37)(14)
5312.19± 4.44	2804.10±12.82	3.89(4)	2.28(2)	6.05(26)(14)	6.82(29)(19)	0.424(18)(12)
2105.89±2.23	777.17±12.70	4.17(2)	2.40(2)	1.49(22)(4)	1.49(22)(4)	0.418(61)(18)
2506.67±2.51	1054.15±12.31	4.96(10)	2.23(2)	2.26(16)(5)	2.05(14)(6)	0.339(23)(12)
2807.26±2.71	1249.64±12.41	5.27(4)	2.28(2)	3.61(29)(11)	3.00(24)(9)	0.390(31)(13)
4009.63±3.54	2006.95±12.31	6.77(8)	2.78(2)	7.87(21)(18)	4.70(12)(13)	0.367(10)(10)
4811.20±4.09	2510.00±12.62	3.23(7)	1.45(2)	3.88(23)(11)	6.85(40)(26)	0.455(27)(17)

Table 5.6: *Results for the activation experiment. The first column shows the different beam energies used in the experiment. The second column shows the corresponding centre of mass energies taking into account the energy lost in the Ni foil and gas target. The third, fourth and fifth columns show the total number of particles of the beam, target and recoils, respectively. The sixth and seventh column show the cross section and astrophysical factor for the $^3He(\alpha,\gamma)^7Be$ reaction. The uncertainties for each value are shown between brackets. When only one contribution appear it refers to the systematic error, in case of two contributions the first one refers to the statistical and the second to the systematic error. Recall that the energies in $S_{34}(E)$ and $\sigma_{34}(E)$ refers to E_{CM}.*

The S_{34}(E) values are plotted in Figure 5.10 together with the results from [DGK09, PK63]. The errors displayed in the plot are the statistical uncertainties as it is usually done. Just by eye, it can be seen that our results follow the trend of the ERNA data [DGK09] better than the Parker's results [PK63]. Among all the points, the two at ∼2 and ∼2.5 MeV centre of mass energies are specially relevant. Due to their low uncertainty, they clearly show a complete agreement with ERNA and are rather discrepant comparing with Parker values. Also of special interest is the point at around ∼1 MeV. The same activation and counting setups were used in [NHNEH04] where a measurement at the same energy was performed. An agreement within the experimental errors bars between these points strongly supports the reliability of the new set of measurements.

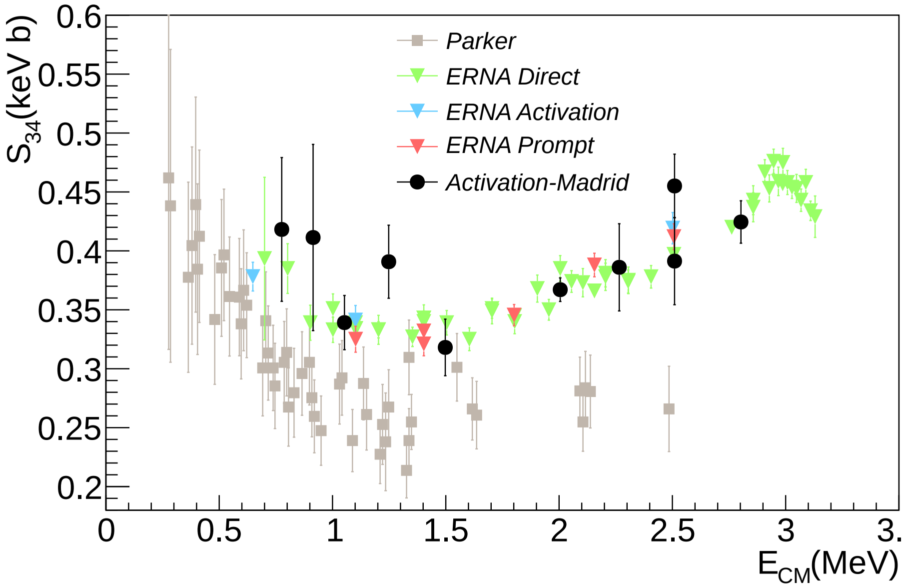

Figure 5.10: *Astrophysical S-factor for the $^3He(\alpha,\gamma)^7Be$ reaction using the activation method in Madrid (black dots). For comparison with previous results, triangles and squares show the results from [DGK09] and [PK63] respectively.*

In the next chapter a detailed quantitative analysis comparing our results with both Parker and ERNA is done as well as a comparison with the different theoretical models available.

5.3 Analysis II: Measurements using the Direct Recoil Counting Method

As in the *Activation Experiment*, the astrophysical factor for the *Direct Detection Experiment* is given by the expression 5.1. In this case, the reaction was done using inverse kinematics, that is a ^{4}He beam impinging onto a ^{3}He target, and thus the cross section and centre of mass energy are given by:

$$\sigma_{34} = \frac{Y_{^7Be}}{N^{\circ B}_{^4He} \cdot N^{\circ T}_{^3He}} \tag{5.23}$$

and

$$E_{CM} = \frac{m^T_{^3He}}{m^B_{^4He} + m^T_{^3He}} \cdot E^{beam} \tag{5.24}$$

respectively. Where, in this case, the $N^{\circ B}_{^4He}$ is the total number of beam particles, $N^{\circ T}_{^3He}$ is the gas target areal density, and $Y_{^7Be}$ is the total number of recoils produced. $Y_{^7Be}$ is estimated based on the recoils detected in the final DSSSD placed at the focal plane of the accelerator (Y_{DSSSD}).

The locations marked in Figure 5.11 indicate where the observables required to determine σ_{34} are measured. In the following sections the detailed data analysis of these quantities is outlined.

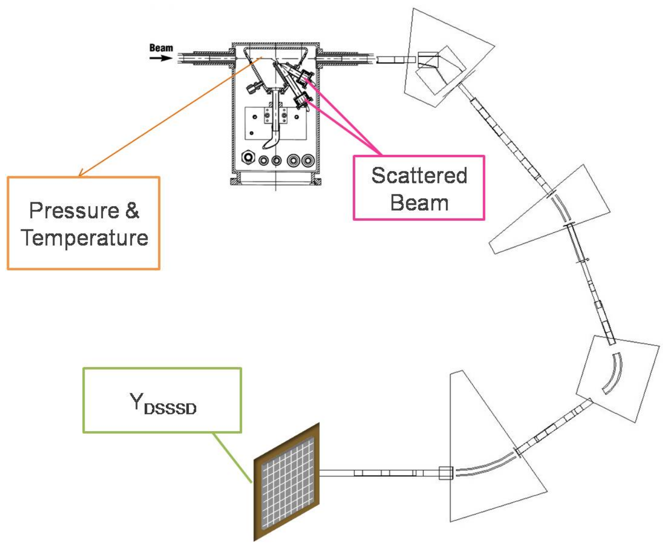

Figure 5.11: *Experimental setup diagram for the Direct Recoil counting method at TRIUMF. The different observables required to extract σ_{34} are indicated. Note that this schematic is not shown to the scale.*

5.3.1 Estimation of the reaction energy at the centre of mass system

In the same way than as in *Activation Method* experiment, we can assume that on average the reaction is produced at the centre of the gas target and thus the averaged centre of mass energy will be given by:

$$E_{CM} = \frac{m_{^3He}}{m_{^4He} + m_{^3He}} \cdot \left(E^{beam} - \frac{\Delta E_{^4He}}{2} \right) \tag{5.25}$$

where $\Delta E_{^4He}$ is the energy loss of the beam in the gas target that has been determined by simulating 10^5 particles using the TRIM code [SRI] following the same procedure as the one explained in section 5.1.4. The associated error is estimated from the standard error propagation of the beam energies (Table 3.5) and the mean value of the energy loss obtained from TRIM. Table 5.7 shows the calculated centre of mass energy for every beam energy in the second column.

$E_{^4He}$ (keV)	E_{CM} (keV)	Temperature (T) (K)	Pressure (P) (Torr)
6553.88±2.78	2813.57±1.80	297.11±1.97	5.73 ± 0.12
5165.97±2.41	2216.55±1.68	297.64±1.99	5.96 ± 0.21
4716.45±2.00	2023.73±1.42	301.55±1.61	5.02 ± 0.19
3521.61±1.50	1508.91±1.29	297.30±2.03	5.96 ± 0.17

Table 5.7: *Beam energies, the corresponding centre of mass energy at the centre of the target cell, the average target pressure and temperature of the gas in the beam path are shown in columns 1, 2, 3 and 4 respectively.*

5.3.2 The ^{3}He gas target areal density: $N^{\circ}T_{^{3}He}$

The gas target areal density is determined by the expression N_t=9.66 · $10^{18}\frac{\ell \cdot P}{T_0+T_C}$. In this case, the beam heating is negligible, i.e. T_C=0.

The pressure and temperature were recorded every five minutes during the measurements. An averaged pressure and temperature is calculated for every run (e.g. Figure 5.17) and a final pressure and temperature for every energy is calculated by averaging the values of all considered runs. The errors associated to the final pressure and temperature are obtained as the standard deviation of the values for the different runs plus a systematic error of 0.1 Torr for the pressure and 1 K for the temperature [GBB04]. An example is shown in Figure 5.12 for the pressure and temperature of the runs taken with ~5.2 MeV beam energy.

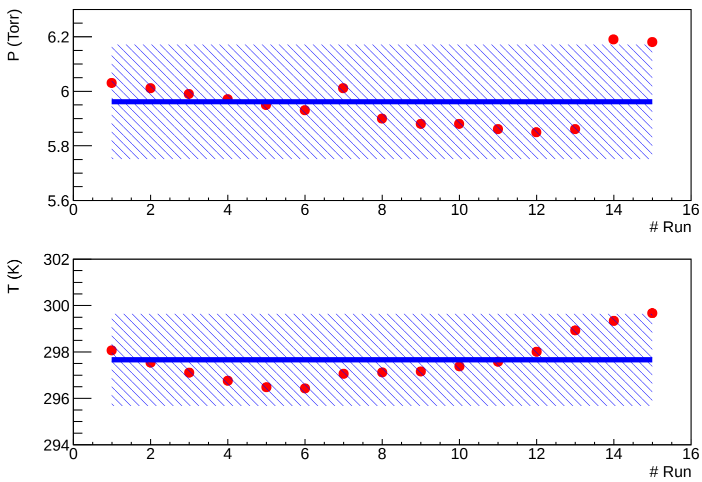

Figure 5.12: *Gas target pressure (top panel) and temperature (bottom panel) for the ~5.2 MeV beam energy case. Each red dot corresponds to the average value for a given run. The blue line gives the average value of the runs. The shaded region show the final errors.*

The red dots indicate the parameter values for different runs, while the blue lines show the final pressure and temperature values calculated as the average of the runs. The shaded regions indicate the uncertainties. Table 5.7 shows the averaged pressures and temperatures for every beam energy.

The effective length of the gas target (ℓ) has been estimated as 12.3±0.5 cm. This is based on two methods; firstly using the energy lost by the ^{12}C beam in the ^{3}He gas target. This measurement was performed to determine the target density profile and the details can be found in section 3.3.3.4. Secondly, using the available systematics from previous experiments where reactions with heavier ions impinging onto ^{4}He gas targets were studied. In the latter case effective lengths were estimated by the beam energy losses.

5.3.3 The number of ^{4}He beam particles: $N^{\circ}B_{^{4}He}$

The number of beam particles is calculated by relating the scattered beam particles detected in the silicon detectors at 30º (Si-30) and 57º (Si-57) with respect to the beam direction, and the Faraday cup readings made at the beginning of each run, that is, approximately every 60 minutes. Due to the fact that the DAQ system was changed between our measurements in 2011 and 2013, two different approaches were used in order to extract the number of beam particles as explained in the following.

The 2011 measurement

The typical spectrum measured in the silicon detector was already shown in Figure 3.36. Complementary to the total spectrum, the information of the number of events per second detected in the silicon detector was also saved, this is the so- called trigger rate (or scaler). Some examples of the trigger rate for each of the three energies in the Si-30 detector are shown in Figure 5.13. The x-axis represents the time, where every channel is two seconds wide and the y-axis corresponds to the number of triggers. Blue (upper panel) and red (lower panel) spectra correspond to the typical runs with constant and with varying trigger rates.

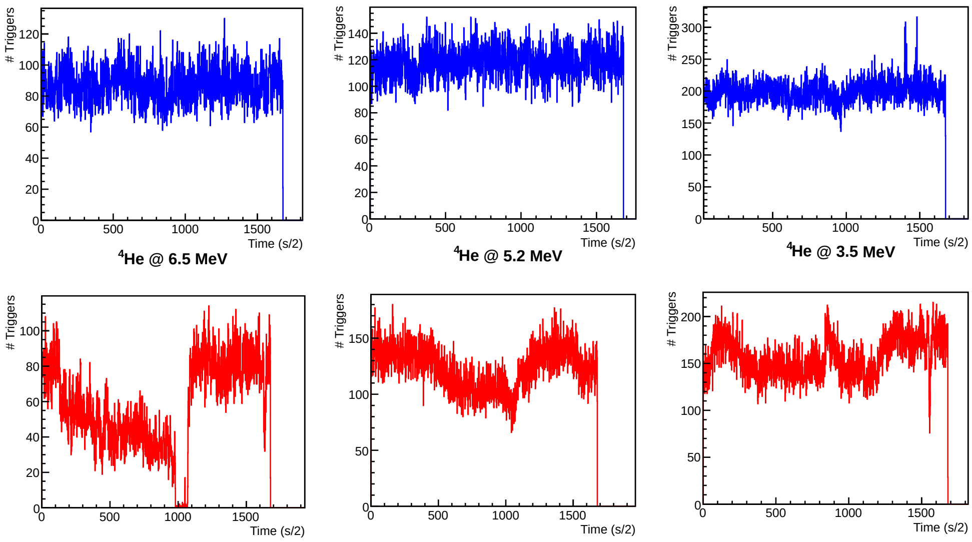

Figure 5.13: *30º silicon detector trigger rates for the different energies measured in the 2011 campaign. For each energy two histograms are plotted. Blue and red runs correspond to nearly constant and largely varying trigger rate conditions, respectively.*

The procedure followed is to obtain an average final normalisation factor (R^F) among those runs with a constant trigger rate (**optimum run**), which essentially means that a constant current throughout the whole run is assumed. Then, this normalisation factor is applied to all the runs to get the number of beam particles. The normalisation factor for an optimum run is defined by:

$$R^{run} = \frac{FC1}{1.602 \cdot 10^{-19} \cdot q} \frac{\text{Time} \cdot \text{Livetime}}{\text{Si-30}} \cdot P \cdot T \tag{5.26}$$

This is the ratio of the number of scattered particles detected in the silicon detector and particles measured with the FC1 at the beginning of each run. Here, "FC1" is the reading of the Faraday cup 1 in Ampere, q=2 is the beam charge state after crossing the target, "Si-30" is the integration of the silicon detector spectrum for each run, "Time" is the time for each run and "Livetime" takes into account the effect of the dead time of the acquisition system. "P" and "T" are the pressure and temperature and are introduced in order to take into account the different number of target particles between different runs.

FC1 readings of of beam current

The current readings were taken automatically at the beginning of each run by using FC4, FC1, FC4, FCCH and FC4 in that sequence. Each measurement took 30 s, approximately. An example for a complete FC1 reading is shown in red in Figure 5.14. The increase and drop in current in the extremes corresponds to the time when the cup is moved in and out, respectively. Therefore, only the central values are considered (see inset in Figure 5.14).

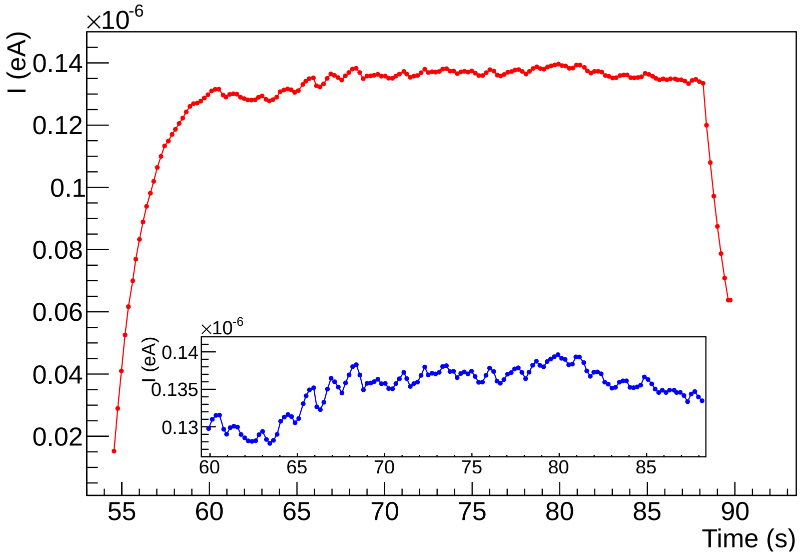

Figure 5.14: *Example for FC1 reading for an optimum run. In red a total measurement for a FC1 reading. The current increase and decrease in the extremes is related to the voltage turned on and off respectively. The inset shows a closer view of the central region considered to extract the averaged value of FC1.*

The average of all the central values of each measurement (i.e. blue points in Figure 5.14 inset) is used as FC1 in the expression 5.26. The error associated to FC1 is the standard deviation of the considered values.

Integration of the peak in the Si-30 spectra

The choice of considering the 30º detector instead of the 57º is based on the statistics. For each of the beam energies measured, Figure 5.15 shows the spectra for the silicon detector at 30º (Si-30) in the upper panel and for the detector at 57º (Si-57) in the lower one at the pressures and temperatures indicated in the figure. The statistics in the scattered peak for the Si-30 spectrum is considerably larger than in the Si-57 one and, due to the kinematics, the higher the energy is the larger the $\frac{\text{Si-30}}{\text{Si-57}}$ ratio is.

As it can be seen in the silicon spectra at 30º, and it was already discussed in section 3.3.2.7, the double peak is due to the scattered ^{4}He beam by the ^{3}He target and vice-versa. The two peaks are clearly separated for the higher energy, while for lower energies it is more difficult to separate both contributions. For this reason, in order to estimate the Si-30 factor in the expression 5.26 the procedure consists of integrating the contribution of both peaks in the optimum files. Figure 5.16 shows an example for the Si-30 spectrum of an optimum run corresponding to ~6.5 MeV beam energy with $1.378{\cdot}10^4$ counts under the two peaks. The associated uncertainty is the square root of the value.

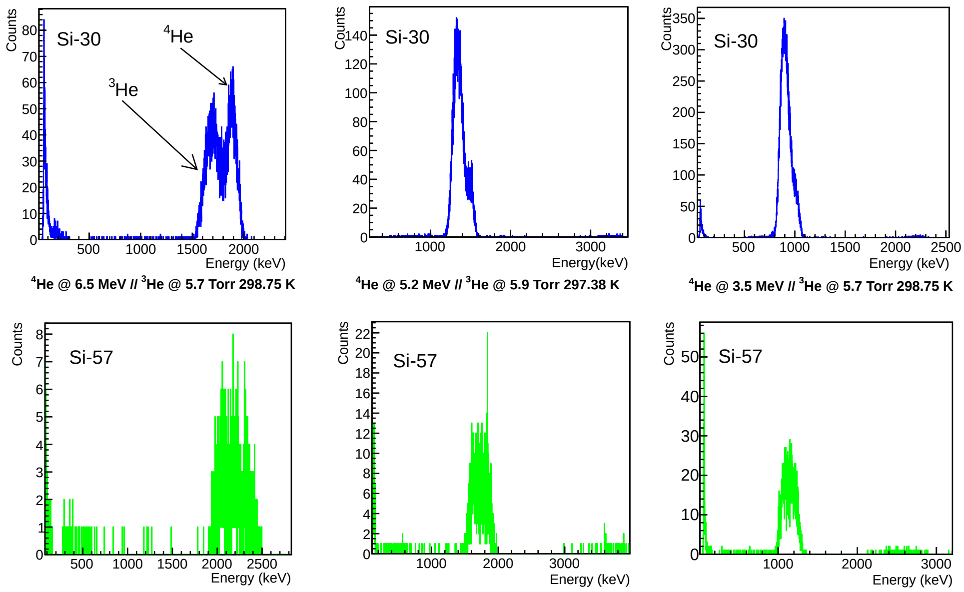

Figure 5.15: *Typical spectra for Si-30 (blue) and Si-57 (green) corresponding to the measurements of the three different energies carried out in 2011.*

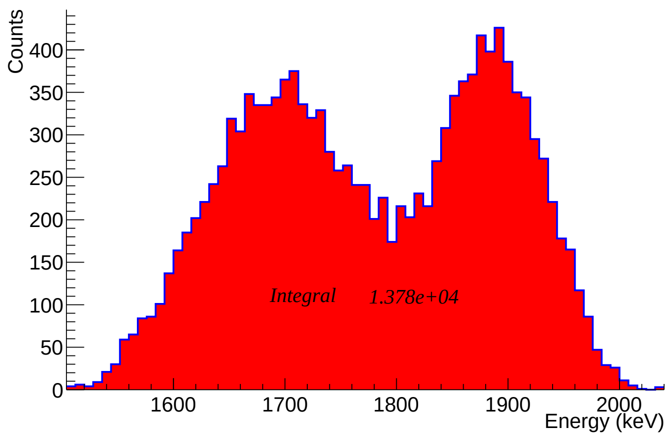

Figure 5.16: *The spectrum shows the scattered particles in the 30° silicon detector for the ^{4}He beam energy of ~6.5 MeV. The integral gives the number of counts under the two peaks corresponding to the Si-30 parameter in the expression 5.26.*

It must be pointed out that for the highest energy case, where the two peaks can be clearly separated, the R^{run} normalisation factors could be calculated by replacing the Si-30 variable by just the integration of the scattered ^{4}He peak. The final results do not depend on whether we use the total spectrum or just the ^{4}He scattered peak.

Time and DAQ livetime

The measurement *time* of each run was saved during the experiment in the MIDAS system.

The *livetime* is calculated by dividing the total number of events recorded (acquired triggers) in the "tail" of DRAGON, by the total number of events received in the tail (total triggers). The latter includes those events which could not be recorded due to the DAQ system was busy processing other events: ($Livetime = \frac{\text{Acq. Trig}}{\text{Total Trig}}$). Considering the square root of the total and acquired triggers as the uncertainties of "Acq. Trig" and "Total Trig" respectively, an associated error to the Livetime has been estimated by using the standard error propagation.

Pressure and temperatures of the target

The pressure and temperature for every run is calculated as the average of the values saved every five minutes. The associated errors are calculated considering the standard deviation of the data plus a systematic error of 0.1 Torr for pressure and 1 K for temperature. Figure 5.17 shows an example for an optimum run taken with 5.2 MeV as beam energy.

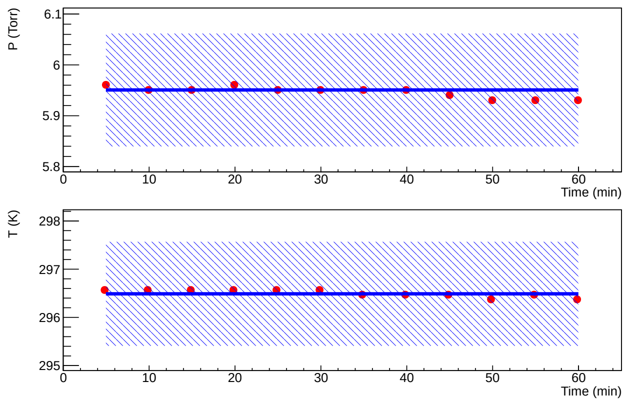

Figure 5.17: *Gas target pressure (top panel) and temperature (bottom panel) for an optimum run of* $\sim$*5.2 MeV beam energy. Each red dot corresponds to one of the values recorded every five minutes. The blue line gives the average value for the given optimum run. The shaded regions show the error considered in order to determine* R^{run}.

After all variables are determined, the normalisation R^{run} factors are obtained for the optimum runs of each energy. The uncertainties associated with the R^{run} factors are calculated using standard error propagation from the errors of every variable (FC1, Si-30, Lifetime, P and T). The final normalisation factors (R^F) are then calculated by the weighed average of all the corresponding R^{run} factors. Figure 5.18 shows the normalisation factors for the three energies. The blue dots are the normalisation factors for the optimums runs (R^{run}) and the red lines show the final R^F factors.

The number of incoming beam particles can then be calculated for any run, including optimum and no optimum runs, by using:

$$N^{oB}_{^4He} = \frac{R^F \cdot \text{Si-30}}{\text{Livetime} \cdot P \cdot T} \tag{5.27}$$

where Si-30, P and T are calculated for any given run using the procedure explained above for the optimum runs. The associated errors in the number of beam particles are calculated by using standard error

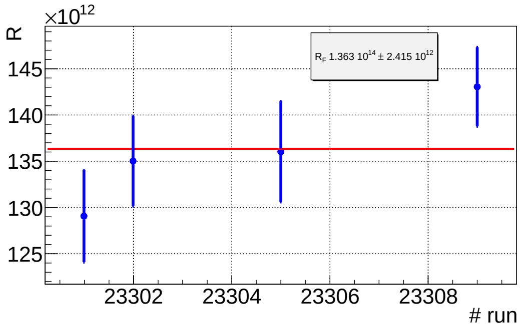

(a)

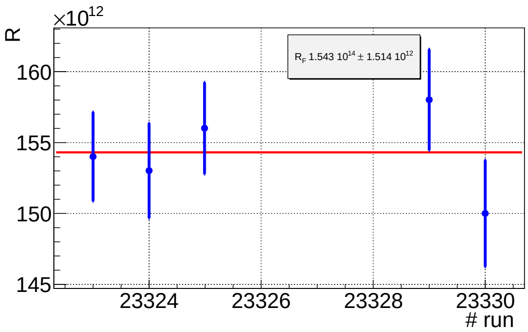

(b)

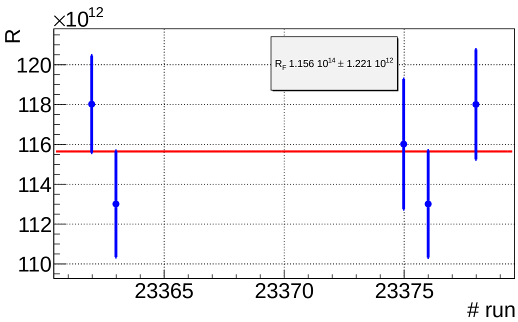

(c)

Figure 5.18: *Normalisation R-factors for the 2011 measurements at energies of ∼6.5 MeV (a), ∼5.2 MeV(b) and ∼3.5 MeV (c). The blue dots represent the normalisation factor for the individual runs, those with a nearly constant trigger rate. The red lines gives the weighted average R_F.*

propagation in the expression 5.27, where the uncertainties for R^F are the ones shown in Figure 5.18 and the uncertainties in P, T, Livetime and Si-30 are calculated as explained above. The total number of beam particles for every energy is obtained by adding $N^{^8B}_{^4He}$ for all the runs.

The 2013 measurements

In the upgraded DAQ system used in 2013, timestamps are recorded for every saved event including those in the silicon spectrum. Therefore, the Si-30 events taken during the same duration than the Faraday cup measurement times could be used to estimate the normalisation factor.

Furthermore, it was already mentioned that during the 2013 measurements, the *Activation Method* was also used with the same beam energy as the *direct recoil counting measurement* (∼4.7 MeV) and target conditions. Therefore, the normalisation factor is the same in both cases and thus all the optimum runs can be taken into account in order to obtain a final R^F factor.

One difference between the *Direct Recoil Counting Method* (direct runs) and the *Activation Method* (implantation runs) at TRIUMF must be considered here: the FC1 is placed after the copper catcher position, therefore just FC4 readings were performed during the implantation runs (see Figure 3.34). Thus, the two R^{run} factors are defined differently for 2013 run as

$$R^{run}_{direct} = \frac{FC1}{1.602 \cdot 10^{-19} \cdot 2} \frac{60 \cdot Livetime}{(Si\text{-}30)^{60s}} \cdot P \cdot T \tag{5.28}$$

for the direct runs and

$$R^{run}_{activ} = \frac{FC4 \cdot Trans}{1.602 \cdot 10^{-19} \cdot 2} \frac{60 \cdot Livetime}{(Si\text{-}30)^{60s}} \cdot P \cdot T \tag{5.29}$$

for the implantation runs. "P","T" and "Livetime" are the same as before and are determined as in the 2011 experiment. "Trans" is the beam transmission through the target, which is the ratio between the FC4 and FC1 readings in the direct measurements, and has been estimated to be 94.09%. Finally, $(Si\text{-}30)^{60s}$ is the total number of scattered events during the first 60 seconds of the run taken in the 30° silicon detector (see example in Figure 5.19).

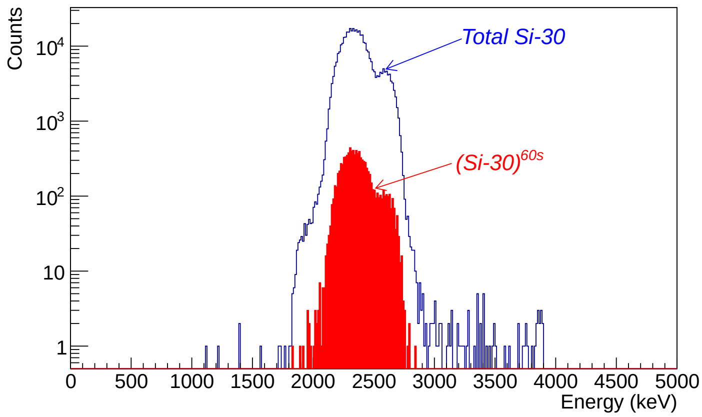

Figure 5.19: *The total 30° silicon spectrum for a 60 minutes run is shown in blue. The part of the spectrum taken during the first 60 s of the run is shown in red. The integral under the red curve is the $(Si\text{-}30)^{60s}$ parameter for the expressions 5.28 and 5.29, as part of the normalisation procedure.*

Figure 5.20 shows the normalisation R^{run} factors (blue) for the optimum runs of the 2013 experiment and the red line shows the final R^F factor obtained as the average of all the values.

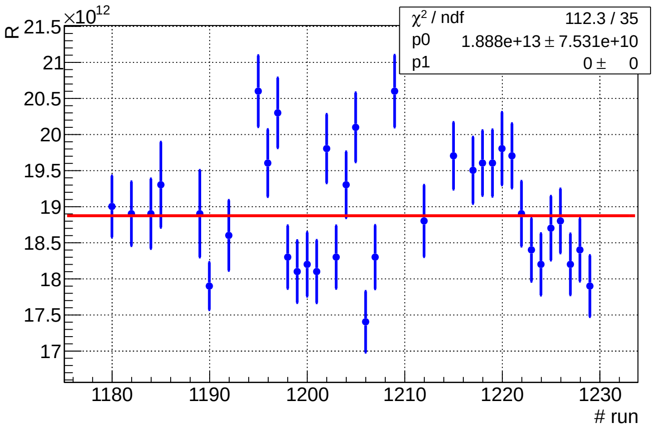

Figure 5.20: *The blue dots show the normalisation factors for the optimum runs in the 2013 measurements. The red line corresponding to the weighted average of the blue dots gives 1.888 ·10^{13} ± 7.531 · 10^{10} for the R^F factor.*

The total number of beam particles for every run is then estimated by using the expression 5.27 with R^F = 1.888 ·10^{13} ± 7.531 · 10^{10}.

5.3.4 The ^{7}Be recoils produced in the direct recoil counting method: $Y_{^7Be}$

The expression 3.16 ($Y_{^7Be} = \frac{Y_{DSSSD}}{t_\ell \cdot q_f \cdot \epsilon_{DRAGON} \cdot \epsilon_{DSSSD}}$) establishes how to determine the total number of recoils for the *Direct Recoil Counting Method* at TRIUMF. In the previous chapter it was discussed how to obtain the acceptance of DRAGON (ϵ_{DRAGON}). In the following, the analysis performed in order to extract the other variables required to estimate $Y_{^7Be}$ is presented.

5.3.4.1 Total counts in the focal plane DSSSD: Y_{DSSSD}

The separator was tuned to select a specific charge state for the ^{7}Be recoils, that were transmitted through the separator and detected in the final DSSSD at the focal plane of the separator (Y_{DSSSD}). Table 5.8 shows the selected charge state and the ^{7}Be recoil energy obtained from the magnetic fields in MD1, for the different incoming beam energies.

$E_{^4He}$ (MeV)	^{7}Be Charge state	$E_{^7Be}$ (keV)	Y_{DSSSD} (Counts)
∼ 6.5	3+	3734.51	33465
∼ 5.2	3+	2940.21	141707
∼4.7	2+	2642.67	52683
∼3.5	2+	1997.32	44135

Table 5.8: *Details of the charge state and energy of the ^{7}Be recoils for the different ^{4}He incoming beam energies. The last column shows the total number of recoils detected in the DSSSD.*

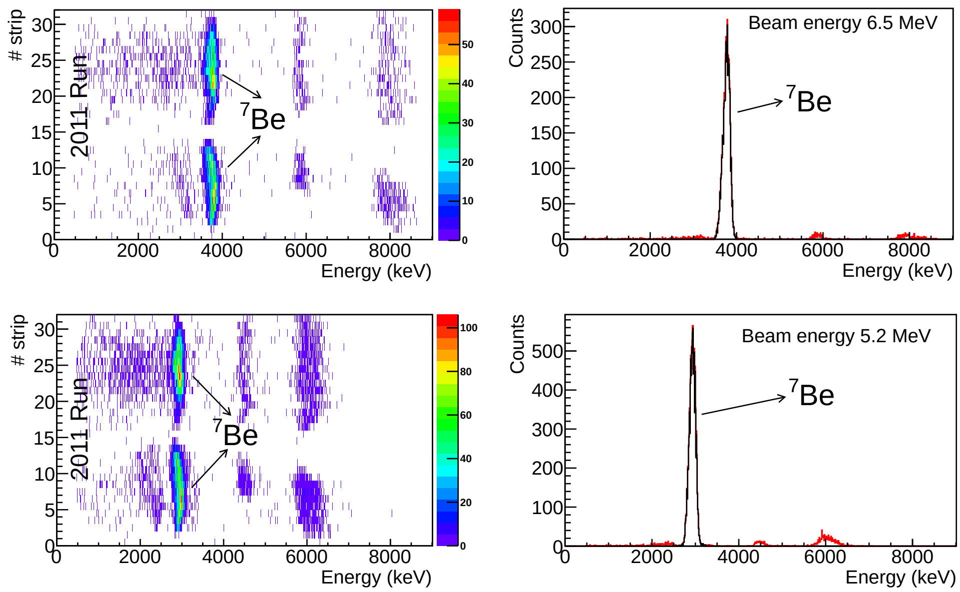

Figure 5.21: *For the two highest energies studied, the left side shows the two dimensional spectra for the ^{7}Be recoils in the DSSSD strips. The right side shows the projected histograms for the strips 1 to 15, in red. The coincide front-back events in the selected energy region are shown in black*

In order to obtain the parameter Y_{DSSSD}, the events in the DSSSD are treated event by event. First of all the calibration equation for the hit strip (see section 3.3.3.1) is applied to the energy channel corresponding to the hit. The result is the value of the deposited energy in the active area of the detector. Then, the energy loss in the dead layer is calculated based on the deposited energy and the values from the SRIM code assuming a ^{7}Be crossing a 0.5 μm effective aluminum layer. The energy loss is added to the deposited energy and thus the incident energy of the recoil is obtained.

For the different beam energies studied, Figures 5.21 and 5.22 show, on the left side, the total energy versus the strip number in two dimensional histograms for the given runs. The recoil peaks are identified in both the front side strips, 0-15, and the back side strips, 16-31. The right side of Figures 5.21 and 5.22 show the projections in the x-axis from strips 0-15, that is, all events in the front strips for the given run. Superimposed, the black spectra show those events in the selected energy region of the recoil peak which have a coincident hit in the back side in the same energy region (front-back coincidence events). Figure 5.21 shows the two highest energies studied where the ^{7}Be charge state was 3^+. As it can be seen, there is not any unreacted beam contribution in the recoil peak as it was expected from the beam suppression studies detailed in the section 3.3.3.2. However, for the two lowest energies, where the recoil charge state selected was 2^+, the unreacted beam particles reaching the DSSSD could interfere with the proper ^{7}Be recoil peak as it can be seen in Figure 5.22.

In order to study a likely contribution of the unreacted beam to the recoil peak for the cases with 2^+ charge state, the MCP device (see section 3.3.2) was placed before the DSSSD detector and some runs were taken during the 2013 measurements. As the beam and recoil ions travel with different velocities, the time for crossing the two MCPs is different. Thus, the idea is to compare the time of flight of the ions between the two MCPs with the DSSSD spectra. The histogram in Figure 5.23 (upper panel) shows the energy in the DSSSD versus the time amplitude converter (TAC) from the two signals of the MCPs, for all the runs taken with the MCP in. As it can be seen the ^{7}Be recoils are clearly identified and separated from the beam particles. Therefore, the energy region shown in black in Figure 5.22, considered for the recoils

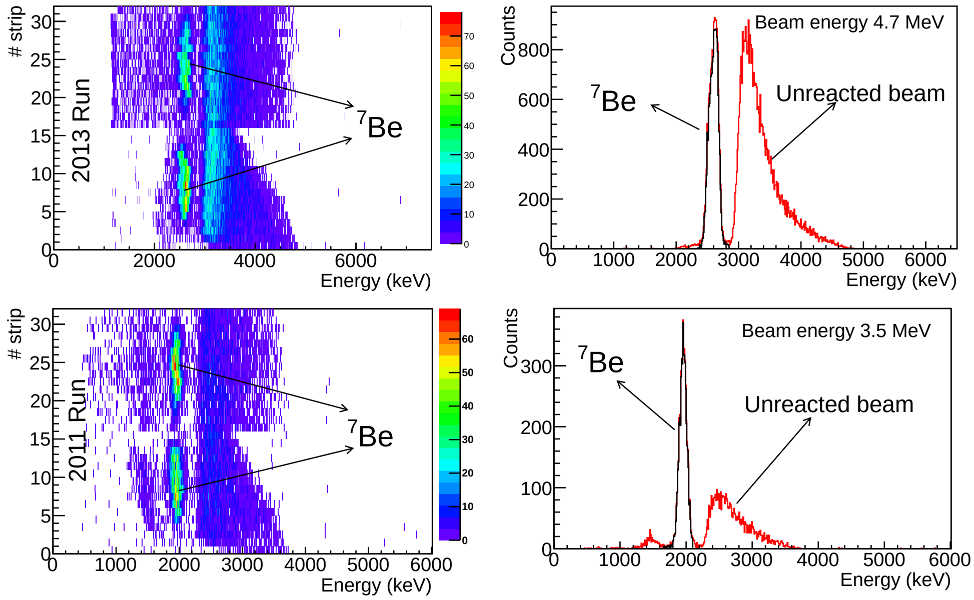

Figure 5.22: *Same as in Figure 5.21 for the two lowest energies studied, with 2^+ charge state.*

selection in the DSSSD, is justified.

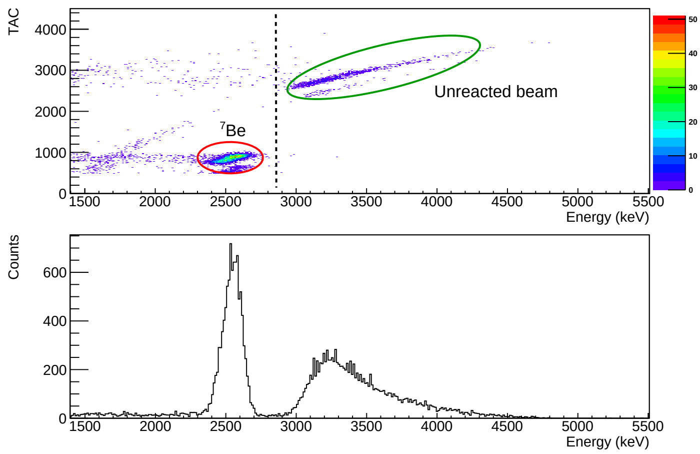

Figure 5.23: *The upper panel shows the DSSSD energy deposited in the DSSSD versus MCP-TAC histogram. The red circle encloses the ^{7}Be recoils which are clearly separated from the unreacted beam particles, enclosed in the green circle. The lower panel shows the projection in the x-axis of the upper histogram.*

It must be pointed out that those runs where the MCP was used are not considered to determine our final cross section. This is due to the fact that some of the recoils are stopped in the MCP strips, resulting in systematic errors. Also, in the lower panel in Figure 5.23 it can be observed that when the MCPs are inside the separation between beam and recoils peaks is even better due to the different energy losses through the MCP. However, the energy losses are small and the separation can be extrapolated to the case with MCPs out.

The number of ^{7}Be recoils has been determined for every run individually by demanding a front-back coincidence in the energy region where the recoils should be in the DSSSD strips. Next, the final number of recoils, Y_{DSSSD}, can be obtained by adding all individuals runs. The values of Y_{DSSSD} for the different energies are shown in the fourth column in Table 5.8 where only the statistical uncertainty is considered for this quantity.

5.3.4.2 Experimental efficiencies: t_ℓ, ϵ_{DSSSD} and q_f

The DAQ livetime (t_ℓ) is determined for every run by dividing the acquired triggers and the total triggers in the "tail" of DRAGON (t_ℓ=$\frac{\text{Acq. Triggers}}{\text{Total Triggers}}$). In order to determine the mean value of t_ℓ for every energy, the acquired and total triggers for all runs have been added. A negligible error is estimated using statistical error propagation of the acquired and total triggers. The second column in Table 5.9 shows the t_ℓ parameter for the different energies of interest.

$E_{^4He}$ (MeV)	t_ℓ (%)	ϵ_{DSSSD} (%)	q_f (%)
∼6.5	84.12	96.15±0.10	(3+)59.05±1.87
∼5.2	92.34	96.15±0.10	(3+)61.87±2.55
∼4.7	94.18	96.15±0.10	(2+)29.31±3.81
∼3.5	98.64	96.15±0.10	(2+)52.30±3.33

Table 5.9: *t_ℓ,ϵ_{DSSSD}, and q_f parameters.*

An efficiency of $\boldsymbol{\epsilon_{DSSSD}}$= 96.15±0.10% has been considered for the DSSSD based on the results in reference [WHRD03]. The loss of efficiency is coming from the insulating gap between the neighbouring strips. When a charged particle hit the gap, it creates a reduced pulse height in the strips in comparison to a particle entering through a proper strip. The authors determined experimentally the effective gap width by using an ^{241}Am α source and a 180 μm slit and compared it with the strips width. The results showed that (3.85±0.10)% of α particles incident on the detector have a reduced pulse height.

The values for the charge state fraction, i.e. q_f, are based on the CSD measurements detailed in section 3.3.3.3 which only depend on the velocity, atomic number of the incident ion and the mass of the target. Therefore, in order to obtain q_f, the velocities (energies per nucleon, -E/u-) of the incoming ^{9}Be beam in the CSD measurements must be matched with the velocities of the ^{7}Be recoils when they are created. However, the ^{7}Be recoils energies depends on where they are created through the gas and the γ-ray emission angle, and thus a central value must be considered. Table 5.10 shows the calculated recoils E/u values for the recoils created at the entrance, centre, and the end of the gas target for γ emission angles of 0º, 90º and 180º in laboratory system. In bold are shown the central energies per nucleon corresponding to the recoils created when the reaction takes place at the centre of the gas target and the γ emission angle is 90°. For the ∼6.5, ∼5.2 and ∼3.5 MeV beam energies, the central recoil energies per nucleon are similar within the errors to the ^{9}Be E/u shown in Table 3.6 for the charge state distribution measurements. Therefore, for these three energies the q_f values shown in Table 5.9 are the same as the charge state distribution in Table 3.6. For the case of ∼4.7 MeV beam energy, the 2^+ charge state fractions have been interpolated to the corresponding 383.30 keV/u recoil energy. Figure 5.24 shows the values for the distribution of the 2^+ charge state for the different energies and a second order polynomial (CSD(2^+)=p0+(E/u)·p1+(E/u)^2·p2) fit.

E^{beam} (^{4}He) (keV)	ENTRANCE (keV/u)	MIDDLE (keV/u)	END (keV/u)	θ_γ (º)
	511.55	511.08	510.61	0
6553.94	533.49	**532.99**	532.50	90
	553.39	553.47	552.96	180
	403.67	403.08	402.49	0
5165.97	420.45	**419.83**	419.22	90
	436.25	435.61	434.97	180
	368.65	368.12	367.60	0
4716.45	383.85	**383.30**	382.75	90
	398.20	397.63	397.06	180
	275.35	274.56	273.77	0
3521.61	286.57	**285.76**	284.93	90
	297.26	296.41	295.56	180

Table 5.10: *For the different incoming beam energies shown in the first column, the third fourth and fifth columns show the energy per nucleon of the recoils depending on where the reaction takes place (entrance, middle or end of the gas target). For each scenario three different energies are shown depending on the γ output angle (0°, 90°, and 180°).*

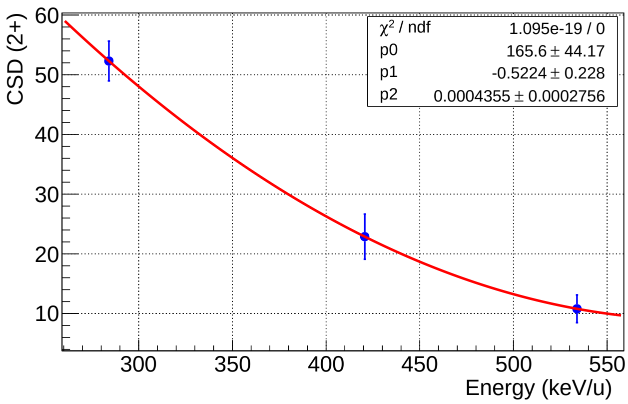

Figure 5.24: *2^+ Charge state distribution interpolation. The blue dots indicate the values for the beam energies used in the charge state distribution measurements for the 2^+ case (see Table 3.6). The red line shows a second order polynomial fit to the values. The parameters from the fit are shown in the plot.*

The q_f value for the 383.30 keV/u recoil energy estimated from the fit is shown in Table 5.9. A detailed description of the associated uncertainties to the q_f values is given in Appendix C.

5.3.5 The ^{7}Be recoils produced in the activation method @ TRIUMF

The procedure followed to determine the number of implanted recoils is the same as in the Madrid experiment. The activated Cu catcher was measured at the same low-background HPGe station in Israel (see Figure 3.12) where the gamma spectrum activity was taken during 12 days and it is shown in Figure 5.25.

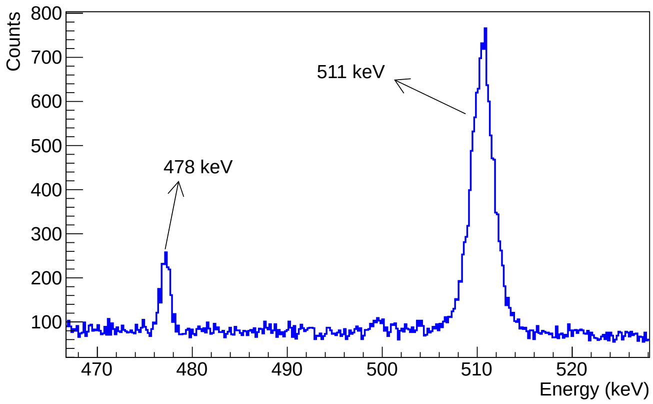

Figure 5.25: *Gamma radiation activity spectrum from sample obtained in the activation measurement at TRIUMF. The 478 keV peak from the de-excitation of ^{7}Li as well as the 511 keV background peaks are marked.*

The number of γ counts under the 478 keV peak is determined as detailed in section 5.1.3.1 and the procedure followed to estimate the total number of ^{7}Be nuclei produced is the one explained in section 5.1.3.2.

Two extra correction factors must be considered in this activation measurement in comparison with the Madrid experiment. Firstly, the Cu catcher is placed further away from the target cell compared to the Madrid experiment, ∼85 cm downstream (see Figure 3.34), and therefore, the recoil spot dimension is larger. Figure 5.26 shows the recoil spot at 85 cm as obtained from GEANT 3 simulations of DRAGON. The efficiency of the HPGe detector for this recoil spot has been obtained by performing GEANT 4 simulations of the recoil distribution and the HPGe detector using a code which has been verified for the activation experiment in Madrid. The efficiency value obtained for the 478 keV γ-ray is 0.0393±0.0012 (3% systematic error).

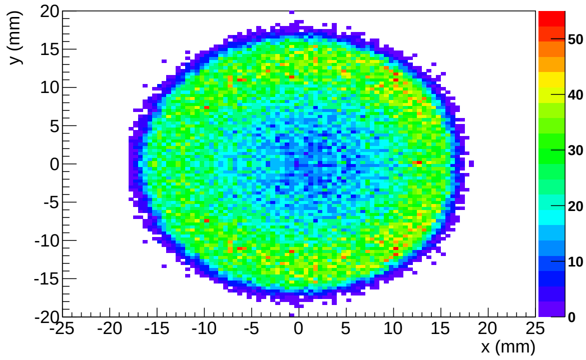

Figure 5.26: *Recoil spot at* 85 *cm obtained from the simulations for activation method at TRIUMF*

Secondly, not all recoils created reach the Cu catcher, being some of them stopped in the target cell, target box, and pumping tubes placed before 85 cm. According to the final series of the simulations, at $E_{beam} \sim 4.7$ MeV (fourth row in Table 4.6) from the 28.3% of the recoils stopped throughout the whole separator, 18.5% are stopped before 85 cm.

Table 5.11 shows the values considered to determine the total number of ^{7}Be produced.

Parameter	Value
Implantation time T_{IMP} (d)	1.16
Decay time T_d (d)	12.0
Lost time T_l (s)	24.5
HPGe efficiency ϵ_A	3.93%
478 keV γ's N	1113
Recoils stopped pumping tubes	18.5%

Table 5.11: *Value of the parameters for the activation measurement at TRIUMF in order to estimate the number of ^{7}Be recoils produced as defined in section 5.1.3.2. The extra factor "Recoils stopped pumping tubes" includes the correction due to the recoils stopped before reaching the Cu catcher as obtained from the GEANT 3 simulations.*

5.4 Astrophysical S-factors II: Measurements using Direct Recoil Counting Method

The results for the all observables together with the obtained cross section and astrophysical S-factor for the direct detection method experiments are displayed in Table 5.12. The errors for all observables, σ_{34} and S_{34}(E) are shown between brackets and a detailed description of how they are obtained is given in Appendix C.

Run	$\sim E_{^4He}$ (MeV)	E_{CM} (keV)	$N^{beam}_{^4He}$ ($\cdot 10^{16}$)	$N^{target}_{^3He}$ ($\frac{\cdot 10^{18}}{cm^2}$)	$N^{recoils}_{^7Be}$ ($\cdot 10^5$)	σ_{34}(E) μb	S_{34}(E) (keV$\cdot$ b)
2011	6.5	2813.6±1.8	0.84(1)	2.29(11)	$1.22(1)(^{+6}_{-14})$	$6.32(8)(^{+44}_{-80})$	$0.393(5)(^{+27}_{-49})$
	5.2	2216.6±1.7	3.25(2)	2.38(13)	$4.47(4)(^{+43}_{-47})$	$5.78(5)(^{+63}_{-69})$	$0.419(4)(^{+46}_{-50})$
	3.5	1508.9±1.3	2.09(1)	2.38(12)	$1.74(1)(^{+15}_{-17})$	$3.48(3)(^{+35}_{-38})$	$0.359(3)(^{+36}_{-40})$
2013	4.7	2023.7±1.4	3.03(3)	1.98(11)	$2.77(3)(^{+38}_{-44})$	$4.62(4)(^{+68}_{-79})$	$0.359(3)(^{+53}_{-61})$
(Impl)	4.7	2023.7±1.4	26.5(1)	1.94(10)	28.8(20)(29)	6.22(44)(72)	0.484(34)(56)

Table 5.12: *Results obtained from the direct recoil counting experiment. The second column shows the different beam energies used in the experiment. The third column shows the corresponding centre of mass energies taking into account the energy losses. The fourth, fifth and sixth columns show the total number of particles in the beam, target and recoils respectively. The seventh and eighth columns show the cross section and astrophysical factor for the ^{3}He(α,γ)^{7}Be reaction. The uncertainties for each value are shown between brackets. When only one contribution is shown, it refers to the systematic error, and in case of two contributions the first one refers to the statistical uncertainty and the second one to the systematic error (positive and negative systematic uncertainties contributions are separated in some cases).*

The results are displayed in Figure 5.27 together with our Madrid results and literature data. As conventional, the errors displayed in the plot are only the statistical errors. As it can be observed, the associated errors for the direct method at TRIUMF are negligible.

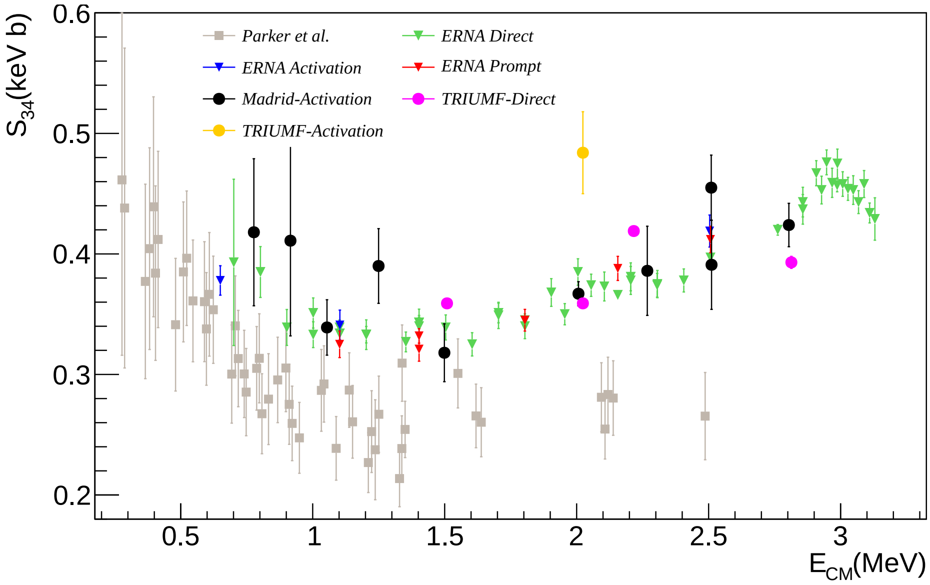

Figure 5.27: *Astrophysical S-factor for the $^{3}He(\alpha,\gamma)^{7}Be$ reaction using the direct recoil counting method (violet dots) and the activation method (yellow dot) in the experiments performed at TRIUMF. For comparison with previous results, the results from [DGK09] and [PK63] are shown with triangles and squares respectively. Our results obtained in the Madrid experiments are shown with black dots.*

At first glance, it can be seen that the astrophysical S-factors obtained agree with the results from Madrid experiment as well as with ERNA data and disagree with Parker ones. In the next chapter the comparison between our results and previous ones will be studied in more detail.

5.5 Conclusion

In this chapter, the results and analysis techniques used to deduce the observables required to determine the astrophysical S-factor for the two experiments have been detailed.

For the activation experiment in Madrid, the two techniques used to determine the number of ^{3}He beam particles have been compared. The pressure stability of the ^{4}He gas target has been shown in order to detail how the number of target particles are estimated. The detailed analysis performed in order to measure the ^{7}Be activity in the Cu catcher as well as the inferred number of recoils produced are given. The results agree with the measurement performed using the ERNA separator [DGK09] and disagree with those in reference [PK63].

For the direct counting recoil experiment at TRIUMF, the number of ^{4}He beam particles was determined using the scattered beam particles with the gas target. Due to the upgrading of the acquisition system between the 2011 and 2013 measurements, the methods used to estimate the number of beam particles are shown separately for the two cases. The number of target particles is determined very precisely due to the continuous monitoring of target pressure and temperature during the measurements. The effective target length is based on the experimental target density profile measurements detailed in

Chapter 3, and previous experiments with DRAGON. For the number of ^{7}Be recoils created, the detailed description of the procedure to obtain the number of recoils reaching the DSSSD is given. Corrections due to the charge state selection in the separator, livetime of the DAQ system, and DSSSD detector efficiency is given. The activation measurement perform at DRAGON in order to cross check the direct counting measurements is also explained. The results are in agreement with the experiment performed in Madrid.

"Your theory is crazy, but it's not crazy enough to be true."

Niels Bohr

CHAPTER 6

DISCUSSION AND FUTURE WORK

Abstract: *In this chapter the results for the astrophysical S-factor obtained from the two complementary experiments are compared to the literature data and calculations from theoretical models. A discussion about the results and the planned future projects will also be presented.*

As it has been discussed in the previous chapters, several experiments have been performed since the first measurements of Holmegren and Johnston [HJ59] aiming to determine the astrophysical S-factor of the ^{3}He(α,γ)^{7}Be and ^{3}H(α,γ)^{7}Li mirror reactions. Prior to the measurements presented in this thesis, there were only two sets of data in the E_{CM} range from 1 to 3 MeV. The results presented here are in the same energy range, allowing for a quantitative comparison with the previous data.

Large discrepancies are also seen among the different calculations. Only the new ab-initio calculations [Nef11] and those in [Moh09] extended the astrophysical S-factor calculations to medium energies, which is important not only to constrain the extrapolations down to the astrophysical energies, but also for understanding the influence of the non-external contribution to the capture reaction cross section. A comparison between such calculations and the data is done to shed light on the current situation with the theoretical description of this reaction.

Finally, some work related to this reaction is still needed in order to constrain the theoretical models and to get a lower uncertainty in the $S_{34}(0)$ value. Future possible experiments and studies to be performed by our collaboration will also be discussed.

6.1 Summary of the S-factor Results

The new experimental results of the astrophysical S-factor for the ^{3}He(α,γ)^{7}Be reaction have been obtained using two experimental techniques, the *activation method* using a setup installed at a beam line of the tandem accelerator in Madrid, and the *direct recoil counting method* using the DRAGON spectrometer setup at TRIUMF in Vancouver. These results are summarised in Table 6.1, where the last column shows the total error calculated as:

$$\Delta S(E)^{\mathrm{Total}} = \sqrt{(\Delta S(E)^{\mathrm{stat}})^2 + (\Delta S(E)^{\mathrm{syst}})^2} \tag{6.1}$$

For the TRIUMF experiment, the systematic uncertainties (ΔS(E)$^{\mathrm{syst}}$) are calculated as an average of the positive (+) and negative (-) values. The average is taken to evaluate the data without implications in the final results.

E_{CM} (keV)	S(E) (keV·b)	ΔS(E)$^{\mathrm{stat}}$ (keV·b)	ΔS(E)$^{\mathrm{syst}}$ (keV·b)	ΔS(E)$^{\mathrm{total}}$ (keV·b)
777.2	0.418	0.061	0.018	0.063
915.8	0.411	0.079	0.015	0.081
1054.2	0.339	0.023	0.012	0.026
1249.6	0.390	0.031	0.013	0.034
1498.9	0.318	0.024	0.011	0.026
2007.0	0.367	0.010	0.010	0.014
2267.7	0.386	0.037	0.016	0.041
2510.0	0.455	0.027	0.017	0.032
2511.1	0.391	0.037	0.014	0.040
2804.1	0.424	0.018	0.012	0.022
1508.9	0.359	0.003	$^{+0.036}_{-0.040}$	0.038
2023.7	0.359	0.003	$^{+0.053}_{-0.061}$	0.057
2216.5	0.419	0.004	$^{+0.046}_{-0.050}$	0.048
2813.6	0.393	0.005	$^{+0.027}_{-0.049}$	0.039
2023.8	0.484	0.034	0.056	0.065

Table 6.1: *Astrophysical S-factors obtained for our experiments at Madrid (top part of the table), and at TRIUMF (bottom values). In the TRIUMF experiment, the thin line separates the direct counting measurements and the activation measurement. As the latter was used to crosscheck our direct recoil counting experiment and due to the limited beam availability, the run was not optimised to obtain good statistics. Therefore, we have large error in this measurement, and for this reason this point was not considered for the fitting procedure (cf. text). The last column shows the total error contribution.*

Around the time of our measurements, two new measurements were performed by other groups; the ATOMKI group determined the astrophysical S-factor at five energies with E_{CM} between 1.5 to 2.5 MeV using the activation technique [BGH13] and the Notre Dame group determined the S-factor in the energy range of E_{CM}=0.303-1.45 MeV and performed a new R-matrix analysis [KUD13]. The new data in the same energy region as that of our measurement show the same tendency discarding the flat energy dependence of Parker and Kavanagh [PK63], as can be seen in Figure 6.1. Data are also shown for the measurements of the Weizmann [NHNEH04], the LUNA [BCC06, GCC07, CBC07], the Seattle [BBS07] and the ERNA [DGK09] groups. The total errors (ΔS(E)$^{\mathrm{total}}$) are used in order to compare different sets of experimental data.

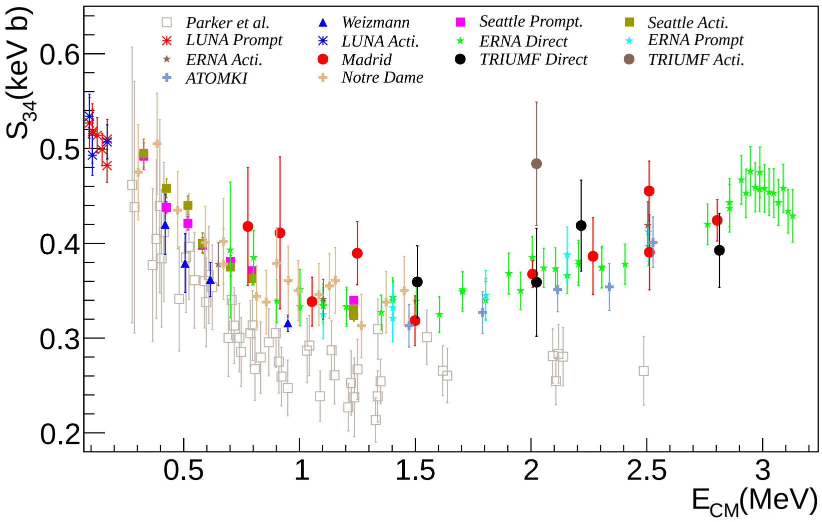

Figure 6.1: *A compilation of the experimental results on the astrophysical S-factors. Our data, (in circles) are shown with the total error $\Delta S(E)^{Total}$ (cf. Table 6.1), which combines the systematic and statistical uncertainties. Data from the measurements performed over the last decade by the Weizmann [NHNEH04], the Seattle [BBS07], the LUNA [CBC07], the ERNA [DGK09], the ATOMKI [BGH13] and the Notre Dame [KUD13] groups, and the old measurements from Parker et al. [PK63], are also shown. See text for more details.*

It should be noted that in the case of the Madrid experiment the statistical uncertainties give the major contribution to the error bars while for the TRIUMF experiment the estimated systematic uncertainties associated with the DRAGON acceptance are the dominant ones (see Table C.1). However, in some of the cases these uncertainties should be taken as an upper limit. For example, in the acceptance uncertainties, some of the most influencing parameters are the beam offsets in both x and y directions (see Table 4.24), which are considered to be around 1 mm. However, the probability of having such a displacement in a typical measurement during our experiment is expected to be smaller, as beam position is controlled continuously with a CCD camera.

The direct counting measurement around E_{CM} ~2 MeV has the highest error contribution from the charge state fraction q_f. This is because measurements of the charge state distribution corresponding to the recoils produced at this energy are yet to be performed and the extrapolation procedure using the measured q_f values resulted in an overestimated error.

6.2 Comparison with Previous Experimental Data and Discussion

The agreement between our results and different experimental data sets has been quantified by evaluating the chi-squared:

$$\chi^2_\nu = \left(\sum_i \frac{(S^i_A - S^i_B)^2}{(\Delta S^i_A)^2 + (\Delta S^i_B)^2} \right) / (\nu - 1) \tag{6.2}$$

where S_A and S_B are the astrophysical S-factor at a given E_{CM} from our experiment and from one of the data sets from the literature, respectively. ΔS^2_A and ΔS^2_B are the corresponding total errors and ν is the number of points considered.

The S_A and the S_B values must be compared at the same E_{CM}. Where this is not possible, the S_B values are calculated by using the average of the available S_B-factors for the closest possible lower (E^-)

	Parker and Kavanagh	ERNA direct	ATOMKI
Madrid	7.40 ($\nu = 10$)	0.75 ($\nu = 10$)	1.14 ($\nu = 4$)
TRIUMF direct	5.98 ($\nu = 4$)	0.54 ($\nu = 4$)	1.40 ($\nu = 3$)

Table 6.2: *χ^2_ν values calculated using expression 6.2. Here, S_A are our astrophysical S-factors and S_B are those from Parker and Kavanagh [PK63], of ERNA [DGK09] or ATOMKI [BGH13].The ν values give the number of data points considered in each case.*

and higher (E^+) energies with respect to E_{CM}. The $(E^-+E^+)/2$ is always within 50 keV of E_{CM}. In order to deduce the astrophysical S-factor at around 2.8 MeV in the case of Parker and Kavanagh, an extrapolation of the data was necessary.

As can be observed the agreement with the ERNA data is considerably better (0.75 and 0.54 for Madrid and TRIUMF data, respectively) compared to that with the Parker and Kavanagh data (7.40 and 5.98). A good agreement when comparing with the new ATOMKI data (1.55 and 1.40) can be also seen. The absolute S-factor values from the ATOMKI data are slightly lower than those from the ERNA group although they agree fairly well within the error bars.

A χ^2_ν value of 0.53 is obtained when comparing *activation* data from Madrid and *recoil counting* data from TRIUMF ($\nu = 4$). This good agreement between the data obtained using the two independent experimental setups and techniques together with the ERNA data justifies the energy dependence seen in this energy region and justifies discarding the old data from Parker and Kavangah. Parker and Kavangah used the prompt method by employing cylindrical NaI(Tl) scintillators to detect the prompt γ-rays produced on a ^{4}He beam capture on a ^{3}He gas target. The discrepancy seen could be due to a contaminated target gas. This speculation is based on the fact that the ^{3}He gas target was replaced by ^{4}He between the measurements in order to perform background measurements, which could have left residual ^{4}He component in the ^{3}He target gas. This provides that the improvements in the detection systems and analysis techniques makes it worthwhile to redo old measurements.

6.3 Comparison with Theoretical Models and Discussion

Different theoretical models available for describing the ^{3}He(α,γ)^{7}Be reaction were discussed in Chapter 2. Figure 6.2 displays some of the representative calculations together with our experimental data. Two different features can be analysed when comparing with the theoretical calculations, namely the absolute scale and energy dependence of the S-factor. As it can be observed, the ab-initio calculations by Neff reproduce both absolute scale and energy dependence of our $S_{34}(E)$ data reasonably well. It is remarkable that there was no need to use any normalisation factor to obtain this agreement. However, this model cannot explain the data for the isospin mirror reaction ^{3}H(α,γ)^{7}Li and these calculations should be treated with some caution. The recent R-matrix analysis from Kontos et al. [KUD13] is also shown in Figure 6.2. This analysis fits all the new published data (123 experimental data points) including those three points with the lowest error bars from our Madrid experiment, and the ^{3}He(α,α)^{3}He elastic scattering data from [BJP64, MAK93]. It can be seen that the R-matrix fit reproduces also the absolute scale and the energy dependence seen in our data.

It is clear from Figure 6.2 that the other theoretical models do not reproduce the absolute scale. However, based on the discussion in Chapter 2, and in that presented in *Solar Fusion Cross Sections II* evaluation [AGR11], the theoretical calculations can be normalised to the experimental data. Therefore, in order to compare both, the energy dependence and the absolute scale, normalisation factors -$\mathcal{N}$- have been obtained by minimising the χ^2 defined as:

$$\chi^2_{\mathcal{N}} = \sum_{i=1}^{14} \frac{(\mathcal{N}S^i_{\mathrm{model}} - S^i_{\mathrm{expe}})^2}{(\Delta S^i_{\mathrm{expe}})^2} / (\nu - 1) \tag{6.3}$$

A program using the MINUIT minimisation library was written for this purpose. In order to

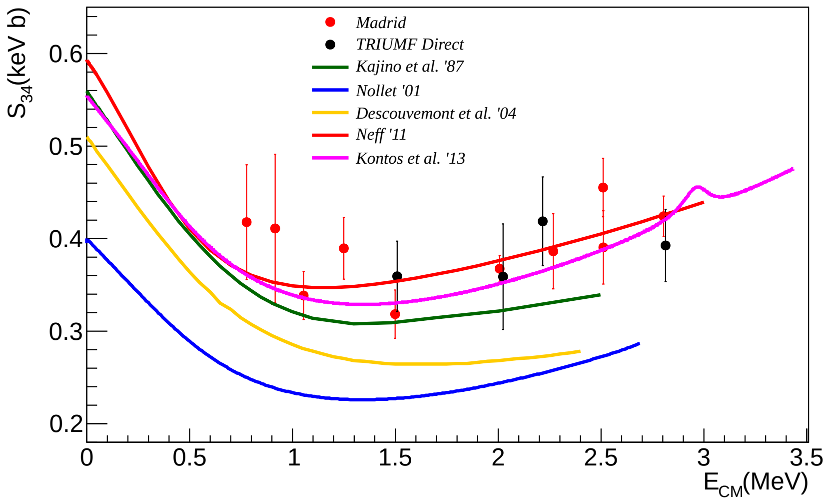

Figure 6.2: *A comparison between theoretical calculations from Kajino et al.'87 [KTA87], Nollet'01 [Nol01], Descouvemont et al.'04 [DAA04], Neff'11 [Nef11], and Kontos et al.'13 [KUD13], with the activation data from Madrid and the direct recoil counting data from TRIUMF experiments. The error bars correspond to ΔS^{Total} (cf. Table 6.1).*

	Kajino et al.	Nollet	Descouvemont et al.	Neff	Kontos et al.
$\mathcal{N}$	1.164±0.002	1.504±0.003	1.374±0.003	0.998±0.002	1.045±0.002
$S_{34}(0)$	0.652	0.601	0.702	0.592	0.577
$\chi^2_{\mathcal{N}}$	0.81	0.73	1.01	0.69	0.71

Table 6.3: *The $\mathcal{N}$-scaling factors defined in expression 6.3 for the representative models and S-factors extrapolated to zero energy $S_{34}(0)$.*

consider all our 14 data points, calculations have been extrapolated up to energies of ∼2.8 MeV. It should be clear that these extrapolations are made by considering the energy trends observed in Figure 6.2, and are used only to compare the energy dependence of our data and the calculations. Table 6.3 shows the $\mathcal{N}$-factors for the different models obtained using the library. The extrapolated values down to zero energy $S_{34}(0)$, obtained from the normalised model calculations plotted in Figure 6.3, are also given.

The $\chi^2_{\mathcal{N}}$ values in the last row indicate the goodness of the fit for the different models to our experimental data, i.e. how well the representative theoretical models reproduce the energy dependence seen in our results. All values are around one unit and therefore, we can say that, after normalisation, all models reproduce the energy dependence in our energy region. However, they lead to very different $S_{34}(0)$ values (a difference of 18% can be seen between the maximum and minimum values). This highlights the different energy dependence in lower E_{CM} range for these models. It is also worth stressing that the large error bars in some of the data points does no allow for the discrimination of the theories based on the shape of the $S_{34}(E)$ curves.

It is worth noting that Kontos et al. already include in their R-matrix analysis our three points published in [CGNB12]. Indeed, they used a 0.976 normalisation factor to our three points in order to get an optimal fit to all the given experimental data. According to all the results presented in this thesis work, this normalisation factor should be increased, although they used also the ERNA data, which also constrain the normalisation factor. On the other hand, the ab-initio calculations by Neff reproduce our

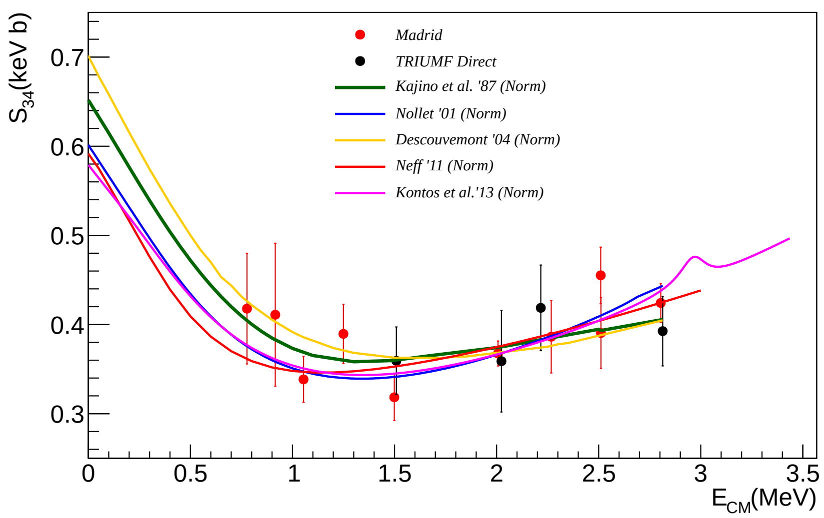

Figure 6.3: *Theoretical models normalised with the $\mathcal{N}$-factors in Table 6.3.*

results rather well without any normalisation factor (0.998±0.002∼1).

The normalised theoretical models are plotted together with all the modern data in Figure 6.4. As it can be seen, neither the Kajino nor the Descouvemont model can reproduce the energy dependence of our data and the Weizmann and the low energy data from LUNA (violet and red stars points, respectively) at the same time. The same fact can be observed from Nollet calculations, although the energy dependence is better reproduced. Therefore, we argue that the Neff ab-initio and the Kontos et al. R-matrix fit are the best among the model calculations reproducing the energy dependence a large energy range. For Neff calculations, the difference between the $S_{34}(0)$=0.593 keV b before, and the $S_{34}(0)$=0.592 keV b after the normalisation are negligible. However, the value of Kontos et al. of $S_{34}(0)$=0.554 keV b is increased a 7% after the normalisation ($S_{34}(0)$=0.577±0.001 keV b). It is worth pointing out that among the new literature data only those from the LUNA work are measured in the lowest energy region, which constrain the low energy dependence. New astrophysical S-factor in the range of E_{CM}=100-300 keV by using, for example, the *direct recoil counting technique* are recommended in order to improve the present situation.

The agreement between the Weizmann [NHNEH04] and the current Madrid work experiments at around 1 MeV, which were performed using the same setup, supports the reliability of the Madrid data obtained using the activation method. However, none of the representative models can explain both sets of data in a fully consistent manner. For example, an analysis of the Weizmann data and our three points at ∼ 1, ∼ 2 and ∼ 2.8 MeV from the Madrid experiment using the Neff model gives χ^2 ∼18 (of which ∼14 comes from the most accurate data point at 950 keV from Weizmann). This is evident in Figure 6.4, where the blue triangle is away from the red curve by more than 2σ.

6.4 S_1/S_0 Ratio and γ-rays Angular Distributions

For the TRIUMF experiment, the S_1/S_0 ratio, i.e. the ratio between the probability of the first excited and ground states in ^{7}Be getting populated by the direct capture state, is obtained by fitting the simulated intensities of the two gamma peaks ($\gamma_{429}/\gamma_{g.s.}$) with those from the experimental spectra. It is worth noting that in both cases the γ spectra are taken in coincidence with recoils detected in the focal plane DSSSD detector (see section 4.5.5). The resulting S_1/S_0 ratio for the different E_{CM} is shown in Table 4.19 and in Figure 6.5 together with some of the existing modern data. As it can be seen, we have

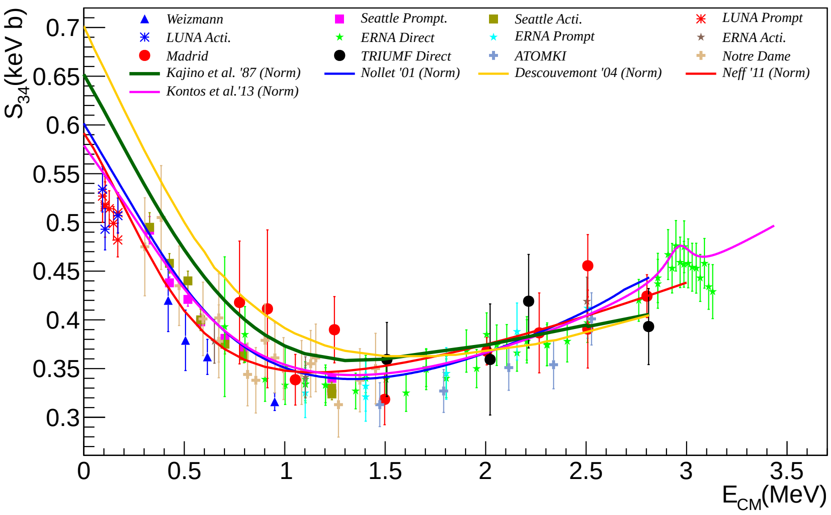

Figure 6.4: *The modern experimental data for the $^3He(\alpha,\gamma)^7Be$ reaction together with the theoretical calculations normalised using the $\mathcal{N}$-factors from Table 6.3. The normalised theoretical models from Neff and Kontos et al. are the best ones reproducing our data together with the LUNA data. The difference between the normalised $S_{34}(0)$ values from both models results in $\sim$2.6%.*

determined the branching ratio at the highest E_{CM} so far, which points out to the energy independent nature of S_1/S_0 in the entire range between 1 and 3 MeV.

These results should be treated with caution as the branching ratios in the simulations are obtained assuming an isotropic γ-ray emission. The recoil angle, thus the recoil acceptance of the separator, depends on the angular distribution of the emitted γ-ray. Therefore, different γ-ray distributions for the two γ-rays would imply different corresponding acceptances and S_1/S_0 ratios obtained using the γ-events in coincidence with the recoils accepted by the separator. However, the changes in the acceptance due to the variations in the γ-rays angular distributions (see section 4.5.6) are within the systematic errors when varying other parameters. Therefore, we can consider the branching ratios obtained assuming isotropic angular distributions and assume the systematic uncertainties in the acceptance. Thus, our error bars in Figure 6.5 display both statistical and systematic contributions. In contrast to our data, the existing modern data do not suffer from the recoil acceptance dependence. Therefore, the evaluated S_1/S_0 values from [CD08] were considered in the simulations, and the variations in S_1/S_0 have been taken as potential uncertainties in the astrophysical factors.

In order to get further insight in the γ-rays angular distributions, a comparison of the experimental and simulated BGO hit-maps was performed assuming both, the isotropic angular distributions and those from Parker and Tombrello [PK63] (see Tables 4.7 and 4.22). Only small differences were found that have been considered as systematic error contributions in the separator acceptance. From systematic variation of the angular distribution coefficients it is possible to get better agreement between the experimental and the simulated BGO-hit maps. The resulting γ-rays angular distribution coefficients would constrain the theoretical models. But, on the other hand, we could not use all the γ-events due to the high number of background events seen in the BGO detectors, i.e. we can consider only those in coincidence with ^{7}Be recoils. This fact would introduce an error from the acceptance in the obtained coefficients. A new experiment aiming to precisely determine the prompt γ-ray angular distributions, thereby constraining the coefficients in expression 4.4, is planned by our collaboration.

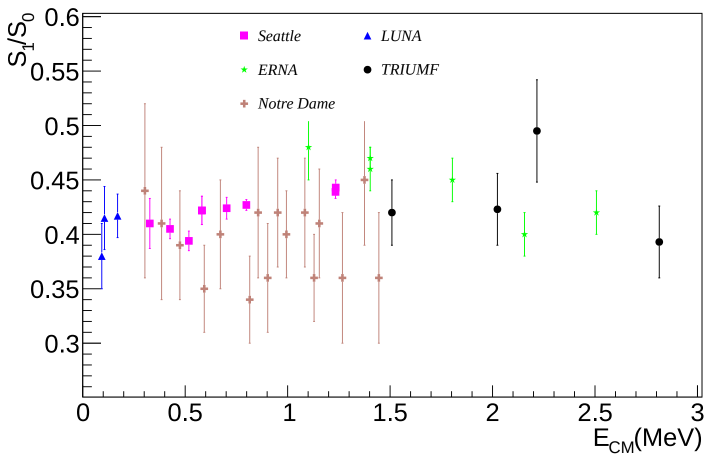

Figure 6.5: *The S_1/S_0 ratios obtained using the prompt-γ events detected by the BGO array surrounding the gas target in our TRIUMF experiment (black dots). For a comparison, existing modern data are also shown.*

6.5 Impact on Astrophysics

The $S_{34}(0)$ value, obtained using the FMD model calculations, [Nef11] and Kontos et al. R-matrix fit [KUD13] has a direct influence on the predictions of the Big-Bang Nucleosynthesis and of the Standard Solar Model.

- In order to evaluate and compare the impact on the Standard Solar Model, we consider the value for $S_{34}(0)$=0.56 keV b recommended in the revision *Solar Fusion Cross Section II* [AGR11]. The R-matrix fit from Kontos et al. including three of our points from the Madrid experiment estimates $S_{34}(0)$=0.554 keV b and therefore, practically no deviations in the neutrino fluxes are estimated. However, our value considering all, the Madrid and the TRIUMF data, and the renormalisation of Kontos et al. is $S_{34}(0)$=0.577 keV b, which is ∼3% larger than the one in [AGR11], and this translates to a ∼2.61% and ∼2.45% increase in the ^{7}Be ($\phi_\nu(^7\mathrm{Be})$) and ^{8}B ($\phi_\nu(^8\mathrm{B})$) solar neutrino fluxes, respectively, calculated using the expressions in [CD08].

  The changes are higher if we consider the normalised value from the Neff model, $S_{34}(0)$=0.592 keV b. This value is very close to the one obtained without any normalisation ($S_{34}(0)$=0.593 keV b) and therefore we can consider this model as the one that reproduces our results with the best agreement. On the other hand it should be recalled that this model is based on ab-initio calculations thus, without considering any of the experimental data it can reproduce both phase shifts and capture reaction cross sections. The increase of 5.89% in the $S_{34}(0)$ value compared to that from [AGR11] translates into an 5.05% and 4.75% in $\phi_\nu(^7\mathrm{Be})$ and $\phi_\nu(^8\mathrm{B})$, respectively.

- Concerning the BBN it was already discussed that the ^{7}Li problem will not be solved by means of obtaining precise rate for the $^3\mathrm{He}(\alpha,\gamma)^7\mathrm{Be}$ reaction. However, any change in the recommended $S_{34}(0)$ value has a direct impact on the estimations of the primordial ^{7}Li abundance. A calculation of a new primordial ^{7}Li abundance is out the scope of this work, however a qualitative analysis can be done. According to [DGK09], a primordial ^{7}Li abundance of ^{7}Li/H=(5.4±0.3) 10^{-10} is obtained using $S_{34}(0)$=0.57 keV b. This abundance is a factor 3 or more larger than the observational values. In our case the $S_{34}(0)$ is a 3.86% larger than that considered in [DGK09] and therefore, the corresponding calculated primordial ^{7}Li abundance becomes even larger than the current value, thus worsening the disagreement between the calculations and the observations (see for example [CFO08]).

6.6 Future work

The present situation for the ^{3}He(α,γ)^{7}Be reaction is far from being settled both from the theoretical and experimental points of view. It is worth pointing out the situation at around E$_{CM}$ $\sim$ 1 MeV, where the theoretical models start to deviate. A lot of experimental points around this energy agree between themselves when the uncertainties are taken into account. However, the Neff calculation, which reproduces the experimental S-factor at higher energies with the best agreement compared to the other considered models, deviates from the precise data of Weizmann at 950 keV by $\sim 4\sigma$. Moreover, this model cannot reproduce the absolute scale of the S-factor curve for the ^{3}H(α,γ)^{7}Li reaction. On the other hand, the experimental data of this reaction were obtained more than 20 years ago. Therefore, new experimental information is required in order to constrain the theoretical models and thus the S$_{34}$(E) extrapolation to zero energy. Our collaboration plans to perform new experiments in order to constrain the experimental information of the ^{3}He(α,γ)^{7}Be reaction.

One of our aims is to determine the experimental cross section of the **^{3}H(α,γ)^{7}Li mirror reaction** using ^{3}H implanted targets [WRH00], as none of the calculations can simultaneously reproduce the energy dependence and absolute value of both this reaction and the ^{3}He(α,γ)^{7}Be reaction. Moreover, the previous experiments studying this reaction were done using ^{3}H targets of only 1 $\mu g/cm^2$. This measurements would give more accurate results due to the higher number of target atoms with no target deterioration.

One of our other objectives is to determine the prompt γ-rays angular distributions for both ^{3}He(α,γ)^{7}Be and ^{3}H(α,γ)^{7}Li reactions, for which we plan to use Germanium detectors from arrays such as the TIGRESS array at TRIUMF [SAA05]. These measurements will also aim at determining the absolute cross section of both reactions by using the prompt γ-detection technique, not used so far by our collaboration. These measurements will help us determining the different partial wave (s,d, etc...) contributions to this cross section experimentally and compare with the expectations from calculations in order to constrain theoretical extrapolations and give more accurate extrapolated S$_{34}$(0) values.

Finally, we plan to measure the ^{3}He(α,α)^{3}He elastic scattering channel. In Chapter 2, it was discussed how potential models cannot simultaneously reproduce the phase shifts and capture cross section considering only the dominating extranuclear/direct capture [Moh09]. On the other hand, the FMD model reproduces the phase shifts as well as the reaction rates for the ^{3}He+α system, but fails to explain the results for the same channel in the ^{3}H+α system. Also, accurate elastic scattering data are needed for energies above E$_{CM}$ $\sim$2 MeV that should be compared with the calculations including the ^{6}Li+p break up channel. We aim to achieve $\sim 5\%$ accurate elastic data by using a chamber placed at DRAGON target chamber, which has ports for particle detection at angles of 30, 50, 60, 70, 90, 100, 120, 130, 135 and 140 degrees with respect to the beam direction

All of this, apart from a likely elastic scattering measurement of ^{3}H(α,α)^{3}H with implanted targets using for example TUDA setup will lead us to a consistent comparison with the calculations for both these reactions and constrain the errors in the extrapolated S$_{34}$(0) factor.

6.7 Conclusion

In this chapter the main results and conclusions of the work in this thesis have been discussed. The experimental results obtained in both the Madrid and TRIUMF experiments have been compared with previous experimental works in the same energy region, solving the discrepancies among them and discarding those old results from Parker and Kavanagh [PK63]. Later, our results have been compared with different theoretical models, determining the normalisation factors required to obtain good fits to our astrophysical S-factor data. The ab-initio FMD model calculations by Neff [Nef11] reproduce our measurements rather well. Therefore, the adopted value of 0.593$\pm$0.02 keV b is recommended for S$_{34}$(0). The impact on the SBBN and the SSM of this adopted value has been discussed and finally the future work to be done by our collaboration has been briefly mentioned.

"Science does not know its debt to imagination"

Ralph Waldo Emerson

CHAPTER 7

CONCLUSIONS

The $^{3}He(\alpha,\gamma)^{7}Be$ reaction rate is an input parameter and therefore has a determining role in the estimations of the solar neutrino flux by the SSM and the prediction of primordial ^{7}Li abundance predictions by the SBBN. Large discrepancies are seen in the rate or S-factor for this reaction among the different data sets and theoretical calculations, specially in the range of E_{CM}=1-3 MeV. In this region, contributions from the non-external capture is expected, but a clear picture is missing due to the limited experimental and theoretical works.

Driven by these primary, nevertheless, very broad interest, this reaction has been studied in this thesis work, by employing two complementary experimental techniques: the *activation method* using a 5 MV tandem accelerator at CMAM laboratory in Madrid, and the *direct recoil counting method* using the DRAGON separator at TRIMF, Vancouver.

Some important outcomes are:

- Two experimental set-ups have been completely characterised in order to study the $^{3}He(\alpha,\gamma)^{7}Be$ reaction
- Ten new S_{34}(E) values with low systematic uncertainty have been obtained in the range of E_{CM}=1-3 MeV using the *activation* technique and by employing a very well controlled ^{7}Be production and a γ-counting setup
- Three of the measurements using the *activation* technique has special relevance due to the low statistical uncertainty and good accuracy
- The density profile of the ^{3}He gas target in the DRAGON cell has been measured for the first time and can be used for future experiments at the DRAGON separator

- The charge state distribution of Be nuclei after crossing the ^{3}He target gas has been determined for the first time, using target pressures between 1 to 6 Torr, that indicates charge state equilibrium at 1 Torr
- A very high suppression of the incident beam has been measured when the ^{7}Be recoils from the ^{3}He(α,γ)^{7}Be reaction are selected by the DRAGON separator
- The GEANT-3 DRAGON code has been modified and adapted to perform extensive simulations, including a new specific prompt γ-rays angular distributions which will be used for the design of future experiments
- Several tests have been performed in order to constrain the angular distribution of the prompt γ-rays. The variation of the angular distributions has been introduced as potential uncertainties in the acceptance and intense simulations with the adapted GEANT-3 code could lead to a better constrain in the coefficients of the γ-ray angular distribution
- Four new data points for the S_1/S_0 branching ratios have been determined. This includes the point corresponding to 2.8 MeV that is the highest energy at which such data has been obtained so far
- Four new S_{34}(E) values have been determined with the lowest statistical uncertainty measured so far using the *direct recoil counting* technique
- A good agreement is seen between the two data sets obtained using two independent techniques
- The results obtained in this thesis clearly agree with those from the ERNA collaboration [DGK09] and fully disagree with those from Parker et al.'s work [PK63], in the same energy region
- Our data show very good agreement with the ab-initio FMD calculations [Nef11]
- Based on our experimental results and the ab-initio calculations we recommend a value of $S_{34}(0)$=0.593 keV b
- From the description of our results and other experimental sets further data are yet required in a wide energy range using different techniques for a comparison of the results and to perform consistent data evaluations
- None of the current theoretical calculations can describe simultaneously the two mirror reactions ^{3}He(α,γ)^{7}Be and ^{3}H(α,γ)^{7}Li. New measurements of the mirror reaction are strongly suggested as well as elastic scattering data of the ^{3}He(α,α)^{3}He reaction in order to constrain the theoretical models
- Due to the discrepancies between the theoretical models of the s- and p-wave contributions to the S_{34}(E) factor, precise angular distributions of the prompt γ-rays are also recommended.

"It has become appallingly obvious that our technology has exceeded our humanity"

Albert Einstein

APPENDIX *A*

SILICON DETECTOR AND ELECTRONIC MODULES

Abstract: *In this appendix, the general details of semiconductor detectors and in particular of this used in the Activation experiment will be briefly described. As an example of the typical electronic modules used in Nuclear Physics experiments, those used in the activation experiment in Madrid will be also detailed.*

A.1 The Silicon Detector used in Activation Experiment

In the activation experiment performed at CMAM laboratory in Madrid, a semiconductor detector was used to detect the scattered ionised ^{3}He beam ions.

For semiconductor materials, the energy gap between the valence and conduction bands is $\sim$1eV. This is small compared to insulators ($\sim$5eV) and allows the creation of electron-hole pairs (electrons from the valence band are excited to the conduction band) when a charged particle crosses the material [Kno00]. At non zero temperature, a small number of electrons gain enough thermal energy and get elevated to the conduction band, creating the corresponding hole in the valence band. Both the hole and the electron take part in the random thermal motion. To control this movement of charge, some small quantities of doped elements, with 3 (p-type semiconductor) or 5 (n-type semiconductor) valence electrons are added to the semiconductor material. When a p-type and a n-type are joined, the electrons from n-type material spread through the p-type material and neutralise the holes there, creating a depletion region (active area). An electric field is created in the depletion zone due to the remaining effective positive charge in the n-type material and negative charge in the p-type. When a charged particle go through the depletion zone the created electron-hole pairs move in opposite directions following the electric field, creating an electric signal whose amplitude is proportional to the incoming energy. In practice, a reverse bias is applied to the detector in order to enlarge the active area and increase the electric field strength for the efficient charge collection. The drawback in the process is that some amount of leakage current is created.

For the activation experiment a surface silicon barrier detector reverse biased with +120V was

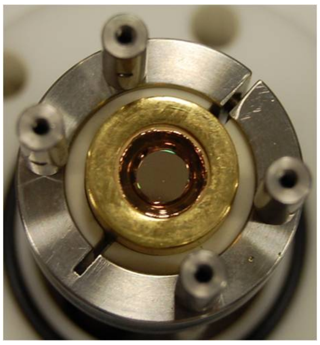

(a)

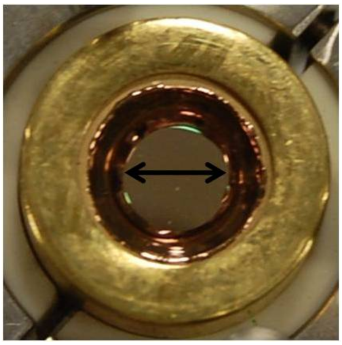

(b)

Figure A.1: *(a) A photo of the silicon surface barrier detector placed in the holder used in the activation experiment performed at CMAM laboratory in Madrid. (b) A schematic of the p-material, gold layer, and the depletion zone that is extended due to the reverse bias applied.*

used (see Figure A.1). These types of detectors consist of a p-type thin layer material on top of a n-type doped silicon and an evaporated gold layer on the front surface acting as electric contact. For more details about semiconductor detectors see Chapter 11 in reference [Kno00].

A.1.1 Electronic modules

Section 3.2.1 describes both electronic chains used to process the electronic signal of the silicon detector and the integrated electric charge in the chamber. A diagram showing the processing of the different chains using electronic modules is displayed in Figure 3.8. In the following details of the modules will be given:

Preamplifier:

The main purpose of the preamplifier is to amplify the low amplitude signals from the detector introducing minimal amount of noise and avoiding capacitance effects. The preamplifier is therefore placed as close to the detector as possible. The preamplifier used in this experiment is *charge sensitive* type and integrates the whole charge from the detector pulse in a capacitor removing the detector capacitance dependence. Thus, the output voltage signal depends only on the charge and the capacitance of the capacitor. The module used in the experiment was MPR-I manufactured by MESYTEC [MES].

Amplifier:

Before being digitised, the signal must be further amplified and shaped in the amplifier. Shaping the pulse, e.g. as a Gaussian function, is important for different reasons: the output pulse from the preamplifier has a long tail, from 40 μs to hundreds of μs then, a new signal from the detector may come during this time. In order to avoid the overlapping between different signals this tail must be eliminated by integrating the pulse in the amplifier for an appropriate time, which corresponds to the shaping time of 1 μs for this experiment. The model used in this experiment was: *Dual Amplifier-855* manufactured by ORTEC [ORT].

Time Filter Amplifier (TFA):

This is a type of amplifier in which the pulse is shaped optimising the pulse/noise ratio and preserving the temporal information of the signal. In this case, the TFA was used to amplify the signal to be used in the *coincidence setup*.

Constant Fraction Discriminator (CFD):

The CFD is designed to provide a timing signal corresponding to the original signal with an amplitude above a threshold relevant to the experiment. A CFD eliminates those pulses coming from the electronic noise and keeps the pulses from the detector. The signals above the threshold are transformed to one volt digital signals to be used in the rest of the *coincidence setup*. In this experiment the threshold was set in order to avoid the electronic noise and the background radiation.

Gate and Delay Generator:

A gate and delay generator module generates a logic output signal during a period in the order of μs. The temporal gate is generated when the module receives a logic signal, in this case from the CFD. The output width of the gate is set by looking at the signal in the oscilloscope and fitting to the same width as that from the amplifier signal. The output gate is sent to the Linear Gate and Stretcher together with the signal from the amplifier in order to select just the "good" events to be digitised (those selected by the threshold in the CFD).

Linear Gate and Stretcher (LGS):

The module 542 manufactured by ORTEC is useful to select or discard pulses according to coincidences and temporal conditions, that is, the hardware coincide is carried out. The module has two inputs, the output signal from the amplifier and the temporal gate from the *Gate and Delay Generator*. During the experiment it was used to select the coincidence pulses coming from the energy chain and those from the temporal chain, where just the events above the threshold in the CFD were considered.

Multichannel Analyzer (MCA):

An MCA consist of a device which classifies and counts events in real time. The classification can be made based on different parameters of the incoming pulse (one pulse per event). Once the pulses are classified, they will be accumulated together in some channels, where each channel stores events with the same characteristics. Most common MCAs classification is based on the height of the incoming pulse, *pulse height*, which in our case is proportional to the deposited energy in the detector. Once the pulses are classified in the MCA, they are saved as histograms. For this experiment the software MAESTRO®-32 version 6 developed by ORTEC ([ORT]) was used together with a multichannel buffer plate (MCB) in a computer. After the direct digitisation of the output signal from LGS, the software showed the spectra online and the data were saved in ASCII format.

Charge Integrator and Scaler

A charge integrator (ORTEC-439 [ORT]) and a scaler (QUAD CALER AND PRESENT COUNTER TIME [CAE]) were used to monitor and determine the beam intensity. Using the accelerator electrical ground as zero voltage, a BNC cable was connecting directly the reaction chamber to the charge integrator (all the appropriate elements in the chamber were electrically connected and together they acted as a Faraday Cup). The output of the integrator, as a number of pulses, (10^{-10} C/pulse), was sent to the Scaler module, where the number of pulses per second and the accumulated number of pulses for each run were displayed. The accumulated number and the count rate pulses were manually recorded each half an hour to monitor the beam stability. At the end of each measurement the number of pulses was saved.

"Never memorize something that you can look up"

Albert Einstein

APPENDIX B

KINEMATICS

Abstract: *In this appendix, some general expressions useful to understand the kinematics related to the capture reactions A+B⟶C+γ will be given. Firstly, the transformation between laboratory and centre of mass coordinate systems will be presented ,and after that, the reaction kinematics will be detailed.*

B.1 From Laboratory to Centre of Mass System

The nuclear reactions are observed in a reference frame which is at rest in the Laboratory (*Laboratory System*). However, from a physics point of view the movement of the centre of mass does not play a role in the reaction itself. Therefore, it is more convenient to use a frame in which the centre of mass of the nuclei is at rest (*Centre of Mass System*).

Figure B.1 shows the velocities involved in a radiative capture reaction in both *Laboratory* and *Centre of Mass* systems. The target is considered to be at rest in the laboratory system. In the following, variables without the prime symbol,', will correspond to the laboratory system and those with "'" to the centre of mass system.

Utilising the definition of the centre of mass system, before the collision, we have:

$$|\vec{p}_1'| = |\vec{p}_2'| \tag{B.1}$$

$$\vec{V}_1' = \vec{V}_1 - \vec{V}_{CM} \tag{B.2}$$

$$\vec{V}_2' = -\vec{V}_{CM} \tag{B.3}$$

here $\vec{V}_{CM}$ is the velocity of the centre of mass in the laboratory system and 1 and 2 represent the projec-

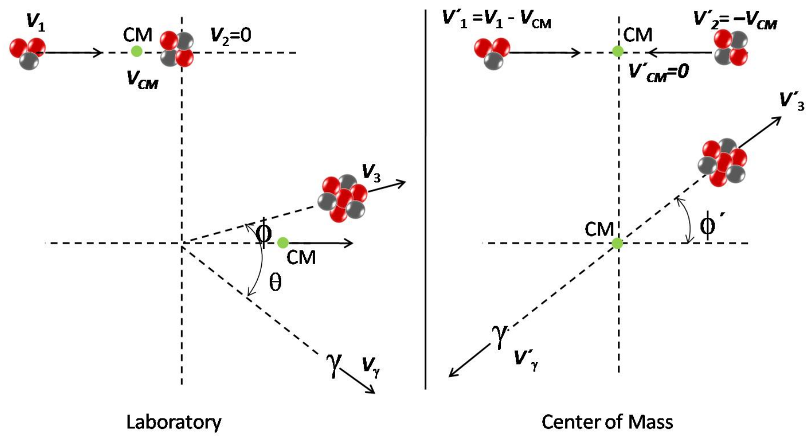

Figure B.1: *Velocities involved in a capture reaction 1(2,γ)3 given in the laboratory system (left) and centre of mass system (right). Top and bottom shows the situation before and after the reaction takes place, respectively. The target, 2, is at rest in the laboratory system, 1 is the incoming beam, and the green dots indicate the centre of mass position.*

tile/beam and target, respectively. After working out some algebra, we have

$$\vec{V}_{CM} = \left(\frac{m_1}{m_1+m_2}\right)\vec{V}_1 \tag{B.4}$$

$$= \left(\frac{m_1}{m_1+m_2}\right)\sqrt{\frac{2\mathrm{E}_1}{m_1}} \tag{B.5}$$

where the m_1 and m_2 are the masses of the interacting nuclei, the velocities of which in the centre of mass system are given by:

$$\vec{V}_1' = \left(\frac{m_2}{m_1+m_2}\right)\vec{V}_1 \tag{B.6}$$

and

$$\vec{V}_2' = \left(\frac{m_1}{m_1+m_2}\right)\vec{V}_1. \tag{B.7}$$

The kinetic energy in the centre of mass system, T′ is then given by

$$\mathrm{T}' = \mathrm{T}_1' + \mathrm{T}_2' = \frac{1}{2}m_1 V_1'^2 + \frac{1}{2}m_2 V_2'^2 \tag{B.8}$$

which, utilising B.6 and B.7, becomes

$$\mathrm{T}' = \frac{m_2}{m_2+m_1}\mathrm{T}_1. \tag{B.9}$$

here, T_1 is the kinetic energy of the incoming beam (particle 1 in Figure B.1) in the laboratory system. The T′ energy, that is a $\frac{m_2}{m_2+m_1}$ fraction of the beam energy, is the real available energy for the nuclear reaction. Therefore, what is the rest of beam energy used for?

In order to understand where the remaining energy is utilised, let's take a look to the kinetic energy in the laboratory system and perform some algebra:

$$\begin{aligned} \mathrm{T} &= \frac{1}{2}V_1^2 m_1 = \frac{1}{2}V_1^2 m_1\left(\frac{m_2+m_1}{m_2+m_1}\right) = \frac{1}{2}V_1^2\left(\frac{m_2m_1+m_1^2}{m_2+m_1}\right) \\ &= \frac{1}{2}V_1^2\left(\frac{m_2m_1}{m_2+m_1}+\frac{m_1^2}{m_2+m_1}\right) = \frac{1}{2}V_1^2 m_1\left(\frac{m_2}{m_2+m_1}\right)+\frac{1}{2}V_1^2\left(\frac{m_1^2}{m_2+m_1}\right) \end{aligned}$$

and taking into account the expressions B.4 and B.9, it becomes

$$\mathrm{T} = \mathrm{T}' + \mathrm{T}_{\mathrm{CM}}. \tag{B.10}$$

where T_{CM} is the kinetic energy of the centre of mass point in the laboratory system ($\mathrm{T}_{\mathrm{CM}} = \frac{1}{2}(m_1 + m_2)V_{\mathrm{CM}}^2$). Therefore, from the total initial kinetic energy (T), only part is available in the nuclear reaction (T') while the rest is spent on the movement of the centre of mass. This will be transferred to the movement of the nucleus and γ radiation in the exit channel but do not participate in the reaction itself.

Conventionally, the kinetic energy in the centre of mass system before the collision is named E_{CM} as it is the available total energy for the reaction, and in this form it has been called through this thesis. Also the $\mathrm{E}_{\mathrm{rel}}$ is used in literature indicating that this is the *relative* energy of the interacting nuclei in the laboratory system.

Now, let us consider the situation after the collision. In the same way as before the collision, $\mathrm{V'}_{\mathrm{CM}}$=0 after the collision, and then,

$$|\vec{p}_3'| = |\vec{p}_4'| \tag{B.11}$$

The kinetic energy in the centre of mass system after the collision ($\mathrm{E}_{\mathrm{CM}}^f$) is given by

$$\mathrm{E}_{\mathrm{CM}}^f = \mathrm{E}_{\mathrm{CM}} + Q \tag{B.12}$$

being Q the Q-value of the reaction (see expression 1.1).

Finally, the relation between the laboratory and centre mass angle of the emitted photon can be given by

$$\cos\theta = \frac{\cos\theta' + \beta}{1 + \cos\theta'}, \tag{B.13}$$

where the relativistic parameter β is defined as

$$\beta = \frac{\sqrt{\mathrm{T}_1(\mathrm{T}_1 + 2m_1c^2)}}{m_2c^2 + m_1c^2 + \mathrm{T}_1} \tag{B.14}$$

B.2 Kinematics for Capture Reactions in the Laboratory System

In order to obtain the kinematic expression for the radiative capture reactions, let us assume the target nucleus 2 to be stationary in the laboratory system (Figure B.1 left). Conservation of energy and linear momentum yield the equations:

$$m_1c^2 + T_1 + m_2c^2 = m_3c^2 + T_3 + \mathrm{E}_\gamma \tag{B.15}$$

$$\sqrt{2m_1\mathrm{E}_1} = \sqrt{2m_2\mathrm{T}_2}\cos(\phi) + \frac{\mathrm{E}_\gamma}{\mathrm{c}}\cos(\theta) \tag{B.16}$$

$$0 = \sqrt{2m_2\mathrm{T}_2}\sin(\phi) + \frac{\mathrm{E}_\gamma}{\mathrm{c}}\sin(\theta). \tag{B.17}$$

(B.18)

Here, E_γ, ϕ and θ are the photon energy, the recoil and γ-ray emission angles, respectively. After performing some algebra and eliminating T_2 and ϕ and solving for the energy of the emitted photon, we have

$$E_\gamma = Q + \frac{m_2}{m_3}T_1 + E_\gamma\frac{V_2}{c}cos\theta - \frac{E_\gamma^2}{2m_2c^2} = Q + \frac{m_2}{m_3}T_1 + \Delta E_{\text{Dopp}} - \Delta E_{\text{rec}}. \tag{B.19}$$

Therefore, the photon energy is given by the sum of four terms: (i) the Q-value, $Q = (m_1+m_2-m_3)c^2 = T_3 + E_\gamma - E_1$, (ii) the bombarding energy in the centre of mass system, (iii) the *Doppler shift* due to the photon is emitted by a nucleus at a speed of V_3=$V_1(m_1/m_3)$, and (iv) the recoil shift which is caused by the energy shift on the recoiling nucleus [Ili07]. The numerical expressions for the two last terms are given by:

$$\Delta E_{\text{Dopp}} = 4.63367\cdot 10{-}2\frac{\sqrt{M_1T_1}}{M_3}E_\gamma cos\theta \tag{B.20}$$

$$\Delta E_{\text{rec}} = 5.36772\cdot 10{-}4\frac{E_\gamma}{M_3} \tag{B.21}$$

where, all energies are in units of MeV and the rest masses are in units of u. These two terms represent relatively small corrections.

The expression B.19 shows E_γ both on left and right hand sides. When a precision of ~keV is sufficient, we have the approximated relationship $E_\gamma \approx Q + T_1(m_2)/m_3$, where the masses are given by integer u unit masses. To achieve better accuracy, the masses in B.19 should be replaced by: $m_i + E_i/(2c^2)$ and the exact relativistic expression for the photon energy is then given by:

$$E_\gamma = \frac{Q(m_1c^2 + m_2c^2 + m_3c^2)/2 + m_3c^2T_1}{m_1c^2 + m_3c^2 + T_1 - cos\theta\sqrt{T_1(2m_1c^2 + T_1}} \tag{B.22}$$

where E_γ denotes the photon energy for the ground state transition. Thus, the kinetic energy of the recoiling nucleus in the laboratory system is given by

$$T_3 = Q - E_\gamma + T_1 \tag{B.23}$$

On the other hand, the relation between the emission angles for the photon (θ) and recoil (ϕ) is given by

$$\phi = \arctan\left(\frac{\sin\theta}{E_\gamma^{-1}\sqrt{2m_1c^2T_1} - \cos\theta}\right) \tag{B.24}$$

The maximum recoil angle, ϕ_{max}, is obtained when the photon is emitted perpendicular to the incident beam direction, $\theta = 90°$, which is given by

$$\phi_{\text{max}} = \arctan\left(\frac{E_\gamma}{\sqrt{2m_1c^2T_1}}\right) \tag{B.25}$$

Therefore, the recoils are emitted in forward direction into a cone of half-angle ϕ_{max}.

If an excited state in nucleus 3 is populated, then the Q-value in the above expressions must be replaced by Q=Q_0-E_{ex} where Q_0 corresponds to the ground state.

B.3 From Kinetic Energy to Momentum

In the previous section it has been derived how to obtain the kinetic energy of the recoiling nucleus in the laboratory system (expression B.23). Here, the relation between the kinetic energy and the momentum will be given. The equations relating the total relativistic energy E_3, the kinetic energy T_3 and the momentum p_3 of a particle with mass m_3 are given by:

$$\mathrm{T}_3 = \mathrm{E}_3 - m_3c^2 \tag{B.26}$$

$$\mathrm{E}_3^2 = p_3^2c^2 + m_3^2c^4 \tag{B.27}$$

and with some rearrangement,

$$\mathrm{E}_3 = \mathrm{T}_3^2 + m_3^2c^4 + 2\mathrm{T}_3m_3c^2 \tag{B.28}$$

and substituting for E_3, we have

$$p_3^2c^2 = \mathrm{T}_3^2 + 2m_3c^2. \tag{B.29}$$

As we often use the energy expressed as MeV/u, we can define

$$T_3(\mathrm{MeV}) = \widetilde{T}_3 \cdot A \tag{B.30}$$

where A is the mass number and $\widetilde{T}_3$ is the energy per nucleon in [MeV/u]. Noting that

$$m = A \cdot A_m \tag{B.31}$$

with $A_m = 931.494\,\mathrm{MeV}/c^2$ and inserting the two previous equations in equation B.29, we have

$$p_3 = A\sqrt{\widetilde{T}_3(\widetilde{T}_3 + 2A_m)} \qquad \mathrm{MeV/c}. \tag{B.32}$$

"An expert is a person who has made all the mistakes that can be made in a very narrow field"

Niels Bohr

APPENDIX *C*

ERRORS

Abstract: *In this appendix some procedures followed to obtain systematic and statistical error in parameters such as number of beam particles, target particles, cross section or astrophysical S-factor will be discussed. Some general concepts will be used to demonstrate how errors are extracted for the observables in this thesis and their propagation is discussed.*

In the following sections some expressions will be given without any proof, and the reader is referred to [Tay82] and [RBKR03] for more details and extended discussion.

C.1 Systematic and Statistical Uncertainties

Systematic uncertainties are those which cannot be revealed by repeating the measurements as they are related to the inaccuracies in the knowledge of various parameters. On the other hand, the statistical uncertainties will arise from overall statistical fluctuations in the measured observables over a finite amount of time and not from the lack of precision in the measuring instruments.

Statistical uncertainties are usually related to count events in a detector. Let us assume that we repeat an experiment where we count in a detector the alpha particles emitted by a standard source under the same conditions and times. The distribution of the results for the number of counts will follow a Poisson Distribution whose standard deviation (σ), is determine by:

$$\sigma = \sqrt{\mu} \tag{C.1}$$

here, μ is the value of the mean counting rate. Therefore, in our case, where we usually do one measurement, we consider σ as the statistical uncertainty associated with the measurement.

On the other hand, **systematic uncertainties** will be related to the measurement equipment or technique, how well calibrated the system is or how stable the experimental conditions are. These uncertainties are highly important as the accuracy (how close the result of our experiment is to the true value) of our experiment is related to how well we can control and understand the systematic uncertainties. Errors of this type have to be carefully estimated with a good understanding of the setup. Therefore, a careful characterisation of the setup to understand and minimise all possible systematic uncertainties plays an crucial role in an experiment.

C.2 Statistical Treatment of Data

The random errors, i.e. errors than can be revealed by repeating the measurements, can be treated statistically as they are considered as fluctuations in observations that yield different results each time we do the experiment. Therefore, for N measurements of a quantity x_i, the best value is given by the mean value $\overline{x}$, defined by:

$$\overline{x} = \frac{\sum\limits_{i=1}^{\mathrm{N}} x_i}{\mathrm{N}} \tag{C.2}$$

while the average uncertainty associated to each measurement is given by the standard deviation, defined by:

$$\sigma_x \equiv \sqrt{\frac{1}{\mathrm{N}-1}\sum(\mathrm{x}_i - \overline{x})^2} \tag{C.3}$$

which we can adopt as the uncertainty associated to a single measurement. It could be demonstrated by performing a single measurement that we would find a probability of 68.27% , that our result will be within σ_x of the correct valued. On the other hand, it can be proved the uncertainty $\overline{x}$ value is given by the standard deviation of the mean ($\sigma_{\overline{x}}$):

$$\sigma_{\overline{x}} = \frac{\sigma_x}{\sqrt{N}} \tag{C.4}$$

C.2.1 The Normal Distribution

In order to perform statistical analysis of an experiment, several measurements are required. The distribution from the measurements is usually plotted as histograms (x-y plots), where x-axis shows the values and y-axis shows the number of times the measurement results in that value. The X-axis is usually divided in bins, the corresponding y-value gives the number of times the result takes a value within the range of the bin.

Typically, Normal Distribution or Gaussian Distributions are seen when fluctuations in measurements are affected only by randoms errors. After sufficient number of measurements the number of times the data takes a value above and below the "true" value will be the same. Thus, it will result in a distribution centred on the "true" X-value[a] and, the larger the deviation from the "true" X-value is, the smaller the frequency it is obtained with. These normal distributions can be expressed as:

$$G(x) = \frac{N}{2\sqrt{2\pi}} e^{-(x-X)^2)/2\sigma^2} \tag{C.5}$$

where X is the central or "true" value, x is the value corresponding to a given measurement, σ is the width of the distribution and N is the normalization constant. An example of a Gaussian distribution with N=1, σ=1, and X=0 is shown in Figure C.1.

[a]There is no measurement which can exactly determine the correct value of any continuous variable. Thus, the true value in a Gaussian distribution is the one which occurs with the highest frequency.

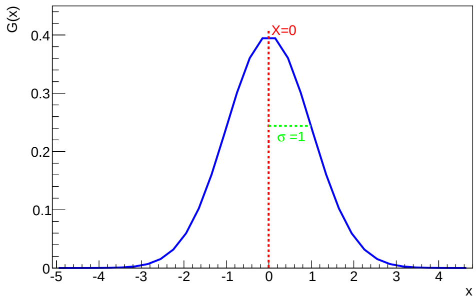

Figure C.1: *Gaussian distribution with N=1, $\sigma = 1$, and X=0.*

It can be proved that the Gaussian function width σ, is the standard deviation of the distribution (σ_x):

$$\sigma = \sigma_x \tag{C.6}$$

with the same meaning and effect as σ_x defined in C.3 . Therefore, σ can be considered as the error of a single measurement.

It is worth mentioning that when systematic errors are added to the random errors all values get shifted in one direction and the distribution will have a new "true" X-value shifted in the same direction.

C.3 The χ^2 Testing Method

The χ^2 testing procedure is the standard analysis technique to compare the results between different measurements, or between a given set of measurements and a given theory. If we make n measurements, χ^2 is usually defined as:

$$\chi^2 = \sum_{k=1}^{n} \left(\frac{\text{observed value-expected value}}{\text{Error}} \right)^2 = \sum_{k=1}^{n} \frac{(O_k - E_k)^2}{\sigma^2} \tag{C.7}$$

where O_k is the measured value with a standard deviation of σ and E_k is the expected value. Often, the *reduced* χ^2 value, denoted by $\bar{\chi}^2$ and defined as:

$$\bar{\chi}^2 = \chi^2/d \tag{C.8}$$

is also used, where d is the number of degrees of freedom. If the value of $\bar{\chi}^2$ is around one, then the agreement between the compared values should considered as good and if $\bar{\chi}^2$ is much larger than one then the two sets of compared values should be seen as in disagreement.

C.4 Least-squares Fits and Errors

Measurements and data analysis usually take advantage of the mathematical relationship between different variables. For example, the study in Figure 3.35, where a linear relationship is seen between the magnetic field required to bend the ^{4}He beam and the pressure in the gas target. The analytical method of finding the best fit line is called *linear regression* or *least-squares fit*.

Let us consider a measurement where two observables assume a linear relationship, $y_i = Ax_i + B$. The best functional fit to the data can then be given by the A and B values which minimise the value of χ^2, i.e.

$$\chi^2 = \sum_{i=1}^{N} \frac{(y_i - A - Bx_i)^2}{\sigma_{y_i}^2}. \tag{C.9}$$

Minimising χ^2 with respect to the parameters A and B, we have:

$$A = \frac{\sum_{i=1}^{N} w_i x_i^2 \sum_{i=1}^{N} w_i y_i - \sum_{i=1}^{N} w_i x_i \sum_{i=1}^{N} w_i x_i y_i}{\Delta} \tag{C.10}$$

$$B = \frac{\sum_{i=1}^{N} w_i \sum_{i=1}^{N} w_i x_i y_i - \sum_{i=1}^{N} w_i x_i \sum_{i=1}^{N} w_i y_i}{\Delta} \tag{C.11}$$

$$\Delta = \sum_{i=1}^{N} w_i \sum_{i=1}^{N} w_i x_i^2 - \left(\sum_{i=1}^{N} w_i x_i \right) 2 \tag{C.12}$$

where $w_i = 1/\sigma_i^2$ introduce the weight factors for each of measurement. The errors associated to A and B are given by:

$$\sigma_A = \sqrt{\frac{\sum_{i=1}^{N} w_i x_i^2}{\Delta}} \tag{C.13}$$

$$\sigma_B = \sqrt{\frac{\sum_{i=1}^{N} w_i}{\Delta}} \tag{C.14}$$

The same method can be generalised for y which is expected to be a higher order polynomial in x: $y = A + Bx + ... + Hx^n$, although the algebra becomes complex.

C.5 Error Propagation

The values of a variable usually depends on one or more other measured variables. The relevant example from our experiment is that the cross section depends on the number of recoils, beam and target particles. Therefore, we should estimate the propagation of uncertainties from several measured variables $(u, v...)$ to determine the uncertainty in whatever variable x, which depends on $u, v, ...$ The general expression relating the variance σ_x^2 (square of the standard deviation) of the dependent variable x to the variances of $u, v, ..$ is given by:

$$\sigma_x^2 \approx \sigma_u^2 \left(\frac{\partial x}{\partial u} \right) + \sigma_v^2 \left(\frac{\partial x}{\partial v} \right) + ... \tag{C.15}$$

C.6 Error in TRIUMF Experiment

In this section, how the errors are obtained for different variables in our experiment performed at TRIUMF are detailed. The systematic and statistical uncertainties are treated separately. The final systematic (statistical) errors in the cross section and S-factor are obtained by standard error propagation with expression C.15 of the systematic (statistical) uncertainties in the observable that the cross section depends on, namely, numbers of ^{3}He target particles, ^{4}He beam particles and ^{7}Be recoils.

C.6.1 Errors contributions to the number of ^{3}He target particles

No statistical errors are considered in the number of target particles.Taking into account the expression N_t=9.66$\cdot 10^{18} \frac{\ell \cdot P}{T}$, the systematic uncertainty of N_t is obtained from standard error propagation of the uncertainties:

- $\Delta\ell$=0.5 cm, from previous experiments and TDP measurements.
- $\Delta P = (0.1 + \sigma_P)$ Torr and $\Delta T = (1 + \sigma_T)$ k: The final values for pressure and temperature are taken as the average value of the corresponding values recorded each five minutes. However, it is worth noting here that as the pressure and temperature change during the run the average value of the "true" readings do not have the same meaning as in expression C.2 where it is assumed that the "true" value is the same and the deviations are coming from randoms errors. Therefore, the standard deviations of a single measurement (σ_T and σ_P) are considered as errors, instead of the standard deviation of the mean. The 0.1 Torr and 1 K systematics contributions are taken from reference [GBB04].

C.6.2 Error contributions to the number of ^{4}He Beam Particles

The number of beam particles in our measurements is given by (cf. section 5.3.3):

$$\mathrm{N}^{\mathrm{oB}}_{^4\mathrm{He}} = \frac{\mathrm{R^F} \cdot \mathrm{Si\text{-}30}}{\mathrm{Livetime} \cdot \mathrm{P} \cdot \mathrm{T}} \tag{C.16}$$

The statistical error is obtained by standard error propagation of the statistical uncertainty associated with the Si-30 variable (area of the peak in the silicon detector) which is given by the expression C.1:

$$\sigma_{\mathrm{Si\text{-}30}} = \sqrt{\mathrm{Si\text{-}30}} \tag{C.17}$$

The final statistical errors in $\mathrm{N}^{\mathrm{oB}}_{^4\mathrm{He}}$ are smaller than 0.5 %.

The systematic error arises from the systematic uncertainty in P and T calculated as detailed in section C.6.1 and from the systematic uncertainty in R_F from the fits shown, for example, in Figure 5.18.

C.6.3 Error contributions to the number of ^{7}Be recoils

The total number of ^{7}Be nuclei produced is given by (cf. section 3.3.2.7):

$$Y_{^7\mathrm{Be}} = \frac{Y_{\mathrm{DSSSD}}}{\mathrm{t}_\ell \cdot q_{\mathrm{f}} \cdot \epsilon_{\mathrm{DRAGON}} \cdot \epsilon_{\mathrm{DSSSD}}} \tag{C.18}$$

The statistical error in the $Y_{^7\mathrm{Be}}$ can be obtained by propagating i) the error in Y_{DSSSD}, i.e. the ^{7}Be nuclei detected in the DSSSD, which is given by:

$$\sigma_{Y_{\mathrm{DSSSD}}} = \sqrt{Y_{\mathrm{DSSSD}}} \tag{C.19}$$

and ii) the statistical uncertainty associated with $\epsilon_{\mathrm{DRAGON}}$ shown in Table 4.23.

The systematic errors propagated are:

- 0.10% error associated with ϵ_{DSSSD}.
- The systematic uncertainty associated with $\epsilon_{\mathrm{DRAGON}}$ shown in table 4.23.
- The error in t_ℓ calculated from the total and acquired triggers.
- The errors in q_f are obtained from the CSD distribution measurements.

  The two facts, namely the CSD is energy dependent, and the recoils are created with a distribution in energy (see Table 5.10) have been also taken into account. Figure C.2 shows the charge state fractions together within their errors at different energies for both the 2^+ (top) and 3^+ (bottom) charge states of ^{9}Be. Enclosed in circles are the values considered in the data analysis (see Table 3.5) and the green dots are values for the "highest" and "lowest" recoil energies for different sets of S_{34} capture data at different $\mathrm{E_{CM}}$. It should be pointed out that for the 383.30 MeV/u ^{7}Be mean energy corresponding to the 2013 run, both the $\mathrm{q}_f(2^+)$ and the associated error have been calculated by extrapolating the values and errors measured for other energies and the same charge state (blue solid line and dashed red line in Figure C.2(a)). As can be seen, for the four cases the charge state fractions associated to the "highest" and "lowest" recoil energies, (i.e. the limits indicated by the green points) are always within the error bars of the mean values. This, added to the fact that most of the recoils are created along with a 90º γ-emission (assuming isotropic prompt γ-ray angular distributions), which should have the mean CSD values, makes us argue that the uncertainty in q_f to be the same as that for the mean values. An additional error contribution should in principle be considered, which is associated with the fact that the charge state equilibrium was proved only to ∼1 Torr, but not for lower pressures. However, this was not done based on the experience of previous experiments where the charge state equilibria were found even at lower pressures within our considered errors. New measurements proving this fact are planned.

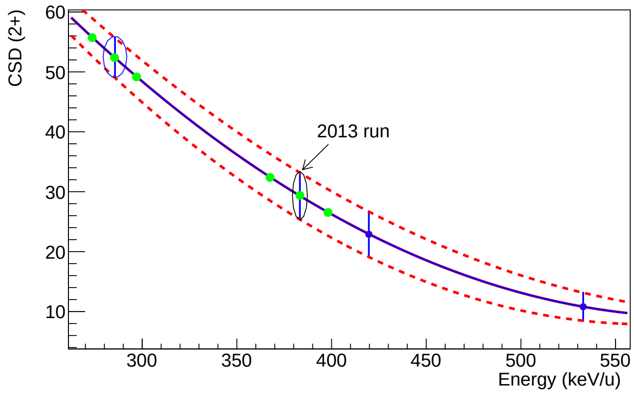

(a)

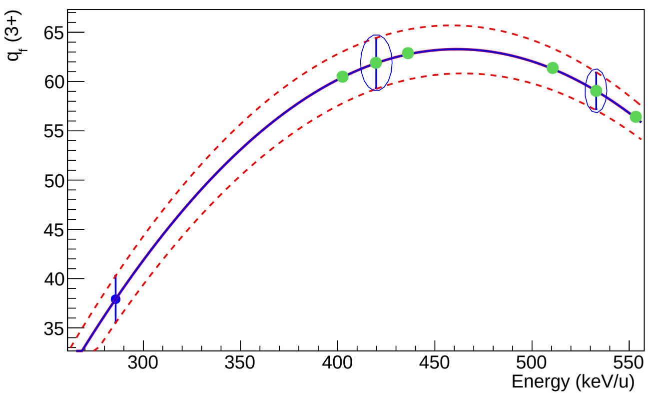

(b)

Figure C.2: *Charge state fractions for 2^+ and 3^+ for the different recoils energies. Enclosed in circles are the mean values of the different q_f used corresponding to the energy of the recoils created at the centre of the gas target with the prompt γ-ray emitted at 90º. The green dots indicate for the maximum and minimum recoils energies the charge state fraction obtained by extrapolation of the measured values.*

C.6.4 Error contributions to the S_{34}(E) factor

Different error contributions to the astrophysical S-factor obtained from the direct counting experiment at TRIUMF are shown in Table C.1 (systematics) and C.2 (statistical).

$E_{^4He}$ MeV	ΔS_{34}^{syt} (%)	ΔE (%)	Δ^4He (%)	Δ^3He (%)	$\Delta\ell$ (%)	(%)ΔP,ΔT (%)	(%)Be (%)	Δq_f (%)	$\Delta\epsilon_{DRAGON}$ (%)	Δt_ℓ, $\Delta\epsilon_{DSSSD}$ (%)
~6.5	$^{+6.96}_{-12.57}$	0.03	1.23	4.62:	4.07	2.19	$^{+5.06}_{-11.62}$	3.17	$^{+3.94}_{-11.18}$	0.26
~5.2	$^{+10.98}_{-11.91}$	0.06	0.60	5.40:	4.07	3.56	$^{+9.53}_{-10.59}$	4.12	$^{+8.60}_{-9.76}$	0.12
~3.5	$^{+10.04}_{-11.00}$	0.09	0.45	4.97:	4.07	2.87	$^{+8.71}_{-9.80}$	6.37	$^{+5.94}_{-7.45}$	0.22
~4.7	$^{14.80}_{17.02}$	0.06	0.98	5.64:	4.07	3.92	$^{+13.65}_{-16.03}$	13.0(*)	$^{+4.15}_{-9.37}$	0.12

Table C.1: *Systematic error contributions to the astrophysical S-factor for the Direct Recoil Counting experiment at TRIUMF. The second column shows the total systematic uncertainties, while the columns titled as ΔE, Δ^4He, Δ^3He, and Δ^7Be show individual contributions from the energy, number of beam particles, number of target particles, and number of recoils to ΔS_{34}^{syt}, respectively. The columns titled as $\Delta\ell$, ΔP, ΔT give error contributions from the target length, pressure and temperature, respectively, to the systematic uncertainty in the number of Δ^3He target particles. The columns titled as Δq_f and $\Delta\epsilon_{DRAGON}$ give contributions from the measured charge state fractions and DRAGON efficiencies , respectively, to the systematic uncertainty in the number of ^{7}Be recoils.*
(*) This relative large error is due to the fact that the q_f at this energy is obtained by extrapolating the errors measured with other energies (see section C.6.3. Measurements of charge state distributions at this energy are planned.)

Run	$E_{^4He}$ MeV	ΔS_{34}^{stat} (%)	Δ^4He (%)	Δ^7Be (%)	$\Delta\epsilon_{DRAGON}$ (%)	ΔY_{DSSSD} (%)
2011	~6.5	1.24	0.37	1.18	1.05	0.55
	~5.2	0.92	0.17	0.91	0.87	0.27
	~3.5	0.77	0.17	0.75	0.59	0.48
2013	~4.7	0.95	0.07	0.94	0.84	0.44

Table C.2: *Statistical error contributions to the astrophysical S-factor for Direct Recoil Counting experiment at TRIUMF. The third column shows the total statistical uncertainties. The columns titled as Δ^4He and Δ^7Be show the contributions from the number of beam particles and number of recoils to ΔS_{34}^{stat}, respectively. The columns titled as $\Delta\epsilon_{DRAGON}$ and ΔY_{DSSSD}, give individuals contributions from DRAGON efficiency and the ^{7}Be counts in the DSSSD to the statistical uncertainty in the number of ^{7}Be recoils,*

"Yo soy yo y mis circunstancias"
José Ortega y Gasset

APPENDIX *D*

SPANISH SUMMARY/RESUMEN EN CASTELLANO

Abstract: *El trabajo presentado en esta tesis versa sobre el estudio de la sección eficaz de la reacción nuclear de interés astrofísico* ^{3}*He(*α*,*γ*)*^{7}*Be. En este apéndice se presentará, en castellano, un amplio resumen del trabajo presentado. En primer lugar se motivará el trabajo desarrollado. Seguidamente se detallarán las técnicas experimentales utilizadas para determinar la sección eficaz de la reacción así como el análisis y los resultados. Por último, se discutirán los resultados obtenidos y su impacto.*

D.1 Estudios sobre la Reacción ^{3}He(α,γ)^{7}Be: Motivación

La sección eficaz de la reacción nuclear ^{3}He(α,γ)^{7}Be juega un papel relevante en dos escenarios astrofísicos importantes: las predicciones de la abundancia del ^{7}Li primordial en el universo a través de la *Nucleosíntesis Estándar del Big Bang* (SBBN por sus siglas en inglés), y las estimaciones del flujo de neutrinos solares procedentes de las desintegraciones del ^{8}B y ^{7}Be a través del *Modelo Solar Estándar* (SSM por sus siglas in inglés).

Desde los primeros estudios llevados a cabo por Holmgrem y Johnston [HJ59], intensos esfuerzos se han llevado a cabo tanto experimental como teóricamente con el objetivo de determinar la sección eficaz de dicha reacción de forma precisa. Actualmente, el estudio de esta reacción sigue siendo objeto de investigaciones con el objetivo de extraer el factor astrofísico S_{34}(E) con una incertidumbre reducida.

D.1.1 La nucleosíntesis del Big Bang y el problema del ^{7}Li primordial

Actualmente la teoría del Big Bang es el modelo cosmológico más aceptado debido a que explica tres aspectos importantes: la expansión del Universo, la radiación de fondo microondas y la nucleosíntesis primordial.

En el marco de la teoría del Big Bang y del modelo estándar de partículas, la SBBN explica la producción de los primeros elementos en el universo entre los 200 y 1000 s después de la explosión del Big Bang. La Figura D.1 muestra la cadena principal de reacciones involucradas en la producción de los elementos primordiales. Ésta comenzó con la reacción $p(n,\gamma)d$, la cual generó el deuterio d, semilla para la producción del resto de elementos. Los principales elementos remanentes de esa nucleosíntesis primordial fueron, d, tritio (t), ^{3}He, ^{4}He y ^{7}Li; la inexistencia de núcleos estables con A=8 evitó la presencia de isótopos primordiales más pesados en abundancias relevantes. Para las condiciones de temperaturas durante la SBBN, el intervalo de energías del pico de Gamow para la reacción ^{3}He(α,γ)^{7}Be es 400 $\geq E_{CM} \geq$ 180 keV, el cual es accesible en los laboratorios.

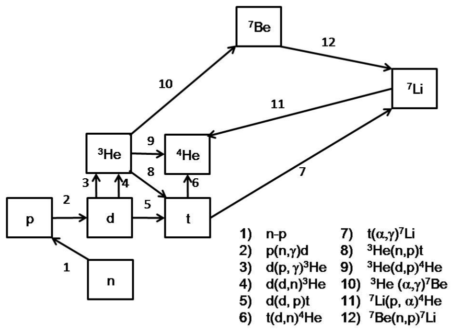

Figure D.1: *Cadena de las principales reacciones involucradas de la Nucleosíntesis del Big Bang.*

La Figura D.2 muestra una comparativa de las estimaciones de las abundancias calculadas con la SBBN y los valores inferidos de la oberación directa.

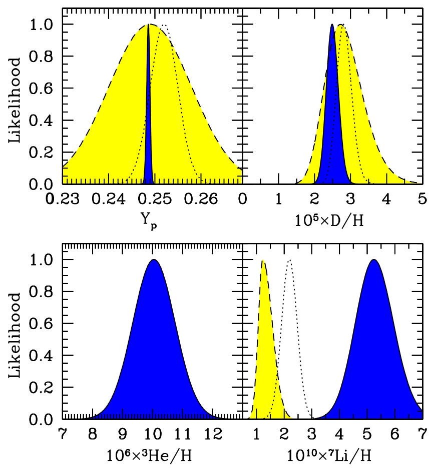

Figure D.2: *Probabilidades calculadas y observadas para la abundancia de los elementos primordiales ^{4}He (Y_p), D/H, ^{3}He/H y ^{7}Li/H. Las regiones en azul muestran las probabilidades estimadas con el SSBN. Las regiones en amarillo y las punteadas muestran las probabilidades obtenidas a partir de la observación directa de diferentes emplazamientos astrofísicos. Para la abundancia del ^{7}Li, (^{7}Li/H), la región amarilla muestra los valores inferidos a partir de la observación de estrellas con halo y la función punteada muestra la determinación mediante la observación de clusters globulares de estrellas. La Figura ha sido obtenida de [CFO08]*

Como puede observarse las abundancias estimadas de los elementos primordiales de *d*, ^{3}He y ^{4}He están en acuerdo con aquellos valores inferidos de las observaciones astrofísicas directas. Sin embargo, las estimaciones sobre la abundancia del ^{7}Li primordial son aproximadamente tres veces superiores a las observadas. Éste es el conocido como *Problema del ^{7}Li primordial*.

El origen de esta discrepancia es aún desconocido. Diferentes soluciones han sido sugeridas incluyendo física más allá del modelo estándar. También se ha discutido ampliamente si la discrepancia puede ser debida a una mala estimación en las tasas de reacciones nucleares implicadas. El ^{7}Li es producido principalmente a través de la reacción ^{3}He(α,γ)^{7}Be y posterior ^{7}Be(n,p)^{7}Li y destruido mediante ^{7}Li(p,α)^{4}He. En concreto, $^7\mathrm{Li/H} \propto \mathrm{S}_{34}^{0.96}$ donde S_{34} es el factor astrofísico de nuestra reacción de interés. A pesar de que actualmente no se cree que una determinación precisa de la tasa de reacción de ^{3}He(α,γ)^{7}Be vaya a resolver el *problema*, reducirá la incertidumbre en los modelos. Por ejemplo, la evaluación de nuevos datos de la sección eficaz de dicha reacción, [CFO08], mostró un desplazamiento de un 16% en el valor central de la abundancia del ^{7}Li primordial.

D.1.2 El sol y el problema de los neutrinos solares

Como la estrella más cercana, el Sol, es la estrella más estudiada. Las condiciones presentes allí hacen del Sol un emplazamiento perfecto para la producción de numerosos procesos nucleares. El origen de estos procesos, desde un punto de vista de nucleosíntesis estelar, es explicado por el *Modelo Solar Estándar*.

La Figura D.3 muestra las principales reacciones nucleares en el Sol agrupadas en la cadena protón-protón, en la cual se genera el 99% de la energía solar, y el ciclo CNO que supone el 1% restante.

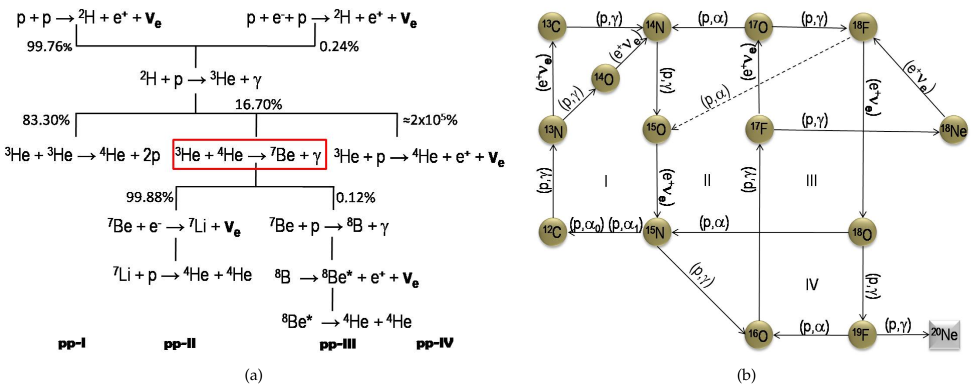

Figure D.3: *Principales reacciones nucleares en el Sol agrupadas en (a) cadena protón-protón, y (b) ciclo CNO.*

Entre otros observables, el SSM predice el flujo de neutrinos solares. Históricamente, las estimaciones de SSM predecían una producción de neutrinos solares de alta energía de aproximadamente el triple comparadas con las detecciones directas en la Tierra. Estas grandes discrepancias fueron parcialmente resueltas mediante la postulación y posterior comprobación de las *oscilaciones de neutrinos*. Actualmente, las estimaciones del flujo de neutrinos solares por el SSM, mostradas en la Figura D.4, no son lo suficientemente precisas. Concretamente, el flujo de neutrinos de alta energía procedente de la desintegración del ^{7}Be y ^{8}B es directamente proporcional al factor astrofísico de nuestra reacción en la forma: $\phi_\nu(^7\mathrm{Be}) \propto \mathrm{S}_{34}(0)^{0.86}$ y $\phi_\nu(^8\mathrm{B}) \propto \mathrm{S}_{34}(0)^{0.81}$, respectivamente [CD08]. Por tanto una determinación precisa de la tasa de reacción es determinante para reducir la incertidumbre asociada al flujo de neutrinos. Concretamente, de la incertidumbre asociada a los parámetros nucleares de entrada del SSM, la sección eficaz de la reacción ^{3}He(α,γ)^{7}Be es la de segunda mayor influencia.

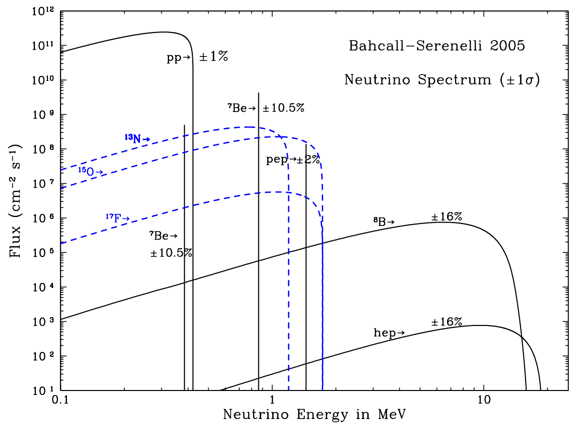

Figure D.4: *Espectro de neutrinos solares estimado por el SSS [BP95].*

D.1.3 Estudios experimentales previos

Dada la importancia de la reacción ^{3}He(α,γ)^{7}Be en el SSM y BBN, la sección eficaz de esta reacción se ha determinando experimentalmente utilizando cada vez métodos con mayor precisión. La Figure D.5 muestra un esquema de como se produce la reacción reacción y la posterior desintegración del ^{7}Be.

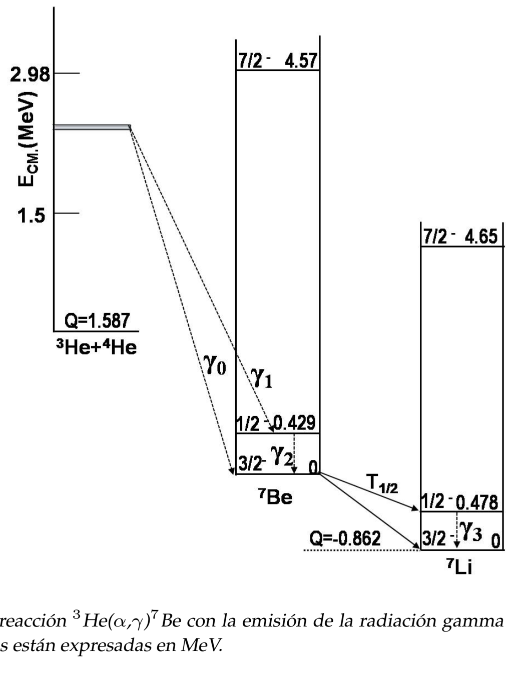

Figure D.5: *Esquema de la reacción ^{3}He(α,γ)^{7}Be con la emisión de la radiación gamma directa y la posterior desintegración del ^{7}Be. Las energías están expresadas en MeV.*

La **captura radiativa** del ^{3}He y ^{4}He forma un núcleo de ^{7}Be siendo el valor-Q de la reacción 1.587(1) MeV. En el proceso de fusión se emite un rayo γ con dos energías disponibles dependiendo de que se pueble el estado fundamental (γ_0) o el primer estado excitado (γ_1) en el ^{7}Be. El el último caso, la desexcitación del estado se produce mediante la emisión de un rayo γ de 429 keV quedando el ^{7}Be en el estado fundamental. El ^{7}Be formado es un nucleo inestable que decae mediante el proceso de captura electrónica con una vida media de 53.24(4) días. El valor-Q de la reacción es 862 keV y con una tasa de 10.44% la desintegración puebla el primer estado excitado del ^{7}Li a 478 keV, el cual se desexcita emitiendo un rayo γ (γ_3) de esa energía.

En función del producto de reacción detectado, tres técnicas experimentales diferentes son usadas para determinar la sección eficaz de la reacción. En el *Método de Activacion* se detecta la radiación gamma procedente de la desexcitación del ^{7}Li tras la colección los núcleos de ^{7}Be producidos. En el *Método de Detección Directa* los núcleos de ^{7}Be son contados directamente. En el *Método de Radiación-γ Directa* se detecta la radiación γ directa producida en la reacción. La Figura D.6 muestra los datos existentes del factor astrofísico previos a la investigación presentada aquí agrupados en función de la técnica utilizada.

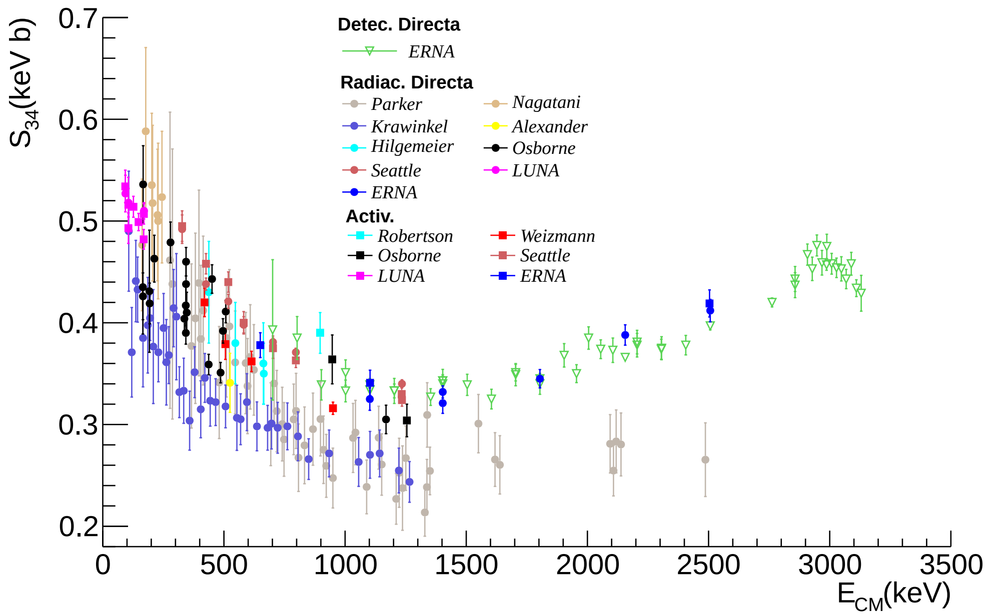

Figure D.6: *Valores del factor-S astrofísico para la reacción $^3He(\alpha,\gamma)^7Be$ (S_{34}). Los datos obtenidos utilizando el Método de Radiación-γ Directa, Método de Activación y el Método de Detección Directa se muestran en círculos, cuadrados y triángulos, respectivamente.*

El rango de energías cubierto en los experimentos previos está entre 93 y 3130 keV. Solo las medidas de Parker y Tombrello [PK63] y la colaboración ERNA [DGK09] realizaron medidas a energías superiores a 1200 keV, las cuales muestran una gran discrepancia entre ellas. Resolver esta discrepancia es uno de los objetivos del trabajo presentado en esta tesis.

Los datos experimentales utilizan diferentes modelos teóricos para obtener el valor del factor $S_{34}(0)$. Una comparativa entre los diferentes valores del factor $S_{34}(0)$ obtenidos mediante las diferentes técnicas experimentales se muestra en la Figura D.7. Como puede observarse, existe una gran discrepancia entre los diferentes valores.

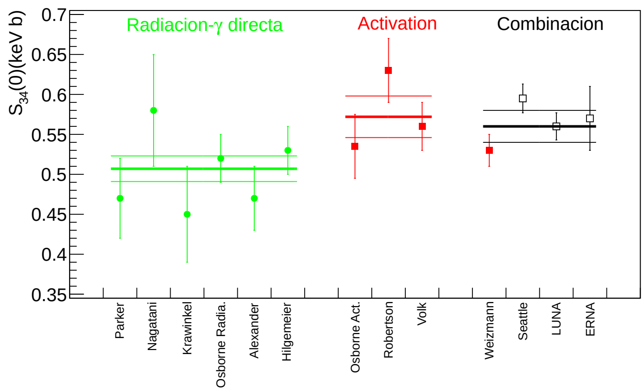

Figure D.7: *Valores del factor $S_{34}(0)$ obtenidos a partir de las diferentes medidas experimentales previas al trabajo presentado en esta tesis. Los resultados fueron obtenidos mediante el método de radiación γ directa (círculos verdes), método de activación (cuadros rojos) y métodos complementarios simultaneamente (cuadros abiertos): Seattle [BBS07] y LUNA [CBC07] utilizaron el método de activación y detección directa de la radiación γ simultáneamente, mientras que la colaboración ERNA [DGK09] convinó los tres métodos. La línea gruesa de color verde es el valor recomendado en [AAB98] basándose en los experimentos de detección de radiación gamma directa al tiempo que se publicó la revisión, y la líneas verdes delgadas muestran el error considerado. Las líneas rojas tienen el mismo significado para el método de activación. La línea negra es el valor recomendado de $S_{34}(0)$ en la revisión en [AGR11] basados en la evaluación de los datos de Weizmann, Seattle, LUNA y ERNA. Debería notarse que mientras que los cuadros abiertos para Seattle, LUNA y ERNA son obtenidos por combinación de diferentes métodos, la evaluación solo tiene en cuenta las medidas de activación de Seattle y LUNA y las de detección directa de ERNA.*

D.1.4 Modelos teóricos

La reacción ^{3}He(α,γ)^{7}Be es un tipo de reacción nuclear directa de las conocidas como *captura radiativa*. Estas son transiciones electromagnéticas entre un estado de "dispersión" inicial y un estado ligado final mediante la correspondiente emisión de radiación electromagnética. Diferentes cálculos teóricos han sido llevados a cabo intentado reproducir los datos experimentales y entender el mecanismo de reacción. Los cálculos pueden ser agrupados en *modelos potenciales*, [KIN81, BBR85, MAK93] y en *modelos microscópicos* [QKT81, KA84] además de aquellos que utilizan análisis de matriz-R [DAA04], o las evaluaciones en [CFO08] y [AGR11], que utiliza los modelos de [Nol01] y [Kaj86]. Recientemente, los primeros cálculos ab-initio utilizando la aproximación de dinámica molecular fermiónica, realizados sin tener en cuenta medidas experimentales [Nef11], son los primeros en reproducir los datos de la colaboración ERNA a energías intermedias.

Modelo/Evaluación	S_{34}(0) (keV·b)
Matriz-R [DAA04]	0.51±0.04
Cyburt y Davids [CD08]	0.580±0.043
Solar Fusion Cross Sections II [AGR11]	0.56±0.02(expt)±0.02(theor)
Cálculos Ab-initio [Nef11]	0.593

Table D.1: *Valores de $S_{34}(0)$ obtenidos con diferentes cálculos teóricos. Matriz-R y Cyburt y Davids utilizan la evalución de datos experimentales. La evaluación Solar Fusion Cross Section II utiliza los modelos de Kajino et al. [KTA87] y Nollet [Nol01] y los datos experimentales más recientes hasta 1 MeV. Por último, lo cálculos ab-initio no utilizan ninguno de los datos experimentales y obtienen directamente el valor de $S_{34}(0)$.*

La Tabla D.1 muestra los valores del factor $S_{34}(0)$ según los diferentes cálculos, evidenciando la discrepancia entre los diferentes modelos teóricos. La Figura D.8 muestra diferentes cálculos conjuntamente con los datos obtenidos a partir de los datos de Weizmann en el año 2004 [NHNEH04]. Como puede observarse, no solo el valor del factor $S_{34}(0)$ es diferente entre los modelos teóricos, además, obviando el factor normalización, la dependencia del factor astrofísico con la energía es diferente, sobre todo a partir de 1 MeV. Nuevos datos a energías intermedias son necesarios puesto que limitarán la dependencia del factor astrofísico con la energía y por tanto las extrapolaciones a energías de interés astrofísico.

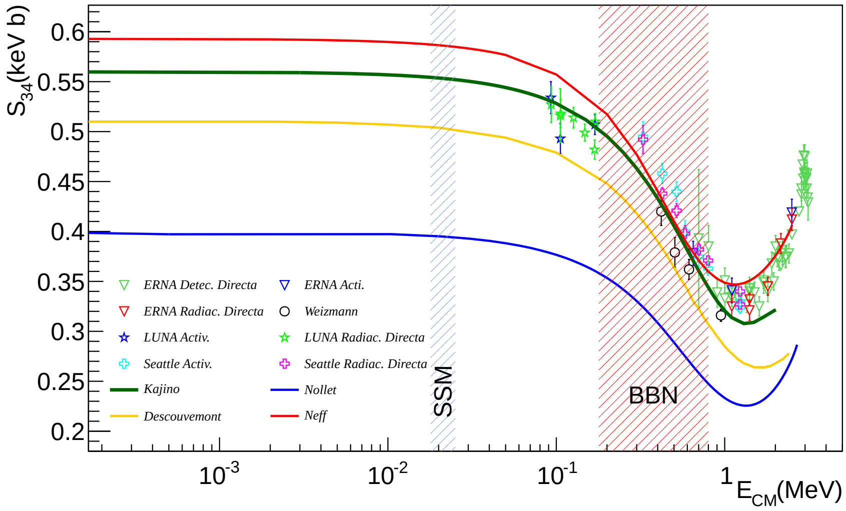

Figure D.8: *Comparación de los diferentes modelos teóricos de Kajino et al. [KTA87], Nollet [Nol01], Descouvemont et al. [DAA04] y Neff [Nef11], junto con los datos experimentales de ERNA [DGK09], Weizman [NHNEH04], LUNA [BCC06, CBC07, GCC07] y Seattle [BBS07]*

Es importante notar que los calculos ab-initio [Nef11], que reproducen los resultados de ERNA [DGK09], a pesar de reproducir la dependencia con la energía de la reacción espejo $^{3}H(\alpha,\gamma)^{7}Li$ discrepan en un 15% en el valor absoluto al comparar con los resultados experimentales de Brune et al. [BWR94].

D.2 Técnicas Experimentales

De entre las tres técnicas experimentales enumeradas en la sección anterior hemos utilizado el *método de activación* y el *método de detección directa* para determinar la sección eficaz de la reacción $^{3}He(\alpha,\gamma)^{7}Be$ en el rago E_{CM}=1-3 MeV. Debido a las limitaciones experimentales la sección eficaz no se puede determinar a las bajas energías astrofísicas, por ejemplo a los 22 keV correspondientes al pico de Gamow en el Sol, por tanto, los modelos teóricos son utilizados para extraer el factor $S_{34}(0)$ a partir de valores determinados a energías superiores. Medidas experimentales en el rango E_{CM}=1-3 MeV son especialmente relevantes puesto que ayudarán a resolver la discrepancia entre los datos existentes en este rango [PK63], [DGK09] y facilitarán la extrapolación a energías de interés astrofísico.

Actualmente existen muchas instalaciones con aceleradores de partículas en todo el mundo. De las dedicadas a física nuclear y astrofísica, algunas están especialmente enfocadas a la producción de haces de iones radiactivos como ISOLDE en el CERN, GSI o RIKEN. Existen también algunas otras que incluyen aceleradores de menor escala como por ejemplo el CNA en Sevilla, las cuales satisfacen las necesidades de energía y estabilidad necesarias en nuestros experimentos.

Por otra parte, para realizar el experimento usando el *método de detección directa*, algunos requerimientos adicionales son necesarios. Debido a la cinemática de la reacción, los núcleos de ^{7}Be son producidos hacia delante siguiendo prácticamente la misma dirección del haz. Por tanto, los iones de ^{7}Be tienen que ser separados e identificados de las partículas del haz antes de ser "contados". En principio se podría utilizar un detector que permita la identificación de partículas como un DSSSD o cámaras de ionización, pero debido a las altas intensidades necesarias en estos experimentos el detector dejaría de ser eficiente al incidir tantas partículas sobre él puesto que se deterioraría.

Basándose en la discusión anterior el experimento de *activación* se ha realizado utilizando el acelerador tandem en el Centro de Microanálisis de Materiales de Madrid, España. Para el experimento de *detección directa* se ha utilizado el separador DRAGON en la instalación TRIUMF, en Vancouver, Canadá

D.2.1 Método de activación

En el experimento llevado a cabo en el CMAM se utilizó un haz de ^{3}He que incidía sobre un blanco gaseoso de ^{4}He el cual estaba almacenado en una cámara de reacción. La Figura D.9 muestra un esquema del montaje experimental. El ^{7}Be formado se depositaba en una placa de cobre situada al final de la cámara y su desintegración era medida posteriormente en una estación de bajo fondo constituida por un detector de germanio de alta pureza. Se utilizaron diez energías incidentes diferentes, cinco medidas en el 2009 y cinco en el 2011. Para cada energía, la sección eficaz de la reacción nuclear (σ_{34}) viene dada en este caso por:

$$\sigma_{34}(E) = \frac{N_{^7\text{Be}}}{N^{\text{haz}}_{^3He} \cdot N^{\text{blanco}}_{^4He}} \tag{D.1}$$

donde $N_{^7\text{Be}}$, $N^{\text{haz}}_{^3He}$ y $N^{\text{blanco}}_{^4He}$ son el número de núcleos de ^{7}Be producidos, el número de partículas incidentes y la densidad superficial del blanco, respectivamente.

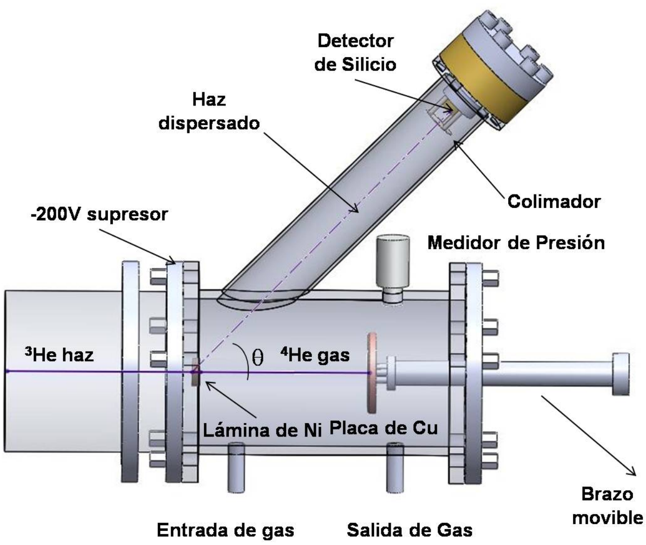

Figure D.9: *Diagrama del montaje experimental. Un haz de ^{3}He incidía sobre el haz de ^{4}He encerrado en la cámara y separado de la línea de vacío mediante una lámina de níquel. Un detector de silicio situado a 45º se utilizó para monitorizar el haz dispersado con la lámina de Ni. En la placa de cobre, situada sobre un brazo movible al final de la cámara, se depositaban los núcleos de ^{7}Be generados. Un supresor de electrones a -200V colocado delante de la lámina de Niquel evitaba que los electrones de la lámina de Ni saliesen repelidos por el impacto del haz.*

Para determinar el número de partículas incidentes $N^{\text{haz}}_{^3He}$ se utilizaron dos métodos simultáneamente. Por una parte la cámara actuaba en sí misma como una taza de Faraday. Todos los elementos de la cámara estaban conectados eléctricamente y separados del la línea experimental mediante material aislante y por tanto la carga depositada en la cámara era medida. Por otra parte el haz dispersado elásticamente con la lámina de Ni era monitorizado en el detector de silicio, y el número de partículas incidentes es determinado teniendo en cuenta la expresión de dispersión Rutherford.

Debido a las bajas presiones utilizadas durante el experimento (≈60 Torr) se puede considerar que el gas se comporta como un gas ideal y por tanto se puede estimar la densidad superficial del mismo mediante la expresión:

$$N_{\text{blanco}} = 9.66 \cdot 10^{18} \frac{\ell \cdot P}{T_0 + T_C} \qquad (at/cm^2) \tag{D.2}$$

donde ℓ en cm es la longitud del blanco, P en Torr es la presión del gas, T_0 en Kelvin es la temperatura ambiente igual a 22.5±1.5ºC y T_C es el aumento de temperatura en el gas debido al impacto del haz. El valor de ℓ se corresponde con la distancia entre la lámina de Ni y la placa de Cu. La placa de cobre era fijada al principio de cada medida y la distancia era determinada tanto al principio como al final de la medida. La presión fue monitorizada durante todo el experimento y el valor efectivo fue determinado como la media entre los valores obtenidos para cada medida. La corrección T_C ha sido obtenida mediante extrapolación lineal de los valores experimentales obtenidos con el mismo montaje utilizado en el Instituto Weizmann para determinar la sección eficaz de la misma reacción a energías más bajas [NHNEH04].

El ^{7}Be creado se depositaba en una placa de cobre por la propia cinemática de la reacción. Se utilizó una placa de cobre para cada energía, las cuales fueron enviadas al Centro de Investigaciones Nucleares SOREQ donde disponen de una instalación de bajo fondo especializada en la detección de radiación γ. Allí se medía la radiación γ procedente de las desexcitación del primer estado excitado del ^{7}Li generado tras la desintegración del ^{7}Be. Un esquema del dispositivo experimental se muestra en la Figura D.10, el cual se compone principalmente de un detector de germanio de alta pureza (HpGe) apantallado por diferentes capas de plomo, hormigón etc...y un plástico centellador usado en anti-coincidencia para reducir la radiación cósmica de fondo.

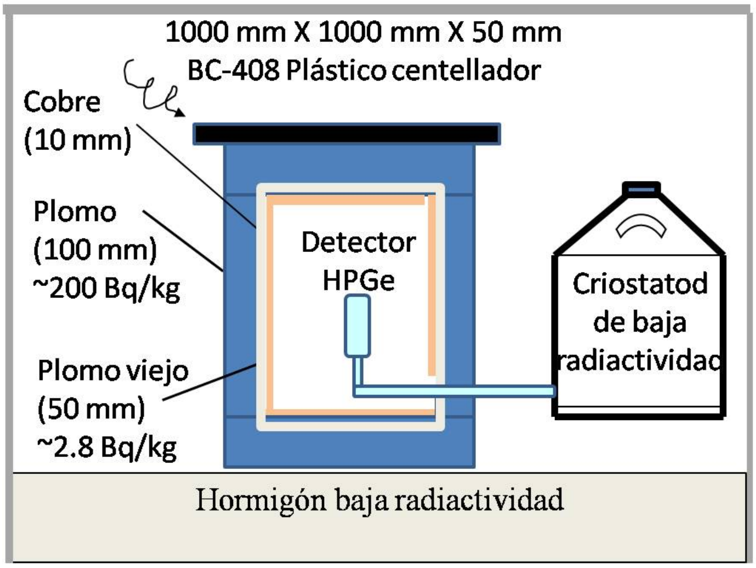

Figure D.10: *Diagrama del la instalación de bajo fondo en SOREQ.*

D.2.2 Método de detección directa

Para el experimento realizado mediante la técnica de detección directa del ^{7}Be utilizamos el separador DRAGON en TRIUMF [HBB03]. Se determinó la sección eficaz de la reacción a cuatro energías diferentes utilizando un haz de ^{4}He que incidía sobre un blanco gaseoso de ^{3}He. Un diagrama del separador se muestra en la Figura D.11. DRAGON consta de cuatro elementos principales: un blanco gaseoso sin ventana el cual se mantiene en la cámara de reacción mediante un complejo sistema de bombas de vacío; una matriz de detectores centelladores BGO que rodean al blanco; el separador, compuesto por dipolos cuadrupolos y sextupolos eléctricos y magnéticos; y un sistema de detección situado en el plano focal del separador, que en nuestro caso fue un detector de silicio de bandas (DSSSD).

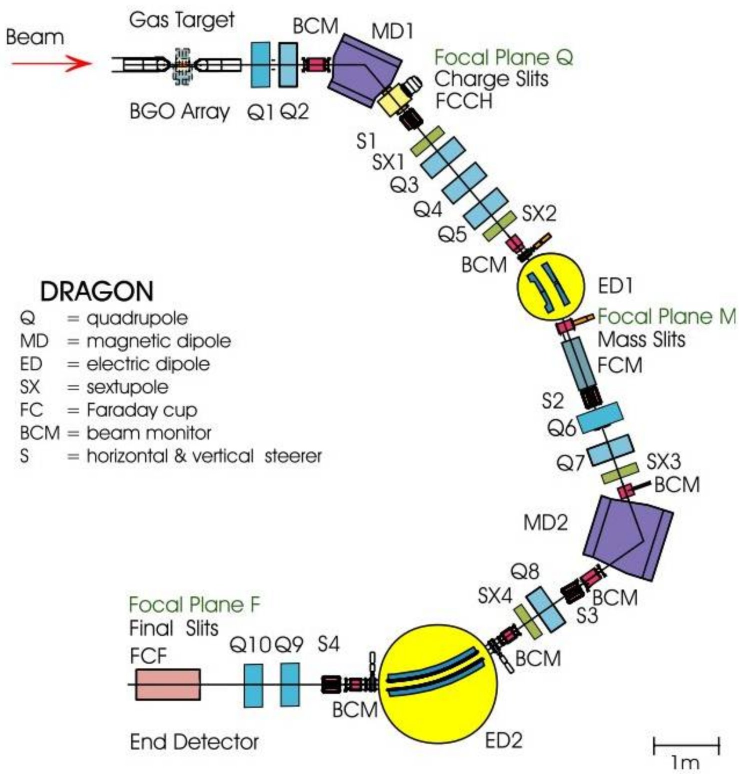

Figure D.11: *Diagrama del separador DRAGON. Los haces de partículas estables o radiactivas inciden en el blanco gaseoso sin ventana, habitualmente hidrógeno o helio a presiones que oscilan de 0.2 a 10 Torr. Los iones procedentes de la reacciónes (p,γ) o (α,γ) salen del blanco con diferentes estados de carga y casi el mismo momento que el haz incidente. Dichos iones son separados de las partículas del haz mediante dos dipolos magnéticos (MD1 y MD2) y dos dipolos eléctricos (ED1 y ED2). Cuadrupolos y Sextupolos magnéticos son utilizados para focalizar las partículas. Un DSSSD se localiza al final del separador donde se detectan los núcleos procedentes de la reacción.*

En este experimento los iones de ^{7}Be generados se separaban de las partículas del haz utilizando los diferentes elementos del separador y eran detectados en el DSSSD situado en el plano focal. La radiación γ procedente de la reacción también era medida en los detectores BGO.

En este caso la sección eficaz de la reacción viene dada por:

$$\sigma_{34}(E) = \frac{N_{^7\mathrm{Be}}}{N^{\mathrm{blanco}}_{^3He} \cdot N^{\mathrm{haz}}_{^4He}} \tag{D.3}$$

donde, el número total de iones de ^{7}Be producidos, $N_{^7\mathrm{Be}}$, se obtiene a partir de los detectados en el DSSSD. El número de partículas en el haz,$N^{\mathrm{haz}}_{^4He}$, se obtiene a partir de las partículas dispersadas y detectadas en dos detectores de silicio situados en la cámara de reacción a 30º y 57º con respecto a la dirección del haz. Por último, debido a las bajas presiones, $\sim$6 Torr, la densidad superficial del blanco gaseoso se obtiene considerando la expresión D.2 donde T_C=0 en este caso.

Este sistema experimental es más complejo que el de activación y requiere de medidas adicionales para obtener la sección eficaz total de nuestra reacción.

Por una parte los iones de ^{7}Be emergen del blanco con diferentes estados de carga (^{7}Be$^{4+,3+,2+,1+}$) mientras que solo uno es seleccionado en el separador. Por tanto es necesario conocer la proporción de iones generados con el estado de carga seleccionado en el separador. Para eso utilizamos un haz de ^{9}Be sobre un blanco gaseoso de ^{3}He y determinamos la fracción de iones que salían con cada estado de carga utilizando las tazas de Faraday situadas a lo largo del separador. Por otra parte se determinó el perfil de densidad del haz puesto que se trata de un blanco sin ventana con bombeo diferencial. Para ello utilizamos la reacción de resonancia ^{3}He(^{12}C,^{14}N)p con un detector BGO. La radiacion γ procedente de la reacción era medida con el detector a diferentes distancias respecto al centro de la cámara y desplazándolo en paralelo a la linea de haz. Mediante la comparativa de la radiación γ detectada en las diferentes posiciones se determina el perfil de densidad del blanco. La Figura D.12 muestra el resultado.

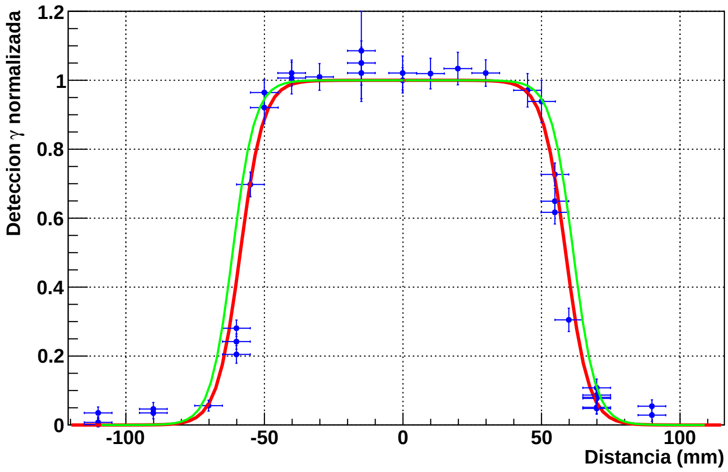

Figure D.12: *Perfil de densidad del haz normalizado. Los puntos azules muestran la producción normalizada determinada experimentalmente, y las curvas rojas y verdes muestran dos de los ajustes realizados a los puntos experimentales utilizando la función de Fermi.*

D.3 Simulaciones del Separador DRAGON

Otro de los parámetros determinantes para el estudio de esta reacción es la aceptancia de DRAGON, es decir, la fracción de los iones creados que alcanzan el final del separador y no chocan con los elementos del mismo. Los cálculos cinemáticos de esta reacción muestran que el máximo ángulo de salida de los núcleos de ^{7}Be puede llegar hasta ∼20 mrad el cual, teniendo en cuenta la dispersión del haz y de los propios iones generados, puede verse incrementado hasta por ∼2 mrad. Estos ángulos están al límite de la aceptancia geométrica del separador y por tanto este efecto debe de ser estudiado en detalle para conocer la fracción de iones que se paran a lo largo del mismo. Para ello el código DRAGON-GEANT3 se ha modificado adaptándolo a nuestro experimento. En este código los diferentes elementos están diseñados acorde al separador real y los parámetros de entrada han sido modificados reproduciendo a las condiciones experimentales durante nuestra medidas. Algunos de los factores considerados son los siguientes:

- El blanco gaseoso utilizado sigue el mismo perfil que el determinado experimentalmente y mostrado en la Figura D.12. Para ello, puesto que GEANT no permite que el material de un volumen definido cambie, se han ajustado los datos experimentales a una función escalón donde cada escalón coincide con cada uno de los volúmenes de GEANT.

- La energía central del haz, $E^{central}$, se ha fijado según la determinada experimentalmente. Para cada evento simulado el programa determina aleatoriamente la energía de una distribución Gausiana centrada en $E^{central}$ y con anchura FWHM=0.1%E, siguiendo las especificaciones del acelerador.

- El tamaño del haz y la divergencia simuladas se han calculado basándose en los parámetros de transmisión del haz a través del blanco medidos durante el experimento.

- La probabilidad de que la reacción tenga lugar es la misma a lo largo de todo el blanco puesto que la energía perdida en el mismo es muy pequeña. Por tanto, la distribución de reacciones producidas sigue el perfil de densidad del gas.

- La distribución angular de la radiación gamma emitida se considera isotrópica [DGK09]

- La probabilidad de que la reacción se produzca poblando el primer estado excitado o el estado fundamental se introdujo basándose en los cálculos en [CD08]

- Los parámetros del separador fueron introducidos basándose en los ajustes reales durante el experimento.

- El posible mal alineamiento de los elementos del separador situados antes del primer cuadrupolo fue medido utilizando un teodolito y los valores fueron introducidos en las simulaciones.

Los valores de transmisión (o aceptancia) obtenidos de las simulaciones de 10^5 partículas incidentes paras las diferentes energía del haz están mostrados en la Tabla 4.6

Año	$\sim E_{^4He}$ (MeV)	^{7}Be creados	^{7}Be detectados	Transmisión
2011	6.5	25931	14873	**57.4±0.6**
	5.2	39694	22907	**57.7±0.5**
	3.5	55383	28392	**51.3±0.3**
2013	4.7	38554	27627	**71.7±0.6**

Table D.2: *Trasmisiones de DRAGON. Para cada una de las energías del haz mostradas en la segunda columna, se han simulado 10^5 iones de ^{4}He incidentes. La tercera columna muestra el número de reacciones producidas o iones ^{7}Be generados mientras que en la cuarta columna se indica el numero de esos que consiguió atravesar todo el separador y depositarse en el DSSSD. La última columna muestra la transmisión con el error estadístico asociado.*

D.3.1 Error sistemático de la transmisión

Las potenciales variaciones de las condiciones experimentales durante las medidas experimentales se han tenido en cuenta como errores sistemáticos asociados a la transmisión. Para cuantificarlos se han realizado simulaciones en las que se han variado los diferentes parámetros de entrada acorde a los posibles cambios que se hubiesen podido ocasionar durante las medidas. La Tabla D.4 muestra en la primera columna los diferentes parámetros testeados y en la última columna el error sistemático asociado la transmisión. Por último la Tabla D.3 muestra los valores finales de la trasmisión así como los errores estadísticos y sistemáticos asociados. El valor final del error sistemático se ha obtenido mediante la suma cuadrática de cada una de las contribuciones mostradas en la Tabla D.4.

Año	$E_{^4He}$ (keV)	Transmisión (%)	Error Estadístico	Error Sistemático
2011	6553.88	57.4	±0.6	$^{+2.3}_{-6.4}$
	5165.97	57.7	±0.5	$^{+5.0}_{-5.6}$
	3521.61	51.3	±0.3	$^{+3.0}_{-3.8}$
2013	4716.45	71.7	±0.6	$^{+3.0}_{-6.7}$

Table D.3: *Transmisiones de DRAGON y errores estadísticos y sistemáticos asociados.*

D.4 Análisis y Resultados

El objetivo de nuestros experimentos es determinar el factor astrofísico de la reacción ^{3}He(α,γ)^{7}Be expresado por:

$$S_{34}(E) = \sigma_{34}(E) \cdot E \cdot e^{2\pi\eta E} \tag{D.4}$$

donde E es la energía en el sisgema centro de masas. Por lo tanto, para cada uno de los dos experimentos se debe determinar, la energía en el sistema centro de masas y la sección eficaz de la reacción. Para la sección eficaz, el número de iones incidentes, la densidad superficial del blanco y el número de iones ^{7}Be producidos deben ser estimados. A continuación se detalla como son extraídos cada uno de los parámetros en los dos experimentos.

D.4.1 Método de activación

La energía de la reacción en el sistema centro de masas viene dada por

$$E_{CM} = \frac{m_{^4He}}{m_{^4He} + m_{^3He}} \cdot \left(E^{haz} - \Delta E_{Ni} - \frac{\Delta E_{^4He}}{2} \right) \tag{D.5}$$

donde las "m" son las masas de los correspondientes iones, E^{haz} es la energía del haz calculada a partir de la tensión del terminal del acelerador tandem y ΔE_{Ni} y $\Delta E_{^4He}$ son las energías perdidas por el haz al atravesar la lámina de níquel y el gas, respectivamente. Estas se han determinado utilizando el código SRIM [SRI].

El número de partículas incidentes se ha calculado a partir de las partículas dispersadas con la lámina de níquel y detectadas en el detector de silicio, y mediante la integración de carga. La Figura D.13 muestra el número de partículas calculadas utilizando los dos métodos para las diferentes energías incidentes. Como puede observarse hay un perfecto acuerdo entre las partículas determinadas utilizando los dos métodos.

Parámetro	Año	$E_{^4\mathrm{He}}$ (MeV)	Error Sistemático (%)
Longitud Efectiva del Blanco	2011	∼6.5	$^{+0.3}_{-2.0}$
		∼5.2	$^{+0.8}_{-0.9}$
		∼3.5	$^{+0.9}_{-0.5}$
	2013	∼4.7	$^{+0.5}_{-0.9}$
Perfil del Blanco	2011	∼6.5	$^{-1.8}_{-1.3}$
		∼5.2	$^{-0.8}_{+0.0}$
		∼3.5	$^{-1.0}_{+0.0}$
	2013	∼4.7	$^{-0.6}_{-0.1}$
Desplazamiento del Haz (eje-x)	2011	∼6.5	$^{+0.2}_{-2.8}$
		∼5.2	$^{+1.2}_{-3.3}$
		∼3.5	$^{+0.7}_{-2.0}$
	2013	∼4.7	$^{+2.2}_{-5.0}$
Desplazamiento del Haz eje-y	2011	∼6.5	$^{-2.2}_{-0.9}$
		∼5.2	$^{-2.5}_{-1.0}$
		∼3.5	$^{-2.0}_{-0.6}$
	2013	∼4.7	$^{-3.5}_{-1.0}$
Transmisión del Haz	2011	∼6.5	$^{-0.2}_{-0.8}$
		∼5.2	$^{+2.6}_{-0.8}$
		∼3.5	$^{+0.7}_{-0.7}$
	2013	∼4.7	$^{+0.2}_{-1.3}$
Divergencia del Haz (eje-x)	2011	∼6.5	$^{-1.1}_{-1.0}$
		∼5.2	$^{+0.0}_{+0.1}$
		∼3.5	$^{-0.6}_{-0.1}$
	2013	∼4.7	$^{-0.3}_{-0.3}$
Divergencia del Haz (eje-y)	2011	∼6.5	$^{-0.8}_{-0.8}$
		∼5.2	$^{+0.0}_{+0.3}$
		∼3.5	$^{-0.2}_{+0.4}$
	2013	∼4.7	$^{-1.2}_{+0.1}$
Energía del Haz	2011	∼6.5	$^{+1.3}_{-3.1}$
		∼5.2	$^{+1.8}_{-1.6}$
		∼3.5	$^{+1.8}_{-1.7}$
	2013	∼4.7	$^{+0.4}_{-0.9}$
S_1/S_0	2011	∼6.5	$^{+1.0}_{-1.7}$
		∼5.2	$^{+1.9}_{-0.8}$
		∼3.5	$^{+1.7}_{-0.3}$
	2013	∼4.7	$^{+1.8}_{-1.4}$
Distribución angular γ	2011	∼6.5	$^{+1.6}_{-1.6}$
		∼5.2	$^{+2.9}_{-2.9}$
		∼3.5	$^{+1.1}_{-1.1}$
	2013	∼4.7	$^{+0.4}_{-0.4}$

Table D.4: *Parámetros analizados para evaluar la transmisión de DRAGON y el error sistematico asociado.*

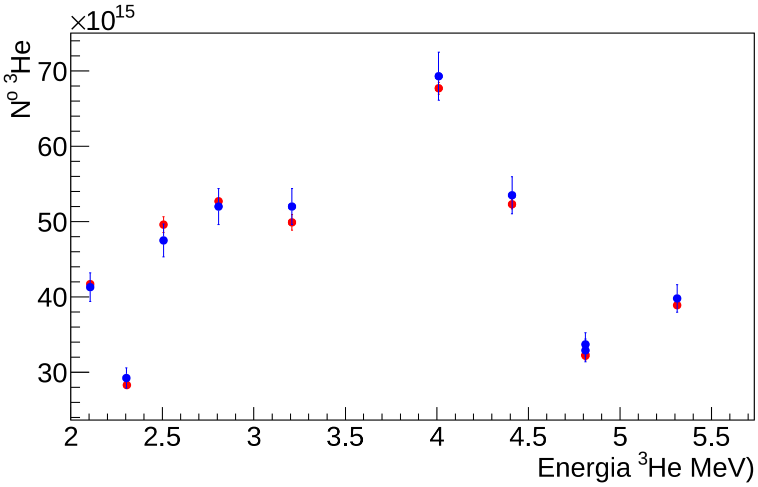

Figure D.13: *Número total de partículas del haz incidente para las diferentes energías del haz medidas en el CMAM. En rojo se muestra el número de partículas estimadas mediante la integración de carga y en azul mediante la dispersión elástica del haz con la lámina de Ni.*

Para determinar la densidad superficial del blanco la presión se controló durante todo el experimento y los valores se anotaron frecuentemente. Para cada energía, la presión se calcula considerando la media entre los valores tomados y el error asociado se determinó como la desviación típica de los valores más 0.1 Torr de error instrumental. Un ejemplo de la estabilidad de la presión y por tanto de la densidad superficial del blanco gaseoso para la energía del haz de 4010 keV se muestra en la Figura D.14 .

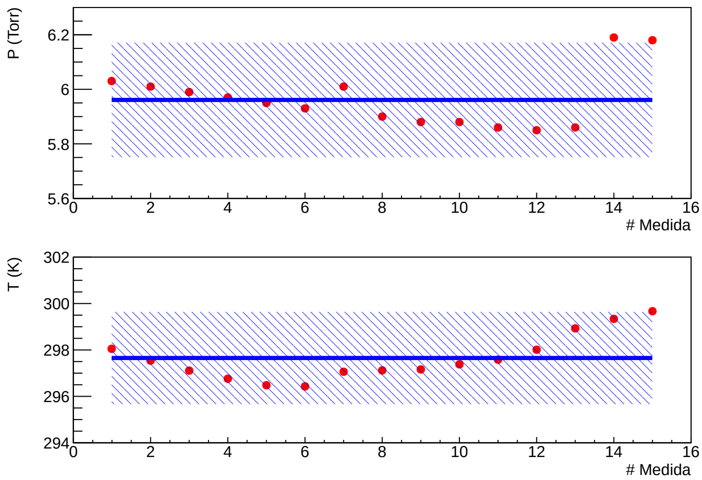

Figure D.14: *Estabilidad de la presión para el método de activación siendo la energía del haz 4010 keV. Los puntos rojos muestran las medidas experimentales de la presión del ^{4}He gaseoso, la línea azul muestra el valor medio considerado y la zona rayada muestra el error asociado al valor medio.*

El número de iones de ^{7}Be producidos se recolectó en las placas de cobre. La radiación γ retardada procedente de la desexcitación del primer estado excitado del ^{7}Li fue medida utilizando la estación de bajo fondo. La Figura D.15 muestra un ejemplo de uno de los espectros adquiridos. En el panel superior se muestra un espectro completo para la energía de haz de 4010 keV y en el panel inferior se muestra la región en torno a 478 keV donde se pueden identificar los picos de interés claramente separados del pico a 511 keV. El procedimiento seguido para la obtención del número de cuentas en el pico de interés es el detallado en [NEHY07]. A partir del número de cuentas en el pico, el numero total de iones producido se calcula teniendo en cuenta la ley de desintegración radiactiva así como los tiempos transcurridos durante la implantación, entre la implantación y el comienzo de medida del espectro y el tiempo de obtención del espectro.

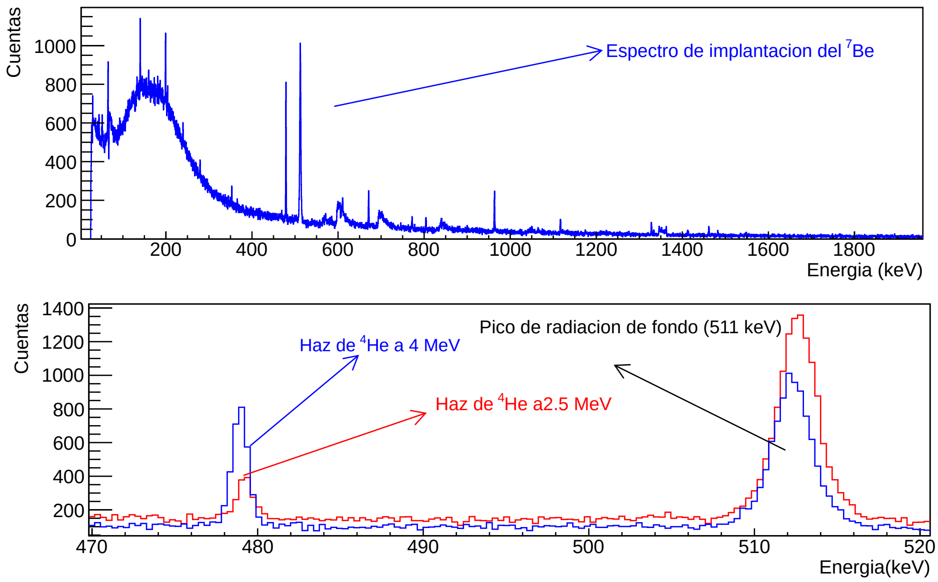

Figure D.15: *Espectros de radiación γ de los núcleos ^{7}Be implantados en las placas de cobre. En el panel superior se muestra el espectro total de ^{7}Be cuando la energía del haz era 4 MeV. In la parte inferior la región de interés para las energías del haz de 4 MeV (azul) y 2.5 MeV (rojo).*

La Tabla D.5 muestra los valores de los diferentes parámetros obtenidos con el método de activación. Para las diferentes energías de haz mostradas en la primera columna, la segunda columna muestra la energía en el sistema centro de masas correspondiente. La tercera, cuarta y quinta columna muestran el número de iones en el haz, la densidad superficial de blanco gaseoso y el número de núcleos de ^{7}Be generados en cada caso, respectivamente. Las columnas sexta y séptima muestran el valor de la sección eficaz y el factor astrofísico para las diferentes energías. Las incertidumbres asociadas a cada valor están mostradas entre paréntesis. Los errores obtenidos para la sección eficaz han sido determinados mediante propagación de errores estándar. Para, $N^{haz}_{^3He}$ y $N^{blanco}_{^4He}$ los errores se refieren a la contribución sistemática, mienta que para $N_{^7Be}$, $\sigma_{34}(E)$ y $S_{34}(E)$ las contribuciones están separadas en estadísticas (primeras) y sistemáticas (segundas).

Los factores $S_{34}(E)$ se representan en la Figura D.18 junto con los resultados obtenidos en el experimento de detección directa y otros valores en la literatura.

$E_{^3He}$ (keV)	E_{CM} (keV)	$N^{haz}_{^3He}$ ($\cdot 10^{16}$)	$N^{blanco}_{^4He}$ ($\cdot 10^{19}/cm^2$)	$N_{^7Be}$ ($\cdot 10^6$)	σ_{34}(E) (μb)	S_{34}(E) (keV$\cdot$ b)
2306.28±2.37	915.78±12.21	2.83(5)	2.34(2)	1.31(25)(3)	1.98(38)(6)	0.411(79)(15)
3208.05±2.99	1498.91±12.56	4.99(10)	2.65(2)	4.05(30)(9)	3.06(23)(10)	0.318(24)(11)
4410.42±3.82	2267.71±12.47	5.23(6)	1.67(5)	4.74(46)(11)	5.43(53)(22)	0.386(37)(16)
4811.20±4.09	2511.12±12.62	3.22(3)	1.68(4)	3.19(30)(7)	5.88(56)(21)	0.391(37)(14)
5312.19± 4.44	2804.10±12.82	3.89(4)	2.28(2)	6.05(26)(14)	6.82(29)(19)	0.424(18)(12)
2105.89±2.23	777.17±12.70	4.17(2)	2.40(2)	1.49(22)(4)	1.49(22)(4)	0.418(61)(18)
2506.67±2.51	1054.15±12.31	4.96(10)	2.23(2)	2.26(16)(5)	2.05(14)(6)	0.339(23)(12)
2807.26±2.71	1249.64±12.41	5.27(4)	2.28(2)	3.61(29)(11)	3.00(24)(9)	0.390(31)(13)
4009.63±3.54	2006.95±12.31	6.77(8)	2.78(2)	7.87(21)(18)	4.70(12)(13)	0.367(10)(10)
4811.20±4.09	2510.00±12.62	3.23(7)	1.45(2)	3.88(23)(11)	6.85(40)(26)	0.455(27)(17)

Table D.5: *Resultados para el experimento de activación. La primera columna muestra las energías del haz. La segunda columna muestra la energía correspondiente en el sistema centro de masas teniendo en cuenta las energías perdidas en la lámina de Ni y el blanco gaseoso. La columnas tercera cuarta y quinta muestran el número de partículas en el haz, en el blanco gaseoso y de núcleos de ^{7}Be producidos respectivamente. Las columnas sexta y séptima muestran la sección eficaz y el factor astrofísico de la reacción ^{3}He(α,γ)^{7}Be respectivamente. Las incertidumbres asociadas a cada valor se muestran entre paréntesis. En caso de que solo exista una incertidumbre se refiere a la contribución sistemática y en caso de que haya dos la primera es la estadística y la segunda es la sistemática.*

D.4.2 Método de detección directa

En el caso del método de detección directa la energía de la reacción en el sistema centro de masas viene dada por :

$$E_{CM} = \frac{m_{^3He}}{m_{^3He} + m_{^4He}} \cdot \left(E^{haz} - \frac{\Delta E_{^3He}}{2} \right) \tag{D.6}$$

El número de partículas en el haz se determina a partir de las partículas dispersadas y detectadas en los detectores de silicio situados as a 30º y 57º en la cámara de reacción y las tazas de Faraday situadas a lo largo del separador. Se han elegido para cada energía las medidas en las que la corriente es estable, y se define para ellas el factor de normalización como:

$$R^{run} = \frac{FC1}{1.602 \cdot 10^{-19} \cdot q} \frac{\text{Time} \cdot \text{Livetime}}{\text{Si-30}} \cdot P \cdot T \tag{D.7}$$

dond FC1 es la lectura de la taza de Faraday situada tras el blanco gaseoso, q=2 es la carga del haz tras atravesar el blanco, Time es el tiempo de cada medida, Livetime es la corrección debida al tiempo muerto del sistema de adquisición y Si-30 es el número de partículas dispersadas en el detector de silicio a 30º. P y T son la presión y temperatura del gas respectivamente. A continuación se promedian los factores R^{run} y se obtiene el factor promedio R^F para cada energía. El número de partículas totales para cada energía viene dado por la suma para medida dada por:

$$N^{oBeam}_{^4He} = \frac{R^F \cdot \text{Si-30}}{\text{Livetime} \cdot P \cdot T} \tag{D.8}$$

La densidad superficial de partículas en el blanco gaseoso se determina mediante la expresión D.2 para lo que se monitorizó la presión y temperatura durante todo el experimento. La Figura D.16 muestra un ejemplo de la estabilidad de presión y temperatura para el caso de la energía del haz ∼5.2 MeV.

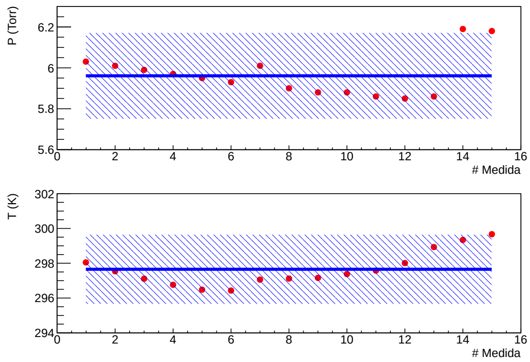

Figure D.16: *Presión (panel superior) y temperatura (panel inferior) del blanco gaseoso para una medida con energía del haz de ∼5.2 MeV Los puntos rojos muestras las diferentes lecturas cada cinco minutos. La línea azul muestra la media de todas las medida y la zona sombreada el error asociado.*

El número total de núcleos de ^{7}Be producidos ($Y_{^7\mathrm{Be}}$) viene dado por la expresión:

$$Y_{^7\mathrm{Be}} = \frac{Y_{\mathrm{DSSSD}}}{\mathrm{t}_{\ell} \cdot q_{\mathrm{f}} \cdot \epsilon_{\mathrm{DRAGON}} \cdot \epsilon_{\mathrm{DSSSD}}} \tag{D.9}$$

donde Y_{DSSSD} es el número de iones detectados en el DSSSD, t_{ℓ} es el tiempo real en que el sistema de adquisición está procesando datos, q_{f} es la fracción de núcleos que abandonan el blanco con el estado de carga seleccionada y determinado mediante las medidas de distribución de estado de carga, $\epsilon_{\mathrm{DRAGON}}$ es la transmisión o aceptancia determinada con las simulaciones (ver Tabla D.3) y $\epsilon_{\mathrm{DSSSD}}$ es la eficiencia de detección del DSSSD. La Figura D.17 muestra un ejemplo de los histogramas obtenidos con el DSSSD para las energías del haz de 6.5 MeV (panel superior) y 5.2 MeV (panel inferior) y la Tabla D.6 muestra los valores obtenidos para los diferentes parámetros necesarios para obtener el valor de $Y_{^7\mathrm{Be}}$.

$\mathrm{E}_{^4\mathrm{He}}$ (MeV)	t_{ℓ} (%)	$\epsilon_{\mathrm{DSSSD}}$ (%)	q_{f} (%)	Y_{DSSSD}
∼6.5	84.12	96.15±0.10	(3+)59.05±1.87	33465
∼5.2	92.34	96.15±0.10	(3+)61.87±2.55	141707
∼4.7	94.18	96.15±0.10	(2+)29.31±3.81	52683
∼3.5	98.64	96.15±0.10	(2+)52.30±3.33	44135

Table D.6: *t_{ℓ},ϵ_{DSSSD}, q_f y Y_{DSSSD} para las diferentes energías*

Los valores de la energía en el sistema centro de masas, $\mathrm{N}^{\mathrm{haz}}_{^4\mathrm{He}}$, $\mathrm{N}^{\mathrm{blanco}}_{^3\mathrm{He}}$ y $\mathrm{Y}_{^7\mathrm{Be}}$ así como la secciones eficaces y factores astrofísicos de la reacción ^{3}He(α,γ)^{7}Be se detallan en la Tabla D.7. Los factores astrofísicos S_{34}(E) para las diferentes energías se muestran en la Figura D.18 junto con aquellos obtenidos en el experimento de activación y algunos de los valores en la literatura.

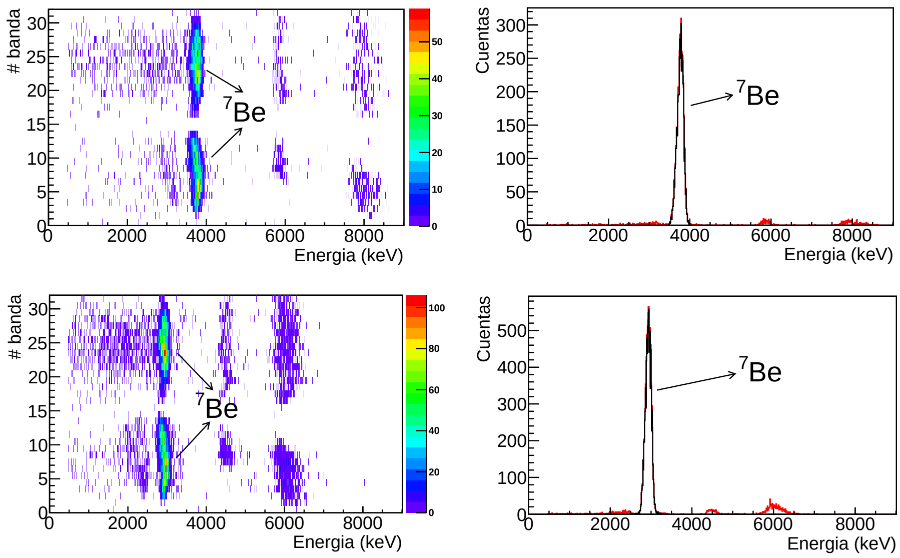

Figure D.17: *Para las dos máximas energías, ∼6.5 y ∼5.2 MeV, a la izquierda se muestran los espectros 2D de los núcleos de ^{7}Be en las diferentes bandas del DSSSD. En la parte de la derecha están mostradas en rojo las proyecciones de las bandas 1-15. En negro se muestras los sucesos en coincidencia entre la parte delantera y trasera en el rango de energía seleccionado.*

Año	$\sim E_{^4He}$ (MeV)	E_{CM} (keV)	$N^{haz}_{^4He}$ ($\cdot 10^{16}$)	$N^{blanco}_{^3He}$ ($\frac{\cdot 10^{18}}{cm^2}$)	$Y_{^7Be}$ ($\cdot 10^5$)	$\sigma_{34}(E)$ μb	$S_{34}(E)$ (keV$\cdot$ b)
	6.5	2813.6±1.8	0.84(1)	2.29(11)	1.22(1)($^{+6}_{-14}$)	6.32(8)($^{+44}_{-80}$)	0.393(5)($^{+27}_{-49}$)
2011	5.2	2216.6±1.7	3.25(2)	2.38(13)	4.47(4)($^{+43}_{-47}$)	5.78(5)($^{+63}_{-69}$)	0.419(4)($^{+46}_{-50}$)
	3.5	1508.9±1.3	2.09(1)	2.38(12)	1.74(1)($^{+15}_{-17}$)	3.48(3)($^{+35}_{-38}$)	0.359(3)($^{+36}_{-40}$)
2013	4.7	2023.7±1.4	3.03(3)	1.98(11)	2.77(3)($^{+38}_{-44}$)	4.62(4)($^{+68}_{-79}$)	0.359(3)($^{+53}_{-61}$)
(Impl)	4.7	2023.7±1.4	26.5(1)	1.94(10)	28.8(20)(29)	6.22(44)(72)	0.484(34)(56)

Table D.7: *Resultados para el experimento de detección directa. La segunda columna muestra las diferentes energías del haz utilizada. En la tercera columna se muestras las energías en el sistema centro de masas correspondientes. La cuarta, quinta y sexta columnas muestran el número de partículas en el haz, el blanco y núcleos de ^{7}Be generados. Las columnas séptima y octava muestran los valores de la sección eficaz y el factor astrofísico de la reacción $^3He(\alpha,\gamma)^7Be$. Las incertidumbres asociadas a cada valor se muestran entre paréntesis. En caso de que solo exista una incertidumbre se refiere a la contribución sistemática y en caso de que haya dos la primera es la estadística y la segunda es la sistemática. La última línea muestra los resultados obtenidos para una medida de activación realizada en TRIUMF utilizando la misma técnica que en el experimento de Madrid.*

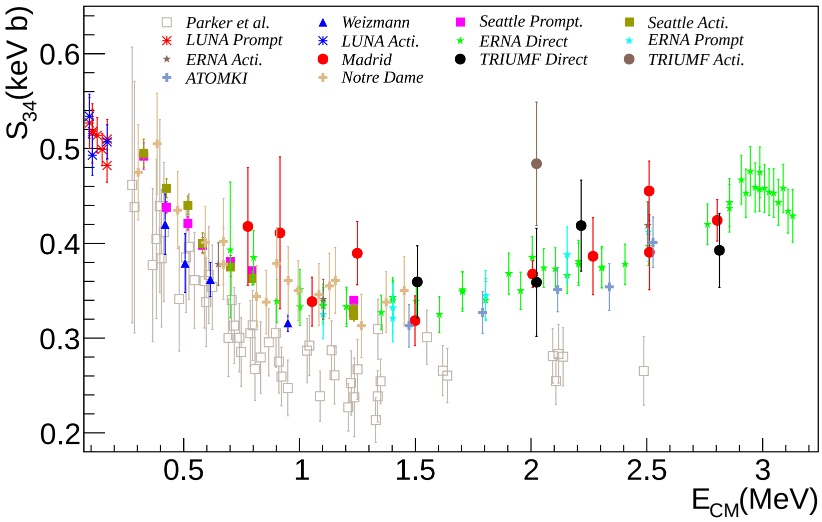

Figure D.18: *Valores astrofísicos de la reacción $^3He(\alpha,\gamma)^7Be$ obtenidos utilizando el método de detección directa(puntos negros) y método de activación (puntos rojos). Como comparativa se muestran los datos de ERNA [DGK09], Parker [PK63], LUNA [GCC07, BCC06], Weizmann [NHNEH04], Seattle [BBS07] y ATOMKI [BGH13].*

D.5 Discusión

Los valores obtenidos para el factor $S_{34}(E)$ se han comparado con diferentes valores experimentales mediante el método de χ^2. La Tabla D.8 muestra los valores obtenidos. Como puede comprobarse nuestros resultados resuelven completamente la discrepancia entre los valores de Parker y Kavanagh y ERNA, pudiendo descartar los primeros. Los datos de ATOMKI, obtenidos al mismo tiempo que los presentados en este trabajo concuerdan también con nuestro resultados.

	Parker and Kavanagh	ERNA	ATOMKI
Madrid	7.40 ($\nu = 10$)	0.75 ($\nu = 10$)	1.14 ($\nu = 4$)
TRIUMF direct	5.98 ($\nu = 4$)	0.54 ($\nu = 4$)	1.40 ($\nu = 3$)

Table D.8: *Valores de χ^2_ν calculados utilizando la expresión 6.2. Nuestros datos de Madrid y TRIUMF conjuntamente se comparan con los datos de Parker and Kavanagh [PK63], of ERNA [DGK09] y ATOMKI [BGH13]. Los valores ν values dan el número de datos comparados en cada caso.*

Los resultados obtenidos también se han comparado con los diferentes modelos teóricos. La Figura D.19 muestran los dos cálculos teóricos que mejor reproducen todos los valores obtenidos a partir de las medidas en Weizmann en 2004 conjuntamente con nuestros resultados. Estos modelos son los cálculos ab-initio realizados por Neff [Nef11] y los cálculos de matriz-R realizados por Kontos et al. [KUD13]. Los cálculos teóricos se encuentran normalizados con un factor 1.045 para Kontos y 0.998 para Neff debido a que con esa normalización los modelos reproducen mejor nuestros valores.

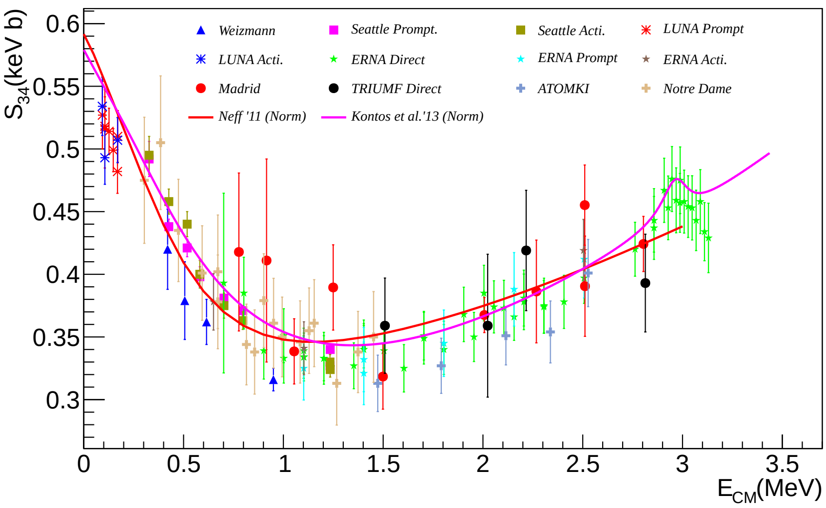

Figure D.19: *Los valores experimentales del factor $S_{34}(E)$ se muestran conjuntamente con los cálculos teóricos de Neff [Nef11] y Kontos et al. [KUD13] normalizados para reproducir nuestros resultados.*

D.5.1 Impacto en astrofísica

Los valores de $S_{34}(0)$ estimados a través de los modelos de Neff y Kontos tienen influencia directa en las predicciones del SBBN y el SSM.

Con el objetivo de comparar el impacto en el SSM, utilizamos como referencia el valor de $S_{34}(0)$=0.56 keV b sugerido en la revisión *Solar Fusion Cross Section II* [AGR11]. Nuestro valor de 0.577 keV b considerando la renormalización del ajuste de matriz-R por Kontos et al. es ∼3% mayor, lo cual se traslada en un aumento de 2.61% y 2.45% en el flujo de neutrinos procedente de la desintegración del ^{7}Be ($\phi_\nu(^7\text{Be})$) y ^{8}B ($\phi_\nu(^8\text{B})$) respectivamente. El análisis de matriz-R de Kontos et al. sin incluir normalización que considera tres de nuestros valores obtenidos en el experimento de activación en Madrid, estima $S_{34}(0)$=0.554 keV b y por tanto sin desviaciones del flujo de neutrinos respecto al valor en [AGR11].

Los cambios son superiores si consideramos el valor normalizado de los cálculos de Neff [Nef11] de $S_{34}(E)$=0.592 keV b. Este valor es muy cercano al obtenido sin considerar factor de normalización de 0.593 keV b, y por tanto podemos considerar este último como el mejor reproduciendo nuestros resultados. Además, se debe mencionar que estos son cálculos ab-initio y por tanto no consideran ninguno de los valores experimentales. El incremento de 5.89% en $S_{34}(0)$ se traduce en aumento de 5.05% y 4.75% en $\phi_\nu(^7\text{Be})$ y $\phi_\nu(^8\text{B})$ respectivamente.

La estimación cuantitativa de la abundancia del ^{7}Li primordial basado en nuestros resultados está fuera del alcance de este trabajo, sin embargo un análisis cualitativo puede ser realizado. De acuerdo a los cálculos en [DGK09], la abundancia del ^{7}Li primordial es ^{7}Li/H=(5.4±0.3) 10^{-10} cuando $S_{34}(0)$=0.57 keV b. En nuestro caso $S_{34}(0)$ es un 3.86% superior, por tanto la abundancia del ^{7}Li primordial se ve incrementada, empeorando por tanto el problema.

D.5.2 Conclusiones

Algunas de las principales conclusiones obtenidas en esta tesis son:

- Dos montajes experimentales han sido completamente caracterizados para estudiar la reacción ^{3}He$(\alpha,\gamma)^7$Be.

- Diez nuevos valores del factor S_{34}(E) con bajo error estadístico han sido obtenidos en el rango E_{CM}=1-3 MeV utilizando el *método de activación*
- El perfil de densidad del gas del separador de DRAGON, así como la distribución de estado de carga de los iones y la supresión del haz para esta reacción han sido medidas experimentalmente
- El código de simulaciones GEANT3-DRAGON se ha modificado y adaptado para reproducir los parámetros experimentales del durante nuestras medidas.
- Cuatro nuevos valores del factor S_{34}(E) con bajo error estadístico se han obtenido mediante el *método de detección directa*
- La comparación entre nuestros datos, obtenidos diferentes técnicas, muestra buen acuerdo entre ellos.
- Los resultados obtenidos en esta tesis están en acuerdo con los de la colaboración ERNA [DGK09] y discrepan de los de Parker y Kavanagh [PK63]
- Nuestros datos muestran acuerdo con los cálculos ab-inito de Neff [Nef11]
- Un valor de S_{34}(0)=0.593 keV b es recomendado in este trabajo basado en nuestros resultados y los cálculos ab-initio

"We build too many walls and not enough bridges"

Isacc Newton

APPENDIX E

ENGLISH SUMMARY

Abstract: *This thesis focuses on the study of the cross section of the astrophysical relevant* $^3He(\alpha,\gamma)^7Be$ *reaction. In this appendix, a summary of the work covering the motivation behind these measurments, the experimental techniques employed, analysis procedures used and the outcomes are presented.*

E.1 Motivation

The cross section of the nuclear reaction ^{3}He(α,γ)^{7}Be plays a determining role in i) the estimations of the primordial ^{7}Li abundance by the Standard Big Bang Nucleosynthesis (SBBN) and ii) the predictions of the solar neutrino fluxes from the ^{7}Be and ^{8}B decay by the Standard Solar Model (SSM). Figure E.1 shows the calculated abundances of the primordial light elements. As it can be observed, there is a high discrepancy between primordial ^{7}Li abundance inferred from direct observations and those calculated using the SBBN. The primordial ^{7}Li is produced by the ^{3}He(α, γ)^{7}Be and subsequent ^{7}Be(p,γ)^{7}Li reactions within the SBBN modelling, therefore a precise determination of the reaction rate is required to provide accurate input.

The solar neutrino calculations using the SSM are shown in Figure E.2. A comparison with the direct neutrino detections reveals that higher accuracies in the calculations, e.g. of neutrinos fluxes from the ^{7}Be and ^{8}B decay, are required. These neutrinos are originated from the pp-chain II and pp-chain III, which are opened by the ^{3}He(α,γ)^{7}Be reaction. Therefore, a high precision data of this reaction rate is required in these estimations.

Due to the experimental limitations, determination of the rate of this reaction at the astrophysica relevantl energies (Gamow peak in the Sun $\sim$22 keV) is impossible. Instead, theoretical models are used to extrapolate the astrophysical factor, $S_{34}(E)=E\cdot\sigma_{34}(E)\cdot e^{2\pi\eta(E)}$ where E is the energy in the centre of mass system, down to zero energy.

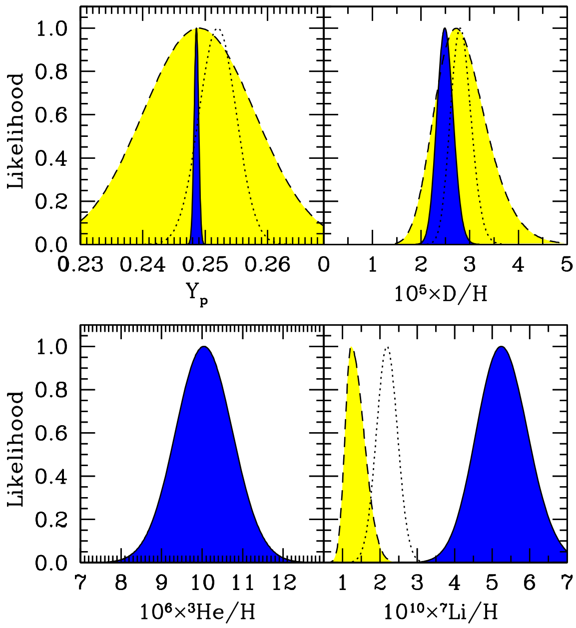

Figure E.1: *Calculated and observed likelihoods for ^{4}He (Y_p), D/H, ^{3}He/H and ^{7}Li/H. The dark blue areas show the likelihood calculated with the SBBN results using the η parameter from the Wilkinson Microwave Anisotropy Probe (WMPA) observations. The observational likelihoods are shown in the yellow shaded region and dotted likelihood functions. For the ^{7}Li/H, the shaded yellow area shows the value inferred from the observation of halo stars. The dotted function shows the determination from a globular cluster. Figure has been taken from [CFO08]*

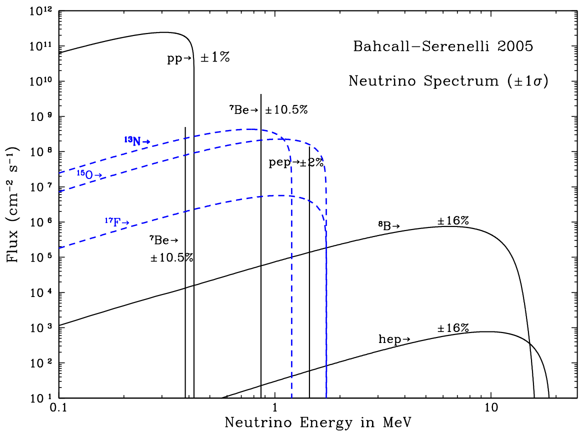

Figure E.2: *The solar neutrino spectra calculated using the Standard Solar Model [BP95].*

Figure E.3 shows a compilation of data (a) and representative calculations (b) of the S-factors. As can be observed there is high discrepancy among the data sets and calculations. This discrepancy is extremely large in the range of E_{CM}=1-3 MeV, between the experimental data from the ERNA collaboration [DGK09] and the Parker and Tombrello [PK63], and among the theoretical models.

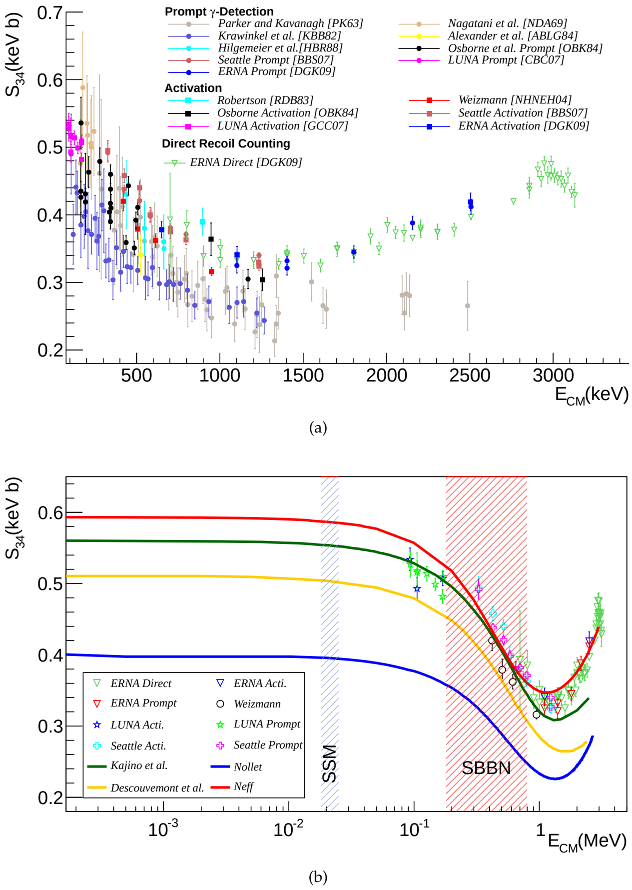

Figure E.3: *(a) The available data of the astrophysical S-factors for the $^3He(\alpha,\gamma)^7Be$ reaction (S_{34}). Data from measurements performed using the Prompt γ-Detection, Activation and Direct Recoil Counting methods are shown in circles, squares and triangles, respectively. (b) A comparison between the theoretical models from Kajino et al. [KTA87], Nollet [Nol01], Descouvemont et al. [DAA04] and Neff [Nef11] plotted together with the modern data from ERNA [DGK09], Weizmann [NHNEH04], LUNA [BCC06, CBC07, GCC07] and Seattle [BBS07]. The energy regions of the interest for SSM and SBBN models are marked by blue and red shaded areas.*

Aiming to fix the energy dependence of the S-factor and constrain the theoretical models required to extrapolate to astrophysical energies, we have measured the cross section of the reaction in the window E_{CM}=1-3MeV using two complementary techniques.

E.2 Experimental Techniques and Results

The decay scheme of the ^{3}He+^{4}He direct capture state is shown in Figure 1.12. This radiative capture reaction creates a ^{7}Be nucleus and has a Q-value of 1.587(1) MeV. Prompt γ-rays with two different energies are emitted in the process corresponding to the population of the ground state (γ_0) or the first excited state (γ_1) in the ^{7}Be. The latter de-excites via emission of a 429 keV γ-ray to the ground state (γ_2). The created ^{7}Be is an unstable nucleus. It decays via electron capture process to ^{7}Li with a half life of 53.24(4) d. The Q value of this process is 862 keV, and with a well known branching ratio of 10.44(4)% the decay populates the first excited state in ^{7}Li at 478 keV from which a γ-ray emanates (γ_3).

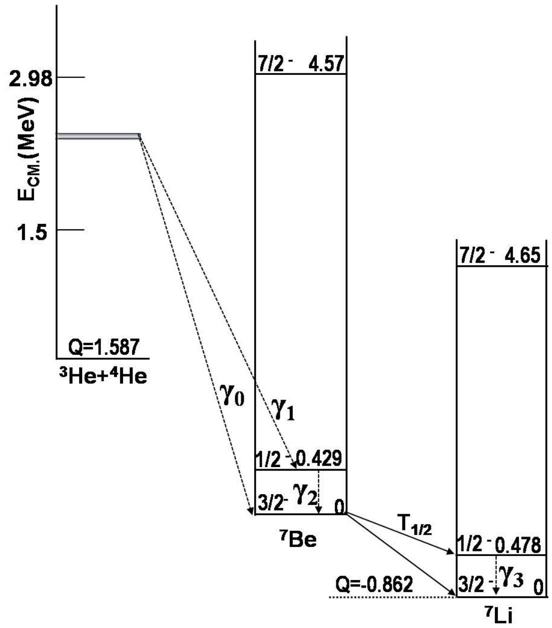

Figure E.4: *Decay scheme of ^{3}He+^{4}He direct capture state with the emission of prompt γ-rays. The ^{7}Be decay to ^{7}Li is also shown. The energies are displayed in MeV.*

Three different experimental techniques are therefore available to determine the cross section, namely, via the detection of the (i) prompt γ_0/γ_1-rays of the reaction ("*Prompt Method*"), (ii) the ^{7}Be recoils ("*Direct Recoil Counting Method*") and (iii) the subsequent γ_3-rays from the de-excitations of the first excited state in ^{7}Li to its ground state ("*Activation Method*").

We have performed measurements using the *Activation Method* at the Centro de Microanálisis de Materiales de Madrid (CMAM) and the *Direct Recoil Counting Method* utilising the DRAGON separator at TRIUMF laboratory in Vancouver.

E.2.1 Measurements using the activation method

The *activation method* setup is shown in Figure E.5. A ^{3}He beam impinged onto a ^{4}He gas target kept inside a reaction chamber using a Ni foil window. The ^{7}Be recoils were deposited in a Cu catcher placed at the end of the chamber. The subsequent delayed γ-activity was measured using a specialised low-background HPGe detector station at the SOREQ centre in Israel (see Figure E.6). The number of incoming beam particles was determined by integrating the electric charge collected by the chamber, which

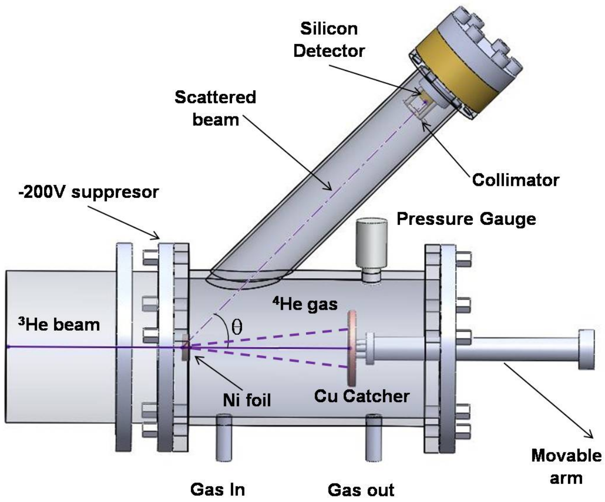

Figure E.5: *A Schematic view of various components that are part of the reaction chamber. A ^{3}He beam impinged onto a ^{4}He gas target that is "vacuum isolated" from the beam line using a Ni foil. A silicon detector was placed at $\approx 45°$ for monitoring the scattered beam from a Ni foil. A Cu catcher placed on a movable arm at the end of the chamber was used to collect the ^{7}Be recoils. An electron suppressor with -200 V was placed before the Ni foil. See text for more details.*

was acting as a Faraday cup. This was cross-checked by detecting the beam, which was elastically scattered from a Ni foil and entering into a silicon detector placed at ≈45°. Due to the low pressures in the chamber (∼60 Torr), the target areal density was obtained by considering an ideal gas expression with a correction in the temperature due to the beam heating

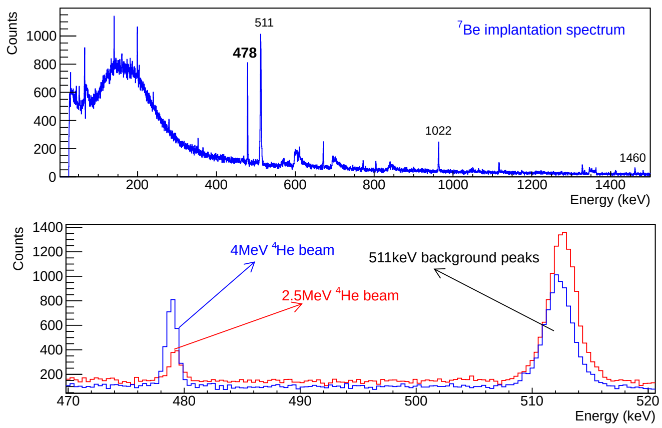

Figure E.6: *Spectra for the γ-rays from the catchers having implanted ^{7}Be. In the upper panel a total spectrum for the ^{7}Be catcher at ∼4 MeV beam energy is shown. Some of the peak energies are labelled. In the lower panel a zoom view for the region of interest is shown for beam energies of 4 MeV (blue) and ∼2.5 MeV (red).*

The values of various parameters corresponding to our measurements using *activation method* as well as the results for the cross section and astrophysical $S_{34}(E)$ factors are shown in Table E.1.

$E_{^3\mathrm{He}}$ (keV)	E_{CM} (keV)	$N^{\mathrm{beam}}_{^3\mathrm{He}}$ $(\cdot 10^{16})$	$N^{\mathrm{target}}_{^4\mathrm{He}}$ $(\cdot 10^{19}/\mathrm{cm}^2)$	$N^{\mathrm{recoils}}_{^7\mathrm{Be}}$ $(\cdot 10^{6})$	σ_{34}(E) μb	S_{34}(E) (keV· b)
2306.28±2.37	915.78±12.21	2.83(5)	2.34(2)	1.31(25)(3)	1.98(38)(6)	0.411(79)(15)
3208.05±2.99	1498.91±12.56	4.99(10)	2.65(2)	4.05(30)(9)	3.06(23)(10)	0.318(24)(11)
4410.42±3.82	2267.71±12.47	5.23(6)	1.67(5)	4.74(46)(11)	5.43(53)(22)	0.386(37)(16)
4811.20±4.09	2511.12±12.62	3.22(3)	1.68(4)	3.19(30)(7)	5.88(56)(21)	0.391(37)(14)
5312.19± 4.44	2804.10±12.82	3.89(4)	2.28(2)	6.05(26)(14)	6.82(29)(19)	0.424(18)(12)
2105.89±2.23	777.17±12.70	4.17(2)	2.40(2)	1.49(22)(4)	1.49(22)(4)	0.418(61)(18)
2506.67±2.51	1054.15±12.31	4.96(10)	2.23(2)	2.26(16)(5)	2.05(14)(6)	0.339(23)(12)
2807.26±2.71	1249.64±12.41	5.27(4)	2.28(2)	3.61(29)(11)	3.00(24)(9)	0.390(31)(13)
4009.63±3.54	2006.95±12.31	6.77(8)	2.78(2)	7.87(21)(18)	4.70(12)(13)	0.367(10)(10)
4811.20±4.09	2510.00±12.62	3.23(7)	1.45(2)	3.88(23)(11)	6.85(40)(26)	0.455(27)(17)

Table E.1: *Results for the activation experiment. Column 1: beam energies used in the experiment. Column 2: the corresponding centre of mass energies taking into account the energy losses in the Ni foil and gas target. Columns 3, 4 and 5 show the total number of particles in the beam, target, and recoils, respectively. Column 6 and 7 show the cross section and astrophysical factor for the ^{3}He(α,γ)^{7}Be reaction, respectively. The uncertainties are shown between brackets. When there is only one contribution it refers to the systematic error, and in case of two contributions the first one refers to the statistical uncertainty and the second one to the systematic error.*

E.2.2 Measurements using the direct recoil counting method

For the *direct recoil counting method*, we used the setup at the DRAGON separator (Figure E.7), designed to determine the reaction rate of astrophysical nuclear reactions. It consists of four main components: a recirculating windowless gas target, a BGO array surrounding the target, the separator composed by electric and magnetic dipoles, quadrupoles and sextupoles; and a final detection system placed at the focal plane of the separator, which in our case consisted of a DSSSD detector. We used a ^{4}He beam impinging onto a ^{3}He gas target and the ^{7}Be recoils were detected in the DSSSD.

As in the case of the activation experiment, the areal target density was obtained by considering an ideal gas behaviour (the pressures in this experiment were ~6 Torr). In order to estimate the effective length of the differentially pumped windowless gas target, we used the ^{3}He(^{12}C,^{14}Nγ)p resonance reaction. The γ-rays were detected in a BGO detector placed close to the target cell at different positions parallel to the beam line. The normalised experimental target density profile (TDP) is shown in Figure E.8. The number of beam particles was estimated using the Faraday cups along the separator and two silicon detectors placed inside the target chamber at 30º and 57º with respect to the beam axis.

The total number of ^{7}Be recoils were obtained using the expression E.1:

$$Y_{^7\mathrm{Be}} = \frac{Y_{\mathrm{DSSSD}}}{\mathrm{t}_\ell \cdot q_{\mathrm{f}} \cdot \epsilon_{\mathrm{DRAGON}} \cdot \epsilon_{\mathrm{DSSSD}}} \tag{E.1}$$

where Y_{DSSSD} are the number of recoils detected in the DSSSD (see Figure E.9), t_ℓ and $\epsilon_{\mathrm{DSSSD}}$ are the livetime and detector efficiency, respectively, and q_f and $\epsilon_{\mathrm{DRAGON}}$ are the fraction of the recoils exiting

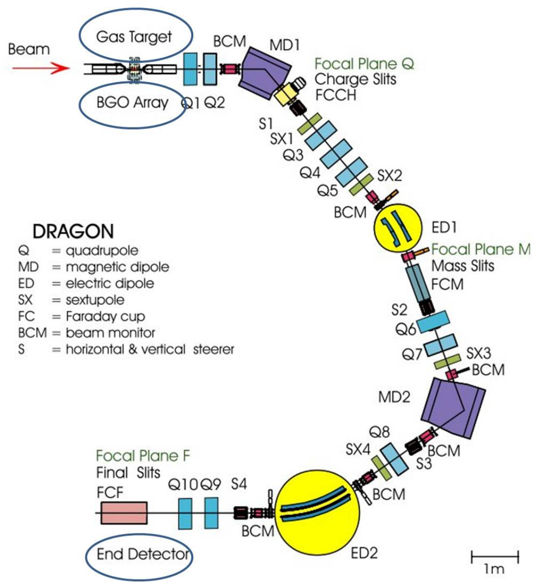

Figure E.7: *Diagram of the DRAGON facility taken from Ref. [EHB05]. The ^{4}He stable beam enters the ^{3}He windowless gas target, with pressures ∼5 Torr. The ^{7}Be recoils produced after the reaction emerge from the target with different charge states and almost with the same momentum of the beam. The recoils are separated from the beam particles using the two magnetic dipoles, MD1 and MD2, and the two electrostatic dipoles, ED1 and ED2. Magnetic quadrupoles and sextupoles are used to focus the particles. Enclosed in circles are the three main components, Gas Target, BGO Array and End Detector.*

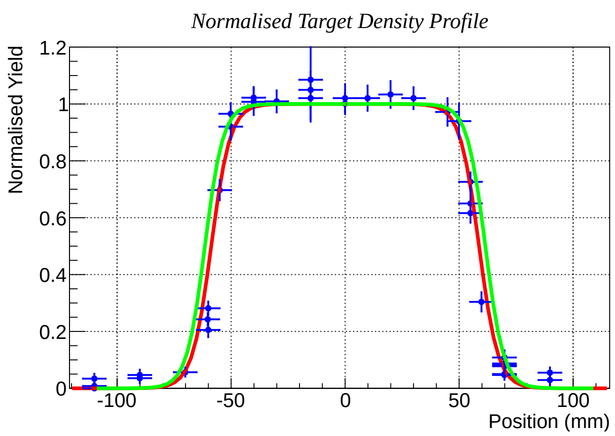

Figure E.8: *Final normalised target density profile. The blue points show the normalised yield corrected with the energy dependence given by the expression 3.21 and after subtraction of a constant background. The red fit shows the "best" fit to the points with a Fermi function obtained using ROOT program and the green curve shows the same fit constraining the effective length to 12.3 cm.*

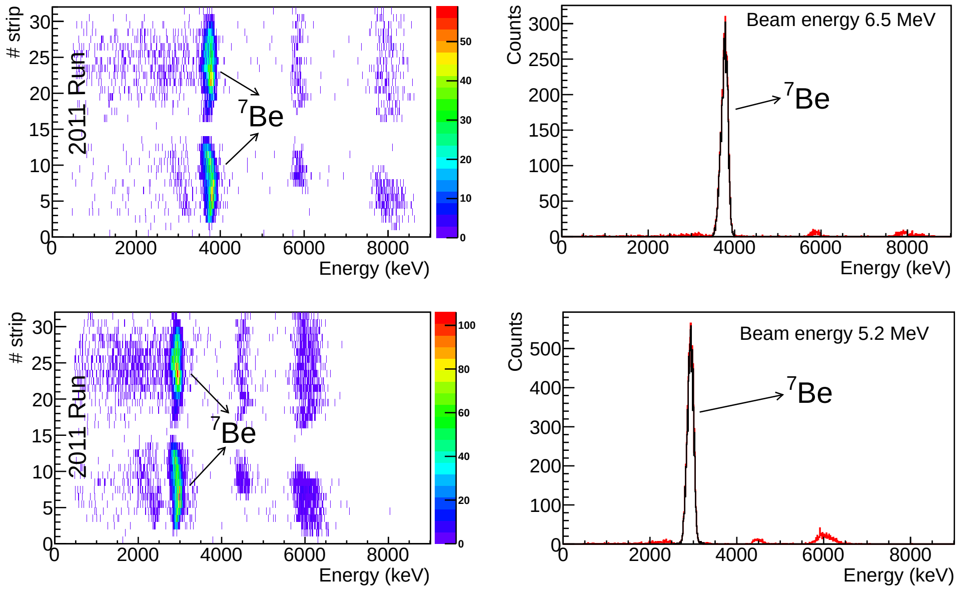

Figure E.9: *(Left) Two dimensional spectra for the ^{7}Be recoils detected in the DSSSD strips for beam energies of 6.5 (up) and 5.2 MeV (down). (Right) Projections histograms for the strips 1 to 15 (red). Events in the selected energy region and detected simultaneously in the back and front strips are also shown (black).*

the gas target with the selected charge state in the separator, and the acceptance of the separator for the corresponding energy.

The determined values for the different parameters in expression E.1 are shown in Table E.2.

$E_{^4He}$ (MeV)	t_ℓ (%)	ϵ_{DSSSD} (%)	q_f (%)	Y_{DSSSD}	ϵ_{DRAGON}
~6.5	84.12	96.15±0.10	(3+)59.05±1.87	33465	$57.4(\pm0.6)(^{+2.3}_{-6.4})$
~5.2	92.34	96.15±0.10	(3+)61.87±2.55	141707	$57.7(\pm0.5)(^{+5.0}_{-5.6})$
~4.7	94.18	96.15±0.10	(2+)29.31±3.81	52683	$71.7(\pm0.6)(^{+3.0}_{-3.8})$
~3.5	98.64	96.15±0.10	(2+)52.30±3.33	44135	$51.3(\pm0.3)(^{+3.0}_{-6.7})$

Table E.2: *Parameter values for determining $Y_{^7Be}$. The q_f shows the selected charge state between brackets and the corresponding charge state fraction. Y_{DSSSD} indicates the number of recoils detected simultaneously in the front and back strips of the DSSSD. The uncertainties in ϵ_{DRAGON} are given from statistical (first) and systematic (second) contributions.*

As the charge state fraction of ions passing through gas target do not depend on the ion mass, the charge state distributions of the ^{7}Be recoils were experimentally determined by using a ^{9}Be and a ^{3}He target. The ^{9}Be velocities were chosen according to the velocities of the ^{7}Be recoils created in the reaction, and different gas target pressures were used. Our results showed that charge state equilibrium have been reached even at 1 Torr.

The acceptance of DRAGON was obtained by performing GEANT 3 simulations for the reactions taking place in the gas target and the ^{7}Be recoils separation process. The real experimental conditions, such as beam transmission, beam energy, beam spot size, target density profile and separator tuning settings were used as input parameters in the simulations. Further simulations were run where the possible changes of these parameters during the experiment were taken into account and the results were used to estimate systematic uncertainties.

The values of various parameters corresponding to our measurements obtained using the *direct recoil counting method* as well as the results for the cross section and astrophysical $S_{34}(E)$ factors are shown in Table E.3 . The values are plotted in Figure E.10, where only the statistical uncertainties are shown.

Run	$\sim E_{^4He}$ (MeV)	E_{CM} (keV)	$N^{beam}_{^4He}$ ($\cdot 10^{16}$)	$N^{target}_{^3He}$ ($\frac{\cdot 10^{18}}{cm^2}$)	$N^{recoils}_{^7Be}$ ($\cdot 10^5$)	σ_{34}(E) μb	S_{34}(E) (keV$\cdot$ b)
hline	6.5	2813.6±1.8	0.84(1)	2.29(11)	1.22(1)($^{+6}_{-14}$)	6.32(8)($^{+44}_{-80}$)	0.393(5)($^{+27}_{-49}$)
2011	5.2	2216.6±1.7	3.25(2)	2.38(13)	4.47(4)($^{+43}_{-47}$)	5.78(5)($^{+63}_{-69}$)	0.419(4)($^{+46}_{-50}$)
	3.5	1508.9±1.3	2.09(1)	2.38(12)	1.74(1)($^{+15}_{-17}$)	3.48(3)($^{+35}_{-38}$)	0.359(3)($^{+36}_{-40}$)
2013	4.7	2023.7±1.4	3.03(3)	1.98(11)	2.77(3)($^{+38}_{-44}$)	4.62(4)($^{+68}_{-79}$)	0.359(3)($^{+53}_{-61}$)
(Impl)	4.7	2023.7±1.4	26.5(1)	1.94(10)	28.8(20)(29)	6.22(44)(72)	0.484(34)(56)

Table E.3: *Results for the direct experiment. Column 2: Beam energies used in the experiment. Column 3: corresponding centre of mass energies taking into account the energy losses. Column 4, 5 and 6 show the total number of particles in the beam, target and recoils, respectively. Column 7 and 8 show the cross section and astrophysical factor for the ^{3}He(α,γ)^{7}Be reaction. The uncertainties are shown between brackets. When only there is one contribution it refers to the systematic error, and in case of two contributions the first one refers to the statistical uncertainty and the second one to the systematic contribution (positive and negative systematic uncertainties are separated in some cases).*

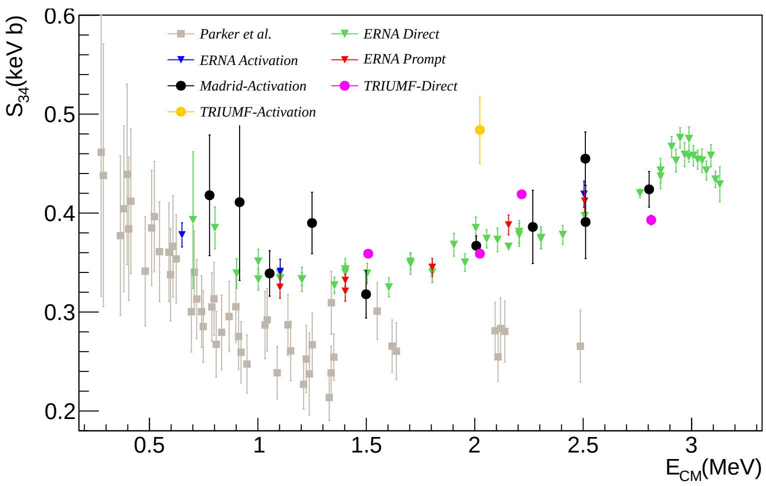

Figure E.10: *Astrophysical S-factor for the ^{3}He(α,γ)^{7}Be reaction using the direct counting method (violet dots) and the activation method (yellow dot) at TRIUMF. For comparison our Madrid data (black dots) and the results from [DGK09] (triangles) and [PK63] (squares) are also shown.*

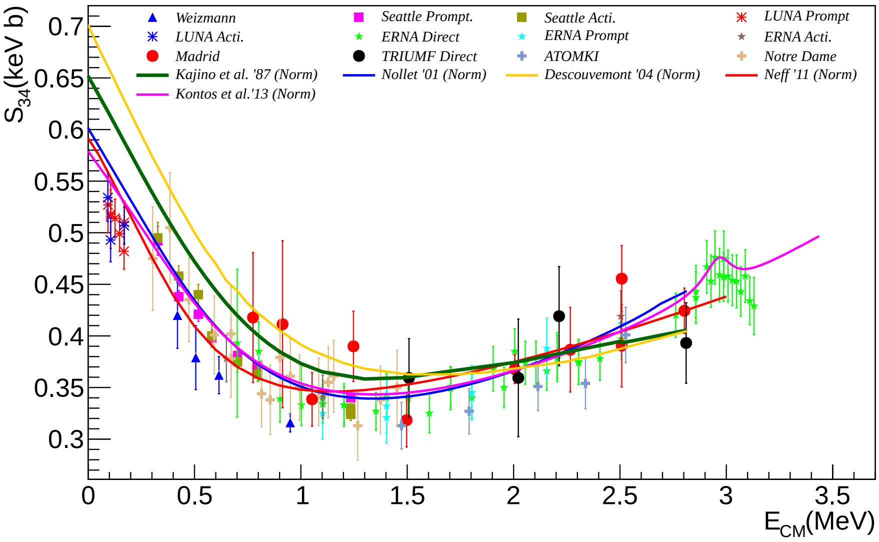

Figure E.11: *The modern experimental data for the $^3He(\alpha,\gamma)^7Be$ reaction together with the theoretical calculations normalised to our experimental results.*

E.3 Discussion and Conclusions

The $S_{34}(E)$ results have been compared with the experimental values available in literature by using the chi-squared method. As can be seen from Table E.4 our results agree with the work from ERNA collaboration. The ATOMKI data, obtained around the time of this thesis, also agree with our results. We therefore conclude that the energy dependence seen in the new data should be considered and the one observed by Parker and Kavanagh should be discarded.

	Parker and Kavanagh	ERNA direct	ATOMKI
Madrid	7.40 ($\nu = 10$)	0.75 ($\nu = 10$)	1.14 ($\nu = 4$)
TRIUMF direct	5.98 ($\nu = 4$)	0.54 ($\nu = 4$)	1.40 ($\nu = 3$)

Table E.4: *χ^2_ν values calculated using expression 6.2. Here, S_A are our astrophysical S-factors and S_B are those from Parker and Kavanagh [PK63], of ERNA [DGK09] or ATOMKI [BGH13].The ν values give the number of data points considered in each case.*

The results were also compared with some of the available calculations. Figure E.11 shows that among the theoretical calculations those by Neff [Nef11] and the R-matrix analysis by Kontos et al. [KUD13] show good agreement with our results and all the new experimental data taken after the measurements at Weizmann in 2004. In order to reproduce our results, the calculated S_{34} curves from the works of Neff and Kontos et al. have been normalised with 0.998 and 1.045 factors, respectively.

E.3.1 Impact on astrophysics

In the present work, $S_{34}(0)$ values have been obtained by extrapolating our data using the FMD model calculations, [Nef11] and Kontos et al. R-matrix fit [KUD13]. Influence of our results on the predictions of the Big-Bang Nucleosynthesis and of the Standard Solar Model can thus be investigated.

In order to compare the impact on the standard solar model, we consider the value for $S_{34}(0)$=0.56 keV b recommended in the revision *Solar Fusion Cross Section II* [AGR11]. Our value of 0.577 keV b considering the renormalisation of Kontos et al. R-matrix fit is $\sim$3% larger and translates to a $\sim$2.61% and $\sim$2.45% increase in the solar neutrino fluxes from ^{7}Be ($\phi_\nu(^7\mathrm{Be})$) and ^{8}B ($\phi_\nu(^8\mathrm{B})$) calculated from the expressions in [CD08]. The R-matrix fit from Kontos et al. including three of our points from Madrid experiment, without considering our normalisation correction, estimates $S_{34}(0)$=0.554 keV b and therefore, practically no such deviations in the neutrino fluxes are estimated.

The changes are even larger if we consider the normalised value from Neff model [Nef11] of 0.592. This value is very close to the obtained without any normalisation consideration of 0.593 and therefore we can consider this model as the one best reproducing our results. On the other hand it should be recalled that this model is based on ab-initio calculation thus, without considering any of the experimental data it can reproduce both phase shifts and capture reaction cross sections. The increase of 5.89% in the $S_{34}(0)$ value compared to that from [AGR11] translates into an 5.05% and 4.75% in $\phi_\nu(^7\mathrm{Be})$ and $\phi_\nu(^8\mathrm{B})$, respectively.

As it was already discussed, it is unlikely that the solution to the observed discrepancy between SBBN calculations and the observations of ^{7}Li abundances will be found by improving the knowledge of the ^{3}He(α,γ)^{7}Be reaction alone. Nevertheless, the recommended $S_{34}(0)$ values have a direct impact on the estimations of the primordial ^{7}Li abundance. A calculation of the new primordial ^{7}Li abundance is out the scope of this work, however a qualitative analysis can be done. According to [DGK09], a primordial ^{7}Li abundance of ^{7}Li/H=(5.4$\pm$0.3) 10^{-10} is obtained using $S_{34}(0)$=0.57 keV b. This abundance is factor 3 larger than the observational values. In our case the $S_{34}(0)$ is a 3.86% larger than that considered in [DGK09]. Therefore, the corresponding primordial ^{7}Li abundance results to become even larger, thus worsening the problem (see for example [CFO08]).

E.3.2 Conclusions

The main outcomes from this work are:

- Two experimental set-ups have been completely characterised in order to study the ^{3}He(α,γ)^{7}Be reaction
- Ten new $S_{34}(E)$ values with low systematic uncertainty have been obtained in the range of E_{CM}=1-3 MeV using the *activation* technique and by employing a very well controlled ^{7}Be production and a γ-counting setup
- Three of the measurements using the *activation* technique has special relevance due to the low statistical uncertainty and good accuracy
- The density profile of the ^{3}He gas target in the DRAGON cell has been measured for the first time and can be used for future experiments at the DRAGON separator
- The charge state distribution of Be nuclei after crossing the ^{3}He target gas has been determined for the first time, using target pressures between 1 to 6 Torr, that indicates charge state equilibrium at 1 Torr
- A very high suppression of the incident beam has been measured when the ^{7}Be recoils from the ^{3}He(α,γ)^{7}Be reaction are selected by the DRAGON separator
- The GEANT-3 DRAGON code has been modified and adapted to perform extensive simulations, including a new specific prompt γ-rays angular distributions which will be used for the design of future experiments
- Several tests have been performed in order to constrain the angular distribution of the prompt γ-rays. The variation of the angular distributions has been introduced as potential uncertainties in the acceptance and intense simulations with the adapted GEANT-3 code could lead to a better constrain in the coefficients of the γ-ray angular distribution

- Four new data points for the S_1/S_0 branching ratios have been determined. This includes the point corresponding to 2.8 MeV that is the highest energy at which such data has been obtained so far
- Four new $S_{34}(E)$ values have been determined with the lowest statistical uncertainty measured so far using the *direct recoil counting* technique
- A good agreement is seen between the two data sets obtained using two independent techniques
- The results obtained in this thesis clearly agree with those from the ERNA collaboration [DGK09] and fully disagree with those from Parker et al.'s work [PK63], in the same energy region
- Our data show very good agreement with the ab-initio FMD calculations [Nef11]
- Based on our experimental results and the ab-initio calculations we recommend a value of $S_{34}(0)$=0.593 keV b
- From the description of our results and other experimental sets further data are yet required in a wide energy range using different techniques for a comparison of the results and to perform consistent data evaluations
- None of the current theoretical calculations can describe simultaneously the two mirror reactions ^{3}He(α,γ)^{7}Be and ^{3}H(α,γ)^{7}Li. New measurements of the mirror reaction are strongly suggested as well as elastic scattering data of the ^{3}He(α,α)^{3}He reaction in order to constrain the theoretical models
- Due to the discrepancies between the theoretical models of the s- and p-wave contributions to the $S_{34}(E)$ factor, precise angular distributions of the prompt γ-rays are also recommended.

BIBLIOGRAPHY

[AAA01] Q. R. Ahmad, R. C. Allen, T. C. Andersen, J. D. Anglin, G. Bühler, J. C. Barton, E. W. Beier, M. Bercovitch, J. Bigu, S. Biller, R .A. Black, I. Blevis, R. J. Boardman, J. Boger, E. Bonvin, M. G. Boulay, M. G. Bowler, T. J. Bowles, S. J. Brice, M. C. Browne, T. V. Bullard, T. H. Burritt, K. Cameron, J. Cameron, Y. D. Chan, M. Chen, H. H. Chen, X. Chen, M. C. Chon, B.T. Cleveland, E. T. Clifford, J. H. Cowan, D. F. Cowen, G .A. Cox, Y. Dai, X. Dai, F. Dalnoki-Veress, W. F. Davidson, P. J. Doe, G. Doucas, M. R. Dragowsky, C. A. Duba, F. A. Duncan, J Dunmore, E. D. Earle, S. R. Elliott, H. C. Evans, G .T. Ewan, J. Farine, H. Fergani, A. P. Ferraris, R. J. Ford, M M Fowler, K Frame, E D. Frank, W. Frati, J. V. Germani, S. Gil, A. Goldschmidt, D .R. Grant, R. L. Hahn, A. L. Hallin, E .D. Hallman, A. Hamer, A.A. Hamian, R. U. Haq, C. K. Hargrove, P. J. Harvey, R. Hazama, R. Heaton, K. M. Heeger, W. J. Heintzelman, J. Heise, R. L. Helmer, J. D. Hepburn, H. Heron, J. Hewett, A. Hime, M. Howe, J. G. Hykawy, M. C. Isaac, P. Jagam, N. A. Jelley, C. Jillings, G. Jonkmans, J. Karn, P. T. Keener, K. Kirch, J. R. Klein, A: B. Knox, R. J. Komar, R. Kouzes, T. Kutter, C. C. Kyba, J. Law, I. T. Lawson, M. Lay, H .W. Lee, K. T. Lesko, J. R. Leslie, I. Levine, W. Locke, M. M. Lowry, S. Luoma, J. Lyon, S. Majerus, H. B. Mak, A. D. Marino, N. McCauley, A. B. McDonald, D. S. McDonald, K. McFarlane, G. McGregor, W. McLatchie, R. Meijer Drees, H. Mes, C. Mifflin, G. G. Miller, G. Milton, B .A. Moffat, M. Moorhead, C. W. Nally, M. S. Neubauer, F. M. Newcomer, H. S. Ng, A. J. Noble, E. B. Norman, V. M. Novikov, M. O’Neill, C. E. Okada, R. W. Ollerhead, M. Omori, J. L. Orrell, S . M. Oser, A. W. Poon, T. J. Radcliffe, A. Roberge, B. C. Robertson, R. G. Robertson, J. K. Rowley, V. L. Rusu, E. Saettler, K. K. Schaffer, A. Schuelke, M. H. Schwendener, H. Seifert, M. Shatkay, J. J. Simpson, D. Sinclair, P. Skensved, A. R. Smith, M. W. Smith, N. Starinsky, T. D. Steiger, R. G. Stokstad, R .S. Storey, B. Sur, R. Tafirout, N. Tagg, N. W. Tanner, R. K. Taplin, M. Thorman, P. Thornewell, P. T. Trent, Y. I. Tserkovnyak, R. Van Berg, R. G. Van de Water, C. J. Virtue, C. E. Waltham, J. X. Wang, D. L. Wark, N. West, J. B. Wilhelmy, J. F. Wilkerson, J. Wilson, P. Wittich, J. M. Wouters, and M. Yeh, *Measurement of the rate of $\nu_e + d \rightarrow p + p + e^-$ interactions produced by ^8B solar neutrinos at the Sudbury Neutrino Observatory*, Physical review letters **87**, no. 7, 071301 (2001).

[AAA02] Q. Ahmad, R. Allen, T. Andersen, J. D.Anglin, J. Barton, E. Beier, M. Bercovitch, J. Bigu, S. Biller, R. Black, I. Blevis, R. Boardman, J. Boger, E. Bonvin, M. Boulay, M. Bowler, T. Bowles, S. Brice, M. Browne, T. Bullard, G. Bühler, J. Cameron, Y. Chan, H. Chen, M. Chen, X. Chen, B. Cleveland, E. Clifford, J. Cowan, D. Cowen, G. Cox, X. Dai, F. Dalnoki-Veress, W. Davidson, P. Doe, G. Doucas, M. Dragowsky, C. Duba, F. Duncan, M. Dunford, J. Dunmore, E. Earle, S. Elliott, H. Evans, G. Ewan, J. Farine, H. Fergani, A. Ferraris, R. Ford, J. Formaggio, M. Fowler, K. Frame, E. Frank, W. Frati, N. Gagnon, J. Germani, S. Gil, K. Graham, D. Grant, R. Hahn, A. Hallin, E. Hallman, A. Hamer, A. Hamian, W. Handler, R. Haq, C. Hargrove, P. Harvey, R. Hazama, K. Heeger, W. Heintzelman, J. Heise, R. Helmer, J. Hepburn, H. Heron, J. Hewett, A. Hime, M. Howe, J. Hykawy, M. Isaac, P. Jagam, N. Jelley, C. Jillings, G. Jonkmans, K. Kazkaz, P. Keener, J. Klein, A. Knox, R. Komar, R. Kouzes, T. Kutter, C. Kyba, J. Law, I. Lawson, M. Lay, H. Lee, K. Lesko, J. Leslie, I. Levine, W. Locke, S. Luoma, J. Lyon, S. Majerus, H. Mak, J. Maneira, J. Manor, A. Marino, N. McCauley, A. McDonald, D. McDonald, K. McFarlane, G. McGregor, R. Meijer Drees, C. Mifflin, G. Miller, G. Milton, B. Moffat, M. Moorhead, C. Nally, M. Neubauer, F. Newcomer, H. Ng, A. Noble, E. Norman, V. Novikov, M. O'Neill, C. Okada, R. Ollerhead, M. Omori, J. Orrell, S. Oser, A. Poon, T. Radcliffe, A. Roberge, B. Robertson, R. Robertson, S. Rosendahl, J. Rowley, V. Rusu, E. Saettler, K. Schaffer, M. Schwendener, A. Schülke, H. Seifert, M. Shatkay, J. Simpson, C. Sims, D. Sinclair, P. Skensved, A. Smith, M. Smith, T. Spreitzer, N. Starinsky, T. Steiger, R. Stokstad, L. Stonehill, R. Storey, B. Sur, R. Tafirout, N. Tagg, N. Tanner, R. Taplin, M. Thorman, P. Thornewell, P. Trent, Y. Tserkovnyak, R. Van Berg, R. Van De Water, C. Virtue, C. Waltham, J.-X. Wang, D. Wark, N. West, J. Wilhelmy, J. Wilkerson, J. Wilson, P. Wittich, J. Wouters, and M. Yeh, *Direct Evidence for Neutrino Flavor Transformation from Neutral-Current Interactions in the Sudbury Neutrino Observatory*, Physical Review Letters **89**, no. 1, 011301 (2002).

[AAA07] B. Aharmim, Q. Ahmad, S. Ahmed, R. Allen, T. Andersen, J. Anglin, G. Bühler, J. Barton, E. Beier, M. Bercovitch, M. Bergevin, J. Bigu, S. Biller, R. Black, I. Blevis, R. Boardman, J. Boger, E. Bonvin, M. Boulay, M. Bowler, T. Bowles, S. Brice, M. Browne, T. Bullard, T. Burritt, J. Cameron, Y. Chan, H. Chen, M. Chen, X. Chen, B. Cleveland, J. Cowan, D. Cowen, G. Cox, C. Currat, X. Dai, F. Dalnoki-Veress, W. Davidson, H. Deng, M. DiMarco, P. Doe, G. Doucas, M. Dragowsky, C. Duba, F. Duncan, M. Dunford, J. Dunmore, E. Earle, S. Elliott, H. Evans, G. Ewan, J. Farine, H. Fergani, A. Ferraris, F. Fleurot, R. Ford, J. Formaggio, M. Fowler, K. Frame, E. Frank, W. Frati, N. Gagnon, J. Germani, S. Gil, A. Goldschmidt, J. Goon, K. Graham, D. Grant, E. Guillian, R. Hahn, A. Hallin, E. Hallman, A. Hamer, A. Hamian, W. Handler, R. Haq, C. Hargrove, P. Harvey, R. Hazama, K. Heeger, W. Heintzelman, J. Heise, R. Helmer, R. Henning, J. Hepburn, H. Heron, J. Hewett, A. Hime, C. Howard, M. Howe, M. Huang, J. Hykaway, M. Isaac, P. Jagam, B. Jamieson, N. Jelley, C. Jillings, G. Jonkmans, K. Kazkaz, P. Keener, K. Kirch, J. Klein, A. Knox, R. Komar, L. Kormos, M. Kos, R. Kouzes, A. Krüger, C. Kraus, C. Krauss, T. Kutter, C. Kyba, H. Labranche, R. Lange, J. Law, I. Lawson, M. Lay, H. Lee, K. Lesko, J. Leslie, I. Levine, J. Loach, W. Locke, S. Luoma, J. Lyon, R. MacLellan, S. Majerus, H. Mak, J. Maneira, A. Marino, R. Martin, N. McCauley, A. McDonald, D. McDonald, K. McFarlane, S. McGee, G. McGregor, R. Drees, H. Mes, C. Mifflin, K. Miknaitis, M. Miller, G. Milton, B. Moffat, B. Monreal, M. Moorhead, B. Morrissette, C. Nally, M. Neubauer, F. Newcomer, H. Ng, B. Nickel, A. Noble, E. Norman, V. Novikov, N. Oblath, C. Okada, H. O'Keeffe, R. Ollerhead, M. Omori, J. Orrell, S. Oser, R. Ott, S. Peeters, A. Poon, G. Prior, S. Reitzner, K. Rielage, A. Roberge, B. Robertson, R. Robertson, S. Rosendahl, J. Rowley, V. Rusu, E. Saettler, A. Schülke, M. Schwendener, J. Secrest, H. Seifert, M. Shatkay, J. Simpson, C. Sims, D. Sinclair, P. Skensved, A. Smith, M. Smith, N. Starinsky, T. Steiger, R. Stokstad, L. Stonehill, R. Storey, B. Sur, R. Tafirout, N. Tagg, Y. Takeuchi, N. Tanner, R. Taplin, M. Thorman, P. Thornewell, N. Tolich, P. Trent, Y. Tserkovnyak, T. Tsui, C. Tunnell, R. Berg, R. Water, C. Virtue, T. Walker, B. Wall, C. Waltham, H. Tseung, J.-X. Wang, D. Wark, J. Wendland, N. West, J. Wilhelmy, J. Wilkerson, J. Wilson, P. Wittich, J. Wouters, A. Wright, M. Yeh, and K. Zuber, *Determination of the νe and total ^{8}B solar neutrino fluxes using the Sudbury Neutrino Observatory Phase I data set*, Physical Review C **75**, 045502 (2007).

[AAB98] E.G. Adelberger, Sam M. Austin, John N. Bahcall, A.B. Balantekin, Gilles Bogaert, Lowell S. Brown, L. Buchmann, F. Edward Cecil, Arthur E. Champagne, Ludwig De Braeckeleer, Charles A. Duba, S. Elliott, S. Freedman, M. Gai, G. Goldring, Christopher R. Gould, Andrei Gruzinov, Wick C. Haxton, K. Heeger, Ernest Henley, Calvin W. Johnson, Marc Kamionkowski, Ralph Kavanagh, Steven E. Koonin, Kuniharu Kubodera, Karlhei Laganke, T. Motobayashi, Vijay Pandharipande, Parker P.D., R. Robertson, Claus Rolfs, R. F. Sawyer, N. Shaviv, T. D. Shoppa, K. Snover, Erik Swanson, Robert E. Tribble, Sylvaine Turck-Chièze, and J. Wilkerson, *Solar fusion cross sections*, Reviews of Modern Physics **70**, 1265 (1998).

[ABB08] C. Arpesella, H. Back, M. Balata, G. Bellini, J. Benziger, S. Bonetti, A. Brigatti, B. Caccianiga, L. Cadonati, F. Calaprice, C. Carraro, G. Cecchet, A. Chavarria, M. Chen, F. Dalnoki-Veress, D. D'Angelo, A. De Bari, A. De Bellefon, H. De Kerret, A. Derbin, M. Deutsch, A. di Credico, G. di Pietro, R. Eisenstein, F. Elisei, A. Etenko, R. Fernholz, K. Fomenko, R. Ford, D. Franco, B. Freudiger, C. Galbiati, F. Gatti, S. Gazzana, M. Giammarchi, D. Giugni, M. Goeger-Neff, T. Goldbrunner, A. Goretti, C. Grieb, C. Hagner, W. Hampel, E. Harding, S. Hardy, F. Hartman, T. Hertrich, G. Heusser, Aldo Ianni, Andrea Ianni, M. Joyce, J. Kiko, T. Kirsten, V. Kobychev, G. Korga, G. Korschinek, D. Kryn, V. Lagomarsino, P. Lamarche, M. Laubenstein, C. Lendvai, M. Leung, T. Lewke, E. Litvinovich, B. Loer, P. Lombardi, L. Ludhova, I. Machulin, S. Malvezzi, S. Manecki, J. Maneira, W. Maneschg, I. Manno, D. Manuzio, G. Manuzio, A. Martemianov, F. Masetti, U. Mazzucato, K. McCarty, D. McKinsey, Q. Meindl, E. Meroni, L. Miramonti, M. Misiaszek, D. Montanari, M. Monzani, V. Muratova, P. Musico, H. Neder, A. Nelson, L. Niedermeier, L. Oberauer, M. Obolensky, M. Orsini, F. Ortica, M. Pallavicini, L. Papp, S. Parmeggiano, L. Perasso, A. Pocar, R. Raghavan, G. Ranucci, W. Rau, A. Razeto, E. Resconi, P. Risso, A. Romani, D. Rountree, A. Sabelnikov, R. Saldanha, C. Salvo, D. Schimizzi, S. Schönert, T. Shutt, H. Simgen, M. Skorokhvatov, O. Smirnov, A. Sonnenschein, A. Sotnikov, S. Sukhotin, Y. Suvorov, R. Tartaglia, G. Testera, D. Vignaud, S. Vitale, R. Vogelaar, F. von Feilitzsch, R. von Hentig, T. von Hentig, M. Wojcik, M. Wurm, O. Zaimidoroga, S. Zavatarelli, and G. Zuzel, *Direct Measurement of the ^{7}Be Solar Neutrino Flux with 192 Days of Borexino Data*, Physical Review Letters **101**, 091302 (2008).

[ABLG84] T.K. Alexander, G.C. Ball, W.N. Lennard, and H. Geissel, *Measurement of the absolute cross section of the ^{3}He(^{4}He,γ)^{7}Be reaction at Ecm=525 kEV*, Nuclear Physics A **427**, 526–544 (1984).

[AEE08] S. Abe, T. Ebihara, S. Enomoto, K. Furuno, Y. Gando, K. Ichimura, H. Ikeda, K. Inoue, Y. Kibe, Y. Kishimoto, M. Koga, A. Kozlov, Y. Minekawa, T. Mitsui, K. Nakajima, K. Nakamura, M. Nakamura, K. Owada, I. Shimizu, Y. Shimizu, J. Shirai, F. Suekane, A. Suzuki, Y. Takemoto, K. Tamae, A. Terashima, H. Watanabe, E. Yonezawa, S. Yoshida, J. Busenitz, T. Classen, C. Grant, G. Keefer, D. Leonard, D. McKee, A. Piepke, M. Decowski, J. Detwiler, S. Freedman, B. Fujikawa, F. Gray, E. Guardincerri, L. Hsu, R. Kadel, C. Lendvai, K.-B. Luk, H. Murayama, T. O'Donnell, H. Steiner, L. Winslow, D. Dwyer, C. Jillings, C. Mauger, R. McKeown, P. Vogel, C. Zhang, B. Berger, C. Lane, J. Maricic, T. Miletic, M. Batygov, J. Learned, S. Matsuno, S. Pakvasa, J. Foster, G. Horton-Smith, A. Tang, S. Dazeley, K. Downum, G. Gratta, K. Tolich, W. Bugg, Y. Efremenko, Y. Kamyshkov, O. Perevozchikov, H. Karwowski, D. Markoff, W. Tornow, K. Heeger, F. Piquemal, and J.-S. Ricol, *Precision Measurement of Neutrino Oscillation Parameters with KamLAND*, Physical Review Letters **100**, 221803 (2008).

[AGR11] E.G. Adelberger, A. García, R.G. Hamish Robertson, K. A. Snover, A.B. Balantekin, K. Heeger, M.J. Ramsey-Musolf, D. Bemmerer, A. Jughans, C.A. Bertulani, J.W. Chen, H. Constantini, P. Prati, M. Couder, E. Uberseder, M. Wiescher, R. Cyburt, B. Davids, S.J. Freedman, M. Gai, D. Gazit, L.Gialanella, G. Imbriani, U. Greife, M. Hass, W.C. Haxton, T. Itahashi, K. Kubodera, K. Langanke, D. Leitner, M. Letner, P. Vetter, L. Winslow, L.E. Marcucci, T. Motobayashi, A. Mukhamedzhanov, R.E. Tribble, Kenneth M. Nollet, F.M. Nunes, T.S. Park, P.D. Parker, R. Schiavilla, E.C. Simpson, C. Spitaleri, F. Strieder, H.P. Trautvetter, K. Suemmerer, and S. Typel, *Solar fusion cross sections . II . The pp chain and CNO cycles*, Reviews of Modern Physics **83**, 195–245 (2011).

[AL55] F. Ajzenberg and T. Lauritsen, *Energy Levels of Light Nuclei. V*, Reviews of Modern Physics **27**, no. 1, 77 (1955).

[Alc06] M. Alcorta, *Study of excited states of ^{12}C in full kinematics*, Master's thesis, Universidad de Huelva, 2006.

[Alc10] M. Alcorta, *Nuclear structure of ^{12}C from 3-body break-up studies by light ion reactions in complete kinematics*, Ph.D. thesis, Universidad Complutense de Madrid, 2010.

[AMHM65] J.C. Armstrong, J.V. Mullendore, W.R. Harris, and J.B. Marion, *Equilibrium charge-state fractions of 0.2 to 6.5 MeV helium ions in caron*, Proceedings of the Physical Society **186**, 1283 (1965).

[Bah64a] John N. Bahcall, *Solar Neutrino Cross Sections and Nuclear Beta Decay*, Physical Review **135**, no. 1B, 137–146 (1964).

[Bah64b] John N. Bahcall, *Solare Neutrinos. I. Theoretical*, Physical Review Letters **12**, 300 (1964).

[Bah66] John N. Bahcall, *Solar Neutrino*, Physical Review Letters **17**, no. 7, 398–401 (1966).

[BB90] John N. Bahcall and H.A. Bethe, *A solution of the Solar-Neutrino Problem*, Physical Review Letters **65**, 2233 (1990).

[BBB11] G. "Bellini, J. Benziger, S. Bonetti, M. Buizza Avanzini, B. Caccianiga, L. Cadonati, F. Calaprice, C. Carraro, A. Chavarria, A. Chepurnov, D. D'Angelo, S. Davini, A. Derbin, A. Etenko, K. Fomenko, D. Franco, C. Galbiati, S. Gazzana, C. Ghiano, M. Giammarchi, M. Goeger-Neff, A. Goretti, E. Guardincerri, S. Hardy, Aldo Ianni, Andrea Ianni, M. Joyce, V.V. Kobychev, D. Korablev, Y. Koshio, G. Korga, D. Kryn, M. Laubenstein, T. Lewke, E. Litvinovich, B. Loer, P. Lombardi, L. Ludhova, I. Machulin, S. Manecki, W. Maneschg, G. Manuzio, Q. Meindl, E. Meroni, L. Miramonti, M. Misiaszek, D. Montanari, V. Muratova, L. Oberauer, M. Obolensky, F. Ortica, M. Pallavicini, L. Papp, L. Perasso, S. Perasso, A. Pocar, R.S. Raghavan, G. Ranucci, A. Razeto, A. Re, P. Risso, A. Romani, D. Rountree, A. Sabelnikov, R. Saldanha, C. Salvo, S. Schönert, H. Simgen, M. Skorokhvatov, O. Smirnov, A. Sotnikov, S. Sukhotin, Y. Suvorov, R. Tartaglia, G. Testera, D. Vignaud, R.B. Vogelaar, F. von Feilitzsch, J. Winter, M. Wojcik, A. Wright, M. Wurm, J. Xu, O. Zaimidoroga, S. Zavatarelli, and G." Zuzel, *Study of solar and other unknown anti-neutrino fluxes with Borexino at LNGS*, Physics Letters B **696**, 191–196 (2011).

[BBBH01] C. Bordeanu, D. Berkovits, E. Boaretto, and M. Hass, *Towards a measurement of $\sigma(^3He(^4He,\gamma)^7Be)$ with Accelerator Mass Spectrometry (AMS)*, Progress in Particle and Nuclear Physics **46**, 97–98 (2001).

[BBH72] W.R. Boykin, S.D. Baker, and D.M. Hardy, *SCATTERING OF ^{3}He AND ^{4}He FROM PO LARIZED ^{3}He BETWEEN 4 AND 10 MeV*, 241–249 (1972).

[BBR85] Brian Buck, Richard A. Baldock, and J. Alberto Rubio, *Cluster model of A = 7 nuclei and the astrophysical S factor for $^3He(\alpha,\gamma)^7Be$ at zero energy*, Journal of Physics G: Nuclear and Particle Physics **11**, L11–L16 (1985).

[BBS68] John N. Bahcall, Neta A. Bahcall, and Giora Shaviv, *Present status of the theoretical predictions for the ^{36}Cl solar-neutrino experiment*, Physical Review Letters **20**, no. 21, 1209–1212 (1968).

[BBS07] T. Brown, C. Bordeanu, K. Snover, D. Storm, D. Melconian, A. Sallaska, S. Sjue, and S. Triambak, *^3He+$^4He \to {}^7Be$ astrophysical S factor*, Physical Review C **76**, 055801 (2007).

[BCC06] D. Bemmerer, F. Confortola, H. Costantini, A. Formicola, Gy. Gyürky, R. Bonetti, C. Broggini, P. Corvisiero, Z. Elekes, Zs. Fülöp, G. Gervino, A. Guglielmetti, C. Gustavino, G. Imbriani, M. Junker, M. Laubenstein, A. Lemut, B. Limata, V. Lozza, M. Marta, R. Menegazzo, P. Prati, V. Roca, C. Rolfs, C.Rossi Alvarez, E. Somorjai, O. Straniero, F. Strieder, F. Terrasi, and H. Trautvetter, *Activation Measurement of the $^3He(\alpha,\gamma)^7Be$ Cross Section at Low Energy*, Physical Review Letters **97**, 122502 (2006).

[BCD67] John N. Bahcall, M. Cooper, and P. Demarque, *Dependence of the ^8B Solar Neutrino Flux on Heavy Element Composition*, Astrophysical Journal, no. 150, 723–724 (1967).

[BD85] D. Baye and P. Descouvemont, *Antisymmetrization Effects in Radiative Capture Reactions*, Annals of Physics **165**, 115–147 (1985).

[Bet72] Hans-Dieter Betz, *Charge States and Charge-Changing Cross sections of fast heavy iones penetrating through gaseous and solid media*, Reviews of Modern Physics **44**, no. 3, 465–539 (1972).

[Bet86] H.A. Bethe, *Possible Explanation of the Solar-Neutrino Puzzle*, Physical Review Letters **56**, 1305 (1986).

[BFI63] J.N. Bahcall, William A. Fowler, I. Iben, Jr., and R.L. Sears, *Solar Neutrino Flux*, Astrophysics Journal **137**, 344 (1963).

[BGH13] C. Bordeanu, Gy. Gyürky, Z. Halász, T. Szücs, G.G. Kiss, Z. Elekes, J. Farkas, Zs. Fülöp, and E. Somorjai, *Activation measurement of the $^3He(\alpha,\gamma)^7Be$ reaction cross section at high energies*, Nuclear Physics A **908**, 1–11 (2013).

[BHL82] John N. Bahcall, Walter F. Huebner, Stephen H. Lubow, Peter D. Parker, and Roger K. Ulrich, *Standar solar models and the uncertainties in predicted capture rates of solar neutrinos*, Review of Modern Physics **54**, 767–800 (1982).

[BJP64] A. C. L. Barnard, C. M. Jones, and G. C. Phillips, *The Scattering of ^3He by ^4He*, Nuclear Physics **50**, 629–640 (1964).

[BM88] B. Buck and A.C. Merchant, *Cluster model of A = 7 nuclei revisited , and the astrophysical at zero energy S factors for $^3He(\alpha,\gamma)^7Be$ and $^3H(\alpha,\gamma)^7Li$*, Journal of Physics G: Nuclear and Particle Physics **14**, L211–L216 (1988).

[BP95] John N. Bahcall and M. Pinsonneault, *Solar models with helium and heavy-element difussion*, Reviews of Modern Physics **67**, 781 (1995).

[Bro11] C. Broggini, *Twenty years of LUNA*, Progress in Particle and Nuclear Physics **66**, 293–297 (2011).

[BSB05] John N Bahcall, Aldo M Serenelli, and Sarbani Basu, *NEW SOLAR OPACITIES, ABUNDANCES, HELIOSEISMOLOGY, AND NEUTRINO FLUXES*, The Astrophysical Journal **621:L**, 85–88 (2005).

[BWR94] C. R. Brune, R. Kavanagh W., and C. Rolfs, *$^3H(\alpha,\gamma)^7Li$ reaction at low energy*, Physical Review C **50**, no. 4, 2205 (1994).

[CAE] CAEN S.p.A., http://www.caen.it.

[CBC07] F. Confortola, D. Bemmerer, H. Costantini, A. Formicola, Gy. Gyürky, P. Bezzon, R. Bonetti, C. Broggini, P. Corvisiero, Z. Elekes, Zs. Fülöp, G. Gervino, A. Guglielmetti, C. Gustavino, G. Imbriani, M. Junker, M. Laubenstein, A. Lemut, B. Limata, V. Lozza, M. Marta, R. Menegazzo, P. Prati, V. Roca, C. Rolfs, C.Rossi Alvarez, E. Somorjai, O. Straniero, F. Strieder, F. Terrasi, and H. Trautvetter, *Astrophysical S factor of the $^3He(\alpha,\gamma)^7Be$ reaction measured at low energy via detection of prompt and delayed γ rays*, Physical Review C **75**, 065803 (2007).

[CD61] R.F. Christy and Ian Duck, *Gamma Rays from an Extranuclear Direct Capture Proccess*, Nuclear Physics, no. 24, 89–101 (1961).

[CD08] R. H. Cyburt and B. Davids, *Evaluation of modern $^3He(\alpha,\gamma)^7Be$ data*, Physical Review C **78**, 064614 (2008).

[CFO08] Richard H. Cyburt, Brian D. Fields, and Keith A. Olive, *An update on the big bang nucleosynthesis prediction for ^7Li: the problem worsens*, Journal of Cosmology and Astroparticle Physics **11**, 012 (2008).

[CGNB12] M. Carmona-Gallardo, B. S. Nara Singh, M. J. G. Borge, J. A. Briz, M. Cubero, B. R. Fulton, H. Fynbo, N. Gordillo, M. Hass, G. Haquin, A. Maira, E. Nácher, Y. Nir-El, V. Kumar, J. McGrath, A. Muñoz Martín, A. Perea, V. Pesudo, G. Ribeiro, J. Sánchez del Rio, O. Tengblad, R. Yaniv, and Z. Yungreis, *New measurement of the $^3He(\alpha,\gamma)^7Be$ cross section at medium energies*, Physical Review C **86**, 032801(R) (2012).

[CGRB14] M. Carmona-Gallardo, A. Rojas, M. J. G. Borge, B. Davids, B. R. Fulton, M. Hass, B. S. Nara Singh, C. Ruiz, and O Tengblad, *$^3He(\alpha,\gamma)^7Be$ cross section measured using complementary techniques*, European Physics Journal Web of Conferences **66**, 07003 (2014).

[CGX12] Alain Coc, Stéphane Goriely, Yi Xu, Matthias Saimpert, and Elisabeth1 Vangioni, *Standard Big Bang Nucleosynthesis Up To CNO With an Improved Extended Nuclear Network*, The Astrophysical Journal **744:158**, (18pp) (2012).

[CL00] A. Csótó and K. Langanke, *Study of the $^3He(^4He,\gamma)^7Be$ and $^3H(^4He,\gamma)^7Li$ Reactions in an Extended Two-Cluster Model*, Few-Body Systems **29**, 121–130 (2000).

[CMA] CMAM, Centro de Microanálisis de Madrid, Universidad Autónoma, Madrid, http://www.cmam.uam.es/en.

[Cyb04] R. Cyburt, *Primordial nucleosynthesis for the new cosmology: Determining uncertainties 1and examining concordance*, Physical Review D **70**, 023505 (2004).

[DAA04] Pierre Descouvemont, Abderrahim Adahchour, C. Angulo, Alain Coc, and Elisabeth Vangioni-Flam, *Compilation and R-matrix analysis of Big Bang nuclear reaction rates*, Atomic Data and Nuclear Data Tables **88**, no. 1, 203–236 (2004).

[Dav94] Raymond Davis, *A review of the homestake solar neutrino experiment*, Progress in Particle and Nuclear Physics **32**, 13–32 (1994).

[DDK95] S.B. Dubovichenko and A.V. Dzhazairov-Kakhramanov, Phy.At. Nucl. **58**, 579 (1995).

[DDS08] A. Di Leva, M. De Cesare, D. Schurmann, N. De Cesare, A. D 'Onofrio, L Gialanella, R. Kunz, G. Imbriani, A. Ordine, V. Roca, D. Rogalla, C. Rolfs, M. Romano, E. Somorjai, F. Strieder, and F. Terrasi, *Recoil separator ERNA: Measurement of $^3He(\alpha,\gamma)^7Be$*, Nuclear Instruments and Methods in Physics Research Section A: Accelerators, Spectrometers, Detectors and Associated Equipment **595**, 381–390 (2008).

[Des01] P. Descouvemont, *Exotic nuclei in a microscopic cluster model*, Riken Review **39**, 102 (2001).

[Des03] P. Descouvemont, *Theoretical Models for Nuclear Astrophysics*, Nova Science Publishers, Inc., 2003.

[DGK09] A. Di Leva, L. Gialanella, R. Kunz, D. Rogalla, D. Schürmann, F. Strieder, M. De Cesare, N. De Cesare, A. D'Onofrio, Z. Fülöp, G. Gyürky, G. Imbriani, G. Mangano, A. Ordine, V. Roca, C. Rolfs, M. Romano, E. Somorjai, and F. Terrasi, *Erratum: Stellar and Primordial Nucleosynthesis of ^7Be: Measurement of $^3He(\alpha,\gamma)^7Be$ [Phys. Rev. Lett. 102, 232502 (2009)]*, Physical Review Letters **103**, 159903 (2009).

[DJHH68] Raymond Davis, Jr., Don S. Harmer, and Kenneth C Hoffman, *Search for neutrinos from the sun*, Physical Review Letters **20**, 1205 (1968).

[EHB05] S. Engel, D. Hutcheon, S. Bishop, L. Buchmann, J. Caggiano, M.L. Chatterjee, A.A. Chen, J. D'Auria, D. Gigliotti, U.Greife, D. Hunter, A. Hussein, C. C. Jewett, A. M. Laird, M. Lamey, W. Liu, A. Olin, D. Ottewell, J. Pearson, C. Ruiz, G. Ruprecht, M. Trinczek, C. Vockenhuber, and C. Wrede, *Commissioning the DRAGON facility at ISAC*, Nuclear Instruments and Methods in Physics Research Section A: Accelerators, Spectrometers, Detectors and Associated Equipment **553**, 491–500 (2005).

[EPI] EPICS, Experimental Physics and Industrial Contro System, available program in: http://www.aps.anl.gov/epics/index.php.

[FFI01] S. Fukuda, Y. Fukuda, M. Ishitsuka, Y. Itow, T. Kajita, J. Kameda, K. Kaneyuki, K. Kobayashi, Y. Koshio, M. Miura, S. Moriyama, M. Nakahata, S. Nakayama, A. Okada, N. Sakurai, M. Shiozawa, Y. Suzuki, H. Takeuchi, Y. Takeuchi, T. Toshito, Y. Totsuka, S. Yamada, S. Desai, M. Earl, E. Kearns, M. Messier, K. Scholberg, J. Stone, L. Sulak, C. Walter, M. Goldhaber, T. Barszczak, D. Casper, W. Gajewski, W. Kropp, S. Mine, D. Liu, L. Price, M. Smy, H. Sobel, M. Vagins, K. Ganezer, W. Keig, R. Ellsworth, S. Tasaka, A. Kibayashi, J. Learned, S. Matsuno, D. Takemori, Y. Hayato, T. Ishii, T. Kobayashi, K. Nakamura, Y. Obayashi, Y. Oyama, A. Sakai, M. Sakuda, M. Kohama, A. Suzuki, T. Inagaki, T. Nakaya, K. Nishikawa, T. Haines, E. Blaufuss, S. Dazeley, K. Lee, R. Svoboda, J. Goodman, G. Guillian, G. Sullivan, D. Turcan, A. Habig, J. Hill, C. Jung, K. Martens, M. Malek, C. Mauger, C. McGrew, E. Sharkey, B. Viren, C. Yanagisawa, C. Mitsuda, K. Miyano, C. Saji, T. Shibata, Y. Kajiyama, Y. Nagashima, K. Nitta, M. Takita, M. Yoshida, H. Kim, S. Kim, J. Yoo, H. Okazawa, T. Ishizuka, M. Etoh, Y. Gando, T. Hasegawa, K. Inoue, K. Ishihara, T. Maruyama, J. Shirai, M. Koshiba, Y. Hatakeyama, Y. Ichikawa, M. Koike, K. Nishijima, H. Fujiyasu, H. Ishino, M. Morii, Y. Watanabe, U. Golebiewska, D. Kielczewska, S. Boyd, A. Stachyra, R. Wilkes, and K. Young, *Solar ^{8}B and hep Neutrino Measurements from 1258 Days of Super-Kamiokande Data*, Physical Review Letters **86**, no. 25, 5651–5655 (2001).

[FHI96] Y. Fukuda, T. Hayakawa, K. Inoue, K. Ishihara, H Ishino, S. Joukou, T. Kajita, S. Kasuga, Y. Koshio, T. Kumita, K. Matsumoto, M. Nakahata, K. Nakamura, K. Okumura, A Sakai, M. Shiozawa, J. Suzuki, Y. Suzuki, T. Tomoeda, Y. Totsuka, K. S. Hirata, K. Kihara, Y. Oyama, M. Koshiba, K. Nishijima, T. Horiuchi, K. Fujita, S. Hatakeyama, M. Koga, T. Maruyama, A. Suzuki, M. Mori, T. Kajimura, T. Suda, A. T. Suzuki, T. Ishizuka, K. Miyano, H. Okazawa, T. Hara, Y. Nagashima, M. Takita, and T. Yamaguchi, *Solar Neutrino Data Covering Solar Cycle 22*, Physical Review Letters **77**, no. 9, 1683–1686 (1996).

[FM62] J. Flegenheimer and Y. Marcus, *Specific activity after intermittent irradiation*, Nucleonics **20**, no. 5, 75–78 (1962).

[GAB94] U. Greife, C. Arpesella, C. A. Barnes, F. Bartolucci, E. Bellotti, C Broggini, P. Corvisiero, G. Fiorentini, A. Fubini, F. Gorris, C. Gustavino, M. Junker, R .W. Kavanagh, A. Lanza, P. Prati, P. Quarati, W. S. Rodney, C. Rolfs, H. P. Tryutvetter, and D. Zahnow, *Laboratory for Underground Nuclear Astrophysics (LUNA)*, Nuclear Instruments and Methods in Physics Research Section A: Accelerators, Spectrometers, Detectors and Associated Equipment **350**, 327–337 (1994).

[Gav01] V.N. Gavrin, *Solar neutrino results from SAGE*, Nuclear Physics B **91**, 36–43 (2001).

[GBB04] U. Greife, S. Bishop, L. Buchmann, M.L. Chatterjee, A.A. Chen, J.M. D'Auria, S. Engel, D. Gigliotti, D Hunter, D.A. Hutcheon, A. Hussein, C.C. Jewett, A.M. Laird, M. Lamey, W. Liu, A. Olin, D. Ottewell, J. Rogers, and C. Wrede, *Energy loss around the stopping power maximum of Ne, Mg and Na ions in hydrogen gas*, Nuclear Instruments and Methods in Physics Research Section B: Beam Interactions with Materials and Atoms **217**, no. 1, 1–6 (2004).

[GCC07] Gy. Gyürky, F. Confortola, H. Costantini, A. Formicola, D. Bemmerer, R. Bonetti, C. Broggini, P. Corvisiero, Z. Elekes, Zs. Fülöp, G. Gervino, A. Guglielmetti, C. Gustavino, G. Imbriani, M. Junker, M. Laubenstein, A. Lemut, B. Limata, V. Lozza, M. Marta, R. Menegazzo, P. Prati, V. Roca, C. Rolfs, C.Rossi Alvarez, E. Somorjai, O. Straniero, F. Strieder, F. Terrasi, and H. Trautvetter, *$^3He(\alpha,\gamma)^7Be$ cross section at low energies*, Physical Review C **75**, 035805 (2007).

[GEA] GEANT, CERN Application Software Group. Geant detector description and simulation tool, CERN program library, April 1995.

[GMH02] A Gottdang, D.J.W. Mous, and R.G. Haitsma, *The novel HVEE 5 MV Tandetron™*, Nuclear Instruments and Methods in Physics Research Section B: Beam Interactions with Materials and Atoms **190**, 177–182 (2002).

[Gro08] Particle Date Group, Phys. Lett. B **667**, 1 (2008).

[GUI] TRIUMF: GUIDE FOR EXPERIMENTERS, Available in: http://www.triumf.info/wiki/exp−prog/index.php.

[HBB03] D.A. Hutcheon, S. Bishop, L. Buchmann, M.L. Chatterjee, A.A. Chen, J.M. D'Auria, S. Engel, D. Gigliotti, U. Greife, D. Hunter, A. Hussein, C.C. Jewett, N. Khan, M. Lamey, A.M. Laird, W. Liu, A. Olin, D. Ottewell, J.G. Rogers, G. Roy, H. Sprenger, and C. Wrede, *The DRAGON facility for nuclear astrophysics at TRIUMF-ISAC: design, construction and operation*, Nuclear Instruments and Methods in Physics Research Section A: Accelerators, Spectrometers, Detectors and Associated Equipment **498**, 190–210 (2003).

[HBO] HBOOK, CERN Application Software Group. HBOOK - Statistical Analysis and Histogramming, CERN program library long writeup w5013, January 1995.

[HBR88] M. Hilgemeier, H.W. Becker, C. Rolfs, H.P. Trautvetter, and J.W. Hammer, *Absolute Cross Section of the* , Zeitschrift für Physik A: Atoms and Nuclei **329**, 243–254 (1988).

[HJ59] H. D. Holmgren and R. L. Johnston, *$H^3(\alpha,\gamma)Li^7$ and $He^3(\alpha,\gamma)Be^7$*, Physical Review **113**, no. 6, 1156–1558 (1959).

[Hoy46] F. Hoyle, *The synthesis of the elements from hydrogen*, Astrophysical J. Suppl. **5**, 343 (1946).

[Hoy54] F. Hoyle, *On nuclear reactions ocurring in very hot stars. I. The synthesis of elementes from carbon to nickel*, Astrophysical J. Suppl. **1**, 121 (1954).

[HRF12] D.A. Hutcheon, C. Ruiz, J. Fallis, J.M. D'Auria, B. Davids, U. Hager, L. Martin, D.F. Ottewell, S. Reeve, and A. Rojas, *Measurement of radiative capture resonance energies with an extended gas target*, Nuclear Instruments and Methods in Physics Research Section A: Accelerators, Spectrometers, Detectors and Associated Equipment **689**, 70–74 (2012).

[HSB72] D. M. Hardy, R. J. Spiger, S. D. Baker, Y.S. Chen, and T.A. Tombrello, *SCATERING OF ^3He AND ^4He FROM POLARIZED* 3*He BETWEEN 7 AND 18 MeV*, Nuclear Physics A **195**, 250–256 (1972).

[Hut02] D.A. Hutcheon, *The gas target density profile*, DRAGON Technical Note.

[Ili07] Christian. Iliadis, *Nuclear Physics of Stars*, WILEY-VCH Verlag GmbH & Co., 2007.

[JAC08] K. Jayamanna, F. Ames, G. Cojocaru, R. Baartman, P. Bricault, R. Dube, R. Laxdal, M. Marchetto, M. MacDonald, P. Schmor, G. Wight, and D. Yuan, *Off-line ion source terminal for ISAC at TRIUMF.*, The Review of scientific instruments **79**, 02C711 (2008).

[JWG10] K. Jayamanna, G. Wight, D. Gallop, R. Dube, V. Jovicic, C. Laforge, M. Marchetto, M. Leross, D. Louie, R. Laplante, R. Laxdal, M. McDonald, G. J. Wiebe, V. Wang, and F. Yan, *A multi-charge ion source (Supernanogan) for the OLIS facility at ISAC/TRIUMF.*, The Review of scientific instruments **81**, 02A331 (2010).

[KA84] T. Kajino and A. Arima, *Resonanting-Group Calculation of Radiative Capture Reactions $\alpha(^3He,\gamma)^7Be$ and $\alpha(t,\gamma)^7Li$ at Astrophysical Low Energies*, Physical Review Letters **52**, 739 (1984).

[Kaj86] T. Kajino, *The 3He(α, γ)7Be and 3He(α, γ)7Li reactions at astrophysical energies*, Nuclear Physics A **460**, no. 3, 559–580 (1986).

[KBB82] H. Kräwinkel, H. W. Becker, L. Buchmann, K. U. Kettner, W. E. Kieser, R. Santo, P. Schmalbrock, H. P. Trautvetter, A. Vlieks, C. Rolls, J. W. Hammer, W.S. Rodney, R.E. Azuma, and W.S. Rodney, *The $^3He(\alpha,\gamma)^7Be$ Reaction and the Solar Neutrino Problem*, Zeitschrift für Physik A: Atoms and Nuclei **304**, 307–332 (1982).

[KBR64] Hsin-Min Kuan, T. W. Bonner, and J. R. Risser, *An investigation of the C^{12}+He^3 Reactions at bombarding energies between 1.8 and 5.4 MeV*, Nuclear Physics **51**, 481–517 (1964).

[KD11] O.S. Kirsebom and B. Davids, *One fewer solution to the cosmological lithium problem*, Physical Review C **84**, 058801 (2011).

[KDN09] E. Komatsu, J. Dunkley, M. R. Nolta, C. L. Bennett, B. Gold, G. Hinshaw, N. Jarosik, D. Larson, M. Limon, L. Page, D. N. Spergel, M. Halpern, R. S. Hill, A. Kogut, S. S. Meyer, G. S. Tucker, J. L. Weiland, E. Wollack, and E. L. Wright, *Five-Year Wilkinson Microwave Anisotropy Probe Observations: Cosmological Interpretation*, The Astrophysical Journal Supplement Series **180**, 330–376 (2009).

[KIN81] B.T. Kim, T. Izumoto, and K. Nagatani, *Radiative capture reaction $^3He(\alpha,\gamma)^7Be$ at low energies*, Physical Review C **23**, no. 1, 33 (1981).

[Kir98] T. Kirsten, *GALLEX Solar Neutrino Results*, Progress in Particle and Nuclear Physics **40**, 85 (1998).

[Kno00] Gleen.F. Knoll, *Radiation Detection and Measurement*, John Wiley & Sons, Inc., 2000.

[KTA87] T. Kajino, H. Toki, and Sam M. Austin, *Radiative Alpha-capture rates leading to A=7 nuclei: applications to the solar neutrino problem and big bang nucleosynthesis*, The Astrophysical Journal **319**, 531–540 (1987).

[KUD13] A. Kontos, E. Uberseder, R. DeBoer, J. Görres, C. Akers, A. Best, M. Couder, and M. Wiescher, *Astrophysical S factor of $^3He(\alpha,\gamma)^7Be$*, Physical Review C **87**, 065804 (2013).

[Lam01] Michael Joseph. Lamey, *A microchannel detection system for dragon*, Master's thesis, Simon Fraser University, 2001.

[Lan86] K. Langanke, *Microscopic potential model studies of light nuclear capture reactions*, Nuclear Physics A **457**, 351–366 (1986).

[Leo87] W.R. Leo, *Techniques for Nuclear and Particle Physics Experiments*, Springer-Verlag Berlin Heidelberg, 1987.

[LIB03] W. Liu, G. Imbriani, L. Buchmann, A. A. Chen, J. M. D. Auria, A. D'Onofrio, S. Engel, L. Gialanella, U. Greife, D. Hunter, A. Hussein, D.A. Hutchon, A. Olin, D. Ottewell, D. Rogalla, J. Rogers, M. Romano, and F. Terrasi, *Charge state studies of low energy heavy ions passing through hydrogen and helium gas*, Nuclear Instruments and Methods in Physics Research **496**, 198–214 (2003).

[LIS] LISE++, Available en: http://groups.nscl.msu.edu/lise/lise.html.

[LT58] A.M. Lane and R.G. Thomas, *R-Matrix Theory of Nuclear Reactions*, Reviews of Modern Physics **30**, no. 2, 257 (1958).

[Lun] The Lund/LBNL Nuclear Data Search, Available in the web page: http://nucleardata.nuclear.lu.se/nucleardata/toi/.

[MAK93] P. Mohr, H. Abele, H. Krauss, H. Oberhummer, and A. Denker, *Alpha scattering and capture reactions in the A=7 system at low energies*, Physical Review C **48**, no. 3, 1420–1427 (1993).

[MBH06] C. Matei, L. Buchmann, W. Hannes, D. Hutcheon, C. Ruiz, C. Brune, J. Caggiano, a. Chen, J. D'Auria, a. Laird, M. Lamey, Zh. Li, Wp. Liu, a. Olin, D. Ottewell, J. Pearson, G. Ruprecht, M. Trinczek, C. Vockenhuber, and C. Wrede, *Measurement of the Cascade Transition via the First Excited State of O16 in the $^{12}C(\alpha,\gamma)^{16}O$ Reaction, and Its S Factor in Stellar Helium Burning*, Physical Review Letters **97**, no. 24, 242503 (2006).

[MES] MESYTEC Gmbh & Co. KG, http://www.mesytec.com.

[MH86] T. Mertelmeier and H.M. Hofmann, *Consistent Cluster Model Description of the Electromagnetic Properties of Lithium and Beryllium nuclei*, Nuclear Physics A **459**, 387–416 (1986).

[Mik86] S.P. Mikheyev, A. Yu. Smirnov, Sov. J. Nucl. Phys. **42**, 913 (1986).

[MM93] Robert A. Malaney and Grant J. Mathews, *Probing the early universe: a review of primordial nucleosynthesis beyond the standard big bang*, Physics Reports **229**, no. 4, 145–219 (1993).

[MN67] W. Meckbach and I.B. Nemirovsky, *Charge Equilibrium of Helium Ions in Helium Gas from 60 to 840 keV*, Physical Review **153**, no. 1, 13 (1967).

[MN02] A. M. Mukhamedzhanov and F. M. Nunes, *Low energy behavior of the astrophysical S -factor in radiative captures to loosely bound final states*, Nuclear Physics A **708**, 437–459 (2002).

[Moh09] Peter Mohr, *Low-energy $^3He(\alpha,\alpha)^3He$ elastic scattering and the $^3He(\alpha,\gamma)^7Be$ reaction*, Physical Review C **79**, no. 6, 1–10 (2009).

[Nar13] B. S. Nara Singh, *NEW ADVANCES FOR THE $^3He(\alpha\ ,\gamma)^7Be$ SOLAR FUSION REACTION* , Acta Physica Polonica B **44**, no. 3, 511–520 (2013).

[NDA69] K. Nagatani, M. R. Dwarakanath, and D. Ashery, *THE $^3He(\alpha,\gamma)^7Be$ REACTION AT VERY LOW ENERGY*, Nuclear Physics A **128**, 325–332 (1969).

[Nef] Thomas Neff, private communication.

[Nef11] Thomas Neff, *Microscopic Calculation of the $^3He(\alpha,\gamma)^7Be$ and $^3H(\alpha,\gamma)^7Li$ Capture Cross Sections Using Realistic Interactions*, Physical Review Letters **106**, no. 4, 1–4 (2011).

[NEHY07] Y. Nir-El, G Haquin, Z Yungreiss, M Hass, G Goldring, S K Chamoli, B S Nara Singh, S Lakshmi, G Heidenreich, and S Teichmann, *Precision measurement of the decay rate of ^7Be in host materials*, Physical Review C (R) **75**, 012801 (2007).

[NHNEH04] B. S. Nara Singh, M. Hass, Y. Nir-El, and G. Haquin, *New Precision Measurement of the $^3He(^4He,\gamma)^7Be$ Cross Section*, Physical Review Letters **93**, 262503 (2004).

[NM10] Christophe Normand and Mª José Gª Borge, *Trazando el paisaje nuclear 50 años de historia de la Karlsruher Nuklidkarte*, Revista Española de Fisica, 76–80 (2010).

[Nol01] Kenneth Nollett, *Radiative α-capture cross sections from realistic nucleon-nucleon interactions and variational Monte Carlo wave functions*, Physical Review C **63**, no. 5, 1–13 (2001).

[NSD12] B. S. Nara Singh, S. K. L. Sjue, B. Davids, M. Hass, P. Adsley, L. Buchmann, M. Carmona-Gallardo, J. Fallis, S. P. Fox, B. Fulton, N. Galinski, U. Hager, D.A. Hutcheon, A. M. Laird, L. Martin, D. Ottewell, S. Reeve, C. Ruiz, G. Ruprecht, A. Shotter, and O. Tengblad, *Cross section measurements of the $^{3}He(\alpha,\gamma)^{7}Be$ reaction using DRAGON at TRIUMF*, Journal of Physics: Conference Series **337**, 012057 (2012).

[Nuc] National Nuclear Data Center (Brookhaven National Laboratory), Available in the web page: http://http://www.nndc.bnl.gov.

[OAB10] Yu. Ts. Oganessian, F. Sh. Abdullin, P. D. Bailey, D. E. Benker, M. E. Bennett, S. N. Dmitriev, J. G. Ezold, J. H. Hamilton, R. a. Henderson, M. G. Itkis, Yu. V. Lobanov, A. N. Mezentsev, K. J. Moody, S. L. Nelson, A. N. Polyakov, C. E. Porter, A. V. Ramayya, F. D. Riley, J. B. Roberto, M. A. Ryabinin, K. P. Rykaczewski, R. N. Sagaidak, D. a. Shaughnessy, I. V. Shirokovsky, M. A. Stoyer, V. G. Subbotin, R. Sudowe, A. M. Sukhov, Yu. S. Tsyganov, V. K. Utyonkov, A. A. Voinov, G. K. Vostokin, and P. A. Wilk, *Synthesis of a New Element with Atomic Number Z=117*, Physical Review Letters **104**, 142502 (2010).

[OBK82] J. Osborne, C. A. Barnes, Ralph Kavanagh, R. M Kremer, G. J. Mathews, J. L Zyskind, Parker P.D., and Howard A. J., *Low-Energy 3He(alpha,gamma)7Be Cross-Section Measurements*, Physical Review Letters **48**, 1664 (1982).

[OBK84] J.L. Osborne, C.A. Barnes, R.W. Kavanagh, R.M. Kremer, G.J. Mathews, J.L. Zyskind, P.D. Parker, and A.J. Howard, *Low-energy behavior of the $^{3}He(\alpha,\ \gamma)^{7}Be$ cross section*, Nuclear Physics A **419**, 115–132 (1984).

[ORT] ORTEC®, http://www.ortec-online.com/.

[OSW00] Keith A. Olive, Gary Steigman, and Terry P. Walker, *Primordial nucleosynthesis: theory and observations*, Physics Reports **333-334**, 389–407 (2000).

[Pas04] C. Pascual Izarra, *Experimental determination of stopping forces for ions in matter*, Ph.D. thesis, Universidad Autonoma de Madrid, 2004.

[PK63] P.D. Parker and R.W. Kavanagh, *$^{3}He(\alpha,\gamma)^{7}Be$ Reaction*, Physical Review **131**, no. 6, 2578 (1963).

[PR64] Philip Pochoda and Hubert Reeves, *A REVISED SOLAR MODEL WITH A SOLAR*, Planetary Space Science **12**, 119–126 (1964).

[QKT81] Q. K. K. Liu, H. Kanada, and Y.C. Tang, *Microscopic study of $^{3}He(\alpha,\ \gamma)^{7}Be$ electric-dipole capture reaction*, Physical Review C **23**, no. 2.

[RBKR03] Philip R. Benington and D. Keith Robinson, *Data Reduction and Error Analysis for the Physical Science*, McGraw-Hill, 2003.

[RDB] R. G. H. Robertson, P. Dyer, T. J. Bowles, Ronald E. Brown, Nelson Jarmie, C. J. Maggiore, and Sam M. Austin, *Cross section of the capture reaction $^{3}He(\alpha,\gamma)^{7}Be$*, Physical Review C **27**, no. 1, 11.

[Ree12] Sarah Reeve, *Determining the transmission efficiency for $^{3}He(\alpha,\gamma)^{7}Be$ in DRAGON*, Master's thesis, Simon Fraser University, 2012.

[Rol88] Clauss E. Rolfs and William S. Rodney, *Cauldrons in the Cosmos*, 1988.

[ROO] ROOT, A Data Analysis Framework-CERN, available program in: http://root.cern.ch/drupal/.

[RSP80] F. Reines, H. W. Sobel, and E. Pasierb, *Evidence for Neutrino Inestability*, Physical Review Letters **45**, no. 16, 1307 (1980).

[SAA05] C. E. Svensson, P. Amaudruz, C. Andreoiu, A. Andreyev, R. A. E. Austin, G. C. Ball, D. Bandyopadhyay, A. J. Boston, R. S. Chakrawarthy, A. A. Chen, R. Churchman, T. E. Drake, P. Finlay, P. E. Garrett, G. F. Grinyer, G. Hackman, B. Hyland, B. Jones, R. Kanungo, R. Maharaj, J. P. Martin, D. Morris, A. C. Morton, C. J. Pearson, A. A. Phillips, J. J. Ressler, R. Roy, F Sarazin, M. A. Schumaker, H. C. Scraggs, M. B. Smith, N. Starinsky, J. J. Valiente-Dobón, J. C. Waddington, and L. M. Watters, *TIGRESS: TRIUMF-ISAC gamma-ray escape-suppressed spectrometer*, Journal of Physics G: Nuclear and Particle Physics **31**, S1663–S1668 (2005).

[Sab03] A. Sabán Iglesias, *Diseño y montaje de una línea en el acelerador de 5 MV de la UAM para física nuclear experimental*, Master's thesis, Universidad Complutense de Madrid, 2003.

[Sea64] R. L. Sears, *Recoil separator ERNA: charge state distribution, target density, beam heating, and longitudinal acceptance*, The Astrophysical Journal **140**, 477–484 (1964).

[SH03] K.A. Snover and A.E. Hurd, *Is e+e- pair emission important in the determination of the ^{3}He+^{4}He S factor?*, Physical Review C **67**, 055801 (2003).

[SL79] G. R. Satchler and W.G. Love, *Folding model potentials from realistic interactions for heavy-ion scattering*, Physics Reports **55**, no. 1, 183-254 (1979).

[SN04] N. Summers and F. Nunes, *^{7}Be breakup on heavy and light targets*, Physical Review C **70**, 011602(R) (2004).

[SR01] Michael S Smith and K Ernst Rehm, *NUCLEAR ASTROPHYSICS MEASUREMENTS WITH RADIOACTIVE BEAMS*, Ann. Rev. Nuclear Part. Sci **51**, 91–130 (2001).

[SRI] SRIM, The Stopping and Range of Ions in Matter, available program in: http://www.srim.org/.

[SSA13] S.K.L. Sjue, B.S. Nara Singh, P. Adsley, L. Buchmann, M. Carmona-Gallardo, B. Davids, J. Fallis, B.R. Fulton, N. Galinski, U. Hager, M. Hass, D. Howell, D.A. Hutcheon, A.M. Laird, L. Martin, D. Ottewell, S. Reeve, C. Ruiz, G. Ruprecht, and S. Triambak, *Beam suppression of the Dragon recoil separator for ^{3}He(α,γ)^{7}Be*, Nuclear Instruments and Methods in Physics Research Section A: Accelerators, Spectrometers, Detectors and Associated Equipment **700**, 179–181 (2013).

[ST67] R. J. Spieger and T.A. Tombrello, *Scattering of He^3 by He^4 and of He^4 by Tritium*, Physical Review **163**, no. 4, 964 (1967).

[TAT86] F.K. Thielemann, M Arnould, and J.W. Truran, *Advances in Nuclear Astrophysics*, vol. 525, eds. E. Vangioni-Flam et al., 1986.

[Tay82] Jonh. R. Taylor, *An Introduction to Error Analysis. The study of uncertainties in physical measurements*, University Science Books, 1982.

[Ten96] O. Tengblad, *Desing of a gas system (internal report)*, 1996.

[TP61] T.A. Tombrello and G.C. Phillips, *Cluster Nature of Li^7 and Be^7*, Physical Review **122**, no. 1, 224–228 (1961).

[TP63a] T.A. Tombrello and P.D. Parker, *Direct-Capture Model for the He*$^3(\alpha,\gamma)$*Be*^{7} *and T*(α,γ)*Li*^{7} *Reactions*, Physical Review **131**, no. 6, 2582 (1963).

[TP63b] T.A. Tombrello and P.D. Parker, *Scattering of He*^{3} *from He*^{4}, Physical Review **130**, no. 3, 1112 (1963).

[VKSW83] H. Volk, H. Kräwinkel, R. Santo, and L. Wallek, *Activation Measurement of the* ^{3}*He*$(^4$*He*$,\gamma)^7$*Be*, Zeitschrift für Physik A: Atoms and Nuclei **310**, 91–94 (1983).

[Vuj14] Brittney Vujcich, *Dragon pumping tube alignment and quadrupole alignement*, Master's thesis, Dalhousie University, 2014.

[Wee37] John A. Weeler, *On the Mathematical Description of Light Nuclei by the Mothod of Resonating Group Structure*, Physical Review **52**, 1107 (1937).

[Whe37] John Archibald Wheeler, *Molecular Viewpoints in Nuclear Stucture*, Physical Review **52**, 1983 (1937).

[WHRD03] Chris Wrede, Ahmed Hussein, Joel G. Rogers, and John D'Auria, *A double sided silicon strip detector as a DRAGON end detector*, Nuclear Instruments and Methods in Physics Research Section B: Beam Interactions with Materials and Atoms **204**, 619–624 (2003).

[WKT84] H. Walliser, H. Kanada, and Y. C. Tang, *Study of the* ^{3}*He*$(\alpha,\gamma)^7$*Be radiative-capture reaction with resonanting-group wave functions*, Nuclear Physics A **419**, 133–147 (1984).

[WRH00] L. Weissman, R. Raabe, M. Huyse, G. Koops, H. Pattyn, G. Terwagne, and P. Van Duppen, *An implanted* ^{4}*He target for experiments with radioactive beams*, Nuclear Instruments and Methods in Physics Research Section B: Beam Interactions with Materials and Atoms **170**, 266–275 (2000).

[WSS95] R.B. Wiringa, V.G.J. Stoks, and R. Schiavilla, *Accurate nucleon-nucleon potential with charge-independence breaking*, Physical Review C **51**, no. 1.